Dielectric Relaxation Time Spectroscopy For Tissue Characterisation

by

Svetlana Jouravleva
BSc MSc

A Thesis submitted in partial fulfilment of the requirements of
Oxford Brookes University for the Degree of

Doctor of Philosophy

School of Engineering
Oxford Brookes University

June 2001

Abstract

This thesis is concerned with Electrical Impedance Spectroscopy (EIS), a non-invasive technique for characterising biological tissue and distinguishing pathology. The thesis is focused on the development of an improved method for extracting physiologically related parameters from the measured impedance data *in vivo* and instrumentation for spectroscopic measurements.

In EIS, the electrical properties of physiological tissues, defined by their composition and structure, are measured as functions of frequency. Experimental observations of the existence of dielectric dispersions caused by distributions of dielectric relaxation time (DRT) constants were made on different types of biological material. It is postulated that widely used approaches for modelling these electrical properties are fundamentally flawed. The research work concentrates on the reconstruction of DRT spectra directly from the measured frequency response. The reconstruction problem involves inversion of a linear operator and like many inverse problems, is complicated by the ill-posed nature of the problem. In this thesis an inversion algorithm - Galerkin Regularised Inverse Method (GRIM) - based on standard mathematical methods is developed. The DRT spectrum establishes a link between the raw impedance data and the physiological structure and function of biological tissues. The GRIM yields a large number of independent parameters each related to process on a different scale. Special care was taken in testing the method on simulated data and improving its resolution.

The thesis is also concerned with the design and practical implementation of EIS systems. Two approaches are considered: systems based on commercially available Impedance Analysers and systems designed specially for studies *in vivo*. To evaluate the GRIM, an Impedance Analyser, benefitting from a higher accuracy and a wider frequency range, is used. To meet the more rigorous specification demanded for studies on living human tissues, an electrical impedance spectrometer is developed. The suitability of different current sources is investigated.

This research work includes studies of animal tissue *in vitro* and *in vivo*. Optimal experiments are defined in terms of the measurement frequency range and the entire experimental protocol for dielectric spectroscopy is established. These biological data are used to evaluate the GRIM. A comparison between different tissue classes *in vivo* is made. From studying ischemic tissues, it is postulated and verified that physiological differences and changes can be measured using the technique of DRT spectroscopy.

Acknowledgements

First of all I would like to thank my supervisor Chris McLeod for his guidance, time, enthusiasm and humour throughout this project. I also wish to express my sincere thanks and appreciation to my second supervisor Kevin Paulson for his invaluable impact on my work and help with mathematical modelling. I wish to express my gratitude to Oxford Brookes University, and in particular to the School of Engineering for providing financial support and facilities.

I would like to thank Dr. Michael Schaefer for organising my visit to the Department of Experimental Surgery at Heidelberg University as well as for help in obtaining biological data and making suggestions for analysis. Also many thanks to his colleagues who played an important role during surgical operations.

Thanks are also due to Prof. Michael Pidcock for his useful comments and suggestions on conference paper presentations.

Sincere thanks go to Alla Cordery with whom it has been a pleasure to work.

Special thanks to Andrea Borsic for endless help and patience, who I hope has enjoyed working with me as much as I enjoyed working with him. For many constructive comments and much support, special thanks go to Andreas Pohlmann who was my first colleague in DM 25. My fellow postgraduates, Dimitar, Rui, Pong and Jorshua have often been a source of a good humour and diversion. Advice and assistance from them is greatly appreciated too.

I would like to give a personal thanks to my old friends in Russia for not complaining about how little I have written them and for their encouragement. Special thanks deservedly belong to Mikhail, who supported my efforts during the past three years on the research and on this thesis. And finally thanks to all my family for constant encouragement and support during my life in England.

To my parents

Contents

Chapter 1

Introduction

1.1 Impedance measurement

It is well known that virtually every liquid and solid is able to pass current when a voltage is applied to it. For a sine wave (AC) voltage, applied to a linear material, a sine wave current flows through it. The ratio of voltage to current (V/I) amplitude is known as the impedance, (Z). In most materials the impedance varies with the frequency of the applied voltage, in a way that is related to the properties of the material. This may be due to the physical structure of the material, to chemical processes within it, or to a combination of both. If a measurement of impedance over a suitable frequency range is made, and the results plotted on suitable axes, it is possible to relate the results to the physical and chemical properties of the material. Since an impedance measurements are repeatable and non–destructive, it can provide valuable information about a wide variety of substances, components and systems.

The features that make impedance measurement attractive over other investigative techniques, such as X–ray, Magnetic Resonance Imaging (MRI), Computerised Tomography (CT) and ultrasound techniques, include:

- Rapid acquisition of data (often within microseconds)
- Accurate and repeatable measurements
- Measurements relate to process activity
- Investigates a wide range of size and time scales
- Non–destructive; completely harmless to biological tissue
- Highly adaptable to a wide variety of different applications

- Low cost.

Impedance measurements find a wide range of application. For example, in electrochemistry the measurements of impedance are used in order to indicate the presence and the rate of corrosion, [1]. Electrical impedance techniques are also used in geophysical prospecting. Practical applications exist in hydrology, mapping of coal or sand deposits, seismological studies and many others, [2]. Electrical impedance is often used in medicine and physiology. For example, it can be used for monitoring changes in fluid volume within the lung, which can be related to the changes in the thoracic impedance. The changes in transthoracic impedance can also be related to the events in the cardiac cycle and in some circumstances cardiac output can be estimated. Investigative techniques using electrical impedance measurements include Electrical Impedance Tomography (EIT) and Electrical Impedance Spectroscopy (EIS). EIT aims to image two and three dimensional volumes containing different types of tissues and physiological functions. EIT systems usually operate at a fixed frequency. EIT relies on the observation that different tissue types have different impedance. At a particular frequency, there are large differences between the impedances of organs. However, in practice, there is no single frequency at which impedance can discriminate all types of tissue. Neither can a single frequency characterise the types of tissue within an organ. Therefore, measurements at a number of frequencies are necessary and this is known as Electrical Impedance Spectroscopy. This latter method is considered in the subsequent chapters and defines the area of the present research.

1.2 Electrical Impedance Spectroscopy

Electrical Impedance Spectroscopy (EIS) is a powerful method for characterising many of the electrical properties of materials and their interfaces with electronically conducting electrodes. EIS has been recognised as a useful analytical tool in material research and development as well as in medicine because it involves relatively simple electrical measurements that can be automated and results can be used for the interpretation of fundamental electrochemical and electronic processes.

In EIS, the impedance of a sample of material can be measured directly in the frequency domain by applying a single–frequency voltage of known amplitude to the interface and measuring the phase shift and amplitude, or real and imaginary parts, of the resulting current at that frequency. Typically the frequency of the

applied voltage is swept across a range of frequencies spanning several decades. Commercial instruments are available which measure the impedance as a function of frequency automatically and which are easily interfaced to Personal Computers. The complexity of the method comes from the difficulty in performing reproducible experiments, the problem of separating the response of the measuring equipment from that of the sample and the interpretation of the measurements.

1.3 EIS in Medicine

This thesis focuses on applications of EIS in medicine. Non-invasive techniques for studying the body have long been popular with both patients and doctors. Most widely used are X–ray photographs, X–Ray computerised Axial Tomography (CAT scan), Ultrasound and MRI. In all these methods, energy is applied to the body in the form of an oscillating field or wave. This interacts with the tissues and the response is measured. Each of these techniques images different properties of the tissue and the operation of organs and so has different applications.

More recently, EIT has been developed as an alternative to complement the methods mentioned above with particular application in functional imaging. EIT is fast, cheap, harmless and can be used for long term monitoring. It may also image rapid changes in the physiological state of tissue such as the beginning of an epileptic fit in the brain. EIT is an area of active research: particularly studies of medical applications, such as measuring lung perfusion, lung ventilation, gastric emptying, cardiac output and locating epileptic foci.

A current research aim is to develop multi–frequency EIT (MEIT). In order to produce MEIT images that are useful for medical diagnosis purposes, the measurement system must identify different tissues located close to each other in the body, such as liver and spleen or muscle and lung. Usually two or more frequencies are used in MEIT. The contrast of the resulting images is higher if the impedance variation with frequency is larger, and is different for different tissues.

Multi–frequency measurements allow the tissue impedance spectrogram to be produced [3], [4]. Typically, multi–frequency electrical data are collected for several tissue types and the measurements are fitted to some mathematical model, such as the Cole model [5]. Some widely used mathematical models will be presented in chapter 2. Fitting parameters are calculated for each type of tissue. These parameters are plotted on a scatter diagram and statistical techniques, such as cluster analysis, are used to test if the different classes of tissue are distin-

Table 1.1: Relative permittivity of Biological Tissues by Gabriel *et al* [17]

	frequency, Hz			
Material	**10**	**10^4**	**10^6**	**2×10^{10}**
Liver, Ovine @ 37°C	1.81×10^7	3.15×10^4	1.56×10^3	20.8
Lung deflated, Human @ 37°C	4.62×10^7	1.63×10^4	5.8×10^2	10.7
Lung inflated, Human @ 37°C	3×10^7	1.63×10^4	5.8×10^2	10.66
Muscle, Ovine @ 37°C				
Parallel Fibers	8.31×10^7	2.86×10^4	4.11×10^2	29.7
Transverse Fibers	4.07×10^7	3.04×10^4	1.57×10^3	28.3
Kidney, Ovine @ 37°C	2.78×10^7	4.15×10^4	1.97×10^3	27.5
Fat, Bovine @ 37°C	1.06×10^7	1.14×10^3	24.7	3.19
Spleen, Ovine @ 37°C	4.77×10^7	1.38×10^4	1.96×10^3	29.9

guishable by these data. A large and growing body of literature exists confirming that multi–frequency electrical measurements of tissue can be used to distinguish different tissues and clinically useful tissue characteristics [6], [7], [8].

This empirical approach is useful in developing clinical techniques but does not directly illuminate the link between impedance measurements and tissue physiology or function. This thesis attempts to extract parameters, related to structure and processes occurring on different size and time scales, from the impedance spectrogram. In later chapters these data are interpreted in terms of cell physiology.

The applicability of EIS for medical purposes hinges on the variation in the electrical properties of normal and pathological tissues as a function of frequency for the different organs. Table 1.1 shows the dependence of dielectric permittivity on frequency for different types of tissue. The dielectric permittivity is directly related to the impedance (see section 2.3). It is clear that soft tissue permittivities range across 7 orders of magnitude as the frequency is swept from 10 Hz to 20 GHz. At the same frequency, the permittivity of soft tissue can vary by a factor of 10.

1.4 Brief History

Ohm presented his famous law in 1827. It establishes a linear relationship between *DC* current and voltage and originally was developed for metals. However, it was

followed by various attempts to measure the resistance of all sorts of materials, including biological tissues. During the 19th century a number of researchers, *e.g.* du Bois–Reymond, demonstrated that the resistance of animal tissues decreased with increasing frequency.

Bernstein postulated that tissue consisted of conductive cells enclosed in an insulating membrane. The cell membrane is slightly permeable to ions and therefore represents the resistive part of cells.

Experimental support for the membrane hypothesis was provided by Hober (1910, 1912, 1913) [9] who measured the impedance of red blood cells over a wide frequency range. He found a large decrease in the resistivity of a sample of blood, after the cells had been haemolysed and the cell membrane destroyed. The conclusion was that the intracellular fluid of the living cell was an electrolyte which played a part in conduction after the destruction of membranes. The first estimates for the low– and high–frequency conductivity values were provided.

Philippson (1921) [10] interpreted tissue impedance in terms of the resistor–capacitor model shown in Fig. 1.1.

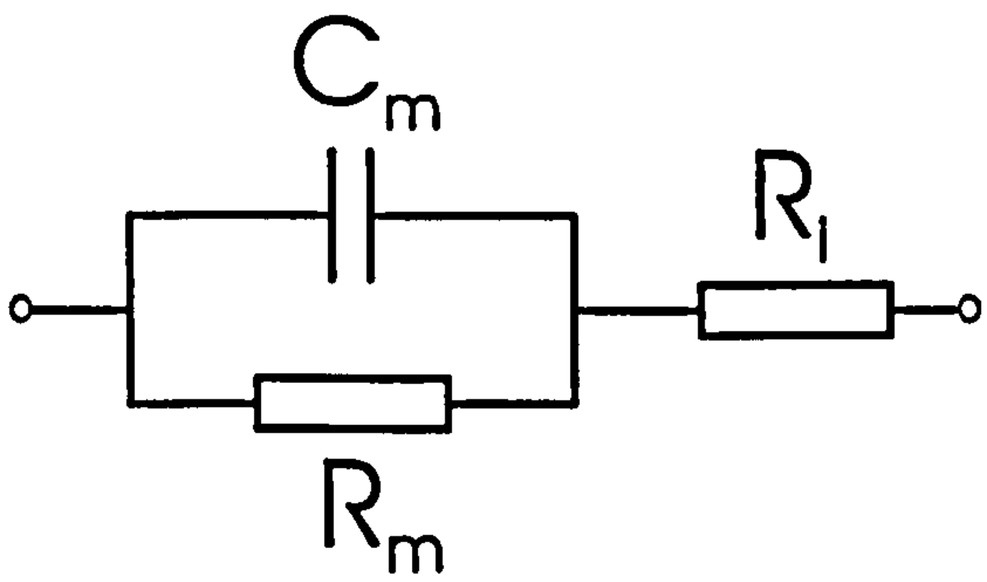

Figure 1.1: *A resistor–capacitor model for the impedance of tissue (Philippson/Lapicque).*

The model was previously proposed by Lapicque (1907) [11] who investigated the behaviour of nerve cell membranes. In this model, at low frequencies the impedance is represented by resistances $R_i + R_m$ because the capacitor C_m has a high impedance and passes little current. With increasing frequency, the impedance of capacitor C_m decreases, and it increasingly "short circuits" R_m. The overall resistance therefore decreases to R_i. R_i was interpreted as the resistivity of the intracellular space, while R_m and C_m the resistance and capacitance of the membrane.

In 1925 Fricke and Morse [12] found that their measurements on suspensions of red blood cells could be accurately fitted to a circuit shown in Fig. 1.2. R represents the resistive properties of the suspending medium, S that of the intracellular space, while C is the membrane capacitance.

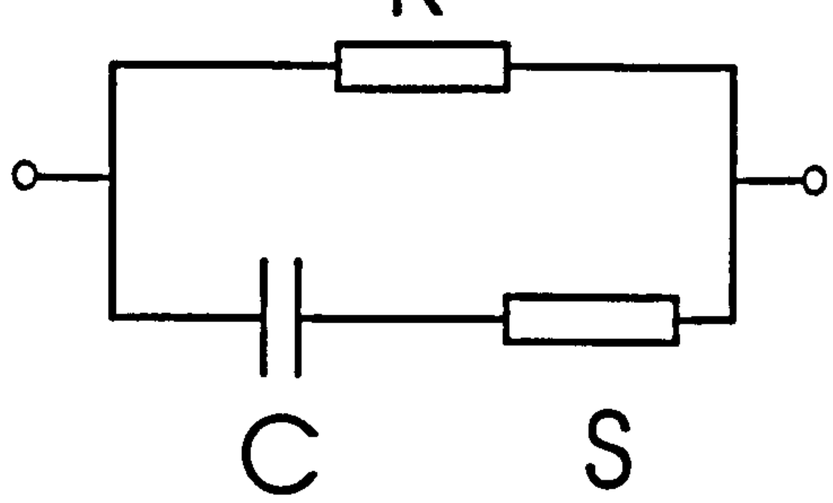

Figure 1.2: *The equivalent circuit model used by Fricke and Morse to represent the electrical properties of cell suspensions.*

However, these simple RC circuits could not explain the form of the impedance loci. The observed steps in the loci were called dispersions and three were identified and labelled α, β and γ. Fricke, Cole and Curtis made the first step to explain the β–dispersion by applying the relevant Maxwell equations to cell suspensions surrounded by membranes.

Cole (1932) [13] noted that many cell membranes could be represented by the series combination of a frequency–dependent capacitance and resistance. He was the first to draw the "depressed" semicircular impedance loci, since known as Cole–Cole plots, for a wide range of biological tissues. The parameters of the circular arcs were used to characterise the tissues. Cole proposed a modified Lapicque equivalent circuit model which included a "constant phase element", Z_{CPE}, related to the frequency dependence of the resistive and capacitive components. The model involves the parallel combination of Z_{CPE} and a resistance. Then the famous "Cole–Cole equation" for the overall impedance of his modified circuit eventually appeared in 1940, see Fig. 2.3.

After 1941, studies by biophysicists Foster, Schwan, *etc.* [14] identified relaxation phenomena as the underlying mechanism leading to Cole–Cole loci. It was determined that distributions of diclectric relaxation times lead to depressed, semi–circular impedance loci.

A more detailed historical overview can be found in the paper of McAdams and Jossinet [15]. Also the most complete tissue data have been published by

Camelia and Sami Gabriel who studied electrical properties of over than 30 tissue types in wide frequency range 10 Hz to 20 GHz [16], [17], [18].

1.5 EIS at Oxford Brookes University

The work of EIT Oxford Polytechnic (Oxford Brookes University since 1991) group was started in 1985. Interest developed in the mathematics of the EIT reconstruction as an inverse problem and led to the design and construction of the first tomograph OXPACT 1, [19]. The system operated only at one frequency, 60 kHz. The subsequent tomograph OXBACT 2 was completed by Q.S.Zhu in 1991, [20]. The new system had important limitations preventing its use *in vivo*. One of the problems was that system had no electrical isolation, which is required by standard patient safety regulations. To conduct experiments *in vivo*, it was decided to design a third generation of the system OXBACT 3. OXBACT 3 is currently being used for clinical studies. It was designed as a multi–frequency tomograph which could operate at three frequencies 10 kHz, 40 kHz and 160 kHz. It was considered that with three frequencies and with a complex measurement scheme, enough information would be available to determine the circle and its parameters, known as the Cole parameters, for internal organs. The overview of hardware on the first and existing systems can be found in chapter 5.

Multi–frequency EIT has primarily been developed for static imaging. Static, or absolute, imaging attempts to calculate the true impedance everywhere in the region to be imaged. It has the potential to combine two techniques, EIT and Spectroscopy. It would have the important advantage that a large volume could be "scanned" and the tissue characterised at all locations within the imaged volume. Technically this goal will be very difficult to achieve due to the hardware problems discussed in chapter 5 and the lack of resolution in EIT measurements far from the electrodes. One of the biggest problems is the connection between the patient and the instrument. There are many potential sources of error introduced by electrode–skin interactions. The work on the design of an impedance probe for EIS measurements *in vivo* was carried out at Oxford Brookes University by K. S. Paulson, [21]. It consists of four circular, concentric electrodes. The size and geometry of the probe allow sampling of localised volume of tissue but with increased sampling depth in comparison with the standard four–electrode probe. This probe is described in detail in section 5.6. In the beginning of this project, it was decided to separate spectroscopy and EIT in order to obtain more detailed information about tissue electrical characteristics.

1.6 The aim and the contents of the thesis

The aim of this thesis is to develop EIS for tissue characterisation. To achieve this aim, work has been carried out on both EIS instrumentation and a mathematical method for data analysis. Different approaches have been considered and will be presented in subsequent chapters.

Even if impedance data could be collected within a wide frequency range in EIS, an effective method to determine the useful information about specific tissue characteristics, such as cell size, shape, number, clustering, hydration and the clinically useful intra–cellular to inter–cellular volume ratio, does not exist. A novel mathematical method for EIS has been developed aiming to establish a link between the electrical measurements on the biological sample and its cell characteristics. The problems of the approaches described by other authors have been also discussed. Attempts have been made to derive tissue physiological information rather than give the raw frequency response. Some of the results that are presented in this thesis have been already published [22], [23], [24]. The purpose of this presentation is not only to summarise these results but to give a theoretical background of the proposed method based on the computation of the dielectric relaxation time distribution. The presented method has been tested with real data. The data have been collected *in vitro* and *in vivo*. The proposed mathematical method has been compared with some other well–known interpretations of data in EIS such as a Cole-Cole model and equivalent circuit analysis. A review of them is also given. Much attention is directed towards an understanding of the permittivity spectra and developing DRT spectroscopy as a possible means of improving their understanding.

The thesis is divided into seven chapters. After the Introduction in chapter 1, the electrical properties of biological tissues are considered in chapter 2. This chapter gives the theoretical basis of relaxation processes in tissue when an electrical field is applied. A review of well–known methods such as parametric model (Cole–Cole), electrical models and equivalent circuit analysis are introduced. Their disadvantages are discussed.

The mathematical relationship between the DRT distribution and the frequency response is presented in chapter 3. Analytic DRT distributions with known frequency responses are reviewed. This chapter introduces the general DRT inverse problem where arbitrary DRT distributions are calculated from impedance spectrograms measured experimentally. The most recent approach for reconstruc-

tion of relaxation spectrum - moving–average formulae - is presented in section 3.4. This chapter introduces important sampling localisation theorems which define the measurement frequency range. The drawbacks of these mathematical approaches for real data are considered.

In chapter 4 a new analysis for Dielectric Relaxation Time Spectroscopy (DRTS) is presented. The GRIM solves a weak form of the inverse problem using the Rayleigh–Ritz Galerkin method. Regularisation techniques are developed to deal with the ill–posedness of the inverse problem. The limitations of the method and possible improvement of the resolving power are discussed in section 4.8. Section 4.10 presents the MatLab implementation. The method is tested with both simulated data and physical electrical models.

Chapter 5 presents a historical overview of hardware developed at Oxford Brookes University. Two approaches are considered for the development of EIS instrumentation: to design a bespoke EIS system or to adapt a commercially available device. The hardware of the bespoke system is based on the design of the existing two voltage channel system working at four frequencies. A new EIS system, suitable for *in vivo* experiment, is designed, built and evaluated. Different current sources are considered and their limitations are highlighted. In section 5.5 an instrument based on a commercial Impedance Analyser is considered as a possible EIS system for use *in vivo*. The comparison of these two approaches is given. This chapter also gives an overview of different electrode systems and possible applications of EIS.

Chapter 6 shows results obtained from the measurements *in vitro* and *in vivo*. After successful results obtained from simulations and resistor/capacitor circuits the GRIM is applied to biological data. An entire experimental protocol for dielectric spectroscopy is established in this chapter. The studies of pathological and *in vivo* tissues are presented. Distributions of relaxation time constants are computed and displayed. This chapter contributes to the understanding of the relationship between the electrical properties and spatial structure of tissue.

In chapter 7 there are discussion and conclusion sections. The results of whole thesis are summed up and suggestions for further development are given.

Chapter 2

Electrical properties of biological tissues

2.1 Introduction

EIS measures the frequency response of a sample of material to AC electrical stimulation. In a typical experiment, a sinusoidal alternating current of angular frequency ω, $I(\omega)$, is applied to a sample of material (typically via electrodes) and the voltage developed across the sample, $V(\omega)$, is measured. The ratio of the complex amplitudes of the voltage and current is the complex impedance of the sample, $Z(\omega)$, Eqn. 2.1.

$$Z(\omega) = \frac{V(\omega)}{I(\omega)} \tag{2.1}$$

The impedance is a property of the sample, its composition and the geometry of the experiment. It is suited to defining the electrical behaviour on the macroscopic scale. At the microscopic level the electrical properties of the tissues are defined by their complex conductivity, σ^*, and complex permittivity, ε^*, (where "*" indicates a complex quantity). These parameters are a function of frequency and position. At steady state, the conductivity at a point may be expressed in a vector equation analogous to Eqn. 2.1.

$$\mathbf{J} = \sigma \nabla \mathbf{V} \tag{2.2}$$

where J is the current density. In a region where the electric field is uniform and the current stream lines parallel, Eqn. 2.2 leads to the macroscopic equation 2.1.

One of the purposes of this chapter is to introduce the main relaxation phenomena which take place when an alternating electrical field is applied to a sample of material. Dielectric relaxation mechanisms are complex phenomena which have

received much attention, [25], and is of particular interest in biological tissues, [14]. This chapter reviews the frequency dependence of the electrical properties of tissues.

The electrical response of biological tissues is often compared to circuits consisting of resistors and capacitors and more exotic elements. The values of these resistors and capacitors, for circuits with similar behaviour as tissue, are often interpreted in terms of tissue physiology and function, [26]. Some examples of circuit model analysis are presented in section 2.6. For human tissue, electrical circuit parameters typically include the resistances which describe the intra- and extracellular fluid conduction pathways, and a reactive component which is determined by the capacitance of the cell membranes.

In some cases, parameters of a circuit model are linked to the empirical Cole–Cole relationship of the frequency dependence of the complex permittivity of the tissue, in order to reproduce the observed resistance–reactance relationship and permit calculation of the parameter values. The Cole–Cole relationship is considered in sections 2.4 and 2.5.

2.2 Dielectric dispersions in Biological Tissues

When the frequency of the applied electrical current increases, the conductivity of the most tissues rises. The increase in conductivity is associated with a decrease in permittivity. The change of the electrical parameters of tissues with frequency can be explained by relaxation phenomena that occur when the current passes through the tissue.

Typically, the permittivity decreases in three major steps which are designated the $\alpha-$, $\beta-$ and $\gamma-$dispersions at low, medium and high frequencies respectively, [27]. Some other minor dispersions such as the $\delta-$dispersion are often reported. The idealised representation of this is shown in Fig. 2.1, [28]. This response is typical for all cellular tissue, although magnitudes and dispersion frequency vary, [14], [27].

The $\alpha-$dispersion dominates at low frequencies between about 10 Hz and a few kHz. The $\alpha-$dispersion is characterised by very large permittivity variations due to charge carrier diffusion effects, [14]. At very low frequencies, the membranes have time to complete charging and discharging within a single period. It causes a large tissue capacitance and, therefore, a high permittivity. The current

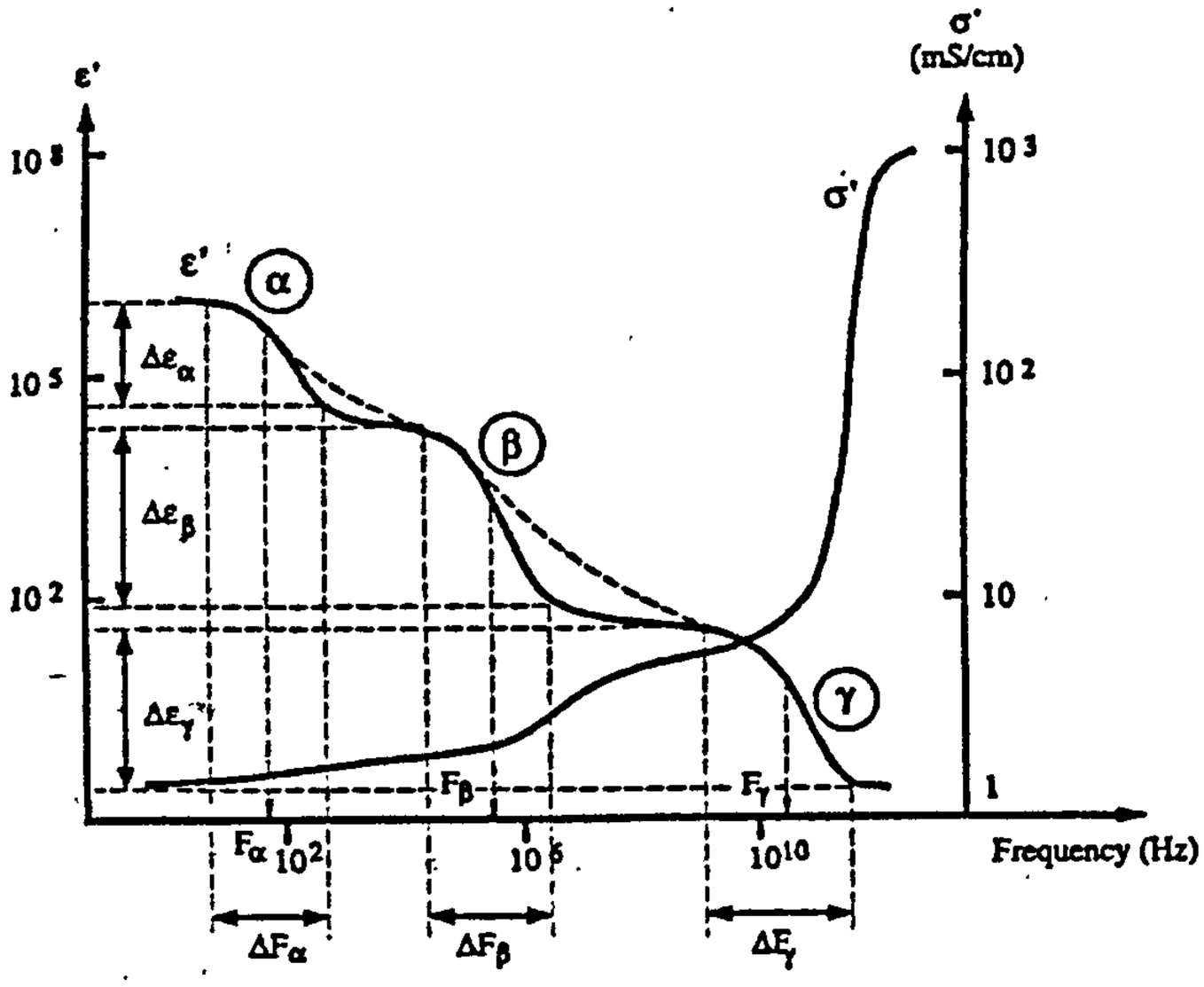

Figure 2.1: *An idealised plot of the frequency variation of permittivity and conductivity for typical biological tissue by Bourne [28]. ε' and σ' correspond to real parts of complex permittivity and conductivity respectively and explained in section 2.3.*

passes only through the extracellular medium. The measured conductivity is the conductivity of the extracellular medium. The $\alpha-$dispersion is usually associated with interfacial polarisations, caused by the formation of electrical double layers, and surface ionic conduction effects at membrane boundaries. This dispersion may be considered as a dipolar relaxation where large dipoles are formed by cells due to the accumulation of charges of opposite polarities at either sides of membrane.

The $\beta-$dispersion takes place in the frequency interval from $10^3 - 10^7$ Hz. The $\beta-$dispersion is due to the polarisation of larger biological molecules and to the capacitive charging of cell membranes. The membrane separates two conducting media. During excitation a charge is built up at the interface of these two dissimilar dielectrics and this increases the interfacial polarisation, known as the Maxwell-Wagner effect. When the frequency increases, the cell capacitive reactance decreases and a larger current flow goes through the intracellular medium. This leads to an increase in the tissue conductivity. On the other hand, the increase in frequency prevents the cell walls being completely charged during a single period causing the decrease in the permittivity. In the high-frequency part of the dispersion the dipolar reorientation of biomacromolecules, such as proteins, appears. Biomacromolecules behave like electrical dipoles in the electrical field. A torque orients each dipole with the applied electrical field but this is countered

by random thermal excitement. An orientation equilibrium is reached with the dielectric relaxation process.

The $\gamma-$ dispersion, at frequencies around 10^{10} Hz is due to the orientation polarisation of water molecules. At microwave frequencies, the membranes are short-circuited and tissues behave as a electrolyte. Their conductivity and permittivity are dominated by the relaxation of the free water molecules.

To conclude, measurements of the complex impedance at low frequencies provide information about extracellular conductivity and cell size. When the measurements are performed in the kilohertz range, cell wall characteristics can be obtained. Information about the cell interior can be obtained from high frequency measurements.

2.3 Complex Conductivity and Permittivity

To establish the relationship between complex conductivity and permittivity consider the example of a parallel plate capacitor in a vacuum, made up of two flat electrodes of area S and distance d apart. If a DC voltage difference V is maintained between the plates, a charge of $+Q$ is developed on the positive plate and a charge of $-Q$ on the negative plate. The capacitance is defined as the ratio of the charge Q to the voltage V and measures a property of the vacuum known as its permittivity, ε_0:

$$C \equiv \frac{Q}{V} = \frac{\varepsilon_0 S}{d} \tag{2.3}$$

If an insulating material is introduced into the space between the capacitor plates, then the charge on the plates is increased to $Q+q$ and a larger capacitance, C', is measured. The extra charge on the plates, q, is due to polarisation, P, of charges within the insulating material. The ratio C'/C defines the relative dielectric permittivity, ε, of the insulating material:

$$\varepsilon \equiv \frac{C'}{C} = 1 + \frac{P}{\varepsilon_0 E} \tag{2.4}$$

If the material between the plates is not perfectly insulating then some current will flow at low frequencies due to the movement of free charge carriers. The conduction current, i, is in phase with the applied electrical field, E, and equals:

$$i = \sigma_s E \tag{2.5}$$

where σ_s is the static conductivity. At low frequencies the polarisation and electrical fields are in phase and so no dielectric loss is observed and the permittivity is at its maximum. The conductivity is constant and equal to σ_s. As the frequency increases, the conductivity changes from σ_s to the frequency dependent value $\sigma^*(\omega)$. If the material undergoes dielectric losses, the capacitance and the relative permittivity become complex. The relationships between the complex conductivity, σ^*, and the complex permittivity, ε^*, have been established by Maxwell, [29], Debye, [30], and Fricke, [31]:

$$\sigma^*(\omega) - \sigma_s = j\omega\varepsilon_0\varepsilon^*(\omega) \tag{2.6}$$

where $j = \sqrt{-1}$.

2.4 Dielectric Relaxations

Certain noninsulating media, such a biological tissues, have dielectric properties due to a capability of storing electrostatic energy by polarisation. The relationship between the applied electric field, E, and the polarisation, P, is given by:

$$P = \varepsilon_0\chi_e E \tag{2.7}$$

where ε_0 is the dielectric permittivity of free space ($\varepsilon_0 = 8.85 \times 10^{-12}$ F/m). χ_e is the sensitivity of the material to the applied electrical field, which is linked to the relative dielectric permittivity by:

$$\chi_e = \varepsilon - 1 \tag{2.8}$$

For noncellular media, the polarisation may be divided into two parts according to the time constant of the response, [32]:

1. Distortion polarisation is due to distortion of crystal lattices and relative displacements of atomic nuclei and electron shells. This distortion occurs approximately 10^{-16} s after the application of an electric field and so can be treated as instantaneous at the frequencies used for EIS.

2. Orientation polarisation occurs as naturally polar molecules, such as water, or molecules with induced polarity, rotate to align with the applied electric field. Depending on the size of the molecule this occurs in the order of 10^{-6} s after the application of an electric field. Orientation polarisation is important at the higher frequencies used in EIS.

2.4.1 Debye Equation

To determine the frequency response of a polarizable material, consider again the parallel plate capacitor filled with a homogeneous material. The capacitor is initially uncharged and at time $t = 0$ a unit voltage is applied across the capacitor. The polarisation charge $P(t)$ shows an initial, almost instantaneous, increase to P_∞ due to distortion polarisation, then a much slower increase to P_s as polar molecules orient with the applied electric field, E. The Debye assumption is that rate of increase in polarisation is proportional to $P_s - P(t)$, [30], *i.e.*

$$P(t) = P_\infty + (P_s - P_\infty)e^{-t/\tau} \tag{2.9}$$

where τ is the relaxation time.

Using the defining Eqn. 2.4, the measured permittivity can be written as a function of time:

$$\varepsilon(t) = \varepsilon_\infty + (\varepsilon_s - \varepsilon_\infty)e^{-t/\tau} \tag{2.10}$$

where ε_s and ε_∞ are respectively the permittivity limits at very low and very high frequencies.

Taking the Laplace transform of Eqn. 2.10 and rearranging yields:

$$\frac{\varepsilon(p) - \varepsilon_\infty}{\varepsilon_s - \varepsilon_\infty} = \frac{1}{1 + p\tau} \tag{2.11}$$

where p is the Laplace parameter. By setting $p = j\omega$ the equation 2.11 yields the frequency response of a material with orientation polarisation time constant τ:

$$\frac{\varepsilon(j\omega) - \varepsilon_\infty}{\varepsilon_s - \varepsilon_\infty} = \frac{1}{1 + j\omega\tau} \tag{2.12}$$

Neglecting the influence of the static conductivity, the Debye equation takes its simplest form, [28]:

$$\varepsilon^*(\omega) = \varepsilon_\infty + \frac{\varepsilon_s - \varepsilon_\infty}{1 + j\omega\tau} \tag{2.13}$$

Nevertheless, the contribution of the static conductivity to the complex permittivity can not be ignored. Therefore, in order to describe the complex permittivity of a polar material, the modified Debye equation is usually used. The permittivity spectrum can be obtained from the conductivity spectrum by separating the real (Eqn. 2.15) and imaginary parts (Eqn. 2.16) of Eqn. 2.6.

$$\varepsilon^*(\omega) = \varepsilon' - j\varepsilon'' = \frac{\sigma^*(\omega) - \sigma_s}{j\omega\varepsilon_0} = \frac{\sigma''}{\omega\varepsilon_0} - j\frac{(\sigma' - \sigma_s)}{\omega\varepsilon_0} \tag{2.14}$$

$$\varepsilon' = \frac{\sigma''}{\omega\varepsilon_0} \tag{2.15}$$

$$\varepsilon'' = \frac{\sigma' - \sigma_s}{\omega\varepsilon_0} \tag{2.16}$$

The modified Debye equation takes the form as:

$$\varepsilon^*(\omega) = \varepsilon_\infty + \frac{\varepsilon_s - \varepsilon_\infty}{1 + j\omega\tau} - j\frac{\sigma_s}{\omega\varepsilon_0} \tag{2.17}$$

The Debye dispersion relations derived above are for a process with a single relaxation time. Biological tissues are heterogeneous media. The dipoles do not all share the same relaxation time τ. Some attempts have been made to extend the Debye model by including processes with more than one relaxation time. If the relaxation processes are considered for distinct time constants, for example, $\tau_1 \ll \tau_2 \ll \tau_3$..., the electrical response is a multiexponential type response:

$$\varepsilon^*(\omega) = \varepsilon_\infty - \frac{j\sigma_s}{\omega\varepsilon_0} + \frac{\Delta\varepsilon_1}{1 + j\omega\tau_1} + \frac{\Delta\varepsilon_2}{1 + j\omega\tau_2} + \frac{\Delta\varepsilon_3}{1 + j\omega\tau_3} + \ldots \tag{2.18}$$

2.4.2 Cole Equation

Cellular tissue does not exhibit distinct time constants but a more complex response due to continuous distributions of time constants. One of the most widely used relaxation functions is the one proposed by Cole, [5]. The function models the dielectric behaviour of the biological materials. It is based on a distribution of the relaxation time constants due to the range of structures that make up the tissue. The complex permittivity is given by the Cole–Cole equation (Eqn. 2.19) which has two parameters; f_c ($\tau_c = 1/(2\pi f_c)$) is the characteristic frequency where the imaginary part of the permittivity has a maximum, and α is the empirical parameter ($0 \leq \alpha \leq 1$).

$$\varepsilon^*(\omega) = \varepsilon_\infty + \frac{\varepsilon_s - \varepsilon_\infty}{1 + (j\omega\tau_c)^{(1-\alpha)}} \tag{2.19}$$

If the static conductivity is taken into account the Cole equation is:

$$\varepsilon^*(\omega) = \varepsilon_\infty + \frac{\varepsilon_s - \varepsilon_\infty}{1 + (j\omega\tau_c)^{(1-\alpha)}} - j\frac{\sigma_s}{\omega\varepsilon_0} \tag{2.20}$$

2.5 Cole–Cole plot

The complex impedance, conductivity or permittivity can be displayed graphically as a Nyquist plot known as the Cole–Cole plot, [33], where the impedance

is plotted on an Argand plane. Plotting the imaginary part of the impedance, $-Im(Z)$, against the real part of the impedance, $Re(Z)$, results in a semi–circle. Such a trace is often referred to as an impedance *locus.*

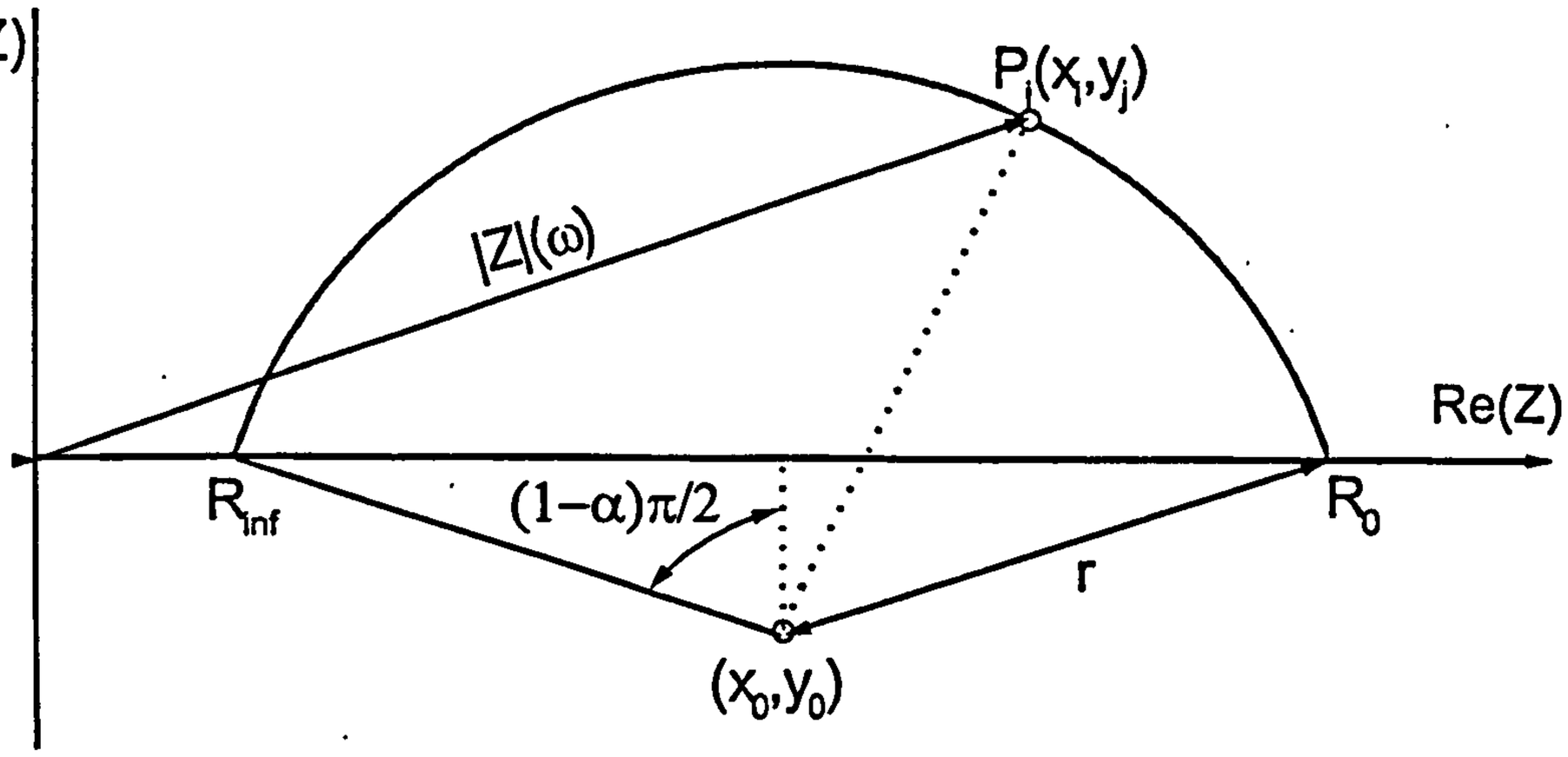

Figure 2.2: *Nyquist plot of the frequency dependence of the complex impedance.*

For the Debye relaxation with a single time constant (Eqn. 2.13), the locus is a semi–circle centred on the real axis. The Cole–Cole plot for biological materials has a semi–circular locus with a centre depressed below the real axis, Figure 2.2. Actually, it is the superposition of a large number of semi–circular arcs (all centred on the real axis) resulting from a continuous distribution of relaxation time constants in the dispersion.

The Cole–Cole curve is described with four parameters: the radius r, centre coordinates (x_0, y_0) and the fundamental frequency $\omega_c = 1/\tau_c$ where the imaginary part of the impedance reaches maximum. Often one of the parameters y_0 or r, is replaced by the angle α describing the depression of the semi–circular arc. If $\alpha = 0$ then a semi–circle is centred on the real axis and is identical to Debye relaxation with a single time constant.

2.6 Electrical Models and Equivalent Circuit Analysis

The most common representation of the electrical properties of tissues is the equivalent, lumped–constant element RC–circuit model (RC stands for a resistor–capacitor pair). A wide variety of models have been proposed whose components are designed to reproduce the complex behaviour of physiological tissue structures.

The response of an equivalent circuit model is fitted to the measured response and the values of individual resistors and capacitors are interpreted in terms of extra–cellular conductivity, cell wall capacitance and intra–cellular resistivity. This well established analysis has two potential problems:

1. An infinite number of different models have identical overall impedance and could be fitted to the same experimental data.
2. Ideal circuit elements represent lumped-constant properties. But, EIS measurements are derived from conduction in an inhomogeneous, three–dimensional medium.

Indeed, representing the real electrical properties of tissues with an electrical circuit that contains only discrete electrical elements is often convenient. However, in the complex impedance or permittivity plane, the electrical response of all biological tissues shows an arc of a circle whose centre is below the real axis. The model elements depend on the microscopic electrical properties ϵ and σ. These properties are themselves frequency dependent. So it is established that ordinary lumped–constant element RC–circuits are inadequate to describe the electrical behaviour of biological tissues. To reproduce a depressed semi–circle using a small number of lumped components, it is necessary to introduce a non–physical, constant phase component.

2.6.1 Distributed Circuit Elements

The locus obtained in the complex plane of the impedance shows the existence of a continuous distribution of tissue properties. Aiming to obtain the best fit to the EIS data, distributed elements in the equivalent circuit are often used.

One of the widely used distributed impedance elements is the "constant–phase element" (CPE) or "pseudo–capacitance", [34], [35]. The CPE is equivalent to an empirical transfer function. The electrical circuit involving CPE, shown in Figure 2.3, was originally proposed by Cole as a model for dielectric systems. It yields capacitances C_s in the $\omega \to 0$ limit and C_∞ in the $\omega \to \infty$ limit.

An ideal or "pure" capacitance can be considered as a constant–phase element with a phase angle of $-90°$. A pseudo–capacitance has a reactance which decreases with frequency, but not in a simple way. The pure capacitance has a complex reactance given by Eqn. 2.21.

$$\frac{j}{\omega C} = -\frac{1}{C}(j\omega)^{-1} \qquad 0 < \delta < 1 \tag{2.21}$$

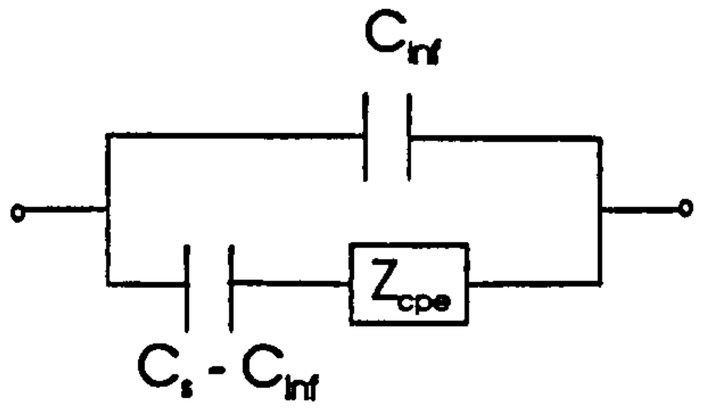

Figure 2.3: *Electrical circuit with CPE.*

Cole's CPE has a reactance:

$$K(j\omega)^{-\delta} \tag{2.22}$$

where K is a constant with units in the form of $\Omega.s^{-\delta}$. Therefore, the term $1/K$ is expressed in $\Omega^{-1}.s^{\delta}$ and has the dimension of a pure capacitance for $\delta = 1$. Parameter δ has the same meaning as $(1 - \alpha)$ in the Cole equation 2.19. CPE has an impedance rather than a reactance, because $(j\omega)^{-\delta}$ has a real component. δ controls how "capacitive" the behaviour of the CPE is.

Consider the Philippson/Lapicque electrical model shown in Fig. 1.1. In this model, replace the capacitance C_m representing the capacitance of the membrane by a constant–phase element. The parameters of the circuit are chosen to be $R_m = R_i = 300\ \Omega$ for resistances representing resistivities of membrane and intracellular space respectively, $C_m = 1\ \mu F$ for the capacitance of the membrane. The impedance data for two different δ parameters are displayed in Fig. 2.4.

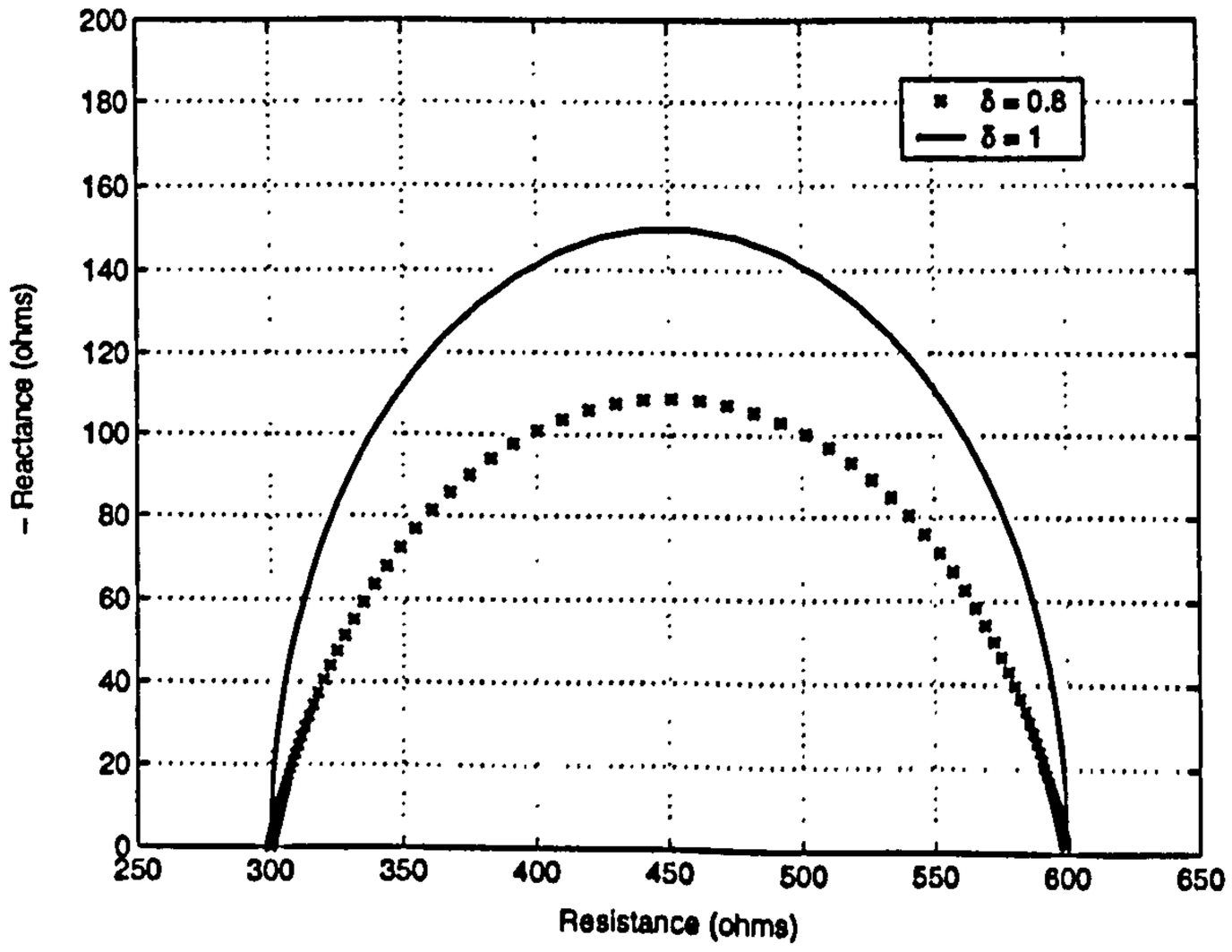

Figure 2.4: *Plots of reactance against resistance for the circuit with CPE.*

In Figure 2.4 the solid line represents the record obtained when CPE is equivalent to a "pure" capacitance. The centre of its semicircle is on the real axis. The cross line is for the case where the capacitor is replaced by a "constant–phase element" with parameter $\delta = 0.8$ or Cole parameter $\alpha = 0.2$. In the latter case, the centre of the circle is below the resistance axis. For decreasing δ (increasing α), the centre of the impedance locus becomes increasingly "depressed".

Cole's equation has found widespread use. Some examples of tissue modelling from EIS data have been published. The first parametric electrical impedance images were published by Brown *et al* [37]. They were constructed from combinations of the parameters of the model shown in Figure 2.5, where R and S are respectively the extracellular and intracellular resistances and Z_{cpe} represents the pseudo–capacitance.

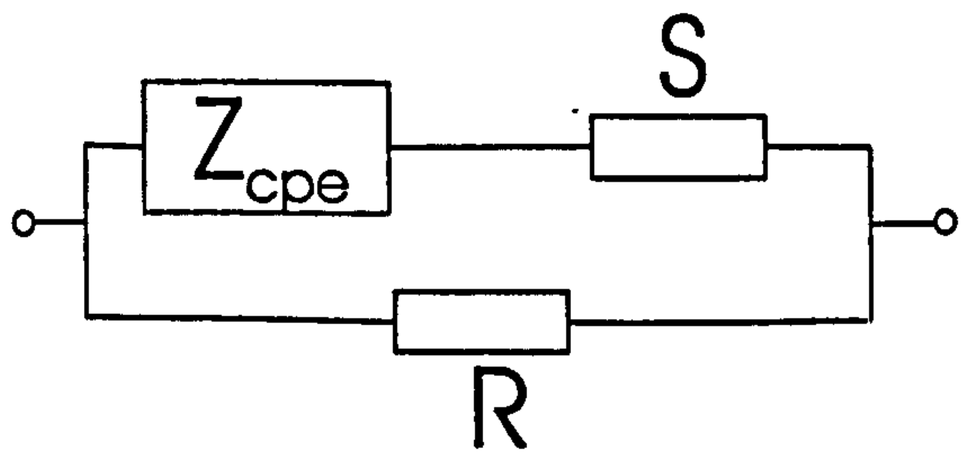

Figure 2.5: *The tissue model used by Brown et al for parametric imaging.*

This model is equivalent to the Cole model. Values of the model's parameters for different tissues can be found in [37] and were confirmed by Rigaud *et al* in [38] who performed electrical impedance measurements *in vitro*. B. Rigaud proposed two other electrical models for tissues exhibiting a single–circle impedance locus and a dual–circle impedance locus when measurements were extended to low frequencies.

The modelling of bioimpedance data measured on normal and cancerous female breast tissue using the $R-S-Z_{cpe}$ model was also reported by N. Chauveau *et al*, [39].

Although equivalent circuit modelling of biological tissues is still proposed in the literature and it is possible to choose parameters so that it accurately represents most tissues, the "constant phase element" is an arbitrary construction that is equivalent to a particular form of the DRT distribution. In order to interpret electrical response changes in terms of physiology, it is necessary to consider the relaxation time distribution and its evolution.

In a typical tissue, there will be a large number of cells with different sizes and shapes. Cole and Cole suggested that this leads to a range of local values of resistance and capacitance within the tissue. Different tissue types have different electrical impedance responses which would change with pathology. It means that in order to use EIS as a non–invasive tool in medicine one should use different electrical models that would fit the data well and that would demonstrate a parametric variation associated with the possible changes during tissue injury.

2.6.2 Ambiguous Circuits

Another potential problem with equivalent circuit analysis is that different models can have the same electrical impedance response.

An equivalent circuit with three or more circuit elements can be rearranged in many ways and still yield exactly the same impedance. An example is presented in Figure 2.6.

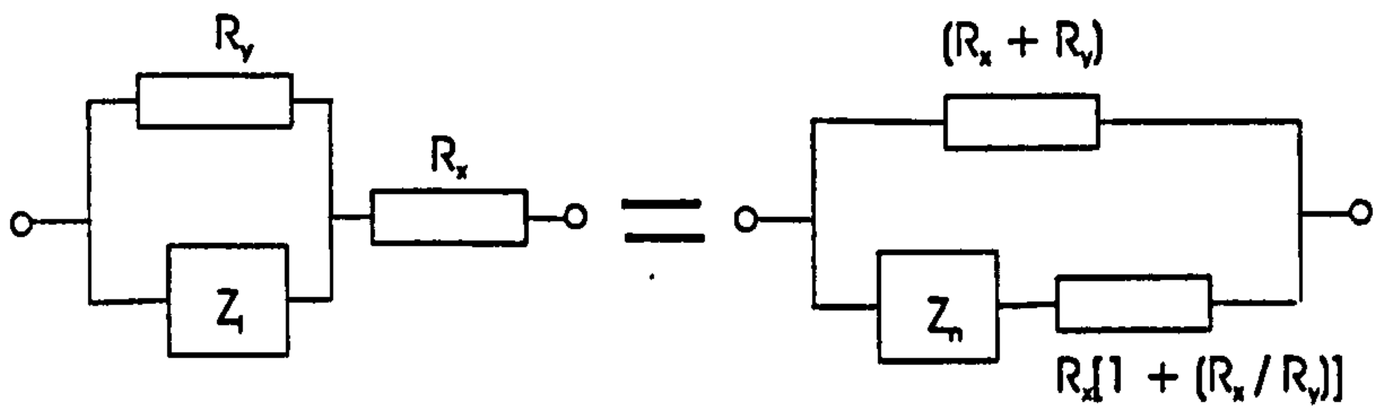

Figure 2.6: *An example of different circuits with the same overall impedance at all frequencies, [32].*

In these circuits the impedance Z_i can be made up of either lumped constant elements, distributed elements or a combination of these types. Having the same frequency response, both suggested tissue models can be fitted to measured data and it is not clear how to interpret the values of the lumped impedances in term of tissue characteristics.

In the study by Aligne *et al* [40] on the *in vivo* characterisation of human breast tumours induced in nude mice, the parameters of three different models can be fitted to the data. These models were the Cole model, the model proposed by Kanai *et al* [41], and a model derived from Kanai model by adding an RC–circuit in parallel with each capacitance.

The variety of different circuits poses the problem of choosing the one that mirrors the tissue structure and also the physiological properties and processes.

2.7 Summary

The purpose of this chapter has been to describe the electrical properties of biological tissue: conductivity and permittivity. These properties are frequency dependent. The behaviour of physiological tissues in an electrical field has been discussed. It has been shown that equivalent circuits can be devised, all with an electrical response similar to tissue. Associating a particular circuit element to some physiological or functional feature of the tissue is dubious. However, distributions of relaxation times do uniquely characterise the electrical response and may be linked to cellular properties.

Chapter 3

Continuous Relaxation Spectra

3.1 Introduction

In this chapter the electrical response of biological materials is related to continuous distributions of relaxation processes.

In the previous chapter the interpretation of impedance spectra with equivalent circuit models was discussed. These models can adequately mimic the behaviour of tissue but the interpretation of the spectra in terms of physiology and function requires knowledge of the relaxation spectra. Here the Cole–Cole model is shown to be equivalent to a particular distribution of dielectric relaxation times.

Dielectric constant measurements are often analysed in terms of a distribution of relaxation times. It is assumed that when the observed results cannot be explained by a simple Debye dispersion involving only a single relaxation time, they arise from a distribution of relaxation times. Depending on the frequency range, different processes lead to distributions of time constants, *e.g.* :

- α–dispersion: existence of cells with various sizes and shapes;
- β–dispersion: existence of cell walls of varying thickness and porosity;
- γ–dispersion: orientation polarisation of an enormous variety of organic molecules experiencing a range of bonds to surrounding molecules.

To establish such a connection between observed results and a distribution of relaxation times is the aim of the present work. The continuous distribution of relaxation time constants can be found from the Debye equation presented in the section 2.4.1:

$$\frac{\varepsilon(j\omega)-\varepsilon_\infty}{\varepsilon_s-\varepsilon_\infty}=\int_0^\infty \frac{G(\tau)}{1+j\omega\tau}d\tau \tag{3.1}$$

where $G(\tau)d\tau$ is the weight of relaxation times in the range $[\tau, \tau+d\tau]$.

In this chapter a number of empirical relaxation functions, proposed to parameterise the observations of the tissue impedance behaviour, are introduced.

3.2 Analytic Spectra Models

3.2.1 Classical Permittivity Loci and Their Relaxation Time Distributions

A small number of theoretical frequency response curves yield continuous distributions of dielectric relaxation times with closed form expressions. The most common model for the EIS data parameterisation is the empirical Cole–Cole model with a frequency response given by the equation 2.19. The complex permittivity $\varepsilon^*(\omega)$ may be separated into real and imaginary parts:

$$\frac{\varepsilon'-\varepsilon_\infty}{\varepsilon_s-\varepsilon_\infty}=\frac{1}{2}\left[1-\frac{\sinh(1-\alpha)x}{\cosh(1-\alpha)x+\cos(\alpha\pi/2)}\right] \tag{3.2}$$

$$\frac{\varepsilon''}{\varepsilon_s-\varepsilon_\infty}=\frac{1}{2}\frac{\cos(\alpha\pi/2)}{\cosh(1-\alpha)x+\sin(\alpha\pi/2)} \tag{3.3}$$

where $x = log\omega\tau_0$. The derived distribution function of time constants, $G(\tau)$, is, [32]:

$$G(\tau)=\frac{1}{2\pi\tau}\frac{\sin(\alpha\pi)}{\cosh((1-\alpha)\log(\tau/\tau_0))-\cos(\alpha\pi)} \tag{3.4}$$

The Cole–Cole distribution is symmetrical in logarithmic scale of times, $\ln(\tau)$, with respect to a central frequency or relaxation time. The distribution of time constants is plotted as a function of the variable $s \equiv \log(\tau/\tau_0)$ in Figure 3.1. The distribution has a peak at $\tau = \tau_0$ and the variance increases as α increases. Therefore, increasing spread in the distribution of time constants is associated with increasing depression of the Cole–Cole locus.

As was pointed out in section 2.6.1, dielectric response corresponding to the Cole–Cole function is produced by the circuit shown in Fig. 2.3 which contains a "constant-phase element".

Two other distribution functions are due to Kirkwood and Fuos [42] and Davidson and Cole [43].

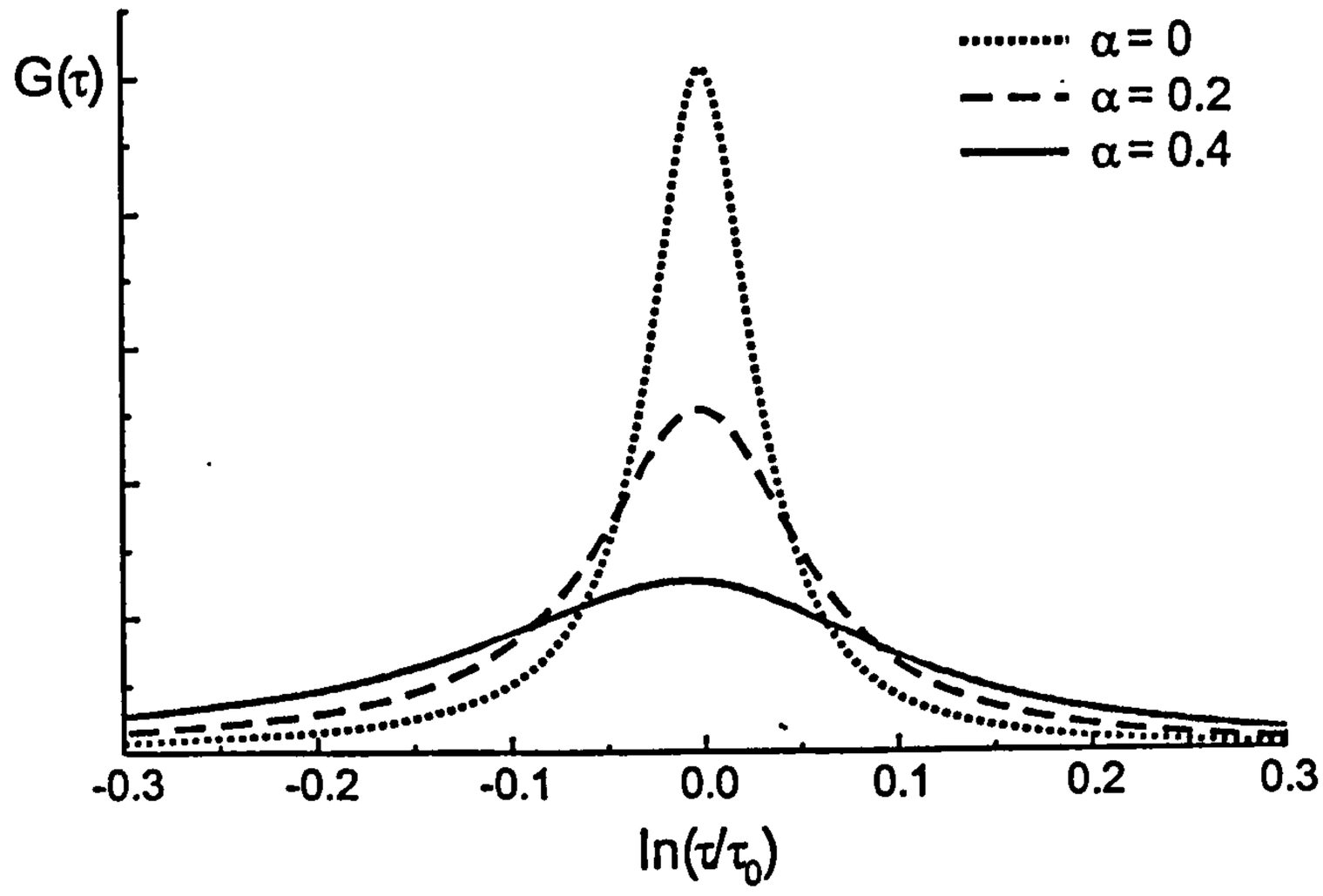

Figure 3.1: *The distribution function associated with the Cole–Cole distribution of relaxation times for different values* α.

The first of these is symmetric, and is again based on an extension of the Debye model. In Debye theory,

$$\frac{\varepsilon''}{\varepsilon''_{max}} = sechx \tag{3.5}$$

where $x = log\omega/\omega_0$. Instead of this, Kirkwood and Fuoss wrote

$$\frac{\varepsilon''}{\varepsilon''_{max}} = sech\gamma x \tag{3.6}$$

which leads to a distribution of the form

$$G(s) = \frac{2}{\pi} \cdot \frac{cos(\gamma\pi/2)\cosh\gamma s}{cos^2(\gamma\pi/2) + sin^2\gamma s} \tag{3.7}$$

where s is again equivalent to $log(\tau/\tau_0)$.

The Davidson–Cole arc is a skewed in the complex ε^* plane, Fig. 3.2, and the equation is:

$$\frac{\varepsilon^* - \varepsilon_\infty}{\varepsilon_s - \varepsilon_\infty} = \frac{1}{(1 + j\omega\tau_0)^\beta} \tag{3.8}$$

The corresponding distribution of the relaxation times is highly asymmetric:

$$G(\tau) = \begin{cases} \frac{\sin\beta\pi}{\pi}\left(\frac{\tau}{\tau_0 - \tau}\right)^\beta & 0 \le \tau \le \tau_0 \\ 0 & else \end{cases} \tag{3.9}$$

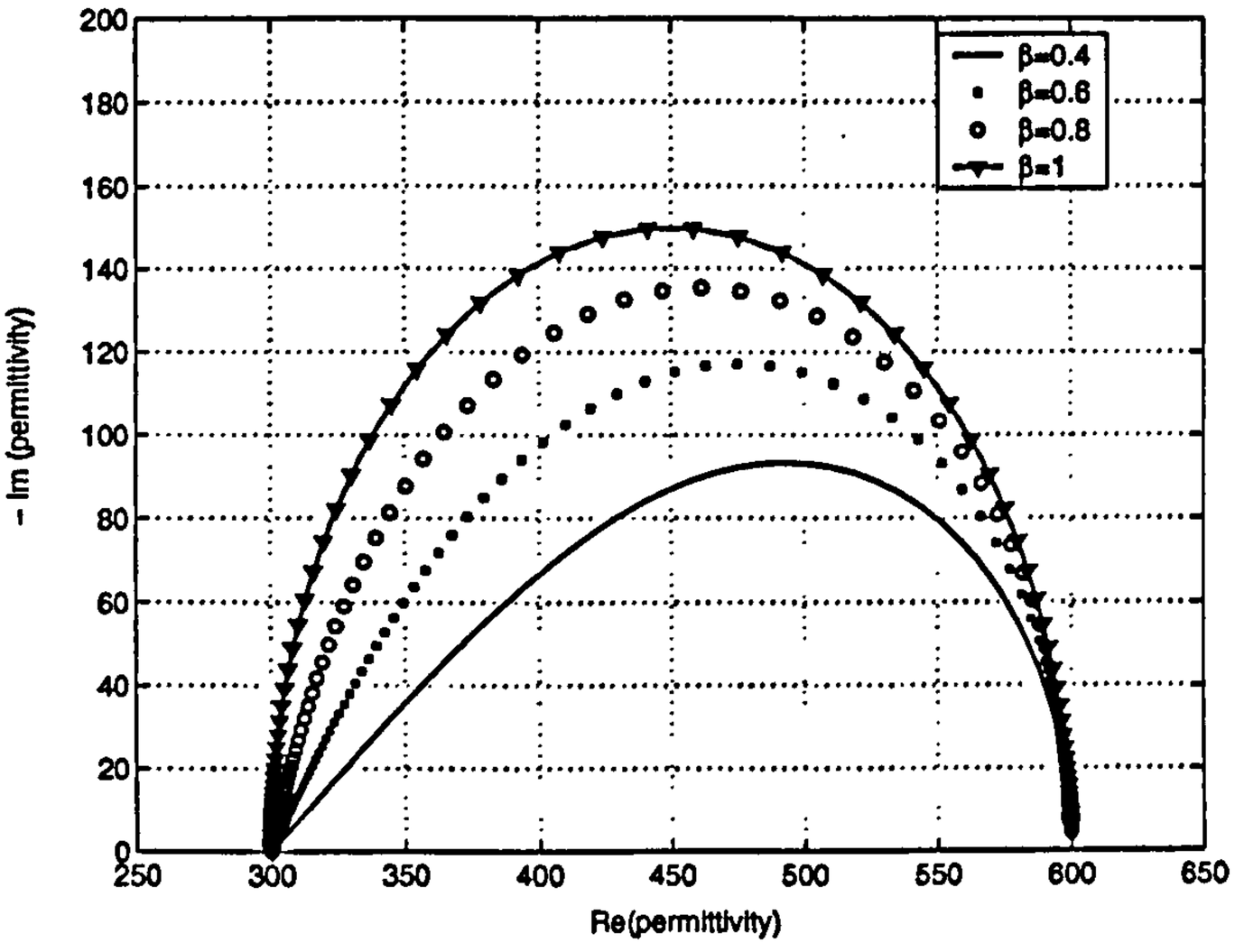

Figure 3.2: *Davidson–Cole arc.*

3.2.2 Parametric Models

Several parametric models were developed to describe the variation of dielectric properties of tissues as a function of frequency. Parameterisation of EIS data is often based on the empirical Cole–Cole model. However, only few independent parameters can be found.

Examples of parametric models for brain tissue have been reported by Foster *et al*, [44]. The range of applicability of the models was limited by the data available to above 1 MHz, *e.g.* the γ–dispersion frequency range.

A similar, but more extensive analysis was carried out by Hurt [36], who published the data for muscle in the frequency range from 10 Hz to 10 GHz. Hurt modelled the dielectric spectrum by the summation of five Debye dispersions in addition to a conductivity term:

$$\varepsilon^*(\omega) = \varepsilon_\infty + \sum_{n=1}^{5} \frac{\Delta\varepsilon_n}{1 + j\omega\tau_n} + \frac{\sigma_s}{j\omega\varepsilon_0} \tag{3.10}$$

Gabriel *et al*, [18], recently used the Hurt approach to compile and describe the dielectric behaviour of biological tissues over a broad frequency range. The spectrum from 10 Hz to 100 GHz was modelled as four dispersion regions. The frequency dependence within each region was expressed as a Cole–Cole term:

$$\varepsilon^*(\omega) = \varepsilon_\infty + \sum_{n=1}^{4} \frac{\Delta\varepsilon_n}{1 + (j\omega\tau_n)^{(1-\alpha_n)}} + \frac{\sigma_s}{j\omega\varepsilon_0} \tag{3.11}$$

The model assumes the existence of the specific, continuous distributions of relaxation times. The DRT spectrum was assumed to consist of four near symmetrical peaks as in Figure 3.1. Although each peak is broadened by its own, independent distribution parameter α, no effort was made to extract more information about the shape of each peak from the data. Choosing appropriate parameters for each tissue it was only used to predict the dielectric behaviour over a frequency range from Hz to GHz.

The parametric model can be used to obtained the dielectric spectrum over a wide frequency range and can be used to distinguish different classes of biological tissues. The empirical approach is useful in developing clinical techniques but does not directly illuminate the link between specific non-electrical tissue characteristics (cell size, shape, number, clustering, *etc.*) and its raw frequency response. The methods of Hurt and Gabriel yield, indirectly, discrete and continuous distributions of dielectric relaxation times.

3.3 Inversion Formulae

3.3.1 The Analytic Inverse Problem

In electrical impedance spectroscopy the inverse problem is to determine the distribution of relaxation times from electrical measurements made on a material.

Introducing the proportion of dielectric time constants in the range $[\tau, \tau+d\tau]$ as $G(\tau)d\tau$ and the frequency response of the material, $Q(\omega)$, the following expression can be derived from the Debye equation:

$$Q(j\omega) = \frac{\varepsilon(j\omega) - \varepsilon_\infty}{\varepsilon_s - \varepsilon_\infty} = \int_0^\infty \frac{G(\tau)}{1 + j\omega\tau} d\tau \tag{3.12}$$

The network function $Q(\omega)$ is the measured data in EIS. The above type of the integral equation is known as a Fredholm integral equation of the first kind. The function $k(\omega, \tau) = \frac{1}{1+j\omega\tau}$ is known as the kernel of the integral equation. It is well known that as long as $Q(\omega)$ is in the range of the integral operator then the solution $G(\tau)$ is unique up to the addition of a function in the null space. The inversion of this type of integral is known to be Hadamard *ill-posed*, [45]. Ill-posed problems are considered in detail in section 4.2. In particular, small changes in the measured network function $Q(\tau)$ can lead to arbitrarily large changes in the relaxation spectrum $G(\tau)$. The kernel $k(\omega, \tau)$ is not self-adjoint but when Eqn. 3.12 is split into real and imaginary parts, the new kernels are real and symmetric

and hence self-adjoint:

$$Q'(\omega) - jQ''(\omega) = \int_0^\infty \frac{G(\tau)}{1+\omega^2\tau^2}d\tau - j\int_0^\infty \frac{\omega\tau G(\tau)}{1+\omega^2\tau^2}d\tau \tag{3.13}$$

A more detailed introduction to Fredholm equations of the first kind and problems associated with their solution as well as a stabilising techniques will be discussed later.

3.3.2 Analytic Expressions

There exist several analytic expressions for the direct calculation of relaxation time distributions from permittivity data. They are generally not useful for the inversion of incomplete and noisy data due to ill–posedness of the inverse problem but are included here for completeness.

The equation 3.12 can be rewritten in terms of parameter $p = j\omega$:

$$Q(p) = \int_0^\infty \frac{G(\tau)}{1+p\tau}d\tau \tag{3.14}$$

In order for the distribution function $G(\tau)$ be physically reasonable and realisable, it must satisfy certain conditions. First, it must be real and always positive for any value of the variable τ between 0 and ∞. Also, from 3.14, it must be normalised so that:

$$\int_0^\infty G(\tau)d\tau = Q(0) = 1 \tag{3.15}$$

Macdonald, [46], has shown that by applying the transformation $\lambda \equiv \tau^{-1}$ and $\lambda^{-1}G(\lambda^{-1}) \equiv D(\lambda)$ to Equation 3.14 yields:

$$Q(p) = \int_0^\infty \frac{D(\lambda)}{p+\lambda}d\lambda = \mathfrak{LL}(D(\lambda)) = S(D(\lambda)) \tag{3.16}$$

where $\mathfrak{L}$ represents the Laplace transform and S represents the iterated Laplace transform or Stieltjes transform. Thus, $D(\lambda)$ and hence $G(\lambda)$ can be recovered from $Q(p)$ by iterated inverse Laplace transforms. The Laplace transform may be formally inverted using the Riemann Inversion Formula, which involves a complex integral along a Bromwich contour. The inverse Laplace transform is well known to be exponentially ill–posed. Algorithms exist for calculating values of the inverse Laplace transform of functions known only at discrete, purely imaginary values of p, such as Talbot's Method [47] and later variants [48].

Working on the same integral equation in the field of rheology, Davies and Anderssen [49] derive an expression for the direct inversion of the complex part of the permittivity. Consider the real part of Eqn. 3.13:

$$Q'(\omega)\omega = \int_0^\infty \frac{\omega}{1+\omega^2\tau^2} G(\omega) d\tau \tag{3.17}$$

Applying the transformations $\tau = e^{-s}$, $\omega = e^{-t}$, $\Theta(t) = \omega Q'(\omega)$ and $\Psi(s) = G(\tau)$ to Eqn. 3.17 yields:

$$\begin{aligned}\Theta(t) &= \int_0^\infty \frac{e^{t-s}}{1+(e^{t-s})^2}\Psi(s)ds \\ &= \int_0^\infty sech(t-s)\Psi(s)ds\end{aligned} \tag{3.18}$$

The right hand side of equation 3.18 is in the form of a convolution and so, assuming the Fourier transforms $\hat{\Theta}(p) = \mathcal{F}\Theta(t)$ and $\hat{\Psi}(p) = \mathcal{F}\Psi(s)$ exist:

$$\hat{\Psi}(p) = \frac{2}{\pi}\hat{\Theta}(p)\cosh(\frac{1}{2}\pi p) \tag{3.19}$$

Thus $\hat{\Psi}(p)$ and hence $G(\tau)$ can be recovered from the inverse Fourier transform of a filtered Fourier transform of $\Theta(t)$.

3.4 Moving–Average Formulae

3.4.1 Introduction

Different attempts have been made by several researchers in the search for direct, numerical inversion algorithms for following equations:

$$Q'(\omega) = \int_0^\infty \frac{G(\tau)}{1+\omega^2\tau^2} d\tau \tag{3.20}$$

$$Q''(\omega) = \int_0^\infty \frac{\omega\tau G(\tau)}{1+\omega^2\tau^2} d\tau \tag{3.21}$$

The pair of equations 3.20 and 3.21 are also encountered in the field of rheology where they describe the distribution of shear waves in a viscoelastic medium. Davies and Anderssen [49], [50], [51] have proposed a direct inversion method for use on shear wave data.

In this chapter it will be shown that their results are equally applicable to the inversion of normalised admittivity data to yield dielectric relaxation times. The continuous moving–average formulae and then their discretised forms will be presented. Two specific Sampling Localisation theorems are considered in detail as they are useful and have the primary importance for the determination of the extent of the interval over which the distribution of relaxation times is completely recovered. An example of the application of the method will reconstruct a single time constant distribution. The detailed derivation of these results are may be found in the referenced articles.

3.4.2 Derivation of Continuous Moving–Average Formulae

In this section the derivation of the moving–average formulae using mid–point product integration is outlined, for more details refer to [50]. The results of Davies and Anderssen are presented in the context of the recovery of dielectric relaxation times.

Let the function $S(\omega)$ be defined as:

$$S(\omega) = j\omega Q(\omega) \tag{3.22}$$

Writing Eqn. 3.13 in terms of $S(\omega)$ and taking real and imaginary parts yields:

$$S'(\omega) + jS''(\omega) = \int_0^\infty \frac{G(\tau)\omega^2\tau^2}{1+\omega^2\tau^2}\frac{d\tau}{\tau} + j\int_0^\infty \frac{G(\tau)\omega\tau}{1+\omega^2\tau^2}\frac{d\tau}{\tau} \tag{3.23}$$

These equations are identical to the equations investigated by Davies and Anderssen where S' is the storage modulus and S'' is the loss modulus of shear waves in a viscoelastic fluid and $G(\tau)$ is the relaxation spectrum.

Let η_{ab} denote the contribution from dielectric relaxation times in the range $a < \tau < b$; and $\bar{G}_{ab}$ be the mean of the relaxation time distribution over this interval, *i.e.*

$$\eta_{ab} = \int_a^b G(\tau)d\tau \tag{3.24}$$

$$\bar{G}_{ab} = \frac{\eta_{ab}}{b-a} \tag{3.25}$$

Davies and Anderssen show that, provided $\ln(b/a) < \pi$ then:

$$\eta_{ab} \equiv \eta'_{ab} = \int_{-\ln(b)-\pi/2}^{-\ln(a)+\pi/2} [E''(\ln(b\omega)) - E''(\ln(a\omega))] \frac{S''(\omega)}{\omega} \frac{d\omega}{\omega}$$

$$\equiv \eta''_{ab} = \int_{-\ln(b)-\pi/2}^{-\ln(a)+\pi/2} [E'(\ln(b\omega)) - E'(\ln(a\omega))] \frac{S'(\omega)}{\omega} \frac{d\omega}{\omega} \tag{3.26}$$

where:

$$E'(x) = \lim_{\delta \to 0} E'_\delta(x) \qquad E''(x) = \lim_{\delta \to 0} E''_\delta(x)$$

$$E^*_\delta(x) = E'_\delta(x) + iE''_\delta(x) \equiv \frac{1}{\pi} erf\left(\frac{x + \frac{1}{2}\pi i}{\sqrt{2}\delta}\right), \delta > 0 \tag{3.27}$$

Eqn. 3.26 provides two alternative routes to calculate $S(\omega)$ which, given complete and noiseless data, should yield the same result. The elementary sampling function $E^*_\delta(x) : \delta \to 0$ in the functional representations of η_{ab} is composed of an infinite number of pulses of infinite amplitude in the interval $-\pi/2 < x < \pi/2$. Davies and Anderssen used this result to prove the two Sampling Localisation Theorems introduced in the subsequent section.

3.4.3 Sampling Localisation Theorems

Davies and Anderssen provided the answer to the fundamental question:

"What precise range of frequencies $\omega_{min} < \omega < \omega_{max}$ need to be sampled in order to determine the relaxation spectrum over a given range of relaxation times $a < \tau < b$?"

Throughout this thesis, reference will be made to the Sampling Localisation Theorems and how limitations in the measurements of the permittivity data lead to restrictions in the recoverable relaxation spectrum.

The First Sampling Localisation Theorem

If $1 < b/a < e^\pi$, then the distribution of dielectric relaxation times in the interval $a < \tau < b$ is completely determined by the admittivity in the angular frequency range:

$$\frac{e^{-\frac{\pi}{2}}}{b} < \omega < \frac{e^{\frac{\pi}{2}}}{a} \tag{3.28}$$

Table 3.1: Three Transcendental numbers.

e^{π}	$= 23.14069263$	$= 10^{1.3647635}$
$e^{\frac{\pi}{2}}$	$= 4.81047738$	$= 10^{0.68218818}$
$e^{-\frac{\pi}{2}}$	$= 0.20787958$	$= 10^{-0.68218818}$

The Second Sampling Localisation Theorem

If $b > ae^{\pi}$, then the dielectric relaxation times in the interval $a < \tau < b$ are completely determined by the admittivity in the two angular frequency ranges:

$$\frac{e^{-\frac{\pi}{2}}}{b} < \omega < \frac{e^{\frac{\pi}{2}}}{b} \quad and \quad \frac{e^{-\frac{\pi}{2}}}{a} < \omega < \frac{e^{\frac{\pi}{2}}}{a} \tag{3.29}$$

Three constants are important to introduce here: e^{π}, $e^{\frac{\pi}{2}}$ and $e^{-\frac{\pi}{2}}$. Floating point approximations to these numbers are given in Table 3.1. Referring to this table, the first theorem can be rewritten as:

$$\frac{\omega_{max}}{\omega_{min}} = 10^{1.36}\left(\frac{b}{a}\right) \tag{3.30}$$

Thus, determining the dielectric relaxation time density in the range $a < \tau < b$ requires knowledge of the permittivity in the frequency range 1.36 decades broader than the reciprocal range $a^{-1} < \omega < b^{-1}$, 0.68 decades on either side.

The next conclusions follow from the above theorems:

- To recover the dielectric time constant distribution over a decade of relaxation times it is necessary to measure the permittivity over 2.36 decades of frequency; *i.e.* , 0.68 decades either side of the reciprocal relaxation time range.

- The measurements of the permittivity over at least 1.36 decades of frequency are needed to tell anything about the relaxation spectrum.

3.4.4 Discretisation and Numerical Implementation

A numerical algorithm for the inversion of the normalised permittivity data to yield the approximate relaxation time distribution can be obtained by the discretisation of Eqn. 3.26. Davies and Anderssen used mid-point product integration. This results in two, simple, moving-average formulae linking the permittivity sampled at specific frequencies to the mean relaxation time density over intervals.

The strategy proposed by Davies and Andessen can be summarised as follows.

To establish a correspondence between the continuous and discrete formulae, the nature of the discretisation has to be defined. The permittivity data are assumed to be available at discrete set of $K+1$ frequencies:

$$\omega_k, \qquad k = 0, 1, ..., K \tag{3.31}$$

which increase as a function of k. To apply the formulae it is necessary to have permittivity data exponentially sampled at frequencies given by:

$$\omega_k = \omega_0 \exp(hk) \qquad 0 \leq k \leq K \tag{3.32}$$

where h is a constant which is constrained by the length L of the moving-average formulae, where $L \geq 2$. The lowest frequency, ω_0, is unconstrained. The relaxation time distribution will be estimated at points in the reciprocal range $\tau_k = 1/\omega_k$. Each relaxation time sample is at the geometric centre of an interval $\left[e^{-\frac{h}{2}}\tau_k, e^{\frac{h}{2}}\tau_k\right]$. If η_k is defined as the integral of the relaxation time density function over this interval, then the moving average formulae of length L are of the form:

$$\eta'_j = \sum_{l=-L}^{L} \alpha_l Q'(\omega_{j+l}) \quad j = L, L+1, ..., K-L$$

$$\eta''_j = \sum_{l=-L}^{L} \beta_l Q''(\omega_{j+l}) \quad j = L, L+1, ..., K-L \tag{3.33}$$

where $\eta_j = \eta'_j = \eta''_j$.

A numerical procedure for the calculation of the coefficients α_i and β_i, based on the discretisation of Eqn. 3.26, is given in Davies and Anderssen [50].

The coefficients α_l and β_l may be determined by fitting the dual model:

$$S'_N(\omega) = \sum_{j=1}^{N} \frac{(\eta_j \omega_j)\omega^2\tau_j^2}{1+\omega^2\tau_j^2} \tag{3.34}$$

$$S''_N(\omega) = \sum_{j=1}^{N} \frac{(\eta_j \omega_j)\omega\tau_j}{1+\omega^2\tau_j^2} \tag{3.35}$$

where η_j is defined by Eqn. 3.33.

As an example, consider a DRT spectrum consisting of a single relaxation with a time constant of one unit, *i.e.* $G(\tau)$ is the delta function centred at $\tau = 1$:

$$G(\tau) = \delta(\tau - 1) \tag{3.36}$$

then

$$S'(\omega) = \frac{\omega^2}{1+\omega^2} \qquad S'' = \frac{\omega}{1+\omega^2} \tag{3.37}$$

Using the formulae in Eqn. 3.33 with $L = 4$ the dielectric relaxation time density based on 20 analytically calculated, permittivity samples at frequencies $\left\{\omega = \exp(\pm\frac{i\pi}{7}), i = 0, 1, ..., 10\right\}$ was reconstructed [22]. Figure 3.3 illustrates obtained results.

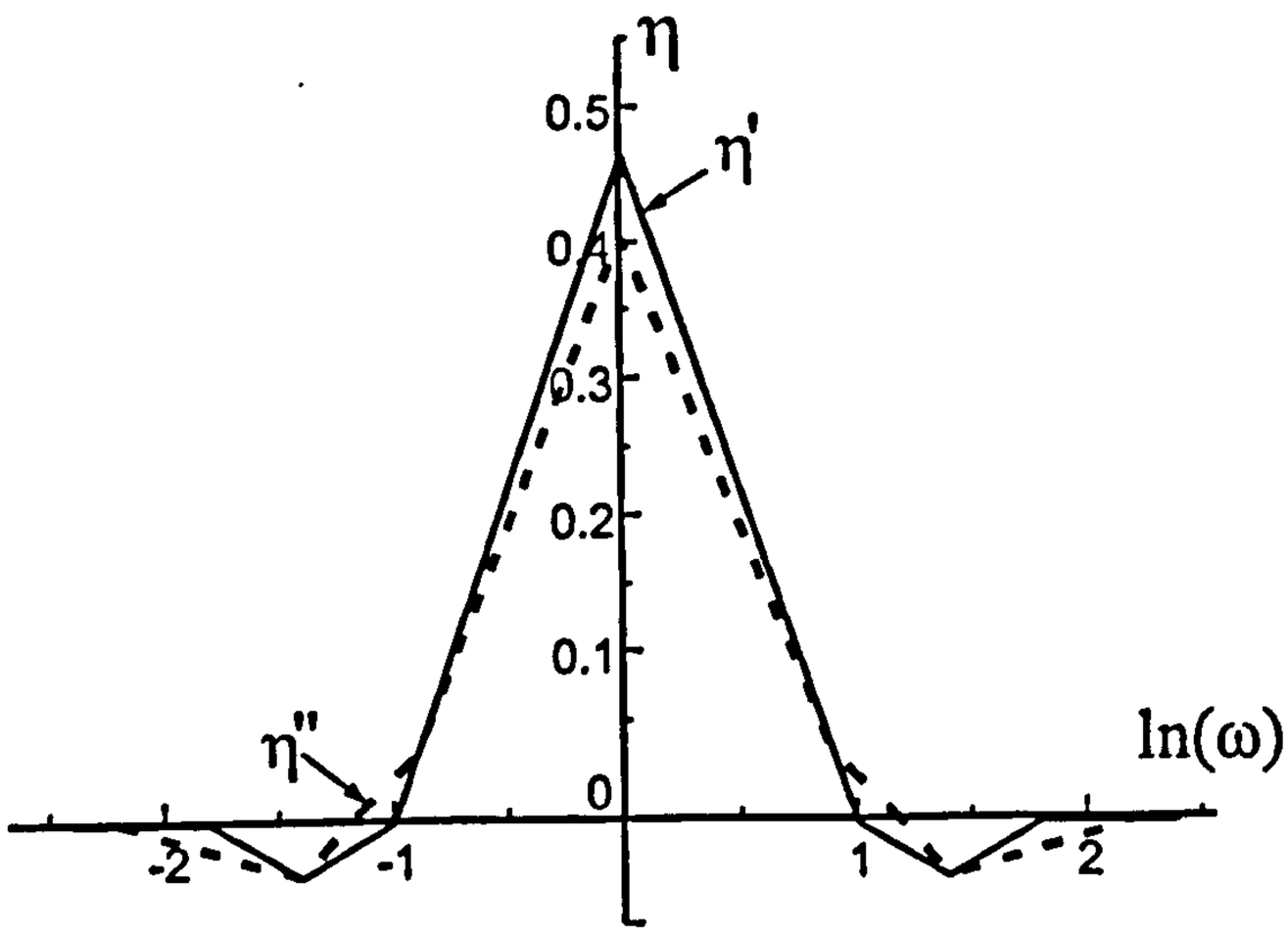

Figure 3.3: *The reconstruction of a relaxation time distribution* $G(\tau) = \delta(\tau - 1)$ *using moving-average formulae of length 4.*

The recovered relaxation spectrum is broadened due to the sampling of the data space and the truncation of the moving-average filter. It can be seen that α–formulae has recovered a better resolved spectrum than β–formulae for the same length of filter L.

The alternative estimates for η_j from Eqn. 3.33 have different properties; η'_j has higher noise amplification than η''_j but also has higher resolving power. Similarly, as the formula length L increases, the resolving power decreases but the formulae become more robust to noise. L acts as a discrete regularisation parameter. Due to this, one application of the formula may not be sufficient to recover an accurate spectrum when using noisy data and so successive iterations of the formulae are needed. Increasing the filter length, L, will smooth the spectrum and some information about the spectrum contained in the original data will be lost. It may be concluded that proposed formulae are sensitive to noise and, even for perfect, noiseless data, the temporal resolution is limited by the finite sampling interval of the data. The inflexibility of the method to regularisation is a major handicap.

3.5 Summary

Analytic spectrum models and inversion formulae were discussed in this chapter. Several models were introduced that represented permittivity spectra as sums of Debye or Cole–Cole responses. Each response is controlled by a small number of parameters. DRT spectra may be calculated by finding the best-fit parameterised permittivity spectrum to the measured data.

The Davies–Anderssen method was more sophisticated in that it imaged arbitrary DRT spectra.

All the methods suffer from the inherent ill-posedness of the inverse problem. Practical inversion algorithms must be robust and adaptable to noisy, inconsistent and limited data.

Two important theorems in the section 3.4.3 define the measuring frequency limits for the reconstruction of the complete distribution of relaxation times for the area of interest. The knowledge of this theorems will define the frequency range for experiments (Chapter 6).

Chapter 4

Galerkin Regularised Inverse Method

4.1 Introduction

In the previous chapter, analytical and semi analytical methods for recovering relaxation spectra were discussed. These methods lacked adaptability to the range of noise and errors likely to be present in real data.

In this chapter a *Galerkin Regularised Inverse Method (GRIM)* is proposed. It applies standard mathematical methods to recover the relaxation time spectrum from measurements of the real and imaginary parts of the impedance. As this method solves the Fredholm integral, Eqn. 3.23, this leads to a general review of inverse and ill–posed problems. The method is based on the *Rayleigh–Ritz Galerkin Approximation* which will be shown in detail. In the presentation it is assumed that the analytic problem (*e.g.* integral equation) has been discretised and discussion is therefore based on the finite–dimensional systems. However, finite dimensional problems have properties very similar to those of continuous ill–posed problems. To deal with the ill–posedness, the *Tikhonov regularisation method* is used and presented in subsequent sections.

Finally, the resolution of the method and some attempts to improve it are discussed.

4.2 Inverse and Ill–posed Problems

The problem of determining the relaxation spectrum from permittivity measurements involves the inversion of one or both of the following pair of integral equations:

$$S'(\omega) = \int_0^\infty \frac{G(\tau)\omega^2\tau^2}{1+\omega^2\tau^2}\frac{d\tau}{\tau} \tag{4.1}$$

$$S''(\omega) = \int_0^\infty \frac{G(\tau)\omega\tau}{1+\omega^2\tau^2}\frac{d\tau}{\tau} \tag{4.2}$$

The common form of these equations is:

$$\int_a^b K(x,y)f(y)dy = g(x) \tag{4.3}$$

Each integral equation is a linear Fredholm integral of the first kind, where $K(x,y)$ is called the kernel, $g(x)$ is a given function (usually called "data"), and $f(y)$ is an unknown function which is sought. This equation is important in the theory of the inverse problems since many inverse problems lead to a linear Fredholm integral equation, *e.g.* diffusion problems. Equation 4.3 could be also written in terms of operators, *i.e.*

$$Kf = g \tag{4.4}$$

where f is in the space Y, g is in the space X and K is a mapping from the space Y into space X. A direct problem would be one where $K(x,y)$ and $f(y)$ were known and $g(x)$ is to be calculated. Assuming K was well–defined and continuous, then for a given f there is a unique g, and small changes in f would lead to small changes in g.

However, if instead of knowing f, the g function is known, or alternatively f and g are known but not K, then there is an inverse problem, which is less straightforward to solve. The questions of existence, uniqueness and stability of solutions arise.

At the beginning of the last century J. Hadamard formalised the concept of *well–posedness.* He said that a well–posed problem was one where

1) a solution exists, *i.e.* for each g in Y there is a f in X (existence)

2) the solution is unique (uniqueness)

3) the solution depends continuously on the data (stability)

An ill–posed problem would be one where one or more of the above criteria does not hold. Usually mathematicians are more concerned with (2) and (3) since (1) can usually be enforced. Clearly for (1) to hold there must be the equation $Y = K(X)$, that is, the mapping $K: X \rightarrow Y$ must be surjective. If a solution does exist it may not be unique and the choice of the "best" one is required. Non-uniqueness may be introduced because the data is discrete. Since the data is also likely to have error or noise, then if the solution does not depend continuously on the data these errors, even if small, will have a large effect on the solution.

A problem which is not well–posed is called *ill–posed.* In this case many functions f satisfy $Kf = g$ within the accuracy that g is known. Some other information is needed to choose one f from the many possible answers. Typically, the f is chosen which optimise some smoothness criteria. This process for solving ill–posed problems is known as *regularisation.*

In EIS it would be useful to calculate the Relaxation Time Distribution $G(\tau)$. Unfortunately, the relaxation spectrum cannot be measured directly in experiments. It is therefore necessary to use the equations which relate the relaxation spectrum and the function $S(\omega)$ defined by Eqn. 3.22. The link between the measured permittivity data and related relaxation spectrum is:

$$S(\omega) = j\omega Q(\omega) = j\omega\left(\frac{\varepsilon(j\omega) - \varepsilon_\infty}{\varepsilon_s - \varepsilon_\infty}\right) = \omega Q'' + j\omega Q' =$$

$$= \int_0^\infty \frac{G(\tau)\omega^2\tau^2}{1+\omega^2\tau^2}\frac{d\tau}{\tau} + j\int_0^\infty \frac{G(\tau)\omega\tau}{1+\omega^2\tau^2}\frac{d\tau}{\tau} \tag{4.5}$$

It is thus evident that equations for real and imaginary parts of $S(\omega)$ are Frcdholm integral equations of the first kind, and the problem of calculating $G(\tau)$, knowing $S'(\omega)$ and $S''(\omega)$ is inverse and ill–posed. The ill–posedness of this problem is demonstrated in section 4.5.1. The experimental data, $S'(\omega)$ and $S''(\omega)$, will be noisy, discrete and from a limited range of frequencies.

Further, note that $G(\tau)$ may be rccovered from either the real or the imaginary part of $Q(\omega)$. This redundancy is an opportunity for noise reduction. It also implies that the real and imaginary parts of $Q(\omega)$ are not independent and so all noisy data will be inconsistent. These issues are discussed further in section 4.9.

4.3 Rayleigh–Ritz Galerkin Approximation

In this section the Rayleigh–Ritz Galerkin numerical inversion technique is applied to the computation of relaxation spectra. This method is chosen as it clarifies the ill-conditioning of the problem and allows regularisation of the inverse problem to be adapted to the noise characteristics.

The Rayleigh–Ritz Galerkin Approximation is based on the discretisation of the continuous operators. Knowing that the data will only be measured at a discrete set of frequencies, ω_k, the relationship between the continuous formulae and their discrete counterparts will be defined.

4.3.1 Sampled, Frequency Limited Data

From equations 3.22 and 3.12, which demonstrate the linear relationship between the relaxation time distribution and the normalised permittivity function:

$$S(\omega) = j \int_0^\infty \frac{G(\tau)\omega}{1 + j\omega\tau} d\tau \tag{4.6}$$

Assume that the permittivity has been measured for frequencies:

$$-\xi < \ln(\frac{\omega}{\omega_0}) < \xi \tag{4.7}$$

where ω_0 is the geometric centre of the range of frequencies and $\omega_0 = \sqrt{\omega_{\min}\omega_{\max}}$.

The range $[-\xi, \xi]$ corresponds to $[\ln(\frac{\omega_{\min}}{\omega_0}), \ln(\frac{\omega_{\max}}{\omega_0})]$. Therefore the measured frequencies have to be exponentially sampled

$$\omega_k = \omega_0 e^{k\frac{\xi}{N}} \qquad k = 0, \pm 1, \pm 2, \ldots, \pm N \tag{4.8}$$

which corresponds to uniform sampling in the log-frequency domain

$$\ln(\omega_k) = \ln(\omega_0) + k\frac{\xi}{N} \qquad k = 0, \pm 1, \pm 2, \ldots, \pm N \tag{4.9}$$

By the sampling localisation theorem this restricts the knowledge of the relaxation time distribution to no more than the reciprocal range: $-\xi < \ln(\frac{\tau}{\tau_0}) < \xi$; where $\tau_0 = 1/\omega_0$ is the geometric centre of the range of time constants.

Assume that the time constant is zero outside this range. Making the substitution $u = \ln(\frac{\omega}{\omega_0})$ and $v = \ln(\frac{\tau}{\tau_0})$ into Eqn. 4.6 yields

$$S_u(u) = j\int_{-\xi}^{\xi} G_v(v)\frac{\omega_0 e^u \tau_0 e^v}{1+je^{u+v}}dv = \int_{-\xi}^{\xi} G_v(v)\frac{je^{u+v}}{1+je^{u+v}}dv \tag{4.10}$$

where $S_u(u) = S(\omega)$ and $G_v(v) = G(\tau)$. Note also that $\omega_0\tau_0 = 1$.

By rationalising the denominator and splitting into real and imaginary parts:

$$S'_u(u) + jS''_u(u) = \int_{-\xi}^{\xi} G_v(v)\left[\frac{e^{2(u+v)}}{1+e^{2(u+v)}} + j\frac{e^{u+v}}{1+e^{2(u+v)}}\right]dv =$$

$$= \int_{-\xi}^{\xi} G_v(v)\frac{e^{2u+2v}dv}{1+e^{2u+2v}} + j\int_{-\xi}^{\xi} G_v(v)\frac{e^{u+v}dv}{1+e^{2u+2v}} \tag{4.11}$$

The kernels of these two integrals, $k'(u,v) = \frac{e^{2u+2v}}{1+e^{2u+2v}}$ and $k''(u,v) = \frac{e^{u+v}}{1+e^{2u+2v}}$ are both bounded, real and symmetric and hence compact and self-adjoint when the range of integration is finite.

4.3.2 Discretisation of the Integral Equation

The integral operators in Eqn. 4.11 may be discretised by approximating the functions $S'_u(u)$, $S''_u(u)$ and $G_v(v)$ in some finite basis $B = \{B_i, i = 1, 2, ..., N_B\}$ which is orthonormal with respect to some inner product, *i.e.*

$$(B_i, B_j) = \int_{-\xi}^{\xi} B_i(z)B_j(z)dz = \delta_{ij} \tag{4.12}$$

$$S'_u(u) \simeq \sum_i S'_i B_i(u) \qquad S''_u(u) \simeq \sum_i S''_i B_i(u) \qquad G_v(v) \simeq \sum_i g_i B_i(v) \tag{4.13}$$

By orthogonality, the projection of the function S'_u onto the subspace spanned by the basis can be found using $S'_i = \int_{-\xi}^{\xi} S'_u(u)B_i(u)du$, and similar for S''_i.

By replacing the functions S'_u and G_v by their finite dimensional approximations, the real part of Eqn. 4.11 is transformed to:

$$\sum_i S'_i B_i(u) = \int_{-\xi}^{\xi} \sum_i g_i B_i(v)K'(u,v)dv = \sum_i g_i \int_{-\xi}^{\xi} B_i(v)K'(u,v)dv \tag{4.14}$$

Multiplying both sides by $B_j(u)du$ and integrating gives

$$\int_{-\xi}^{\xi} \sum_i S_i' B_i(u) B_j(u) du = \int_{-\xi}^{\xi} \sum_i g_i \int_{-\xi}^{\xi} B_i(v) K'(u,v) dv B_j(u) du \Longrightarrow$$

$$\sum_i S_i' \int_{-\xi}^{\xi} B_i(u) B_j(u) du = \sum_i g_i \int_{-\xi}^{\xi} \int_{-\xi}^{\xi} B_i(v) K'(u,v) B_j(u) dv du \qquad (4.15)$$

By orthogonality of the basis functions, the lefthand side is equal to S_j'.

In a similar way a relation for the imaginary part vector $\mathbf{S''} = (S_i'')$ can be derived. Then the discretised approximate equations take the form:

$$\mathbf{S'} = \mathbf{K'G} \qquad \mathbf{S''} = \mathbf{K''G} \qquad (4.16)$$

where $\mathbf{K'}$ is a matrix with elements $K_{ij} = \int_{-\xi}^{\xi} \int_{-\xi}^{\xi} B_i K'(u,v) B_j du dv$.

Thus, the Rayleigh–Ritz Galerkin method has transformed the integral equations 4.5 into a discretised weak form equivalent to a system of linear equations where the unknowns are the components of the DRT spectrum in the chosen basis.

4.3.3 Choice of Basis functions

For most choices of basis functions, the one and two dimensional integrals required to evaluate the data vectors $\mathbf{S'}$ and $\mathbf{S''}$, and the operator matrices $\mathbf{K'}$ and $\mathbf{K''}$, can not be evaluated exactly. In these cases some approximate *quadrature rules* are required. Here the *Gaussian quadrature* is applied. If the N points x_j are the abscissas and the set w_j are the weights then the Gaussian formula is

$$\int_{x_1}^{x_N} W(x) f(x) dx \simeq \sum_{j=1}^{N} w_j f(x_j) \qquad (4.17)$$

where $W(x)$ is some known weight function.

In Gaussian quadrature the weights and abscissas are chosen such that the approximation 4.17 is exact if $f(x)$ is a polynomial of degree $2N-1$ or less.

In the fundamental case when $W(x) = 1$ and the range of inversion is the unit interval [-1,1] then the weights and abscissas are derived from zeros and derivatives of a set of polynomials, orthogonal on the unit interval, known as Legendre polynomials. These polynomials satisfy the recurrence relation:

$$P_{-1} \equiv 0 \qquad P_0 \equiv 1$$

$$(j+1)P_{j+1} = (2j+1)xP_j - jP_{j-1} \qquad (4.18)$$

where P_j is Legendre polynomial.

For example, if the quadrature rule is applied to the integral for K' from the right side of Eqn. 4.15 it follows

$$\int_{-\xi}^{\xi}\int_{-\xi}^{\xi} B_i(v)K'(u,v)B_j(u)dvdu \simeq \sum_{j=1}^{N}\sum_{i=1}^{N} w_j w_i B_i(v_j)K'(u_i,v_j)B_j(u_i) \qquad (4.19)$$

Eqn. 4.17 is an approximation as the integrand is effectively of infinite degree due to the exponential nature of the kernel. The basis functions are evaluated at the Gauss points found from the Gauss-Legendre formula 4.18.

The operators K' and K'' are approximated by matrices defined by:

$$\mathrm{K}' = (K'B_i, B_j) \qquad \mathrm{K}'' = (K''B_i, B_j) \qquad (4.20)$$

As the operators are real and self-adjoint, the matrices are real and symmetric. The usefulness of this approximation is that the eigenvalues and eigenvectors of the matrices K′ and K″ approximate the eigenvalues and eigenfunctions of the operators K' and K''. If the eigenvalues of the matrix are ordered $\lambda_1^- \leq ...\lambda_{N_-}^- < 0 < \lambda_{N_+}^+ \leq ...\lambda_1^+$ then the following result holds [52]:

$$\begin{aligned} &if \quad N_- > 0 \quad then \quad \mu_n^- \leq \lambda_n^- \quad n = 1,...,N_- \\ &if \quad N_+ > 0 \quad then \quad \mu_n^+ \geq \lambda_n^+ \quad n = 1,...,N_+ \end{aligned} \qquad (4.21)$$

where μ_i^- and μ_i^+ are the negative and positive eigenvalues of the corresponding operator. As the eigenvalues are extreme values of the Rayleigh quotient $R_k(p) = (Kp,p)/(p,p)$, where p is the corresponding orthonormal sequence of eigenvectors, the eigenvalues are better approximated than the eigenfunctions.

Now consider approximating the operators K' and K'' using basis functions:

$$B_n = \sqrt{\frac{2n+1}{2\xi}} P_n(\frac{x}{\xi}) \qquad (4.22)$$

where P_n is the nth monic Legendre polynomial. This basis is orthonormal with respect to the inner-product, Eqn. 4.12.

The basis functions are odd when n is odd and even when n is even. The kernel $k''(u,v) = \frac{e^{u+v}}{1+e^{2u+2v}} = \frac{1}{2}sech(u+v)$ has the property that $k''(u,v) = k''(-u,-v)$ and thus it preserves the even or oddness of the function it acts upon, *i.e.* :

$$
\begin{aligned}
if \quad K''B_j(u) &= \int_{-\xi}^{\xi} B_j(v)k''(u,v)dv \quad then \\
K''B_j(-u) &= \int_{-\xi}^{\xi} B_j(v)k''(-u,v)dv \qquad (4.23) \\
&= \int_{-\xi}^{\xi} B_j(-v)k''(-u,-v)dv \\
&= \int_{-\xi}^{\xi} B_j(v)k''(u,v)dv \\
&= \begin{cases} K''B_j(u) & B_j \quad even \\ -K''B_j(u) & B_j \quad odd \end{cases}
\end{aligned}
$$

It follows that $\mathrm{K}'' = (K''B_i, B_j) = 0$ if B_i is odd and B_j is even, or vice versa. Thus, reordering the basis B into even functions followed by odd functions naturally partitions the eigenvalue problem into two independent eigenvalue problems *i.e.*

$$\mathrm{K}'' = \begin{pmatrix} \mathrm{K}''_{even} & 0 \\ 0 & \mathrm{K}''_{odd} \end{pmatrix} \qquad (4.24)$$

The eigenvalues of K''_{even} are positive and decrease to zero, as the eigenfunctions become more oscillatory. Similarly, the eigenvalues of K''_{odd} are negative and increase to zero, as the eigenfunctions become more oscillatory.

A data vector may be calculated from experimental measurements: $\mathrm{S}'' = (S''_u, B_i)$, then the relaxation time distribution can be reconstructed by solving the system

$$\mathrm{S}'' = \mathrm{K}''\mathrm{G} \qquad (4.25)$$

where $\mathrm{G} = (G_v, B_i)$.

Similar results hold for the operator K' with kernel $k'(u,v) = \frac{e^{2u+2v}}{1+e^{2u+2v}} = \frac{1}{2}(1+\tanh(u+v))$.

If the kernel is separated into odd and even parts, *i.e.* $k'_{even}(u,v) = \frac{1}{2}$, $k'_{odd}(u,v) = \frac{1}{2}\tanh(u+v)$ then:

$$K'_{even}B_j = \int_{-\xi}^{\xi} B_j(v)\frac{1}{2}dv \qquad (4.26)$$

$$= \int_{-\xi}^{\xi} B_j(v)\frac{1}{2}\sqrt{2\xi}B_0(v)dv$$

$$= \begin{cases} \sqrt{\xi/2} & j=0 \\ 0 & else \end{cases}$$

$$(B_i, K'_{even}B_j) = \int_{-\xi}^{\xi} B_j(v)\begin{cases} \xi B_0(v) & j=0 \\ 0 & else \end{cases} dv \qquad (4.27)$$

$$= \begin{cases} \xi & i=j=0 \\ 0 & else \end{cases}$$

and, as $k'_{odd}(u,v) = -k'_{odd}(-u,-v)$, the odd part reverses the even or oddness of the function it acts upon, *i.e.* :

$$if \quad K'_{odd}B_j(u) = \int_{-\xi}^{\xi} B_j(v)k'_{odd}(u,v)dv \quad then \qquad (4.28)$$

$$K'_{odd}B_j(-u) = \int_{-\xi}^{\xi} B_j(v)k'(-u,v)dv$$

$$= \int_{-\xi}^{\xi} B_j(-v)k'_{odd}(-u,-v)dv$$

$$= -\int_{-\xi}^{\xi} B_j(-v)k'_{odd}(u,v)dv$$

$$= \begin{cases} -K'_{odd}B_j(u) & B_j \ \ even \\ K'_{odd}B_j(u) & B_j \ \ odd \end{cases}$$

Reordering the basis B into B_0, the n even functions followed by n odd functions leads to a block representation of K′:

$$\mathrm{K}' = \begin{pmatrix} K'_{00} & 0 & K'_{0o} \\ 0 & 0 & K'_{eo} \\ (K'_{0o})^T & (K'_{eo})^T & 0 \end{pmatrix} \qquad (4.29)$$

where $K'_{00} = \xi$ is a scalar, $K'_{0o} \in \Re^{1\times n}$ and $K'_{eo} \in \Re^{n\times n}$ are a non-symmetric matrices.

If S′ and G are similarly blocked then this system may be solved in the following steps:

1. solve

$$\mathrm{K}'_{eo}(\mathrm{G}_v)_o = (\mathrm{S}'_u)_e \tag{4.30}$$

2. calculate

$$(\mathrm{G}_v)_0 = ((\mathrm{S}'_u)_0 - \mathrm{K}'_{0o}(\mathrm{G}_v)_o)/\xi \tag{4.31}$$

3. solve

$$(\mathrm{K}'_{eo})^T(\mathrm{G}_v)_e = ((\mathrm{S}'_u)_o - (\mathrm{K}'_{0o})^T(\mathrm{G}_v)_0) \tag{4.32}$$

Both the systems $S'_u = K'G_v$ and $S''_u = K''G_v$ contain information about G_v. Where S'_u and S''_u are derived from experimental measurements the system of equations:

$$\begin{pmatrix} \mathrm{K}' \\ \mathrm{K}'' \end{pmatrix} \mathrm{G} = \begin{pmatrix} \mathrm{S}' \\ \mathrm{S}'' \end{pmatrix} \tag{4.33}$$

form an overdetermined, inconsistent set of equations. Solving this system in the least-squares sense is equivalent to finding the *maximum a posteriori* (MAP) relaxation time distribution.

4.4 Tikhonov regularisation

In this section a technique for stabilising the ill-posed inverse problems will be introduced. Regularisation aims to replace the ill-posed problem by nearby well-posed problem. There are many nearby problems each with a different solution. The choice of a nearby problem, generally controlled by a regularisation parameter, is important as it directly drives the calculations. The resulting accuracy of the recovered spectrum is controlled by this choice and the understanding of it will be discussed in the next sections.

The main difficulty in solving a Fredholm integral equation of the first kind arises from the instability of the inverse operator. In the forward transformation, from f to g, some information is greatly attenuated or lost altogether. By necessity, when solving the inverse problem, small features in the data are greatly amplified to recover f. When the data are noisy, the amplification of noise features leads to arbitrarily large artefacts in f. In particular, small oscillations in measurements of the permittivity data can yield arbitrarily large oscillations in

the spectrum $G(\tau)$. In order to mitigate this problem *Tikhonov regularisation* will be applied. Regularisation aims to amplify components of the data where signal dominates while reducing the amplification of components dominated by noise. More details can be found in [53].

Tikhonov regularisation replaces the original problem: solve $Kf = g$, with the problem of minimising the functional

$$\min_f \left\{ \| g - Kf \|^2 + \mu \| f \|^2 \right\} \tag{4.34}$$

where $\mu > 0$ is a regularisation parameter, $\| \cdot \|$ is a *norm* and K is an operator which could be linear and discretised.

The solution of 4.34 when K is linear and discretised and the standard Euclidian norm is used, known as the *standard Tikhonov regularised solution*, is

$$(\mathbf{K^T K} + \mu \mathbf{I})\mathbf{f} = \mathbf{K^T g} \tag{4.35}$$

$$\mathbf{f} = (\mathbf{K^T K} + \mu \mathbf{I})^{-1} \mathbf{K^T g} \tag{4.36}$$

where superscript "T" indicates transpose and I is identity matrix.

Since $\mathbf{K^T K}$ has nonnegative eigenvalues, for any positive value μ, the matrix $(\mathbf{K^T K} + \mu \mathbf{I})$ has nonnegative eigenvalues bounded below by μ. Thus the problem 4.34 is well–posed and the solutions given above are unique [45].

Many regularisation schemes, including a standard Tikhonov regularisation can be obtained by applying *Singular Value Decomposition* which will be discussed in the following section.

4.5 Singular Value Decomposition

Singular Value Decomposition, or SVD, methods are based on the following theorem of linear algebra:

Any $M \times N$ matrix K whose number of rows M is greater than or equal to its number of columns N, can be written as the product of an $M \times N$ column-orthogonal matrix U, an $N \times N$ diagonal matrix Λ with positive or zero elements (the *singular values*), and the transpose of an $N \times N$ orthogonal matrix V, *e.g.*

$$\mathbf{K} = \mathbf{U} \Lambda \mathbf{V^T} \tag{4.37}$$

In SVD the non zero elements of the diagonal matrix $\Lambda = diag(\lambda_1, \lambda_2, \ldots, \lambda_k)$, k=min$\{M, N\}$ are the monotonically decreasing positive singular values λ_i. The columns of U and V are the left and right singular vectors of the matrix K and could be determined, respectively, from:

$$\mathbf{K}v_j = \lambda_j u_j \qquad \mathbf{K}^{\mathbf{T}} u_j = \lambda_j v_j \tag{4.38}$$

The procedure using SVD and applying Tikhonov regularisation can be directly applied to the inverse problem of EIS for recovering the distribution of relaxation times.

Consider the discretised Fredholm integrals of the first kind written in terms of matrix operators, Eqn. 4.33. Decomposing matrix K into $\mathbf{K} = \mathbf{U}\Lambda\mathbf{V}^{\mathbf{T}}$ the following system is obtained:

$$\mathbf{U}\Lambda\mathbf{V}^{\mathbf{T}}\mathbf{G} = \mathbf{S} \tag{4.39}$$

Multiplying by transposed matrix $\mathbf{U}^{\mathbf{T}}$ from right side the equation takes the form:

$$\mathbf{U}^{\mathbf{T}}\mathbf{U}\Lambda\mathbf{V}^{\mathbf{T}}\mathbf{G} = \mathbf{U}^{\mathbf{T}}\mathbf{S} \tag{4.40}$$

The matrices U and V are orthogonal in the sense that their columns are orthonormal,

$$\sum_{i=1}^{M} U_{ik}U_{in} = \delta_{kn} \qquad 1 \le k \le N, \quad 1 \le n \le N \tag{4.41}$$

$$\sum_{j=1}^{N} V_{jk}V_{jn} = \delta_{kn} \qquad 1 \le k \le N, \quad 1 \le n \le N \tag{4.42}$$

According to the definition of the orthogonality $\mathbf{U}^{\mathbf{T}}\mathbf{U} = \mathbf{I}$ and $\mathbf{V}^{\mathbf{T}}\mathbf{V} = \mathbf{I}$ where I is understood to be the identity matrix of the appropriate dimension. Then

$$\Lambda\mathbf{V}^{\mathbf{T}}\mathbf{G} = \mathbf{U}^{\mathbf{T}}\mathbf{S} \tag{4.43}$$

where Λ is diagonal matrix and $\Lambda^{-1} = diag(1/\lambda_1, 1/\lambda_2, \ldots, 1/\lambda_n)$.

Thus

$$\mathbf{V}^{\mathbf{T}}\mathbf{G} = \Lambda^{-1}\mathbf{U}^{\mathbf{T}}\mathbf{S} \tag{4.44}$$

Multiplying again by V from the right similar as it was done for U the final solution is

$$\mathbf{G} = \mathbf{V}\Lambda^{-1}\mathbf{U}^{\mathbf{T}}\mathbf{S} \tag{4.45}$$

or

$$G = \sum_i V_i \frac{(U_i, S)}{\lambda_i} \tag{4.46}$$

where $(\cdot, \cdot)$ is the standard inner product.

SVD gives some idea about the ill-posedness of the matrix K which can be defined via the *condition number*. The condition number is defined as the ratio of the largest to the smallest eigenvalues:

$$k = |\lambda_{max}/\lambda_{min}| \tag{4.47}$$

If the matrix equation $\mathbf{Ax} = \mathbf{b}$ is perturbed to $(\mathbf{A} + d\mathbf{A})(\mathbf{x} + d\mathbf{x}) = (\mathbf{b} + d\mathbf{b})$ then the relative error in the solution is bounded by:

$$\frac{\|dx\|}{\|x\|} \leq k \left(\frac{\|dA\|}{\|A\|} + \frac{\|db\|}{\|b\|} \right) \tag{4.48}$$

Thus, the condition number k indicates how relative errors in the data vector b or the operator matrix A are amplified into relative errors in the solution vector x. A large condition number indicates an ill-posed problem.

The singular values λ_i are the eigenvalues of the least squares matrix $\mathbf{K}^{\mathbf{T}}\mathbf{K}$ and so the ratio of the largest to the smallest singular value is the condition number of the least squares inverse problem. The faster the singular values decay to zero, the fewer components of the solution vector can be reliably determined from the data.

For real measured data on physical objects the largest accumulation of errors is in the experimental measurement vector S. These errors are the combination of random errors, such as digital noise in the electronics used for the impedance measurements, and more serious systematic errors such as a matching errors in the driving electronics, inaccuracies in electrode attachment and errors due to inhomogeneity. As indicated above, the ill-posedness of the inverse problem means that small errors in the impedance/admittivity/permittivity data are translated into large errors in the reconstructed relaxation spectrum. A small relative error in S will result in the relaxation spectrum generated by Eqn. 4.46 being dominated by highly amplified noise artifacts.

The problem is partially solved by applying the Tikhonov regularisation technique, *i.e.* solving

$$(\mathbf{K}^{\mathbf{T}}\mathbf{K} + \mu\mathbf{I})\mathbf{G} = \mathbf{K}^{\mathbf{T}}\mathbf{S} \tag{4.49}$$

Repeating the above steps for SVD the solution for a reconstructed distribution of relaxation times is found:

$$G = \sum_i V_i \left(\frac{\lambda_i}{\lambda_i^2 + \mu^2}\right)(U_i, S) \tag{4.50}$$

It is clear from this formulation that the relaxation time distribution is a weighted sum of the right singular vectors where the weighting is a product of an amplification factor, A_i, and the inner product (U_i, S)

$$A_i = \frac{\lambda_i}{\lambda_i^2 + \mu^2} \tag{4.51}$$

The amplification factor grows infinitely as both λ_i and μ approach zero. Note that as $\lambda_i \to 0$, the unregularised inverse amplification factor $1/\lambda_i \to \infty$ while $\frac{\lambda_i}{\lambda_i^2+\mu^2} \to 0$. Figure 4.1 displays the amplification factor with different values of Tikhonov parameter.

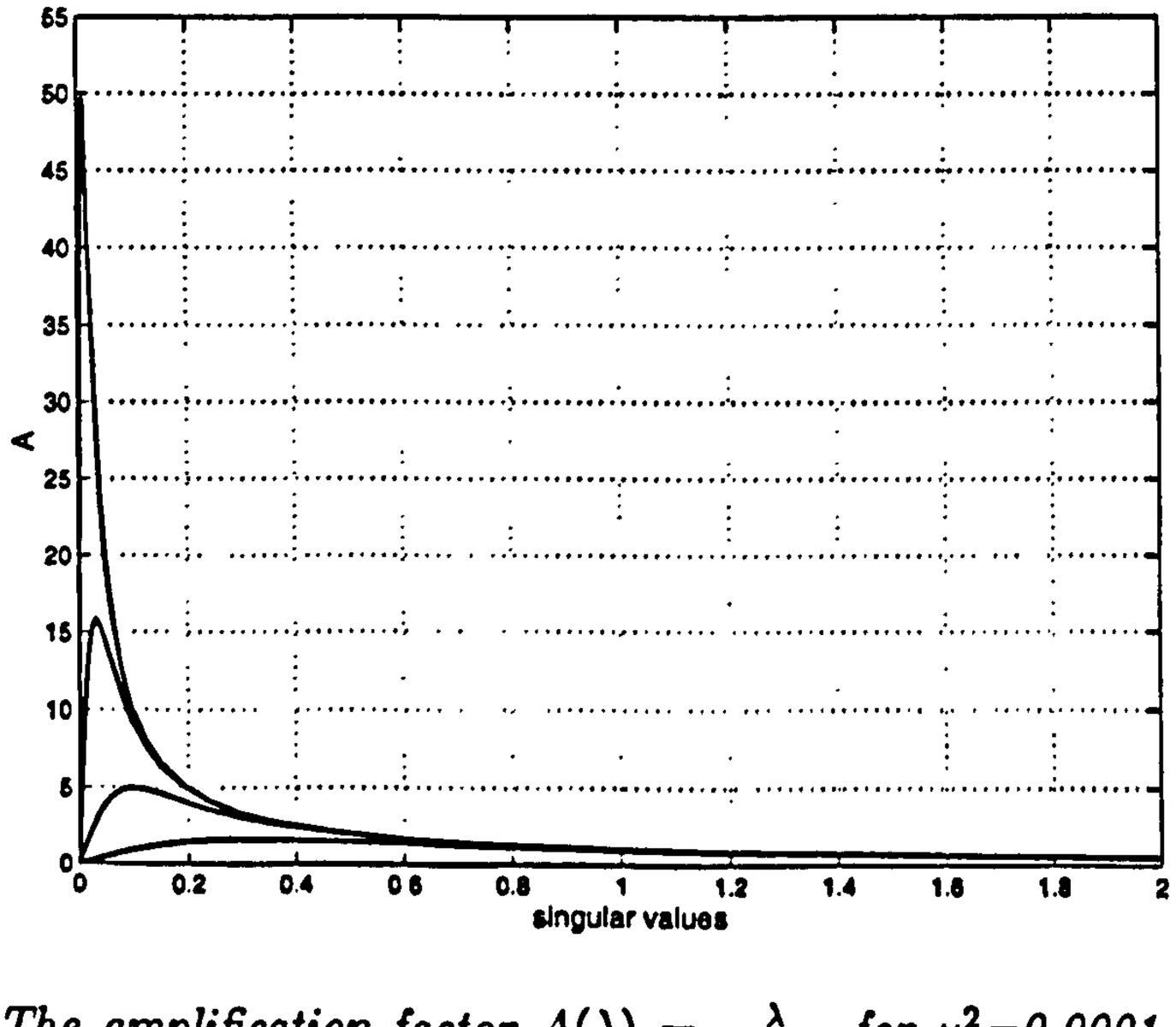

Figure 4.1: *The amplification factor* $A(\lambda) = \frac{\lambda}{\lambda^2+\mu^2}$ *for* μ^2*=0.0001, 0.001, 0.01, 0.1, from top to bottom.*

4.5.1 Error Analysis using Singular Value Decomposition

Singular Value Decomposition helps to understand the ill-posedness of the problem and the effect of varying the Tikhonov regularisation parameter μ.

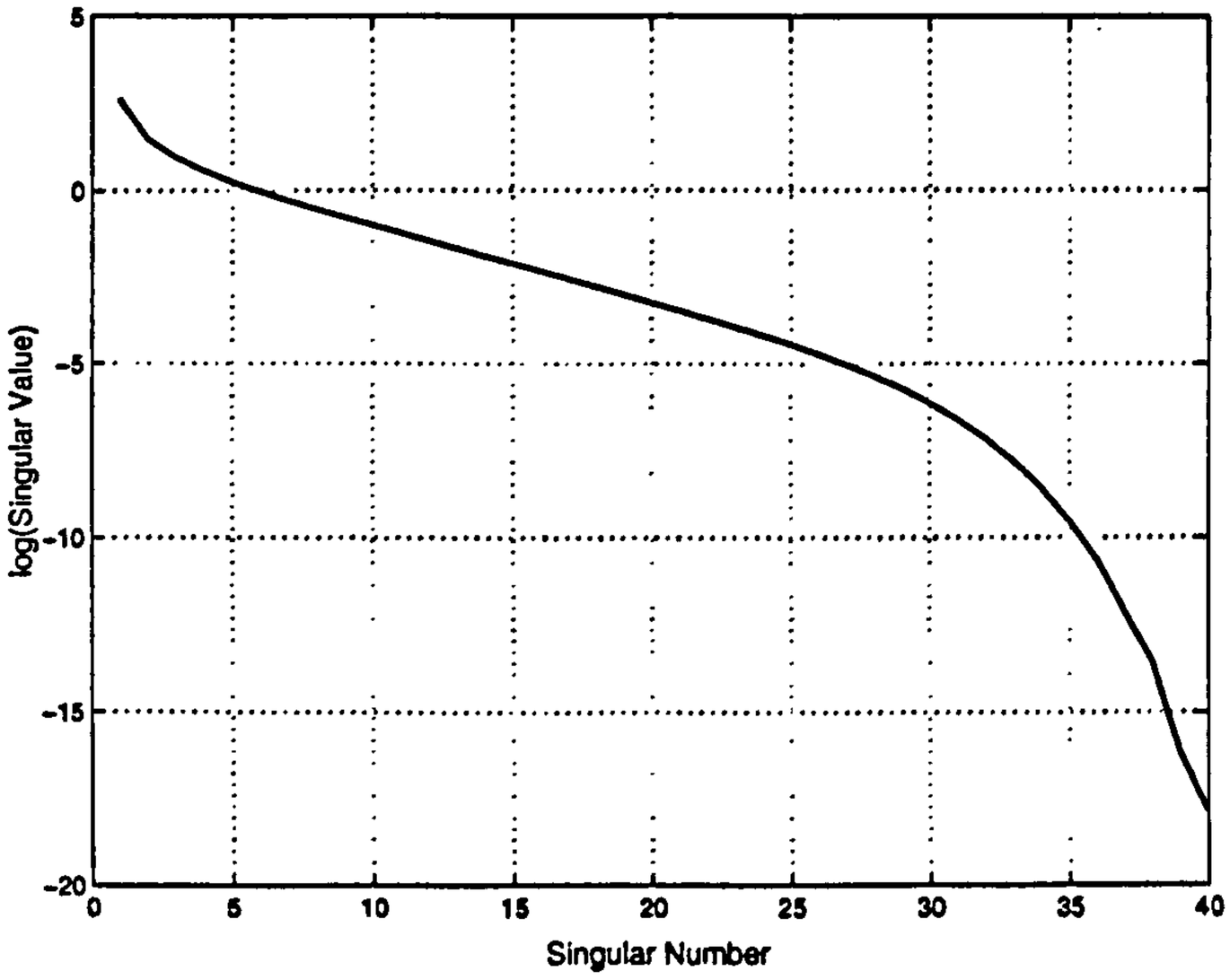

Figure 4.2: *The natural logarithm of the singular values of the derivative matrix* K′.

Figure 4.2 displays the logarithm of singular values of a derivative matrix K′. The decay is approximately linear with a gradient of $-1/4$ for the first 30 singular values and hence the singular values, λ_n, of the system approximately satisfy:

$$\lambda_n \propto e^{-\frac{1}{4}n} \tag{4.52}$$

where n is the singular number. Singular values are effected by choice of number of basis functions.

The decay rate of the singular values indicates the level of the ill–posedness of the inverse problem. In Electrical Impedance Tomography (EIT), known as an extreme ill–posed medical imaging problem, it was found, [54], that the singular values decays as fast as $\lambda_n \propto e^{-n^2}$.

Thus it can be concluded that the calculation of the diclectric relaxation time spectra is much better conditioned than the EIT inverse problem.

The singular basis V spans the space of DRT spectra while U spans the measured permittivity data. If the Tikhonov parameter $\mu = 0$ then the amplification factor is $1/\lambda_i$. Typically the permittivity vector S will be degraded by systematic and random noise introduced by the measurement process. Random noise will include components of all the right singular vectors, U_i. The noise in the components with a small singular values will be greatly amplified when the relaxation time distribution is calculated. The Tikhonov factor limits the maximum ampli-

fication up $1/2\mu$ when $\lambda_i = \mu$. The amplification factor converges to zero as the singular values tend to zero. Singular functions tend to become more oscillatory as the singular values decrease therefore, the component of each singular function in the measured data also decreases for increasing singular number. At some stage the component (U_i, S) becomes dominated by noise and, including terms beyond this in the solution, leads to artifacts looking like high frequency, random oscillations. Thus increasing the Tikhonov factor smoothes the solution from the unregularised solution dominated by high frequency noise artifacts to a smoothed version of a correct answer (necessarily distorted) and eventually into a smooth function close to zero.

Tikhonov regularisation requires the selection of a Tikhonov parameter to fit the singular noise spectrum of electrical measurements. The noise spectrum is uniformly distributed for the most forms of the random noise such as a electronic noise in the data acquisition system. However, due to systematic errors it can be concentrated in few singular components. The singular spectrum of the experimental measurements is typically weighted in the early singular components with the largest singular values. So, large Tikhonov factors include only the most reliable data but also reduce the resolution of the reconstruction.

When the Tikhonov regularisation is used, a significant problem is the choice of a good regularisation parameter μ. As it was shown above this parameter plays essentially the same role as the bandwidth of the filter when smoothing noisy data.

There are several strategies to determine the regularisation parameter. For a detailed analysis see *e.g.* [55], [56] and the references therein. The choice of the parameter is based on *a-priori* information about the solution. In practice, little information is available on the noise spectrum of the experimental measurements, so the Tikhonov factor might be chosen using some very general criteria. In the application of the GRIM presented in the subsequent section the Tikhonov factor will be chosen on the basis of test results of the analytic circuit with known time constants and applied noise.

4.6 Example Application

Consider using GRIM to recover the relaxation time spectra for a material with a single time constant τ_0. Assume that the frequency response of the material is known for a range of frequencies $\ln\left(\frac{\omega}{\omega_0}\right) \in \left[-\frac{10\pi}{7}, \frac{10\pi}{7}\right]$, where $\omega_0 = 1/\tau_0$. In this case the DRT distribution is $G_v(v) = \delta(v)$. It allows direct comparison with the

example application of the moving–average method of Davies and Anderssen in section 3.4.4 (Fig. 3.3). To use the numerical procedure a number of choices need to be made: the number of basis functions to use, the order of Gauss–Legendre integration to use and the Tikhonov regularisation factor to use. In this example six basis functions are used. The order of integration must accurately approximate the integrals in Eqn. 4.15 for the highest degree basis functions. In this example $N = 21$ is chosen. Figure 4.3 illustrates the reconstructed DRT spectrum with no regularisation and using a Tikhonov factor of $\mu = 0.001$.

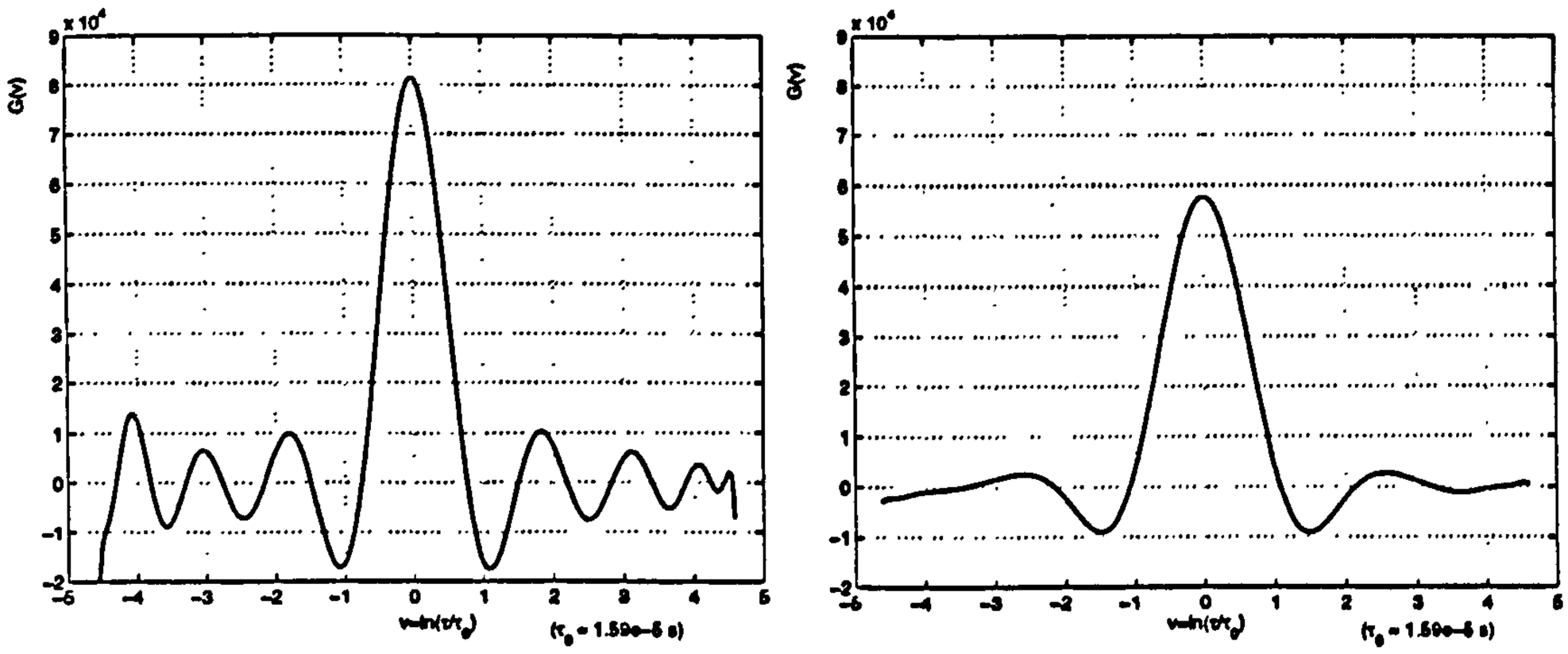

Figure 4.3: *Reconstruction of a DRT distribution $G_v(v) = \delta(v)$ using 21 samples of* S″ *without (left) and with Tikhonov regularisation, i.e. solving Eqn. 4.49.*

The ringing in the reconstructed time constant distribution is a combination of Gibbs effect due to the limited number of basis functions used and noise due to errors in approximate integrals. The ringing can be reduced, at the expense of resolution, by using Tikhonov regularisation or applying a Hamming filter to the calculated spectrum. The Tikhonov regularisation was introduced in the previous section and the decrease in resolution it causes will be discussed in section 4.8.

Fig. 4.4 illustrates the relaxation time distribution reconstructed using the same data as Fig. 4.3, *i.e.* S′ calculated at 21 Gauss-Legendre integration abscissa over the interval $\left[-\frac{10\pi}{7}, \frac{10\pi}{7}\right]$, assuming a single time constant was present $G_v(v) = \delta(v)$. Tikhonov regularisation was used, implemented by filtering the singular values.

In both cases the peak is taller and the relative ripple amplitude is less than the moving–average result although the resolution is similar.

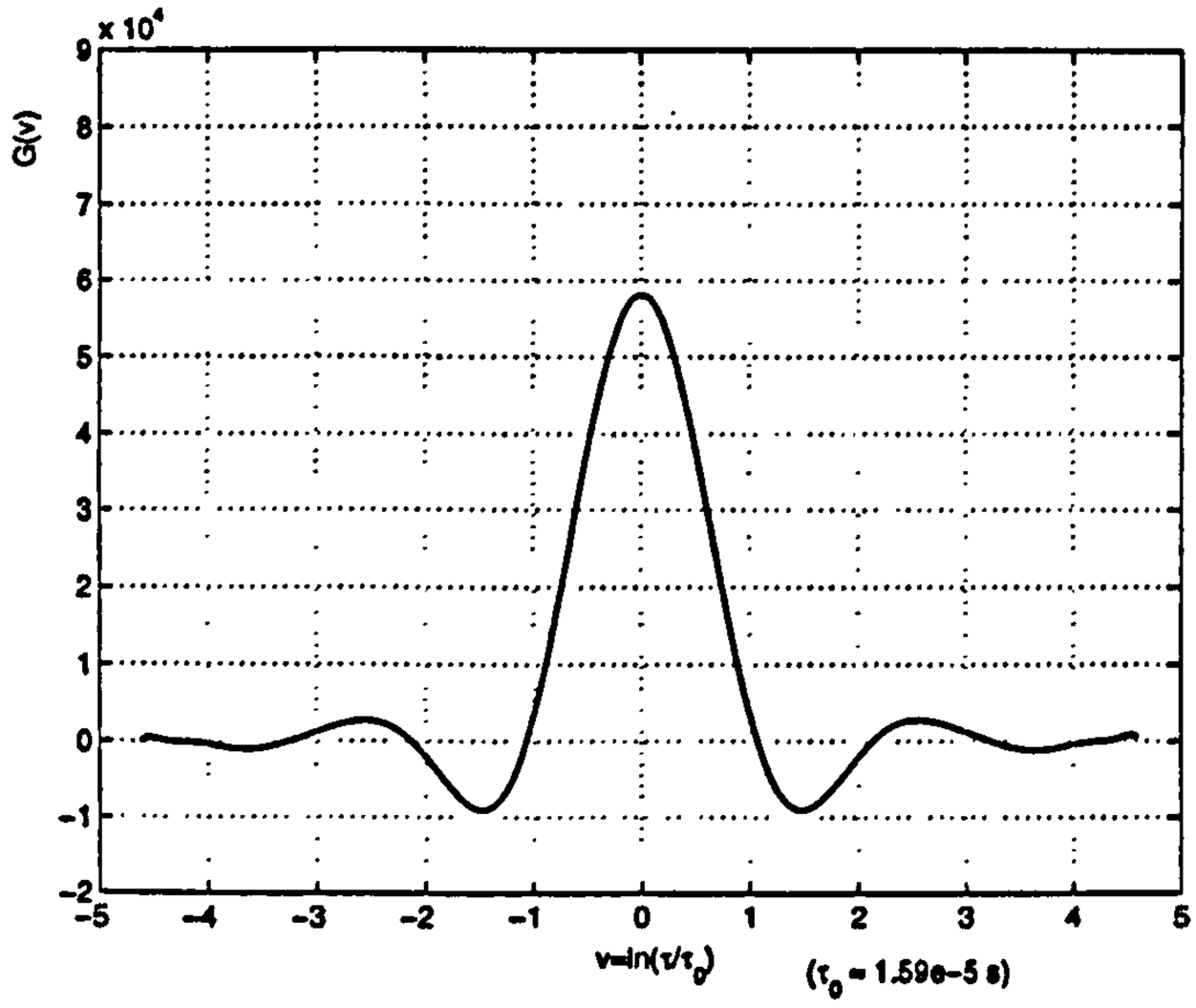

Figure 4.4: *Reconstruction of a time constant distribution $G_v(v) = \delta(v)$ using 21 samples of* S′ *and inverting using Tikhonov regularisation, i.e. solving Eqn. 4.49*

4.7 Calculation of Data Vector

In the example in section 4.6, the components of the data vector $S_i = \int_{-\xi}^{\xi} S_u(u)B_i(u)du$ were calculated from the analytic frequency response using Gauss–Legendre integration. In practise, the frequency response of the material is usually measured at discrete, exponentially distributed frequencies corresponding to equally spaced samples in the logarithmic frequency domain. Also, the data are contaminated by noise. Although the measured data could be interpolated to Gauss points, this would yield a poor estimate of the required integral. Less sophisticated, Newton–Cotes formulae, such as the Trapezoidal or Simpson's rules, use all the measured data and reduce the sensitivity of the low–order components of the data vector to noise in the experimental measurements.

Using the Trapezoidal rule and discretising as described in section 4.3.2 (see Eqn. 4.13), each element of a data vector can be computed as:

$$S_i = \frac{\xi}{N} S(u_0)B_i(u_0) + \frac{2\xi}{N} \sum_{j=1}^{N-1} S(u_j)B_i(u_j) + \frac{\xi}{N} S(u_N)B_i(u_N) \qquad (4.53)$$

where $u = \ln\left(\frac{\omega_i}{\omega_0}\right)$ and N is a number of samples.

For any particular experiment where the measurement noise characteristics are known, the integration method use to calculate S should be chosen to minimise

the sensitivity to the noise.

4.8 Resolving Power

The resolving power of the GRIM is a measure of the ability to separate two neighbouring relaxation times. Ideally, the recovered spectrum should consist of delta–functions at large number of time constants. In practice the relaxation time distribution is recovered as a broadened peak or a series of such peaks, Fig. 4.3.

The breadth of each peak depends on the following:

- the number of basis functions and data truncation;
- the noise characteristics and regularisation used.

Limiting the number of basis functions causes the resulting DRT spectrum to be smoothed and hence some information about the spectrum is lost. It is equivalent to truncated singular value decomposition. Increasing the number of basis functions will increase the time of computation. When the relaxation spectrum is recovered, an ill–posed problem must be solved. The resolution is limited by the minimum of the number of basis functions used and the effective number of singular components used. The latter is determined by the regularisation. As long as a sufficient number of basis functions are used, the number of independent parameters in the solution is determined by the quantity and quality of the measurements. Solving the system 4.33 increasingly amplifies the errors in higher singular components. If the noise spectrum is flat while the data spectrum decays for higher singular values, then the relative error increases in the higher singular components of the data. At some stage in the summation Eqn. 4.13, adding another singular component increases the relative error in the solution.

The matrices K_{ij} are calculated using numerical integration and have some errors too. Typically, these errors will increase for basis functions of higher degree.

The best regularisation depends upon the users objective: optimising the signal to noise ratio in $G(\tau)$ will often require different regularisation to optimising the resolution. For a general method, Tikhonov regularisation is a good compromise. When the noise spectrum of the equipment and experimental protocol are known, the regularisation may be tailored to the users specification.

Consider the resolving power of the algorithm for the perfect data, *i.e.* no noise data compared with noisy data. From the statements above it follows that:

- for the perfect data, increasing the number of basis functions and decreasing Tikhonov factor increases the resolution;

- for the noisy data, increasing the number of basis functions and decreasing the Tikhonov factor introduces components into the spectra with highly amplified noise.

To estimate the optimal number of basis functions and Tikhonov factor, noisy impedance data were simulated for the system with two time constants: $\tau_1 = 1 \times 10^{-7}$ s and $\tau_2 = 1 \times 10^{-4}$ s. Random Gaussian noise with a standard deviation of 0.5% in the amplitude and 1.5% in the phase was applied. Figure 4.5 demonstrates a reconstructed relaxation spectrum for 20, 30 and 40 basis functions. The Tikhonov factor was fixed at 0.001.

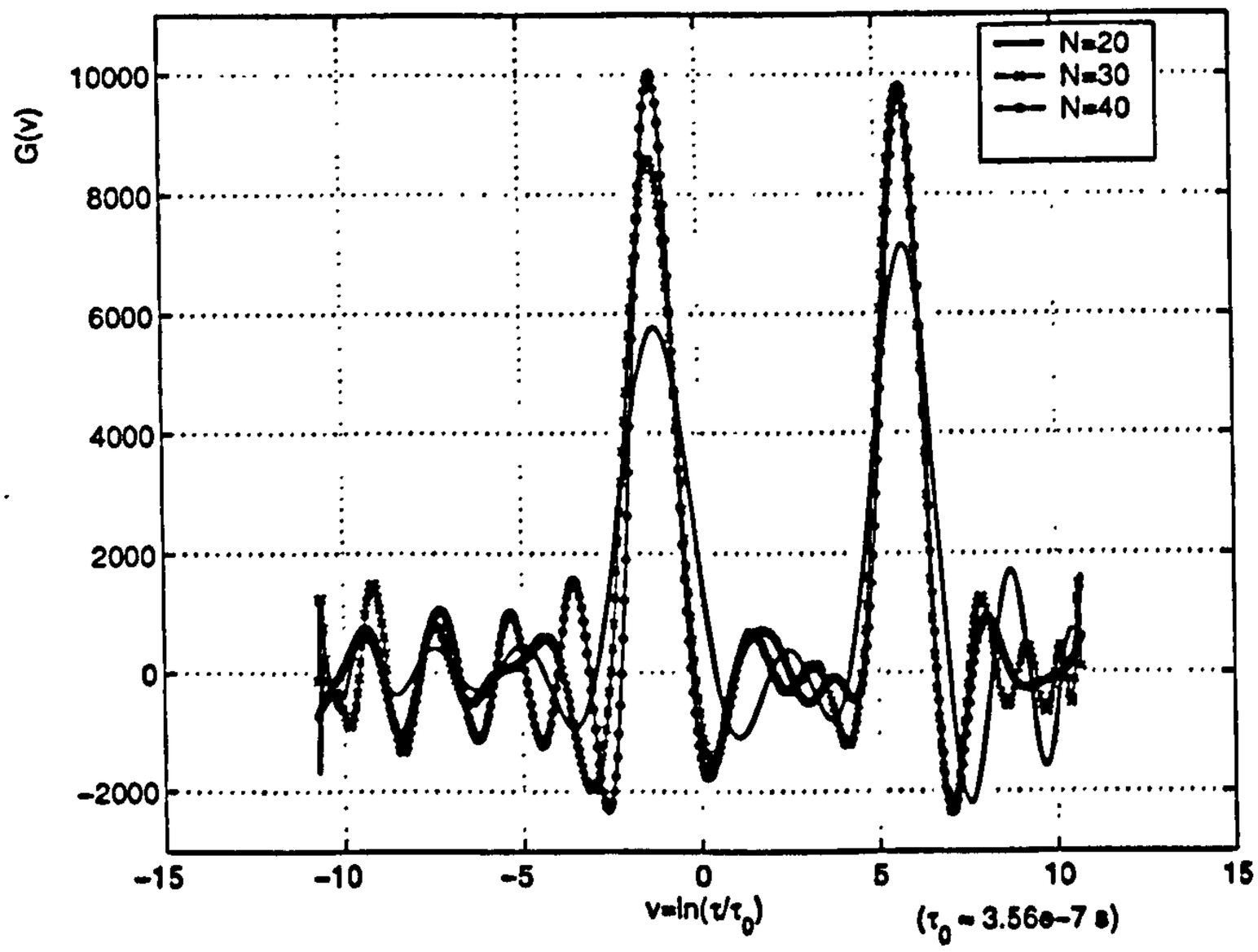

Figure 4.5: *Reconstruction of a relaxation spectrum for different number of basis functions and Tikhonov factor* $\mu = 0.001$.

The obtained results show that increasing the number of basis functions from 20 to 30 makes pulses narrower and therefore the resolving power is higher. The breadth of peaks corresponding to 30 and 40 basis functions stays the same but ringing has been reduced. Further increase of the number of basis functions did not improve the resolution as this was limited by the regularisation applied to control noise introduced by the floating point accuracy of the calculations . The optimal number can also be chosen from Figure 4.2. According to this picture the singular values decays fast after 30 basis functions and so the reconstruction

problem becomes increasingly ill–posed when these components are imaged.

Figure 4.6 illustrates the relaxation time distributions reconstructed for the same data. The number of basis functions has been set to 40. Tikhonov factor was varied and equaled to 0.0001, 0.001 and 0.01.

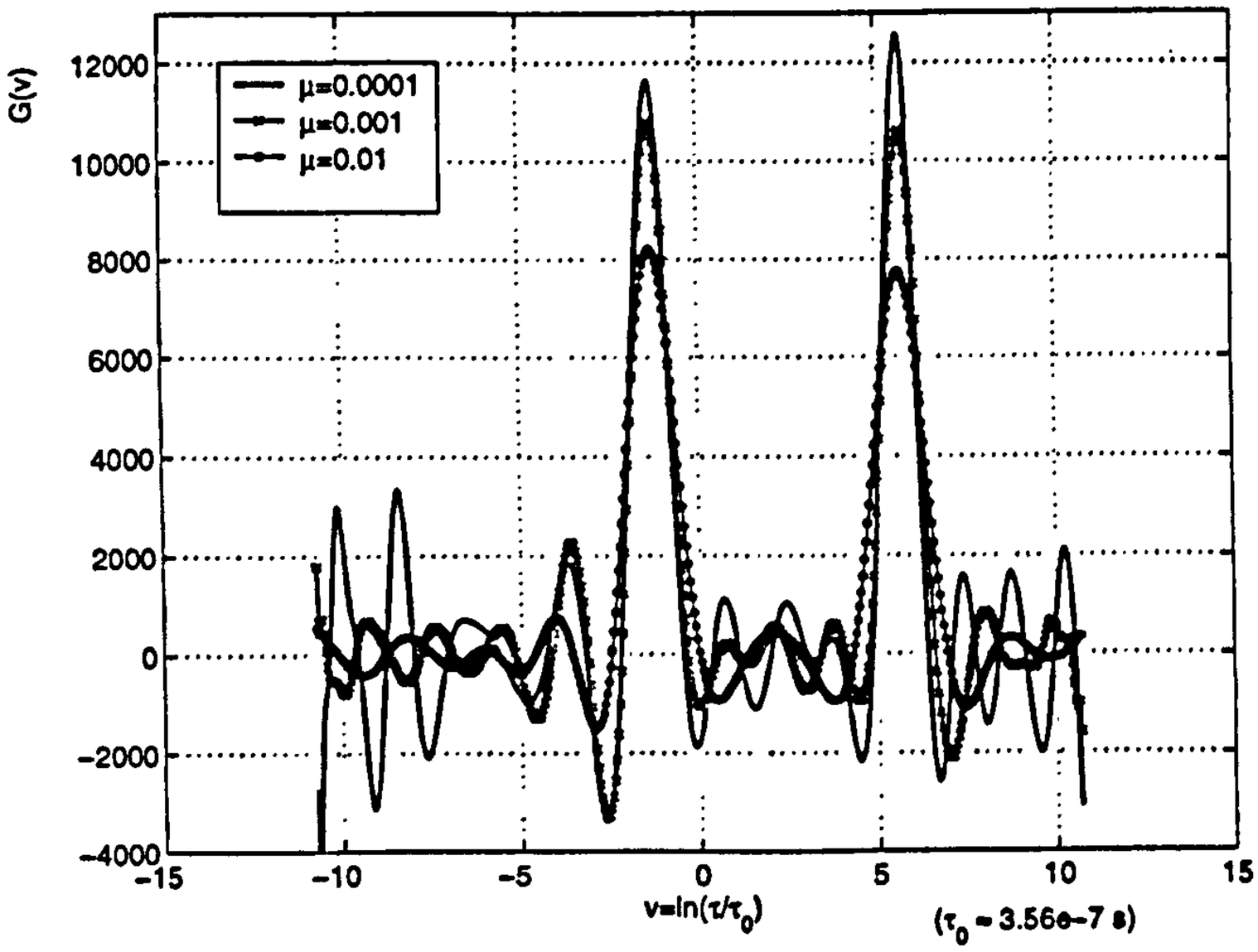

Figure 4.6: *Relaxation spectrum for 40 basis functions and different Tikhonov factor.*

Figure 4.6 shows that the oscillations are of lower amplitude when the Tikhonov factor is large but the final solution is oversmoothed. The relaxation spectrum has a higher resolution for Tikhonov factor equal 0.001. Further decrease of Tikhonov leads to a more oscillatory result especially for a high number of basis functions. The method of choosing the Tikhonov factor was also discussed in the section 4.5.1.

From the above test results the following conclusion can be made: the choice of the number of basis functions is more or less arbitrary and should be done so as not to limit the resolution given the noise. For flexibility, more basis functions than are needed should be used and then the regularisation can be controlled by using the Tikhonov factor.

For the further tests the number of basis functions is set to be 40 and the Tikhonov factor to 0.001.

Two more impedance data sets with added Gaussian noise were simulated. Gaussian noise has been increased and had a standard deviation of 1% and 3% in the amplitude and 2% and 5% in the phase for the first and the second data sets respectively. It has been concluded that, with respect to the data with the random noise, the proposed GRIM is stable. The result becomes closer to the reconstructions obtained using exact data as the level of the noise on the data decreases. For increasing noise level, large Tikhonov factor was required to achieve the subjective best result, *i.e.* narrowest peak for some level of ringing.

4.9 Kramers–Kronig Relationships

In this section the GRIM and Kramers-Kronig (KK) relations are discussed in terms of the frequency–dependent error estimation.

The KK relations, developed in the field of optics, are integral equations which constrain the real and imaginary components of complex quantities (*e.g.* impedance, permittivity and *etc.*) for systems that satisfy conditions of causality, linearity, and stability. The KK transforms can take several mathematical forms. Two integrals below are written for the real and imaginary parts of the impedance $Z(\omega) = R(\omega) + jX(\omega)$:

$$R(\omega_a) = R(\infty) + \frac{2}{\pi}\int_0^\infty \frac{\omega X(\omega) - \omega_a X(\omega_a)}{\omega^2 - \omega_a^2} d\omega \tag{4.54}$$

$$X(\omega_a) = \frac{2\omega_a}{\pi}\int_0^\infty \frac{R(\omega) - R(\omega_a)}{\omega^2 - \omega_a^2} d\omega \tag{4.55}$$

where ω_a is the angular frequency where the imaginary (real) part of the impedance is sought and ω is measured angular frequency.

The frequency response of tissues is casual, stable and, under most conditions, linear. The usual way of using KK equations is to calculate the imaginary component of impedance from the measured real component using Eqn. 4.55 as the real part is less prone to errors. Then the new values X are compared with the values obtained from experiment.

The Kramers–Kronig (KK) relations has been proposed as a means to check the consistency of experimental impedance data or to obtain the imaginary part of the impedance or the permittivity when only the real part is available.

Although the detection of measurement errors is critical to the data analysis, the KK-transforms have not found widespread use in the interpretation of

impedance spectroscopy data due to difficulties with their application. The numerical implementation of KK transformations are complicated by the singular nature of the integrand, the infinite range of integration and problems introduced by noisy, sampled data. The application of KK transforms and their practical limitations were reported in the literature [57].

The use of KK transforms is unnecessary when the new proposed method for calculation of the dielectric time distribution is applied. The transformation to reconstruct the distribution of relaxation times are:

$$\mathbf{K'G_v = S'_u} \quad \textit{and} \quad \mathbf{K''G_v = S''_u} \tag{4.56}$$

where data vectors S′ and S″ are related to the real and imaginary parts of permittivity respectively.

From Eqn. 4.56 it is clear that

$$\mathbf{G_v = (K')^{-1}S'_u} \quad \textit{and} \quad \mathbf{G_v = (K'')^{-1}S''_u} \tag{4.57}$$

where $\mathbf{K^{-1}}$ is the inverse form of matrix K. It follows that:

$$\mathbf{(K')^{-1}S'_u = (K'')^{-1}S''_u} \tag{4.58}$$

$$\mathbf{K''(K')^{-1}S'_u = S''_u} \tag{4.59}$$

So, data vectors S′ and S″ are not independent and related by:

$$KK_1\mathbf{S'} = \mathbf{S''} \tag{4.60}$$

where $KK_1 = \mathbf{K''(K'')^{-1}}$.

The KK transform can written in general form as:

$$KK\varepsilon' = \varepsilon'' \tag{4.61}$$

This equation is equivalent to 4.60 when KK integrals are written in terms of data vector S.

The DRT distribution G can be derived from either S′ or S″. If Eqn. 4.60 is satisfied then the system 4.56 is consistent. If the real and imaginary part of permittivity were measured independently then they will be inconsistent and include different errors. In this case, the system 4.56 can be solved in the least squares sense and then K′G and K″G are the real and imaginary parts of a KK consistent frequency response.

The error estimation is important for the interpretation of relaxation spectrum. Errors can be divided into random and systematic. The stability of GRIM

to the random errors was checked by inverting data with added Gaussian noise and was shown in the previous section. Systematic errors of two different kinds can be expected. The first type of systematic errors is equivalent to impedances in series or parallel (or combination) with the measured one. In this case, the resulting measured value will not be the actual wanted value, but it will have all the properties of an impedance function. The second type of systematic errors yield inconsistent data due to *e.g.* a cross talk between the injection and detection sides.

When Eqn. 4.56 are solved simultaneously, in the minimum error norm sense, the solution DRT distribution has consistent real and imaginary permittivity spectrum which is closest to the inconsistent data. Therefore, the method is relatively insensitive to errors in data vectors S′ and S″ which are not KK consistent.

4.10 MatLab Implementation

A new mathematical method - GRIM - for computation of dielectric relaxation time distributions has been described in previous sections of this chapter. The algorithm has been implemented using programming language MatLab. The flow diagram is shown in Figure 4.7 and the main steps are considered here.

The program has *Input*, *Main body* and *Output*. *Input* includes amplitudes of impedance z, phases of impedance ph_z, frequencies ω, number of basis functions N_B and Tikhonov factor μ. Initial impedance data (z, ph_z) are stored in files. The number of basis functions and a Tikhonov factor can be chosen by means of methods discussed earlier in this chapter.

The *Main body* of the program consists of several subroutines. Firstly, the impedance data are inverted to yield the conductance (σ, ph_σ) and then to a network function $Q(\omega)$ and S–function, Eqn. 4.5. This procedure will be shown in detail in section 6.2, Eqn. 6.1 - 6.8. The first subroutine returns real and imaginary parts (S_{Re}, S_{Im}). At the next step the second subprogram is called. In the flow diagram it is surrounded with dash line. This subprogram solves the existing inverse problem. Inside the subprogram some small subroutines are called to compute Gauss abscissas and weights (w_j, X_j) for Gaussian quadrature formula Eqn. 4.17, K-matrices and data vectors S. As soon as w_j and X_j are known the Legendre polynomials $P_n(\frac{X_j}{\xi})$ are found at the Gauss points over the integration range $[-\xi, \xi]$ where $\xi = \ln(\frac{\omega_{max}}{\sqrt{\omega_{min}\omega_{max}}})$. The Legendre polynomials are orthonormalised and basis functions B_N are computed in accordance with Eqn. 4.22. The initial functions of integral equations, (S_{Re}, S_{Im}), are discretised by approximating them

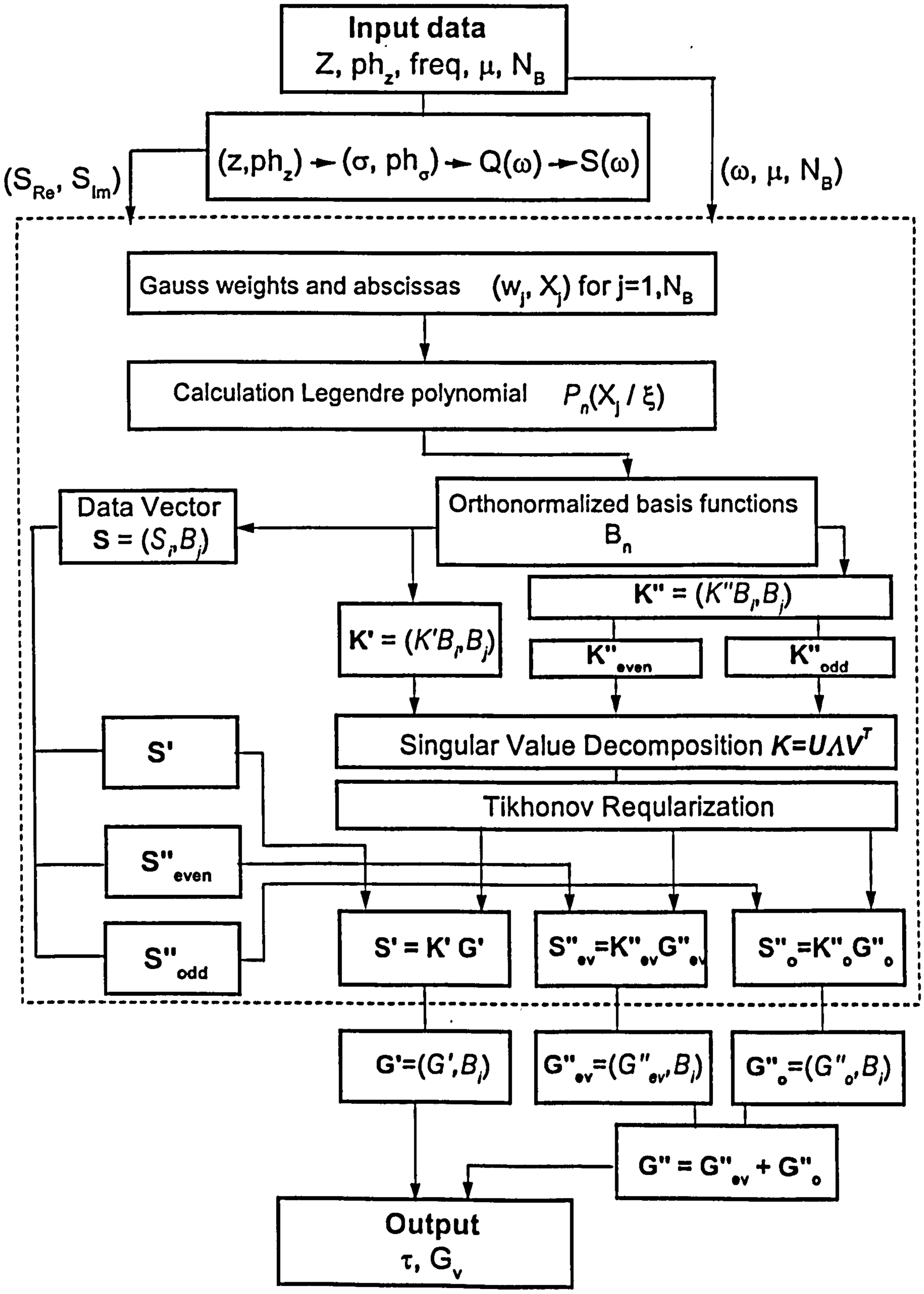

Figure 4.7: *Flow diagram for MatLab program.*

in the finite basis B_N. The vector for the imaginary part $\mathbf{S''}$ is separated into two parts as $\mathbf{S''_{even}}$ and $\mathbf{S''_{odd}}$. Matrices $\mathbf{K'}$ and $\mathbf{K''}$ approximate integral operators of inverse problem and they are real and symmetric. The basis B_N can be reordered into even and odd functions, Eqn. 4.23. The eigenvalue problem is separated into two independent eigenvalue problems $\mathbf{K''_{even}}$ and $\mathbf{K''_{odd}}$. The inverse problem is solved by using the SVD and the Tikhonov regularisation. Three vectors G'_v, G''_{even} and G''_{odd} can be calculated from equation 4.50. Smooth approximations to $G(v)$ may be calculated as linear combinations of basis functions, Eqn. 4.13.

If the frequency range is known then matrices $\mathbf{K'}$ and $\mathbf{K''}$, the SVD of $\mathbf{K^T K}$ and the basis functions can all be pre–calculated. In this case, calculation of $\mathbf{G}$ using Eqn. 4.50 requires $\leq 2N_B^2$ flops which can be performed in milliseconds.

At the *Output* of the program a plot of dielectric relaxation time distributions can be displayed and relaxation times as well as their dispersion amplitudes are calculated.

4.11 Summary

In this chapter the Galerkin Regularised Inverse method has been developed. The method solves an ill–posed, linear, inverse problem. The ill–posedness has been stabilised by applying the standard Tikhonov regularisation which is achieved by filtered SVD. The error analysis is performed and the optimal Tikhonov regularisation parameter as well as the number of basis functions are found for typical levels of random noise. The proposed GRIM has advantages over the methods presented in chapters 2 and 3. It provides information about as many of independent parameters as the data can justify. The method does not rely upon an arbitrary and non–unique equivalent circuit model. Furthermore, the method is adaptable to the noise spectrum of the particular data set and to the users particular interests. The GRIM also checks data for the consistency. The DRT distribution establishes the direct link between raw frequency response of biological sample and the properties of cells. Possible applications of GRIM are considered in the chapter 6.

Chapter 5

Instrumentation

5.1 Introduction

This chapter examines some of the important aspects of the technology used in measuring electrical impedance with the purpose of characterising tissues by their impedance spectra. These aspects include, in particular, the instrumentation and the influence of the electrode/tissue interface impedance. As discussed earlier, a wide frequency range is important for obtaining information about the whole dielectric relaxation time spectrum and hence designing a measuring system able to perform measurements from a few hertz up to megahertz is critical. The chapter gives an overview of available commercial devices and also describes some work carried out on EIS hardware in Oxford Brookes University. Different types of electrodes and a noninvasive impedance probe are presented in the section 5.5. In addition, some potential applications of EIS and biological limitations are described.

5.2 Multi–frequency EIT and EIS: existing and new systems

EIS as implemented in the current research is a noninvasive technique that consists of measuring the voltage induced by passing a current through a sample over wide frequency range. For current densities lower than some mA/cm^2, the dielectric properties of biological tissues can be considered to be linear and to be characterised by a complex electrical impedance, Z, which obeys Ohm's law.

Considerable effort in Electrical Impedance Tomography (EIT) has been directed toward the development of equipment for the accurate measurements of the electrical properties of biological tissue.

Electrical Impedance Tomography is a technique that produces images of the impedance distribution in a slice through a body by means of noninvasive electrical measurements and a reconstruction algorithm. Since different tissues have different impedances, it is possible to generate impedance images and to detect the time course of physiological events. Typically, measurements for EIT are performed by injecting a current by means of a current source and measuring voltages. Such systems are known as *current* driven. However, the opposite scheme of using voltage drives and current measurements (*voltage* driven strategy) can also be adopted. Much of the debate over the benefits of current driven or voltage driven systems come down to semantics. Often the desired currents are driven by applying the appropriate voltages. The data for EIT and EIS systems are simultaneous current and voltage measurements irrespective of which were applied and which were measured.

The work on EIT in Oxford Brookes University has been briefly described in section 1.5. Here it is considered in terms of hardware design. The first EIT system was designed and developed in 1987. The system adopted a current driven approach and operated at a single frequency of 60 kHz. Demodulation was performed with an analogue phase–sensitive detector. The next contribution was made by Q.S.Zhu [20] who developed the second system: OXBACT2. The OXBACT2 system used voltage drivers as opposed to the more widespread use of current sources. This approach was adopted in order to overcome problems associated with designing an accurate and stable current generator with a high output impedance at high frequencies. The system established the desired current distributed on the boundary of the region by using the measured trans–impedance matrix. This matrix performs the transformation between applied voltage and applied current and may be used to determine the correct voltages to be applied to the electrodes to obtain the desired output current field. The operating frequency was 9.6 kHz. A digital signal generator and digital demodulation were implemented allowing a non–uniform sampling scheme to eliminate synchronised random noise. A commercial ADC card PC26A (Amplicon, UK) was used for data acquisition and controlled by a host computer. The data acquisition speed was 80 kHz. The system was used *in vitro* experiments only since it had no electrical isolation which is required by standard patient safety regulations. Further system development was directed to towards developing circuits for using a current driven strategy and thereby preventing the problem of changing load impedances from altering current patterns appearing when the voltage driven front is used. Thus, the new system called OXBACT3 was designed for experiments *in vivo*. The system includes an important innovation - it operates at three frequencies:

10 kHz, 40 kHz, 160 kHz. The system has a 10 MHz sampling rate, uses digital demodulation and is able to measure the real and imaginary components of voltage and current to enable complex impedance values to be determined. The system is able to apply currents and measure voltages sufficiently fast for imaging at 25 frames per second. Measuring at three frequencies provides enough information to determine Cole parameters (angle of depression, coordinates of centre, radius and characteristic frequency where the imaginary part of impedance reaches its maximum). Therefore the measuring system OXBACT3 allows multi-frequency EIT to be performed. One more EIT system was built before the EIS system presented in section 5.3 was designed. OXBACT4 was designed to produce 3D images using 192 current sources and 816 voltage measurement points. It has an operating frequency of 5.6 kHz. Demodulation is performed digitally using a 12-bit PC mounted ADC card (Amplicon PC226).

An experimental two channel multi-frequency EIS system was developed from the OXBACT 3 signal generator. It operated at four frequencies - 10 kHz, 40 kHz, 160 kHz and 640 kHz and employed digital demodulation by means of the PC226 data acquisition card with a sampling speed of 750 kHz. Initially it was thought that the work on this two channel multi-frequency system could include the option of extending the system to include a current measurement. However, it soon became apparent, that the problems introduced by a limited measurement frequency range was critical for spectroscopic purposes and that an independent EIS system was required. It was decided to build an EIS system as a further development of the two channel system with the inclusion of current measurements and expanded frequency range.

Multi-frequency EIT reconstructs images in which tissues can be discriminated by their frequency response. By carefully choosing the measuring frequencies it should be possible to optimise the contrast according to the type of tissue to be visualised. This approach has opened up particularly interesting perspectives for impedance imaging: noninvasive tissue characterisation or EIT spectroscopy. The disadvantages of using Cole parameters for tissue characterisation were discussed in previous chapters. The Cole parameters do not directly establish the link between the frequency response of biological tissues and their non-electrical microscopic characteristics.

A new mathematical method - **GRIM** - has been developed and described in detail in Chapter 4. The algorithm reconstructs a distribution of dielectric relaxation times from impedance measurements. There are three dispersions - α,

β and γ - in biological tissue that take place at different points in the frequency range. Each dispersion is a result of the particular processes happening at the cell level inside tissue. Section 2.2 examined these processes. If a relaxation spectrum is reconstructed over a wide frequency range it may provide some information about, for instance, extracellular and intracellular volumes and cell membranes. So, it is important to be able to collect impedance data in the frequency range from a few hertz (α–dispersion) up to megahertz (β–dispersion). If internal parts of cells are the subject of interest then a measurement system has to be able to work in GHz range. Osypka and Gersing published some results concerning the maximum and minimum limits needed for EIT to include pathological tissue: 1 kHz - 3 MHz, [58]. Usually the widest frequencies of interest for EIS are: 100 Hz - 10 MHz, which include α- and β–dispersions, [28].

Due to the reasons stated above, the existing two channel multi–frequency system is unable to provide the data required by EIS. In the beginning of this PhD project it was decided to design a new system. Section 5.3 describes some of the options available for the design of an EIS data acquisition system and their relative merits.

5.3 Safety

For medical applications and studies *in vivo*, an EIS system has to meet safety requirements. Safety is the most important consideration in medical electronics. When electrodes are applied to the human body, the application of unsafe currents are of greatest concern. Such currents may be due to the current leakage derived from the mains power supply or may be due to the applied current signal.

The IEC (International Electromechanical Committee) 601–1 standard restricts the current applied to a patient to only 10 μA rms for frequencies below 0.1 Hz. This limits the harm caused by the electrolytic action of near DC currents. The allowable currents increase to 100 μA rms at 1 kHz, 1 mA rms at 10 kHz and 10 mA rms at 100 kHz due to the reduction in biological sensitivity to higher frequencies. There is a clear advantage in using relatively high frequencies.

Another safety feature required in the standard is isolation from the mains power supply. The 50 Hz mains supply is of relatively low frequency and hence is relatively dangerous in comparison with the signals applied in EIS.

Three types of leakage currents can be defined:

- Lead–to–ground leakage;
- AC isolation or risk current (when the patient touches mains supply);
- Leakage between leads.

In order to avoid any leakage current, all medical electrical equipment must be tested under all possible combinations of operating conditions and under any single fault condition, *e.g.* with the instruments on and off, with the ground wire broken, *etc.*

For the case of the lead–to–ground leakage and the AC isolation (risk) current, the safety may be provided by isolating the equipment power supply from the mains supply by means of a transformer. Standard transformers do not necessarily provide sufficient DC isolation because of the conduction path through the winding isolation and the magnetic core which may allow greater than the maximum 100 μA. Isolation transformers may be required to provide a sufficient protection. Alternatively, isolation may be provided by running the data acquisition system from a battery–based power supply. This provides excellent isolation but has the inconvenience of adding weight and size to the system or of limiting the operational period. Some more options for system isolation will be considered in next sections.

5.4 System design

A two channel data acquisition system, based on the design of EIT systems, was available at the beginning of this project. The existing system worked at four frequencies: 10 kHz, 40 kHz, 160 kHz and 640 kHz and had two voltage measurement channels. The block diagram is shown in Figure 5.1.

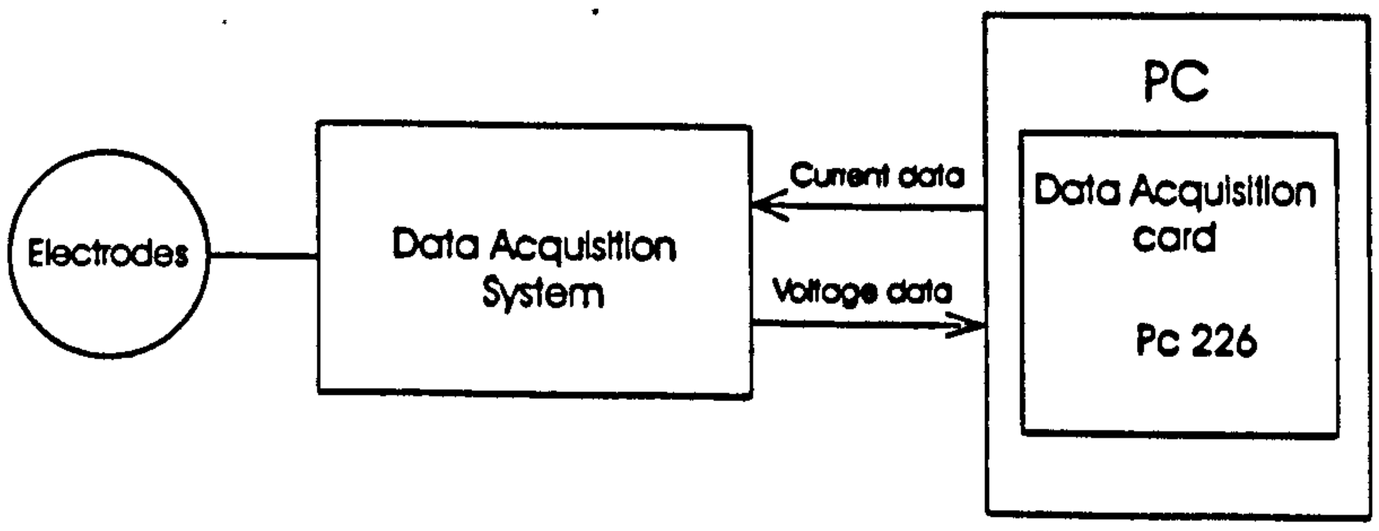

Figure 5.1: *Block diagram for dual channel system.*

Since a wide frequency range is important for EIS measurements, it was decided to build a new EIS system which would allow *in vivo* measurements and

would include a number of further features not included in the two channel experimental EIS system. These are described in the next section.

5.4.1 Hardware requirements

It was decided that the system would operate at more than four frequencies. The permitted current level determined the lowest frequency and the waveform accuracy determined the highest frequency. The frequency range would be from 2.5 kHz to 2.5 MHz.

A new EIS system would be based on a current driven approach used in OXBACT3. The specification for a high quality output current with an accuracy of ±0.012% (12 bit) was set with an acceptable minimum of at least ±0.05% (10 bit).

The current source of a current driven system must have a very high output impedance preventing changing load current if the load impedances changes. To achieve the specified accuracy over a load range of 100 Ω to 3 kΩ, the current generator must have an output impedance of greater than 12 MΩ or at least 3 MΩ as the minimum.

It was decided that the system should be able to measure the amplitude and phase of voltages to enable complex impedance values to be determined. The phase error should be less than 1.27 degrees. Also the system should include a known resistor and a voltage should be measured across it enabling the actual applied current to be measured. The input voltage to the current source should be a bipolar signal with an amplitude ±1 V. The output current should be also a bipolar signal with an amplitude of 1 mA. The system should include the necessary isolation and other safety features for use *in vivo*.

The new EIS system has two main elements: a custom data acquisition board and a commercial data acquisition card (PC 226).

5.4.2 Data Acquisition Card PC 226

The PC 226 is a high performance, fast and accurate data acquisition card with software programmable gain for each individual channel, data FIFO ("First In First Out") and computer bus interface (ISA) for use in a desk top PC. It provides 16 channels of analogue input with 12-bit analogue to digital (A/D) conversion and 24 lines of digital input/output. These digital lines provide a means for trans-

ferring digital data or control signals from the host PC to any system connected to this interface. The required analogue channel can be selected by an address obtained from the FIFO channel list. The programmable gain, instrumentation amplifier provides voltage gain in programmable steps. The gain is automatically selected for each channel by the gain code stored in the channel list. The PC 226 is triggered externally. The single channel mode operation is chosen, initiated by a synchronising trigger from the signal generator. It stops when the preset number of samples (1368) has been completed. In single channel mode a high speed data acquisition up to 750 kHz takes place. A non–uniform sampling scheme has been implemented, [20].

5.4.3 Data Acquisition Board

The data acquisition board generates the sinusoid current from the 12 MHz clock of the data acquisition card. This current is applied to the tissue through electrodes. The four electrode system used for measurements *in vivo* has two current driving and two voltage measuring electrodes. The impedance probe is described in detail in section 5.5. Voltages on the current electrodes are measured in addition to those on the voltage electrodes. The voltages are buffered and multiplexed before being transferred to and sampled by the PC 226. The data are processed by software and displayed. The original software was written in Turbo Pascal. The new data acquisition system was run by software written in Delphi and discussed later. The data acquisition board can be divided into a digital and an analogue part.

Digital Section

The digital part provides two important functions within the system, these being the trigger signal for PC 226 and the generation of the reference cosine signal. The circuit diagram is given in Figure 5.2.

The cosine reference signal is generated digitally by means of a fast DAC (DAC1, Analog Devices AD668) driven by the output of the ROM. The ROM consists of two 8–bit devices (27H010). They operate in parallel to provide a 12–bit output and contain the instantaneous values corresponding to one or more cycles of the cosine reference signal. By applying a sequential series of addresses to the ROM, the appropriate cosine values are generated on the data lines of the ROM. The output of the ROM is latched into two 74HCT273s on the positive edge of the clock. Then the data is passed to DAC1. The binary counter formed from four 74HCT163 4–bit counters generates addresses to the ROM at the rate of 12 MHz. The logic NAND gate (74HCT30) resets the counter after 4864 clocks

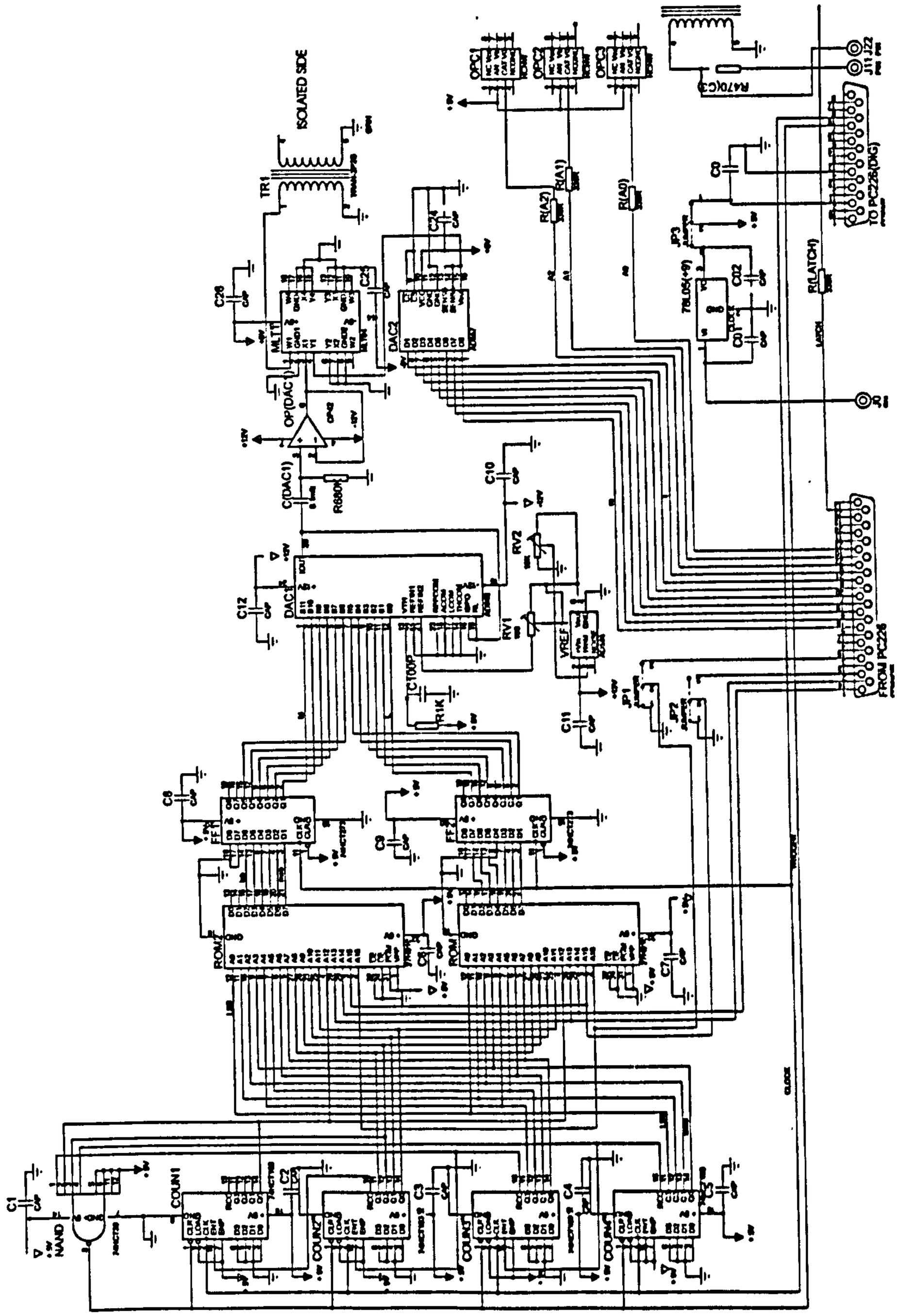

Figure 5.2: *Digital part of the data acquisition board.*

and generates the trigger signal which is used to start the sampling of the PC 226.

The codes corresponding to different frequencies are stored in different areas of the ROM. It was decided to increase the number of frequencies from 4 up to 11. The new signal generator board can generate frequencies from 2.5 kHz up to 2.5 MHz in geometrical progression with a common ratio of 2. 11 different frequencies have been obtained by adding four new signal lines from PC 226 (A13, A14, A15, A16). They select one of sixteen different areas within the ROM. Each carries the binary values for one frequency. The ROM contains a different number of cycles depending on frequency. For example, the 12 MHz clock allows up to 19 independent samples over 4 cycles. In each case the data set is stored in 4864 locations with a single 12–bit value stored in each location.

The cosine wave corresponding to the 12–bit binary value (B1–B12) is generated by the DAC. The output from DAC is a bipolar signal with a peak amplitude of 1 V. The magnitude of the cosine value can be attenuated or amplified by means of the multiplier MLT1 (MLT04)(four-quadrant, with the bandwidth of 8 MHz) in conjunction with DAC2 (AD557)(8 bit voltage output, bipolar). To ensure the required isolation a transformer (TR1) is used.

Analogue Section

The analogue part provides the electrode current drive signal required by EIS. After the transformer the cosine wave voltage is converted to a load independent current by the voltage–controlled current source (VCCS). Two types of VCCS are available on the board: a)transistor arrays plus operational amplifier [59] and b) operational transconductance amplifier; either can be chosen by switching of the jumper JP4. Both VCCSs are discussed in the subsequent section. Figure 5.3 shows the analog part of the data acquisition board for the new EIS system.

The output of a current generator is connected to the core of the coaxial cable which links the current generator to the current electrodes of the impedance probe. To prevent DC leakage passing through the current electrodes, a DC blocking capacitor is included in series with the current source output. The current which is applied to the tissue is measured as the voltage across a known series resistor. The voltage on the reference electrode is also measured, see section 5.5. High bandwidth amplifiers AD8004 and AD8002 are used for current cable screen and to screen the signal lines from the voltage electrodes. The amplifiers are connected as unity–gain buffers. The signals from these amplifiers go to five channels of the high–speed video multiplexer MAX440 (8 channels). Note that all the electrode screens are actively driven with a buffered version of the signal in the core.

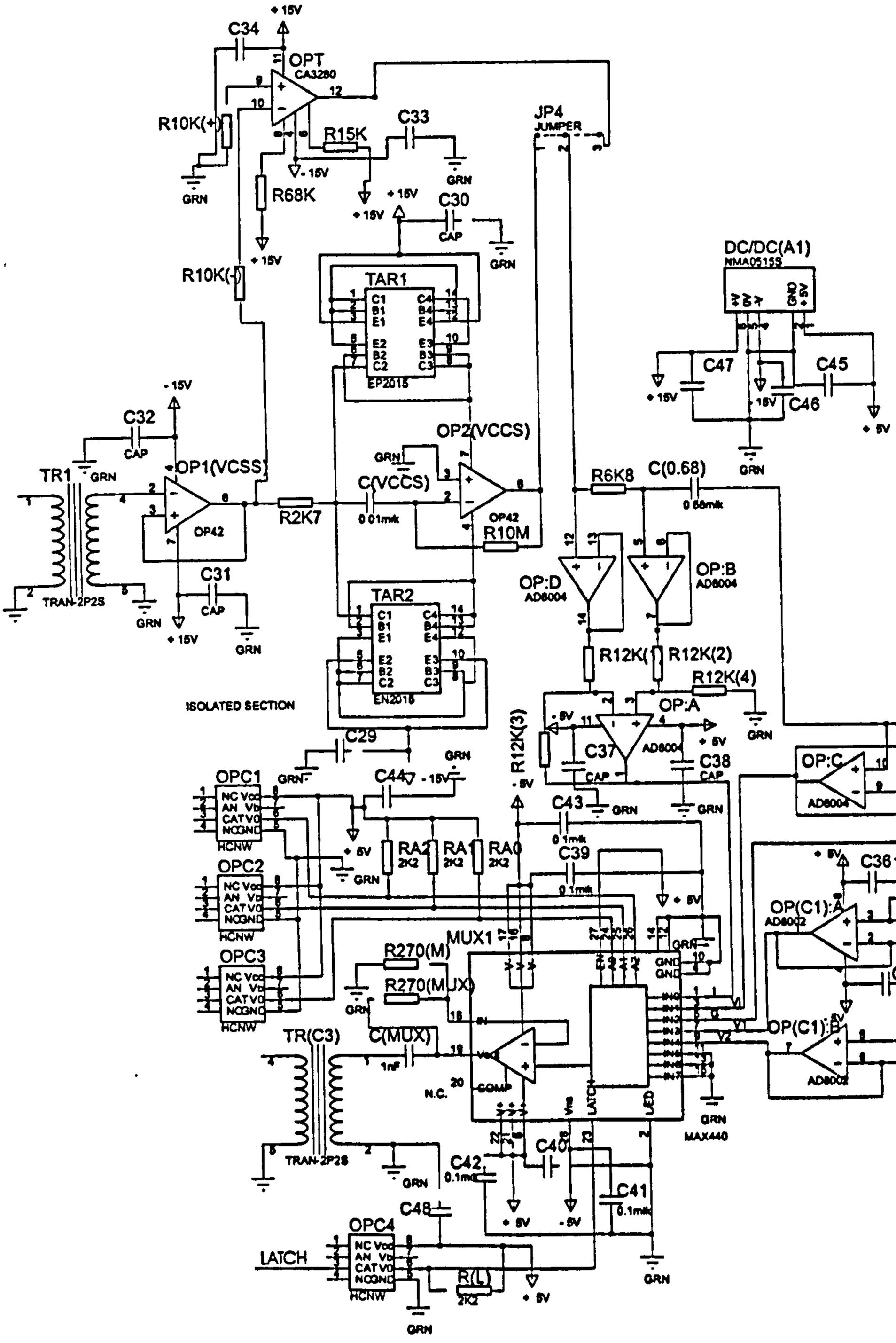

Figure 5.3: *Analog part of the data acquisition board.*

The multiplexer architecture ensures that no two input channels are ever connected together. The channel selection is performed by applying a binary code from PC 226 to the address inputs (A0, A1, A2). The input EN is driven high and the address latch is provided. When the LEVEL/EDGE is low, this indicates that the latch operates in the edge–triggered mode. The addresses are transferred from PC 226 through single channel high speed optocouplers (Hewlett Packard HCNW136). These diode–transistor optocouplers use an insulating layer between an LED and an integrated photodetector to provide electrical insulation between input and output and guarantee the required isolation. The multiplexer output signal passes through the transformer TR(C3) to maintain isolation.

Two power supplies are available with the data acquisition board: the 5 V power supply directly from the PC and the external 9 V power supply which gives 5 V after the voltage regulator 78L05. To comply with the safety regulations, the DC/DC(A1) converter is used to provide power to the analogue part.

5.4.4 Voltage–Controlled Current Source

The ideal solution for a current–driven system is a current source with an infinite output impedance. In practice, it must be sufficiently high so that the load current will not change significantly if the load impedance changes by the maximum expected extent. Building a current source with high output impedance is extremely difficult especially for a wide frequency range since the output impedance is frequency dependent. In this section several possible solutions are proposed.

The first VCCS uses current mirrors and an operational amplifier (op–amp) that was adopted from the existing dual channel EIS system and originally designed for EIT by Denyer [60]. The circuit diagram is shown in Figure 5.4.

A current mirror is a current–controlled current source (CCCS) with a high output impedance and a current gain which is close to unity. Because the current mirror is a unipolar device two mirrors are needed to provide a bipolar current. An operational amplifier has a very high input impedance. The design provides that the output current is almost equal to the input current and equal to the difference between the supply currents. Because the aim was to build an EIS system for medical applications, the system is required to be isolated (the power supply and input voltage are isolated, see section 5.4.3) and no DC current must be applied. Small mismatches between the input and the output op-amp currents creates an error voltage and the output current changes to restore the match. The output DC voltage is fed back to the inverting input of the op–amp for stable operation. A high value resistor - 10 MΩ - from the output to the input is used to maintain

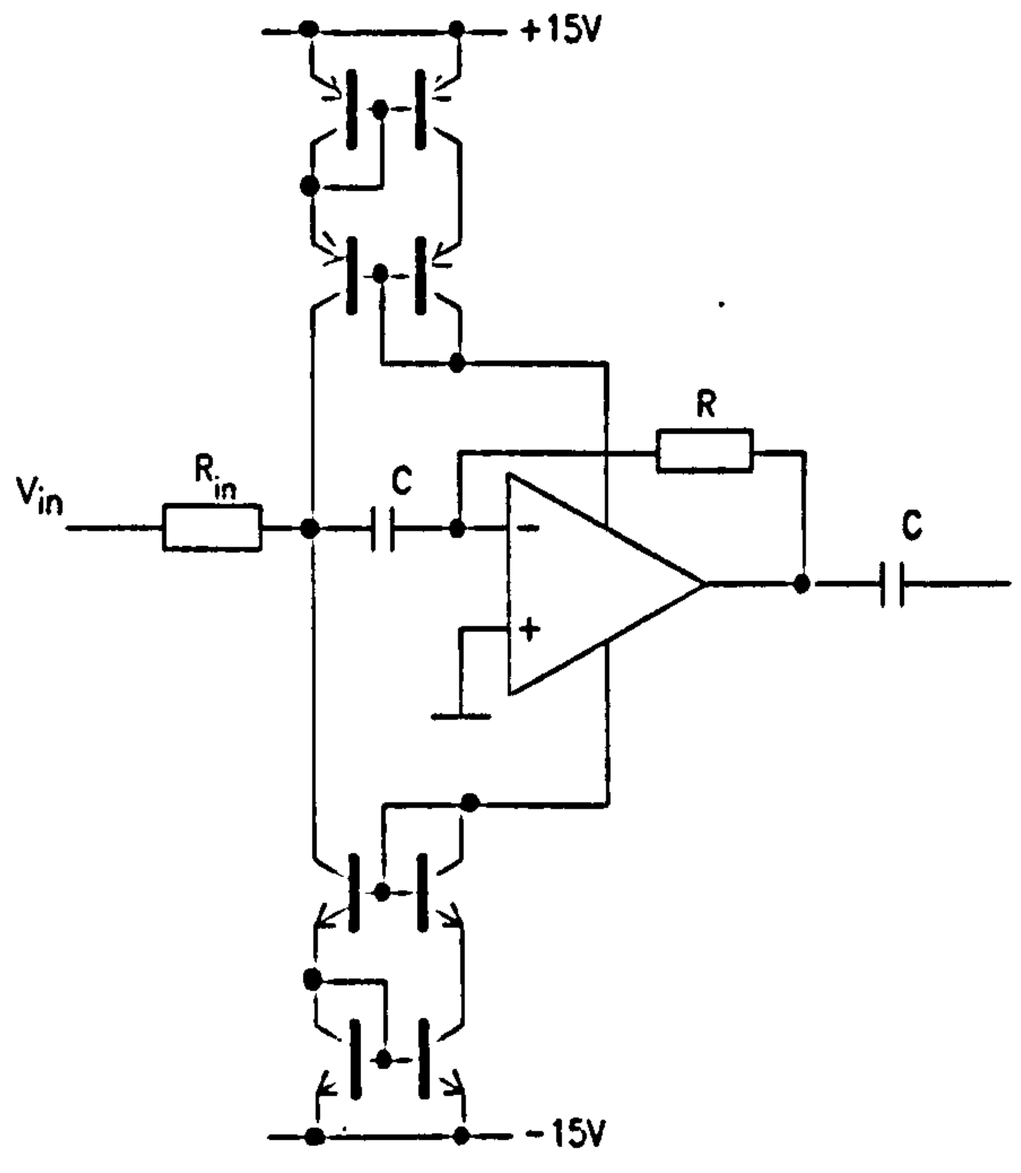

Figure 5.4: *Current mirror source ($R_{in} = 1k\Omega$, $R = 10M\Omega$, $C = 0.1\mu F$).*

very high output impedance. The signal is passed to the same input via a 0.1 μF.

The first op-amp chosen was Analog Devices OP–42 and current mirrors are two transistor array devices Elantec EP2015 and EN2016. The same components were suggested for OXBACT3. The output impedance test diagram of this circuit is presented in Figure 5.5.

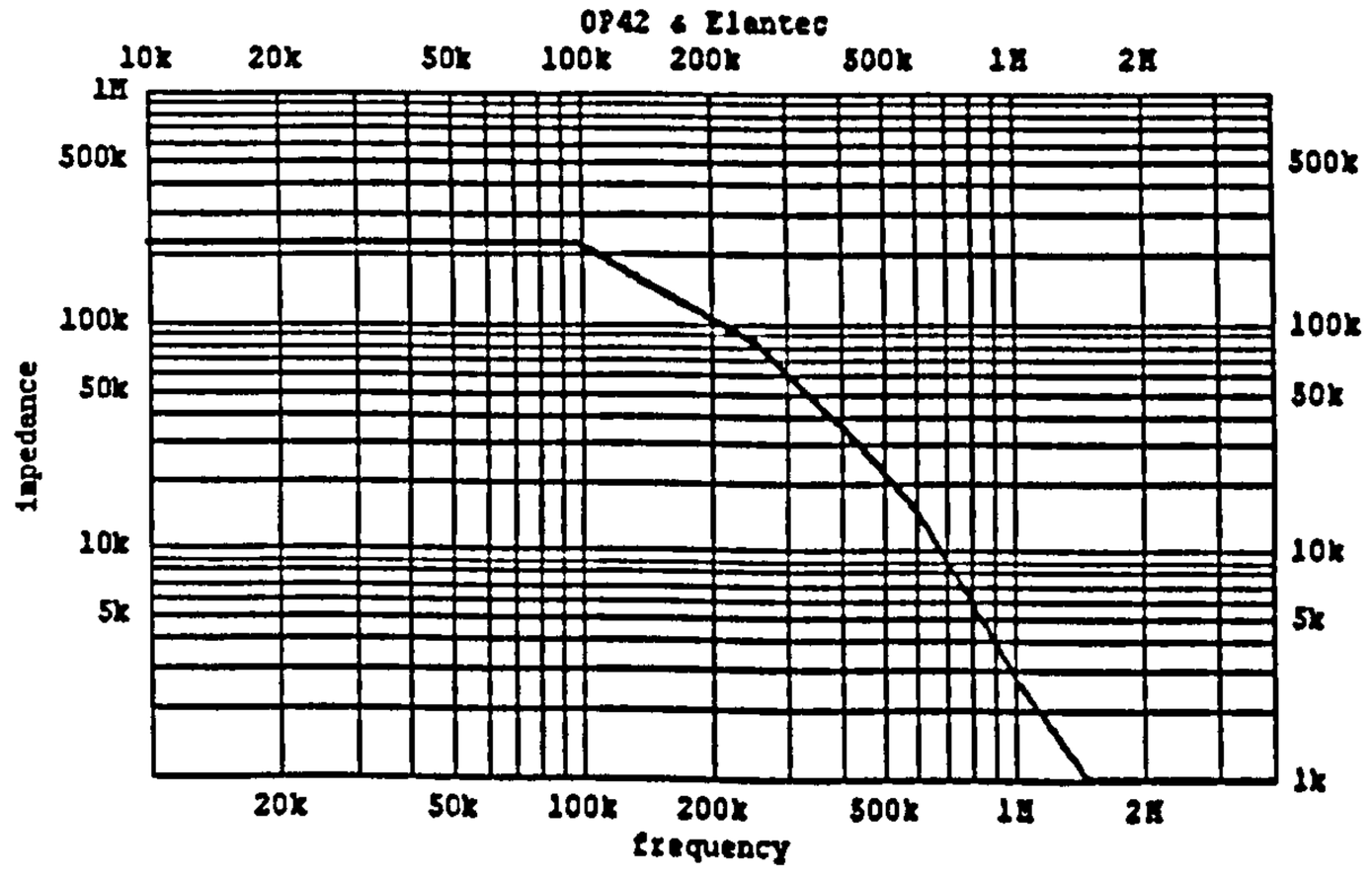

Figure 5.5: *Output impedance for the current source: OP–42 and Elantec transistor arrays.*

The maximum output impedance is 230 kΩ. It decreases very quickly above 100 kHz. The maximum frequency that was targeted is 2.5 MHz. Therefore, the

chosen components are not suitable for a wideband current source.

To improve the existing current source design other possible solutions have been checked. It was decided to test other available components for the replacement in the current source. The gain responses of three op–amps - Elantec EL 2045, Analog Devices OP–42, Analog Devices AD 844 - have been compared as well as the gain responses of two transistor arrays from Elantec and Motorola. The results are shown in Figures 5.6 and 5.7.

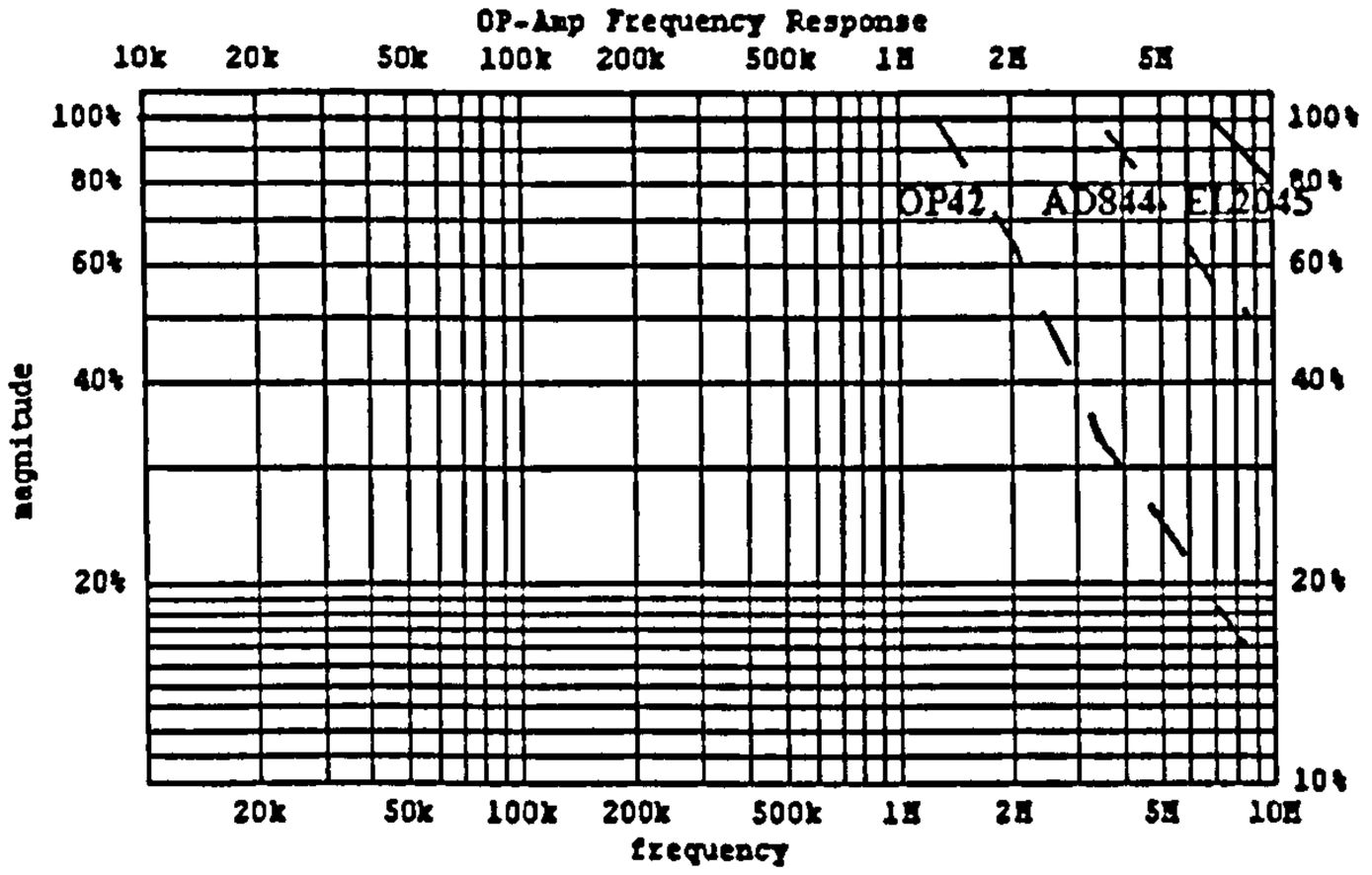

Figure 5.6: *Gain responses of three op–amps.*

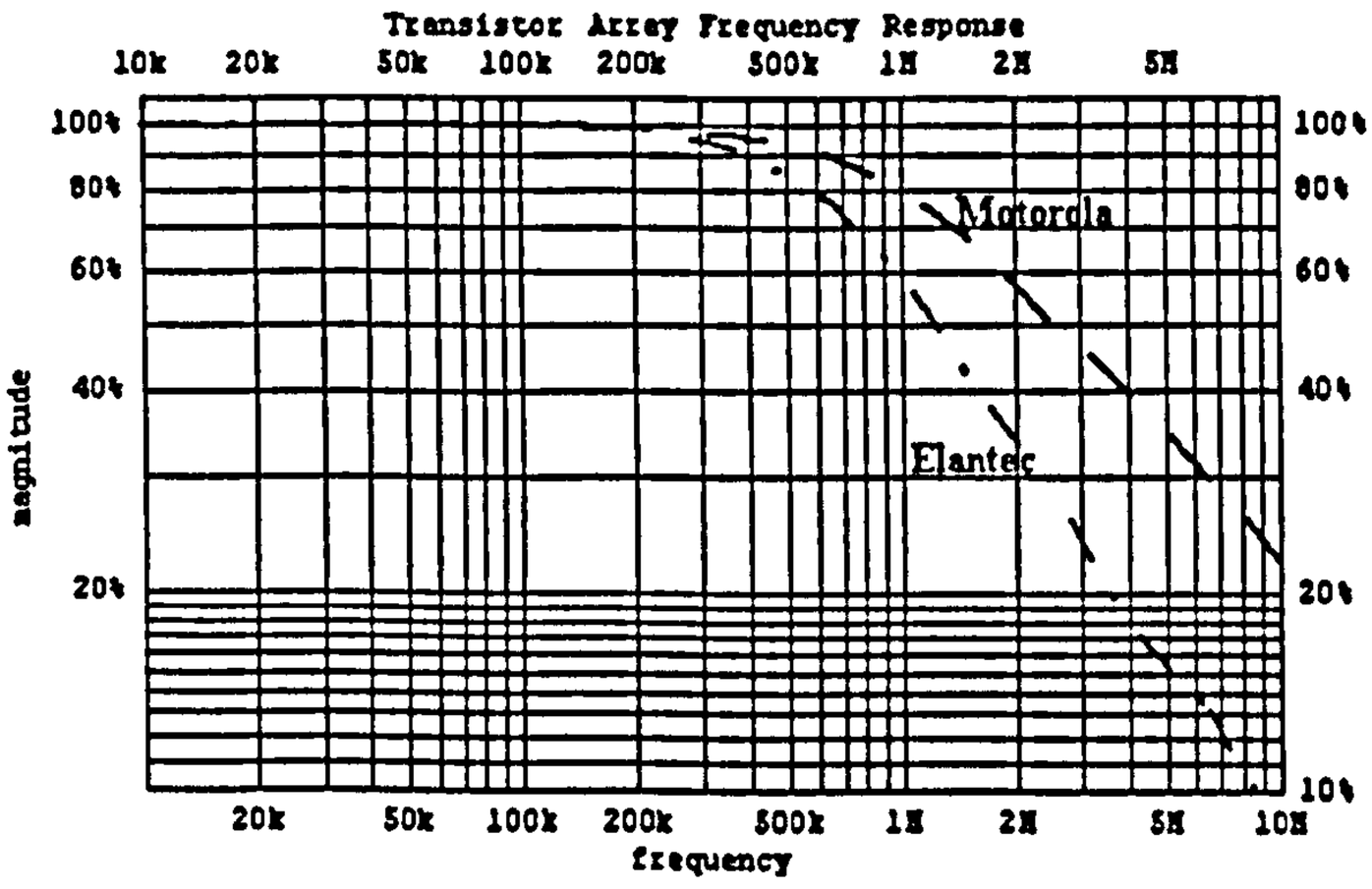

Figure 5.7: *Gain responses of transistor arrays.*

The implemented current source design, known as the Wilson design, must have a high open loop gain, a low bias current (pA), a high full power bandwidth and a high input impedance. None of the three tested op-amps show these features. The OP 42 has the highest input impedance and the highest open loop

gain but it can be used only up to 1 MHz.

Neither transistor array shows the required characteristics; on their own, their ($-3dB$) frequencies are 750 kHz (Elantec) and 1.5 MHz (Motorola).

The second type of VCCS available on the data acquisition board is an operational transconductance amplifier (OTA) CA 3280. The OTA has all the generic characteristics of an operational voltage amplifier except that it has a well–specified transconductance gain rather than voltage gain and the output signal is a current. The transconductance can be varied by adjusting an external DC bias current. The magnitude of the output current is equal to the product of the transconductance and the input voltage. The ideal OTA has infinite input and infinite output impedances. The advantages of this particular OTA are:

- wide frequency range
- internal resistor network, no feedback network needed
- current output
- high output impedance
- low cost
- single chip solution

In practice an OTA has several limitations. Figure 5.8 shows the frequency characteristic of the output impedance of CA 3280.

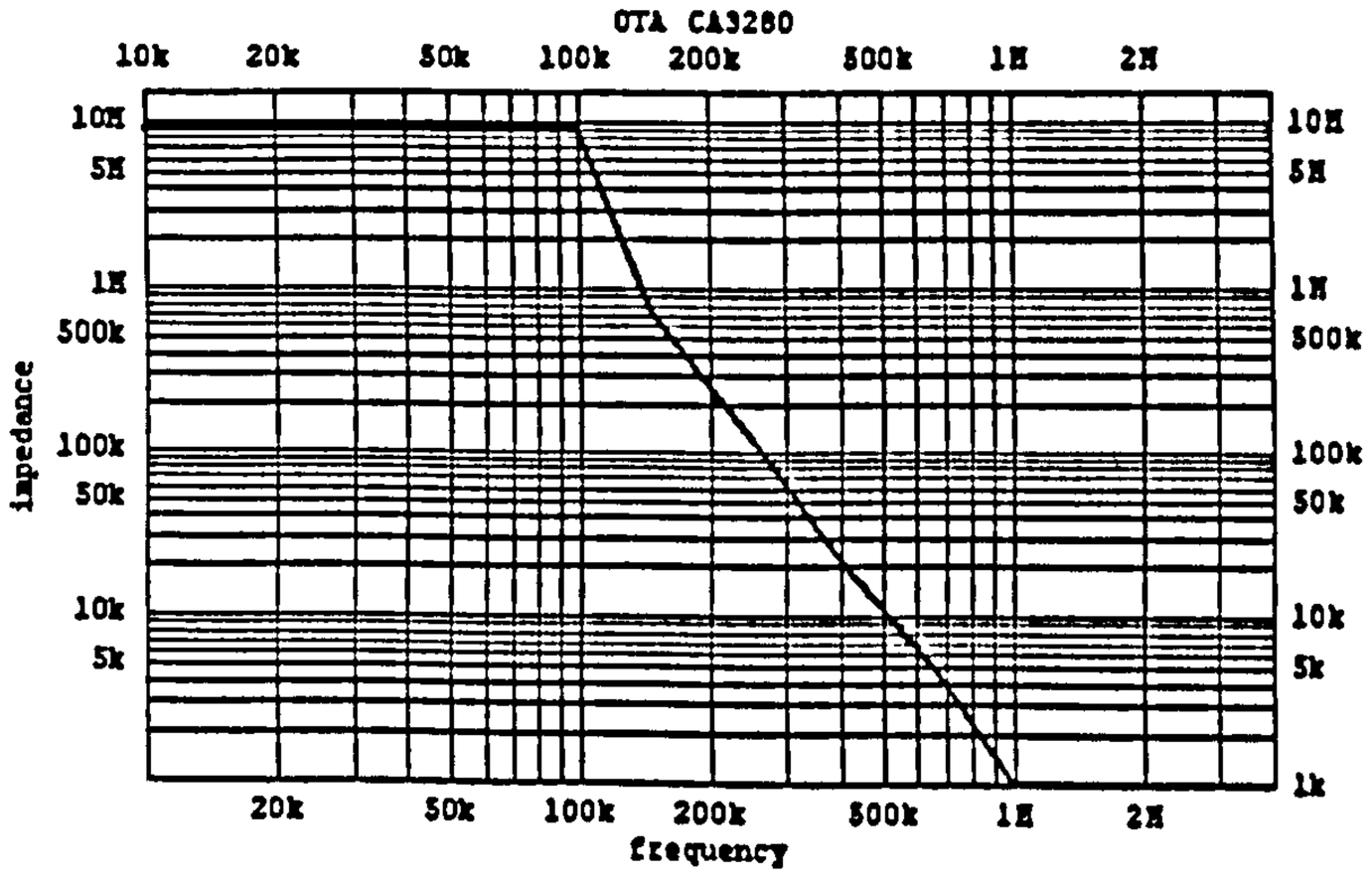

Figure 5.8: *The frequency response of OTA.*

The frequency range of the OTA is limited by the presence of some parasitic elements in the input and output. It leads to the output impedance decreasing

at high frequencies. Also, the transconductance is non–linearly dependent on the bias current and changes with the temperature and other parameters.

However, the output impedance is better than any of the previous circuits. The 10 MΩ output impedance is reached for frequencies up to 100 kHz. For frequencies more than 1 MHz the OTA operates as a voltage source. Nevertheless, this circuit has a better performance than the Wilson circuit. The output impedance at 160 kHz is greater than 300 kΩ. According to the specification in section 5.4.1 the maximum expected load impedance change is assumed to be 3 kΩ - 100 Ω = 2.9 kΩ. These are extremes of electrode impedance and a more realistic figure is the change of impedance during a set of impedance measurements, *i.e.* such that a current measurement at the beginning will still be valid during the corresponding voltage measurements. To maintain 12–bit accuracy, the load current must change by less than ±0.012%. However, since current measurements are also performed by the designed system the output impedance of 290 kΩ is adequate. Also it allows the frequency range to be extended and to increase the number of sampling frequencies. Hence, the new EIS system can accurately measure from 2.5 kHz up to 160 kHz at 7 doubling frequencies and with a care up to 2.5 MHz, and so it was decided to build the OTA into the board.

5.4.5 Operational sequence and Delphi programming

The system is operated by commands from a PC to the data acquisition card PC226 and then to the data acquisition board. The front panel interface is written in the programming language Delphi which gives interactive control of the system. Appendix A provides pictures for the front panel and sub–events from the menu.

The first stage after power up is the setting of the ADC card (address, mode, external trigger, *etc.* and the gain of the programmable gain amplifier (PGA) as well as sending data to DAC2 which sets up the multiplier to amplify or attenuate the signal.

Subsequently, the calibration procedure should be undertaken to determine the applied current for performed measurement. The calibration resistance should be chosen. Then, the appropriate commands are sent to generate the 11 frequencies and to make calibration current and voltage measurements at each frequency.

As soon as the calibration procedure is completed the ADC card is set to take

measurements on current electrodes. Voltage measurements are made and current values at each frequency are calculated and displayed. The graphical panels for this stage are shown in Appendix A.

Data acquisition to collect multi-frequency data may then be undertaken. At each frequency, voltage values and phases are obtained at each channel by sending a set of commands to the multiplexer via the optocouplers. The amplitude of the voltages and their phases are calculated and also displayed.

Finally, the impedance is found as a function of frequency. The impedance and current values as well as all setup data are presented at the front panel. Also displayed are voltage charts for observing the voltages at current and voltage electrodes at each frequency. The disadvantage of the system is that the time to take multi-frequency measurements is too long to allow more than one data point (impedance measurement) within one cardiac cycle.

5.4.6 Advantages and Disadvantages of a self-developed EIS system

A new multi-frequency, printed circuit board (PCB) based EIS system has been designed. The new design has a range of merits that can make the system valuable for the EIS:

1. Measurements at 11 different frequencies from 2.5 kHz up to 2.5 MHz can be made.

2. The measurements of current and voltage at the current elcctrode are included in order to maximise the system's data accuracy. A separate calibration board is not required since a calibration resistor is built on the board. This reduces the complexity of measurements.

3. The system is fully isolated by means of transformers and optocouplers.

4. It is easy to transport as an external power supply can be used. This is important for clinical applications.

5. The data acquisition speed is relatively high.

6. The system is compact, self contained, portable and has a low cost.

7. The easy-to-use software provides control, data acquisition and simple data analysis.

Several important limitations pose problems for using it in EIS. During the PhD a Galerkin Regularised Inverse Method has been developed. It is based on the knowledge of impedance data in a wide frequency range in order to extract information about the distribution of relaxation times. The method requires high accuracy in measurements of the real and imaginary parts of the impedance. Problems associated with systematic errors have been discussed in section 4.9. It became obvious that the bespoke system does not meet such requirements. Firstly, the limitation is the design of a current source with high output impedance at high frequencies. Secondly, the number of sampling frequencies has to be increased further. In addition, there is a problem with isolation as the transformers and optocouplers are also frequency limited. Also, as mentioned above, the data acquisition speed is not enough for measurements within one cardiac cycle. Thus, further work is required on this system. In order to increase a frequency range and a number of sampling points, the use of a DDS Synthesiser, can be suggested. The Synthesiser AD 9851 is a highly integrated device that enables a digitally–programmable frequency synthesiser and clock generator function. The AD 9851 synthesiser generates a stable frequency and phase–programmable, digitised, analog output sine wave. This sine wave can be used directly as a frequency source. The AD 9851 has a 180 MHz clock system.

The development and further improvement of the method demands a new instrument which would enable measurements of impedance over six decades of frequencies. One solution is to use an impedance analyser. A measurement system based on an impedance analyser is discussed in the next section.

5.5 Impedance Analyser

Further experiments were carried out with a Hewlett–Packard HP4192A impedance analyser. Figure 5.9 illustrates the general structure of an impedance analyser setup for *in vitro* measurements of electrical impedance.

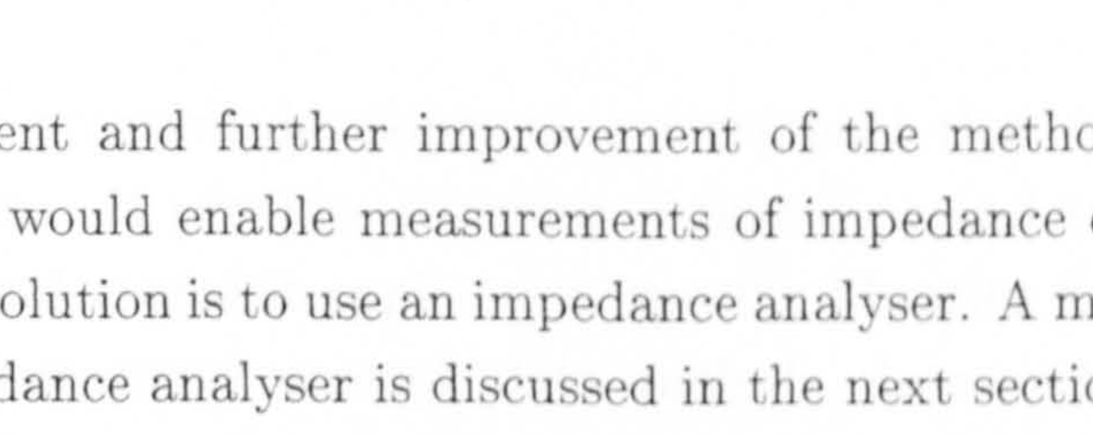

Figure 5.9: *Structure of the measurement system.*

The HP4192A is high accuracy device which can perform measurements of

impedance parameters - amplitudes of impedance and admittance, phase angle, resistance, *etc.* All have a basic accuracy of 0.1% and a resolution of 4 digits. Measuring frequencies can be set from 5 Hz to 13 MHz with 0.005% accuracy. The HP4192A has a very good phase resolution (0.01^0). In addition, impedance parameters can be measured over a wide range, *e.g.* amplitude: $0.1m\Omega$ to $1M\Omega$. A sweep capability permits measurements of parameters to be made in linear or logarithmic frequency steps. The range of frequencies and step values can be easily set up.

The impedance analyser is a programmable device. It is connected to a PC by means of General–Purpose Interface Bus (GPIB). GPIB devices can be talkers, listeners or controllers. A talker sends out data messages. A listener receives data messages. The controller manages the flow of information on the bus. It defines communication links and sends GPIB commands to devices. The impedance analyser is set in the mode of Talker or Listener. The PC handles the Controller function. The computer is equipped with an Amplicon plug and play ISA–GPIB card with a fast transfer rate greater than 300 Kbyte/s. The ISA–GPIB adheres to IEEE–488.2 standard. The data acquisition and management uses software written in a graphical programming language, LabVIEW.

LabVIEW is a program development environment that creates programs in block diagram form. It provides libraries of functions and subroutines for programming tasks and contains application–specific libraries for data acquisition, GPIB and serial instrument control, data analysis, data presentation, and data storage. LabVIEW programs are called *virtual instruments (VIs)* because their appearance and operation can imitate an actual instrument. A VI consists of an interactive user interface and a dataflow diagram. Figure 5.10 shows the interface and the block diagram created to control HP4192A. *In vitro* measurements have been carried out in the frequency range from 1 kHz up to 10 MHz. Data have been saved in a text file and processed. The impedance analyser is supplied with a standard front–panel: direct attachment high frequency fixture (part number 16047C). It has been mainly used only for measurements of lumped–component electrical RC circuits. For experiments *in vitro* a probe designed by Paulson *et al* [21] has been used. Results of experiments are presented in chapter 6.

In practice, it is impossible to connect the instrument with a probe directly to tissue sample. Coaxial cables one meter long have been used. The leads have stray capacitance which is liable to introduce measurement errors. The obtained measurements with this setup are outside the analyser relative error specifica-

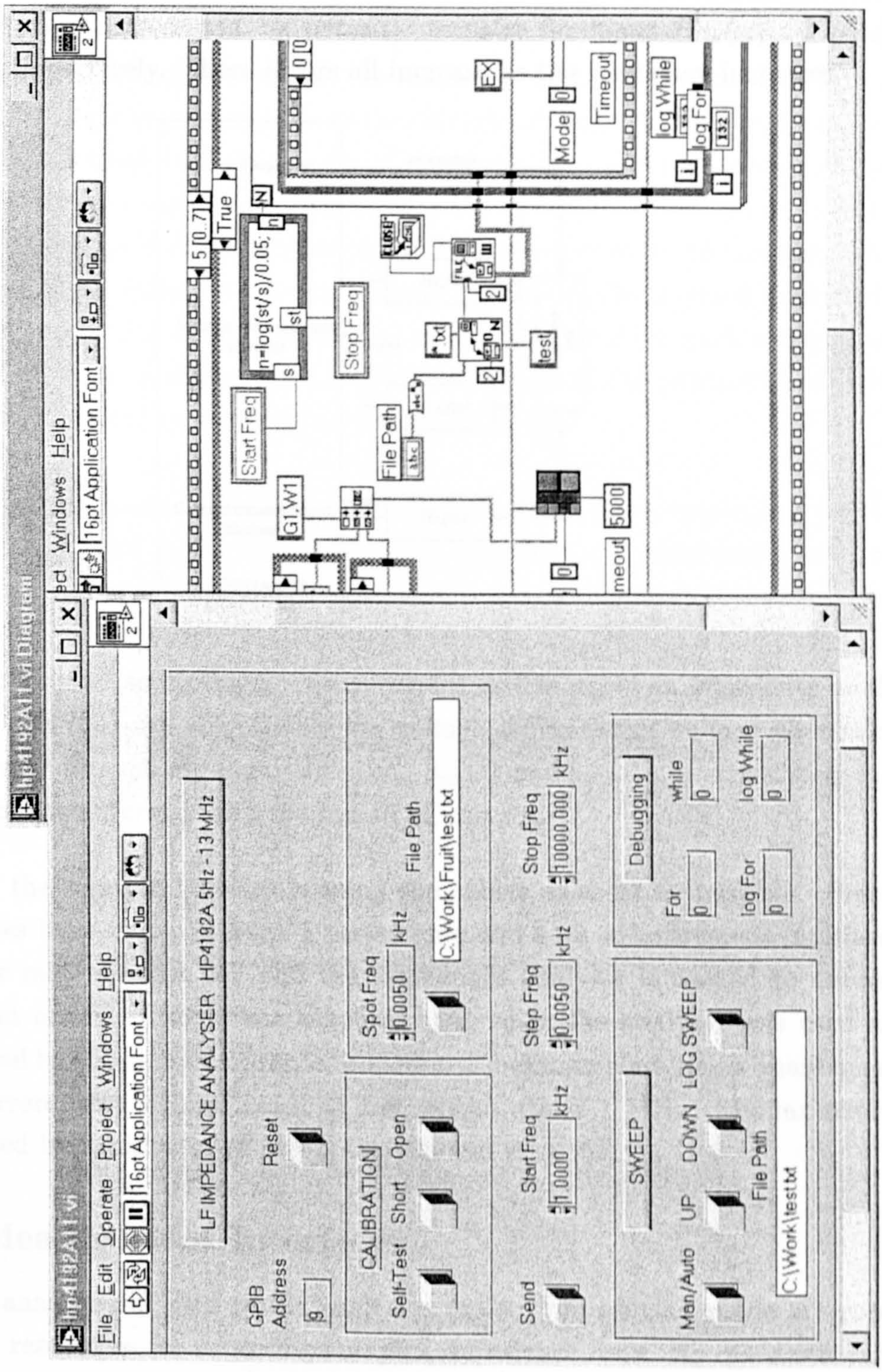

Figure 5.10: *Front panel and block diagram for HP4192A.*

tions for frequencies above a few hundred kilohertz. Figure 5.11 shows that the measurement error includes the combination of errors related to the stray capacitances, the source generator output impedance, and the measurement channel input impedances represented by parasitic transfer functions $Hs_v(\omega)$, $H's_v(\omega)$ and $Hs_i(\omega)$ respectively. These errors all increase as the frequency increases.

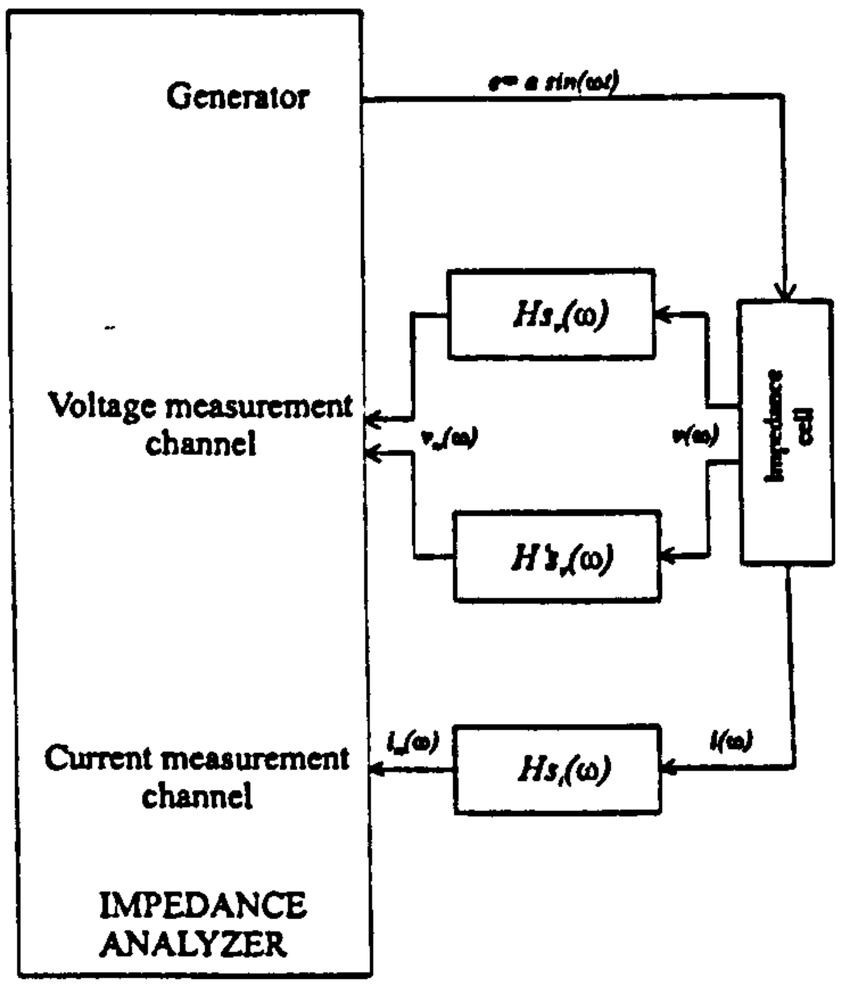

Figure 5.11: *In vitro spectroscopic measurement system using an impedance analyser. $v(\omega)$ and $i(\omega)$ are respectively the voltage difference at voltage electrodes and the current through the impedance cell. $v_m(\omega)$ and $i_m(\omega)$ are respectively the measured voltage difference and the measured current.*

In part, the solution involves keeping the cables as short as possible. Practically, cables have to be at least 1 meter long and so a measurement interface between the measurement cell and the impedance analyser is needed to reduce measurement errors. Also it was observed that when the analyser was used as recommended by the manufacturer for impedance measurements, some phase measurement errors were still obtained at frequencies above 1 MHz. Similar errors were reported by Schmukler *et al* [61] and Rigaud *et al* [62].

5.5.1 Measurement Interfaces

Impedance analysers or gain–phase analysers in the "impedance" mode are popular among researches for acquiring complex impedance data. As discussed earlier, several errors are induced into measured values. Different measurement approaches can be found in the literature and some examples are examined in this section.

The proposed front–end interfaces are analogue. One of the most popular designs was proposed by Gersing *et al* [63] and includes two instrumentation amplifiers. Impedance analysers have four terminals of which two are for voltage measurements and two for current. In Gersing's scheme, the analyser measures two single–ended voltages supplied to the two analyser voltage channels. One of the single–ended voltages is proportional to the voltage difference at the measurement electrodes. The second voltage channel of the impedance analyser measures the voltage across a series resistance to determine the injected current. This requires wide–frequency–range instrumentation amplifiers. In order to avoid measurement errors due to current leakage to ground, one of the current electrodes is grounded. Furthermore, the length of the two coaxial cables is adjusted in such a way that the propagation time in these cables is identical, and then the phase error due to the cables is minimised over the whole frequency range.

Some other approaches use wideband operational amplifiers employing a voltage feedback structure as an instrumentation amplifier or a wideband transconductance amplifier without any feedback. However, the proposed approaches are suitable only for measurements *in vitro* since they do not introduce any isolation.

5.5.2 Isolation

The Model HP4192A impedance analyser has been designed to conform to the safety requirements of IEC discussed in section 5.3.

It is also necessary to isolate the impedance analyser from the mains supply. Isolation can be done by inserting isolation amplifiers between the impedance analyser and the instrumentation amplifiers of the measurement interface. The instrumentation amplifiers available on the market have a limited bandwidth. The ISO 122P (Burr Brown) has a bandwidth 50 kHz, and the ISO102 has a bandwidth 70 kHz. Thus, these components are not suitable for EIS measurements when α- and β - dispersions are observed.

Another possible method of ensuring isolation is to use isolation transformers between the mains power supply and the impedance analyser. For the case of a PC connected to the impedance analyser with the GPIB bus, a laptop operated from a battery-based power supply may be used.

5.5.3 Drawbacks of an Impedance Analyser

Among the drawbacks of using an impedance analyser in a spectroscopic measurement system are:

1. a measurement interface is still needed to reduce measurement errors corresponding to the stray capacitance of the cable and phase errors;

2. electrical isolation for use *in vivo* is necessary;

3. relatively low data acquisition speed for real–time measurements. It is desirable to perform measurements during a single cardiac cycle;

4. the large size of the equipment, especially for work in small sterile rooms and for transportation;

5. the high cost of the whole system including impedance analyser, computer or even laptop, and the measurement interface.

In this case, it may be better to set aside many of the possibilities provided by an analyser and replace it with a compact piece of equipment *e.g.* based on that introduced in the section 5.3.

5.6 An Impedance Probe

The measurements of impedance of living tissue are extremely difficult to make. There are many reasons for this difficulty and some of them were discussed in the previous section, *e.g.* electrically isolating the tissue sample and controlling parameters such as temperature, pH, *etc.* Tissues exhibit inhomogeneities over a wide range of scales. Tissue, such as a muscle, shows a large degree of anisotropy, typically having a transverse impedivity of more than ten times the longitudinal value [64].

In vivo measurements are typically made using an impedance probe which introduces needle or plate electrodes into the region of impedance measurements. Electrodes are needed to inject current into a sample and the same or others are used to measure the induced voltage which is used to calculate the impedance, *i.e.* impedance can be measured using two–electrode or four–electrode experiments. The conduction mechanism changes at the electrode–tissue interface leading to complex electrochemical reactions that create a polarisation effect. This frequency dependent polarisation impedance, known as the contact impedance, is largely capacitive. It depends on the electrode material and also on the nature of the electrolyte [65]. Different methods exist to approximately correct or compensate for the contact impedance. Four–electrode measurements use separate sets of electrodes for current injection and voltage sensing. As the high input impedance, voltage sensing electrodes sink practically no current, the tissue

impedance measurement does not include the contact impedance. High source impedance currents should be unaffected by the contact impedance at the current electrodes.

Probes can be also divided into invasive and non–invasive types. Invasive probes may consist of needles which are inserted into the tissue, [66]. Compound needles pass current and measure voltage between segments of needles. In this case, impedance measurements are affected by a highly conductive layer of blood which surrounds the needles. Also the contact area is small and therefore any variations in the material behaviour at this point strongly affects the impedance measurements. Non–invasive probes make electrical measurements between two or four electrodes on the surface of the tissue. The non–invasive electrode system, designed by Paulson *et al* [21], was used in conjunction with the impedance analyser. The probe, intended for *in vivo* measurements, consists of five, concentric, circular electrodes, see Figure 5.12.

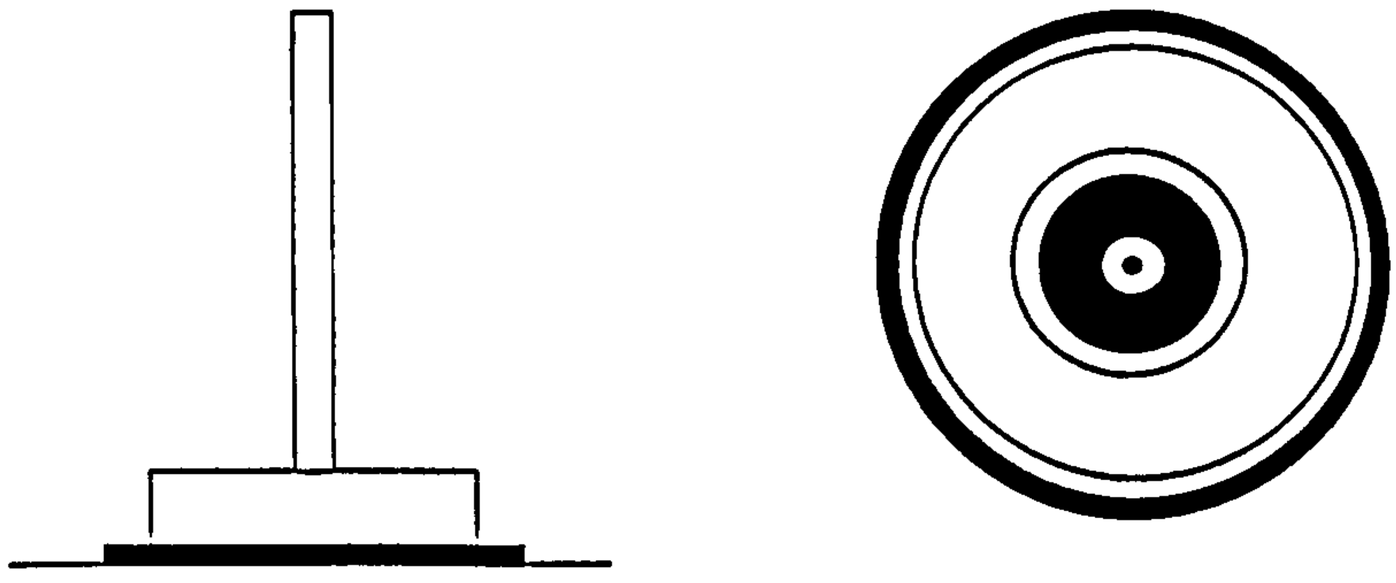

Figure 5.12: *Cross–section through a current driving electrode and the active surface of the impedance probe, [21]*

Current is driven between a central disk shaped electrode and an outer annular electrode. The induced voltage is measured on two, much narrower, ring electrodes, placed between the current driving electrodes. A further measurement point is available in a small insulated area at the centre of the disk electrode. The probe was designed in such a way that it should be small enough to model the organ under investigation as a semi–infinite, homogeneous region and also large enough to reduce the contact impedance and average local cellular and vascular variations. A limit in this design is its rotational symmetry, which makes the probe unsuitable for use with anisotropic materials.

5.7 Application of EIS

The characterisation of tissues by means of their electrical properties is the richest application field for impedance spectroscopy. The electrical properties of biological tissues are related to the microscopic structure of cellular media and to the physiological and pathological state of organs at the macroscopic level. A large and growing body of literature exists showing that multi-frequency electrical measurements of tissue can be used to distinguish different tissues and clinically useful tissue characteristics. Practically all organs have been the subject of impedance spectroscopy measurements to determine electrical or dielectric properties. Data published for tissue impedance are commonly from *in vitro* measurements [67], [68]. These data are mainly used for the development of complex models and for studying the modifications in the electrical parameters according to the measurement conditions and the conditions of the tissue. However, data obtained from *in vitro* measurements do not represent the real properties of living tissues. Data published for blood impedance have demonstrated the large changes which occur with haemocrit, temperature and blood flow rate in extra-corporeal flow rigs, [69]. The impedance of living tissue is strongly influenced by the blood flowing through it.

In vivo measurements of the impedance of living tissue are notoriously difficult to make and published measurements often vary by a factor of two or more, [70]. Some of the reasons behind the difficulty of physical access have been discussed in this chapter. The most recent literature review of dielectric properties of different types of tissues have been provided by Gabriel *et al*, [16]. Some attempts to obtain spectroscopic data for liver, spleen and muscle have been made during this research work.

The studies of pathological tissues mainly correspond to the characterisation of cancerous tissue and the study of ischemia during organ conservation and transplantation. Work on the application of EIS for monitoring of ischemia levels has been published by Gersing *et al* [71] and Schäfer *et al* [72]. The author of the present research has collaborated with Dr. M. Schäfer and the group from Heidelberg University (Germany) in conducting experiments. Impedance spectra were measured and analysed for different types of tissue under ischemia. The experiment setup, measured data and its analysis will be discussed in chapter 6.

5.8 Summary

This chapter has described the EIS system design and the reasoning behind the design choices. It also gives an overview on research carried out in EIT hardware design at Oxford Brookes University prior the EIS system. Different components for the current source implemented from OXBACT3 have been investigated. An alternative current source - an operational transconductance amplifier - has been suggested for use in the EIS data acquisition system. The circuit design of the data acquisition system is shown in section 5.3.2. Disadvantages and limitations of the bespoke system have been discussed. A commercial instrument - a HP impedance analyser - used for the current work has been introduced. Important limitations preventing its use *in vivo* have been given.

Chapter 6

Experimental Results

6.1 Introduction

A method for calculating dielectric relaxation time spectra was proposed in chapter 4. In this chapter the method is applied to permittivity data collected for different types of biological tissues. Tissue structures are complex and hence bring additional complications in the results of analysis. In order to evaluate the GRIM, it has first been tested on data from both computer simulation and measurements on known lumped–constant element circuits. The results are shown in sections 6.2 and 6.3.

The use of noninvasive techniques such as electrical impedance spectroscopy (EIS) would be a great advantage in medicine. Different tissue types have different impedance spectra that are known to change with pathology, but it is often difficult to determine which components of these spectra are important and how their changes relate back to even the most basic physiological parameters, [73], [74]. One of the widely used applications of EIS is for the monitoring of cell death during periods of interrupted blood supply (ischemia). However, it not always easy to see changes in the electrical impedance spectrum during ischemia that show clearly the transition from reversible to irreversible damage. One of the purposes of these studies is to investigate the possibility of using the GRIM to characterise organ tissues and also the level of ischemia. Experimental work has been performed with different tissue types affected by ischemia in a well–established protocol and in which repeatable EIS results have been obtained (see section 6.4). Along with ischemia studies on excised tissue, *in vivo* studies have been carried out and the results are discussed in section 6.5.

It is shown that the GRIM may be a helpful tool for separating different types

of tissue as well as for providing information about the physiological processes inside tissues.

6.2 Results for simulated data

In this section, computer simulated data are used to evaluate the GRIM. Dielectric relaxation time distributions have been calculated for simple lumped–constant element (LCE) circuits with a single RC–arm, two and three RC–arms (here RC stands for a resistor–capacitor pair). For each LCE circuit, complex impedance has been computed at points on a logarithmic frequency scale. This approach is ideal for calculating the DRT distributions since the noise is very small and data can be generated across a wide frequency range. In the examples presented, the frequency has been varied within a range of 9.3 decades. Thus, by the sampling localisation theorem presented in section 3.4.3 this frequency range yields knowledge of the relaxation distribution over 7.9 decades. For simulated data, the time constants can be chosen to lie within this narrower range. However, for real experimental measurements, it is not always the case due to hardware limitations and the range of real relaxation times present in biological media.

The resistor and capacitor values have been chosen arbitrarily in order to simulate EIS measurements in the frequency range from 10 Hz to 20 GHz. The resistors R1, R2, R3 and R4 are equal to 1 Ω (see Fig. 6.1, 6.3, 6.5). Capacitors C1, C2 and C3 have been set to 10^{-4} F, 10^{-5} F and 10^{-6} F respectively. The impedance spectra have been transformed analytically to yield the conductance and then permittivity spectrum. The example below demonstrates the transform stages $Z \rightarrow \sigma \rightarrow \varepsilon \rightarrow Q \rightarrow S$ for the two RC–circuit in Fig. 6.3. The impedance for each arm of the circuit, Z_i, equals to:

$$Z_i = R_i + \frac{1}{j\omega C_i} \tag{6.1}$$

Thus the total conductance is $\sigma_t = 1/Z_t$ and:

$$\sigma_t = \frac{j\omega C1}{1 + j\omega\tau_1} + \frac{j\omega C2}{1 + j\omega\tau_2} + \frac{1}{R3} \tag{6.2}$$

where $\tau_1 = R1C1$ and $\tau_2 = R2C2$.

The static conductance can be calculated accurately from the known parameters of the circuit as $\sigma_s = 1/R3$. From Eqn. 2.6 it follows that:

$$\sigma^* - \sigma_s = \frac{j\omega C1}{1 + j\omega\tau_1} + \frac{j\omega C2}{1 + j\omega\tau_2} = j\omega\varepsilon_0\varepsilon^* \tag{6.3}$$

$$\varepsilon^* = \frac{C1}{\varepsilon_0(1+j\omega\tau_1)} + \frac{C2}{\varepsilon_0(1+j\omega\tau_2)} \tag{6.4}$$

In order to find a network function $Q(\omega)$ from Eqn. 3.12, the permittivity limits have to be determined:

$$\varepsilon_s\Big|_{freq=0} = \frac{C1+C2}{\varepsilon_0} \tag{6.5}$$

$$\varepsilon_\infty\Big|_{freq=\infty} = 0 \tag{6.6}$$

Then the network function $Q(\omega)$ and function $S(\omega)$ are:

$$Q(\omega) = \frac{C1}{C1+C2}\left(\frac{1}{1+j\omega\tau_1}\right) + \frac{C2}{C1+C2}\left(\frac{1}{1+j\omega\tau_2}\right) \tag{6.7}$$

$$S(\omega) = \frac{C1}{C1+C2}\left(\frac{j\omega}{1+j\omega\tau_1}\right) + \frac{C2}{C1+C2}\left(\frac{j\omega}{1+j\omega\tau_2}\right) \tag{6.8}$$

Using self–developed software written in MatLab (see section 4.10) the data vectors $\mathbf{S}'$ and $\mathbf{S}''$ have been generated and calculated at 40 Gauss–Legendre integration abscissa.

Figures 6.2, 6.4 and 6.6 show the relaxation time distributions for the three LCE circuits corresponding to Fig. 6.1, 6.3, 6.5 respectively. Figures 6.1, 6.3 and 6.5 also show Cole–Cole plots for corresponding electrical circuits. The time constants are sufficiently close to each other. The impedance curves show no distinct semi–circles. The reconstruction of DRT distributions does not require prior knowledge about how many relaxation times are present. However, distribution functions $G(\tau)$ clearly show one, two or three positive peaks at the correct time constants for one–, two– and three–RC circuits respectively. The horizontal axis is on a logarithmic scale. The numbers v defined in section 4.3 allow the estimation of time constants. For a single–armed RC circuit: $\tau_1 = 1.003 \times 10^{-4}$ s; for a two–armed RC circuit: $\tau_1 = 1.05 \times 10^{-4}$s and $\tau_2 = 9.57 \times 10^{-6}$ s; for a three–armed RC circuit: $\tau_1 = 1.054 \times 10^{-4}$ s, $\tau_2 = 1.006 \times 10^{-5}$ s and $\tau_3 = 9.59 \times 10^{-7}$ s. The time constants are within a few percents of the values of chosen parameters.

All DRT distributions have been reconstructed using Tikhonov regularisation, *i.e.* solving $(\mathbf{K}'')^{\mathbf{T}}\mathbf{S}'' = ((\mathbf{K}'')^{\mathbf{T}}\mathbf{K}'' + \mu\mathbf{I})\mathbf{G}$, where $\mu = 0.001$. The number of basis function was equal to 40. Calculated spectra are smoothed versions of the actual relaxation time spectra which lead to anomalous negative densities. The smoothing needs to be taken into account when interpreting the spectra. When using areas to estimate the contribution of resolved time constants the effects of

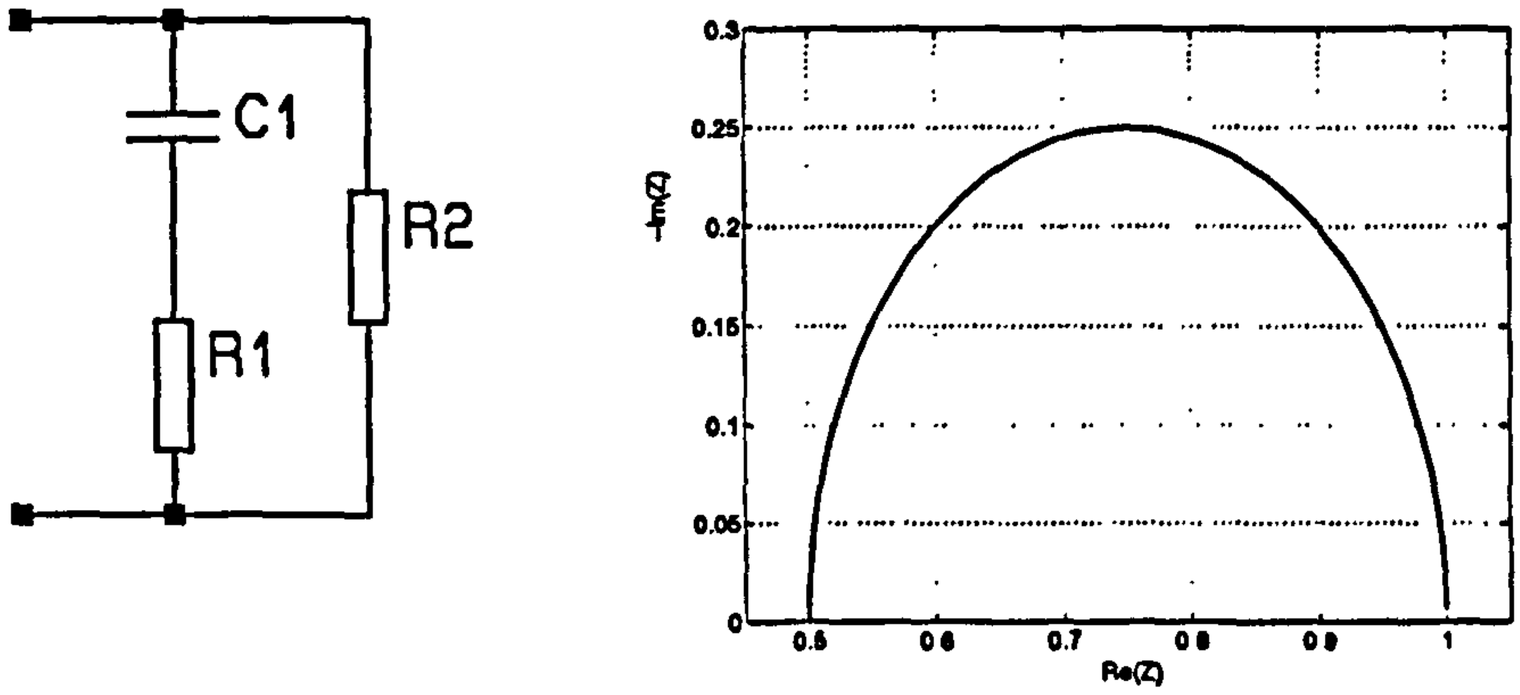

Figure 6.1: *Electrical circuit model:* $R1{=}R2{=}1\Omega$, $C1{=}10^{-4}$ *and its Cole-Cole plot respectively.*

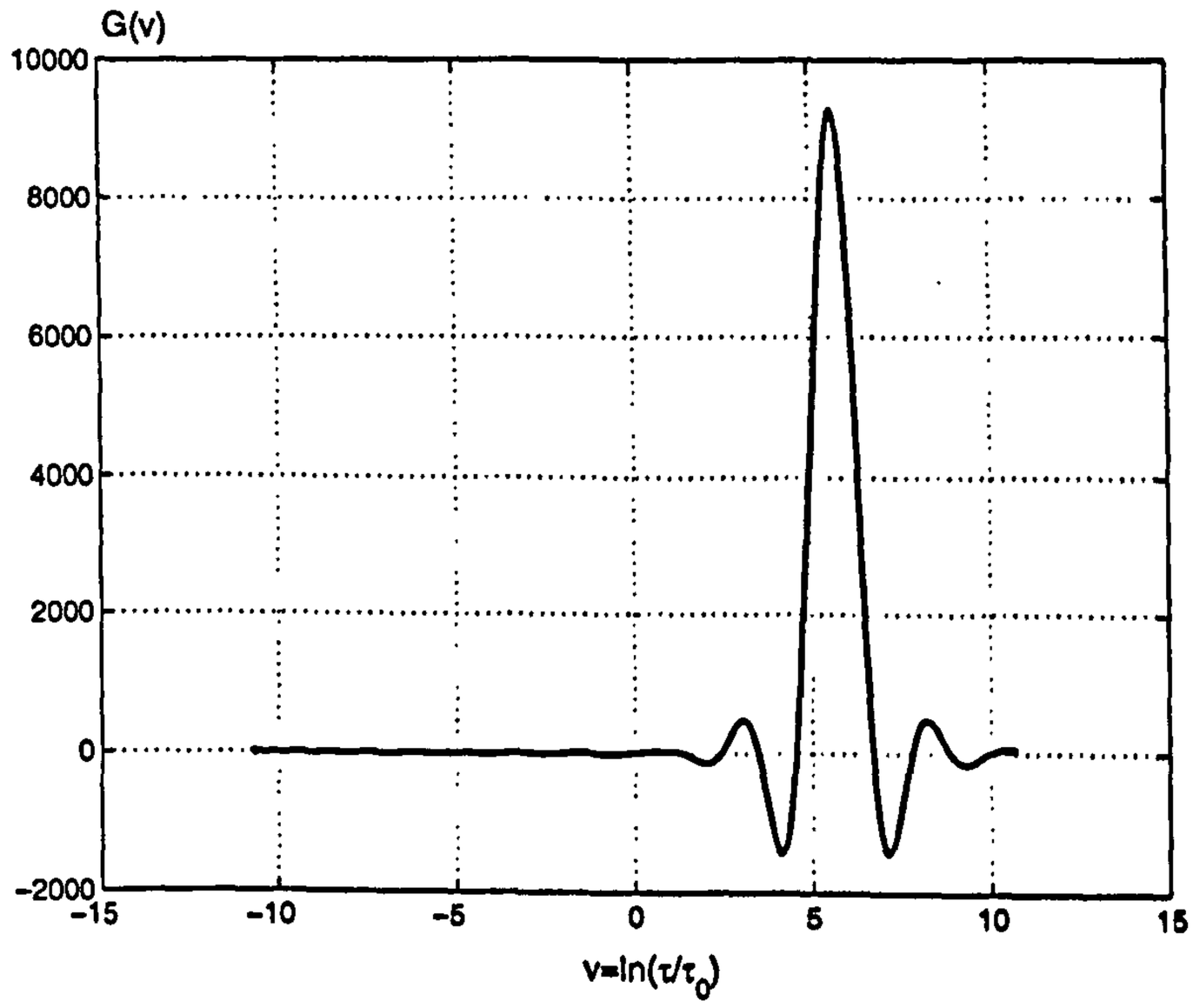

Figure 6.2: *Relaxation spectrum for the single armed RC-circuit.*

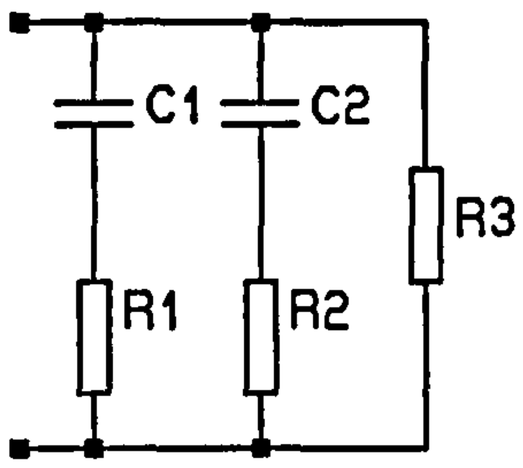

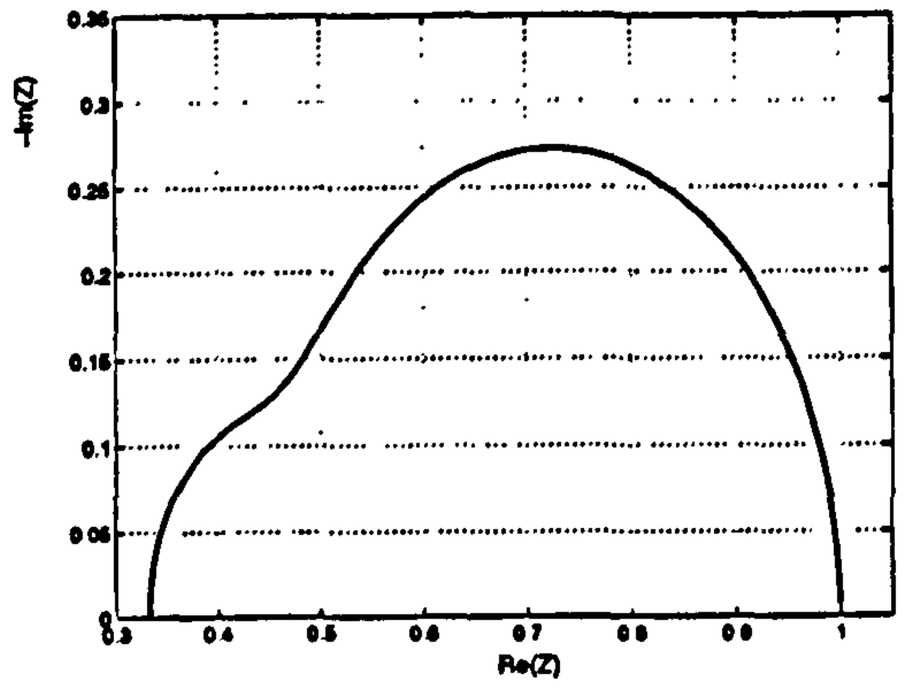

Figure 6.3: *Electrical circuit model:* $R1{=}R2{=}R3{=}1\Omega$, $C1{=}10^{-4}$, $C2{=}10^{-5}$ *and its Cole–Cole plot respectively.*

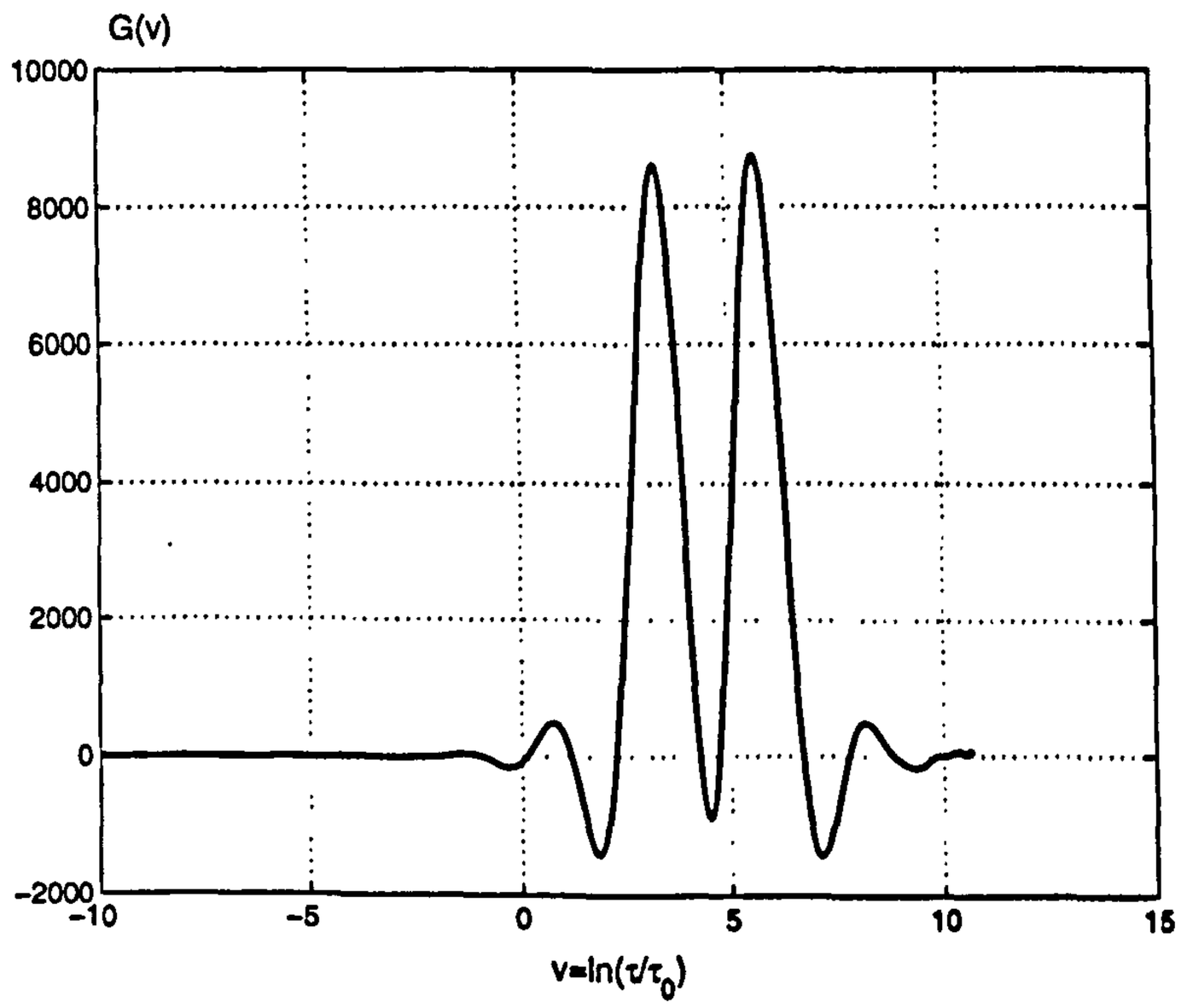

Figure 6.4: *Relaxation spectrum for the two armed RC–circuit.*

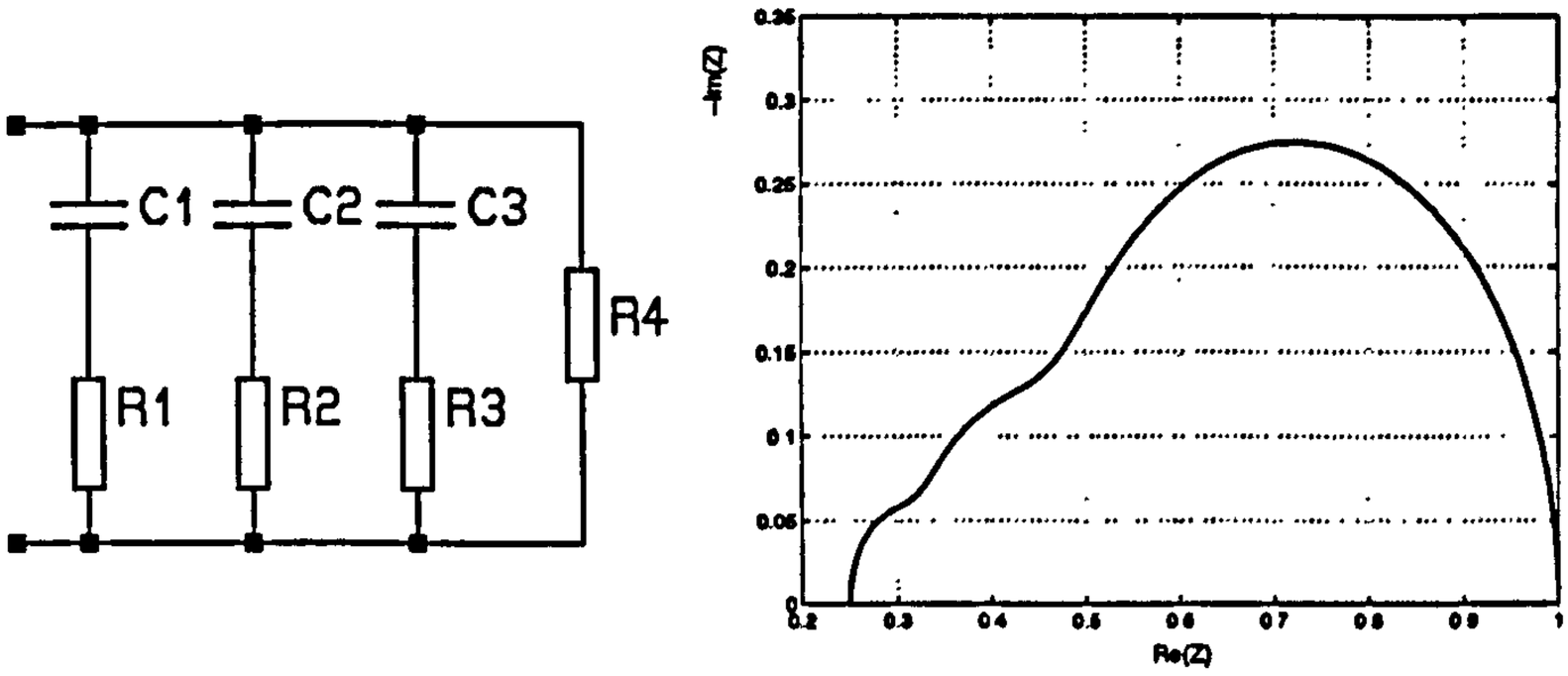

Figure 6.5: *Electrical circuit model: R1=R2=R3=R4*1Ω, *C1*=10^{-4}, *C2*=10^{-5}, *C3*=10^{-6} *and its Cole–Cole plot respectively.*

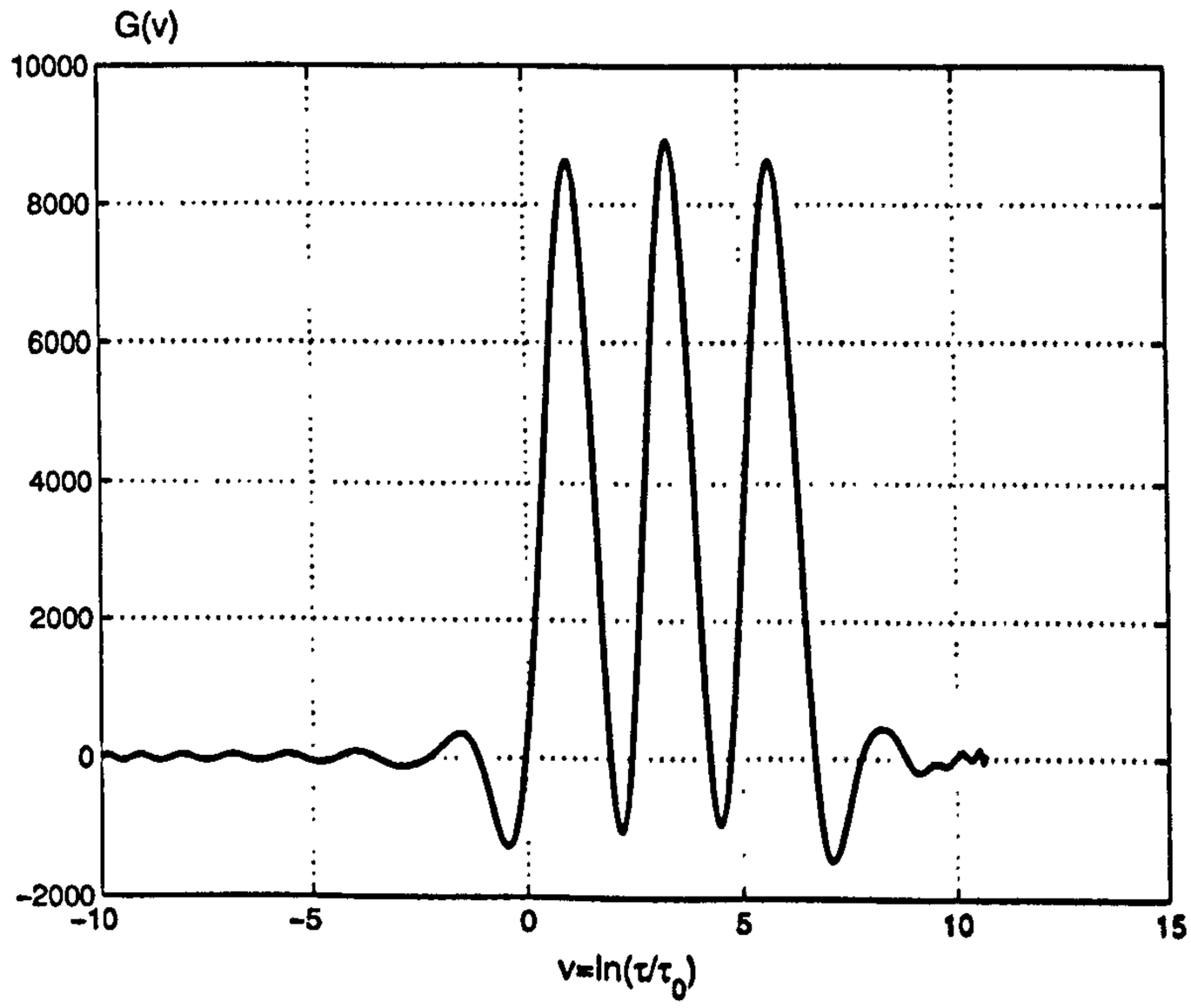

Figure 6.6: *Relaxation spectrum for the three armed RC–circuit.*

band limiting the solution need to be taken into account.

The area of each pulse shows the contribution of each time constant to the relaxation process. For lumped circuits, the weight of the delta–function varies according to the capacitance associated with that time constant. For the relaxation spectrum consisting of two delta–functions centred at $\tau = \tau_1$ and $\tau = \tau_2$:

$$G(\tau) = \frac{C_1}{C_1 + C_2}\delta(\tau - \tau_1) + \frac{C_2}{C_1 + C_2}\delta(\tau - \tau_2) \tag{6.9}$$

The delta–function is the limit of the unit area pulse as it gets infinitely narrow and infinitely tall. In this method the relaxation time axis has a natural logarithmic scale and so two smoothed delta–functions of the same area at different time constants will have different heights. The area enclosed by each peak is equivalent to the capacitance of the respective process. Figures 6.4 and 6.6 illustrate this statement. For example, Fig. 6.4 shows two peaks of approximately the same height. However, taking into account the logarithmic scale the area under the right peak is bigger than the area under the left peak. The ratio of these two areas is equal to the ratio of corresponding capacitor values. Some more examples including area estimates will be shown in the subsequent section.

Results obtained from simulated data have been found to be in good agreement with the preliminary settings of LCE circuit parameters. In summary, this section shows that the GRIM enables different relaxation time constants to be identified and measured.

6.3 Analysis of experimental data for 3–RC electrical model

In order to illustrate the application of the GRIM to actual experimental data, some results on a simple, physical, electrical model representative of a biological tissue are discussed in this section.

A physical, electrical model is similar to the LCE circuit in Fig. 6.5 with known parameters: R1=3309 Ω, R2=1000 Ω, R3=3916 Ω, R4=683.3 Ω, C1=126.2$\times 10^{-12}$ F, C2=C3=3.3 $\times$ 10^{-9} F. In the literature this model is often suggested for simulating *in vivo* tissue impedance measurements, [75]. Experimental data were collected with the HP4192A Impedance Analyser with a standard four terminal front end. The frequency–dependent, complex impedance data were recorded and transmitted to a PC via the GPIB interface. A sketch of the complete experimen-

tal setup has been shown and discussed in section 5.4 (Fig. 5.9). The amplitude and phase of the impedance values have been measured between 2 kHz and 1 MHz at 189 points. In accordance with the sampling localisation theorem, the DRT distribution can be estimated over 1.34 decades only. However, parameters of the physical electrical model have been chosen so that the contributions of the relaxation time spectrum are within the experimental measurement range and reliable results can be obtained. For the numerical analysis the impedance data have been transformed into conductance and then permittivity data. The data vectors $\mathbf{S}'$ and $\mathbf{S}''$ have been estimated and the matrices $\mathbf{K}'$ and $\mathbf{K}''$ have been calculated using the 40 point Gauss integration. The relaxation time constant distribution is presented in Figure 6.7.

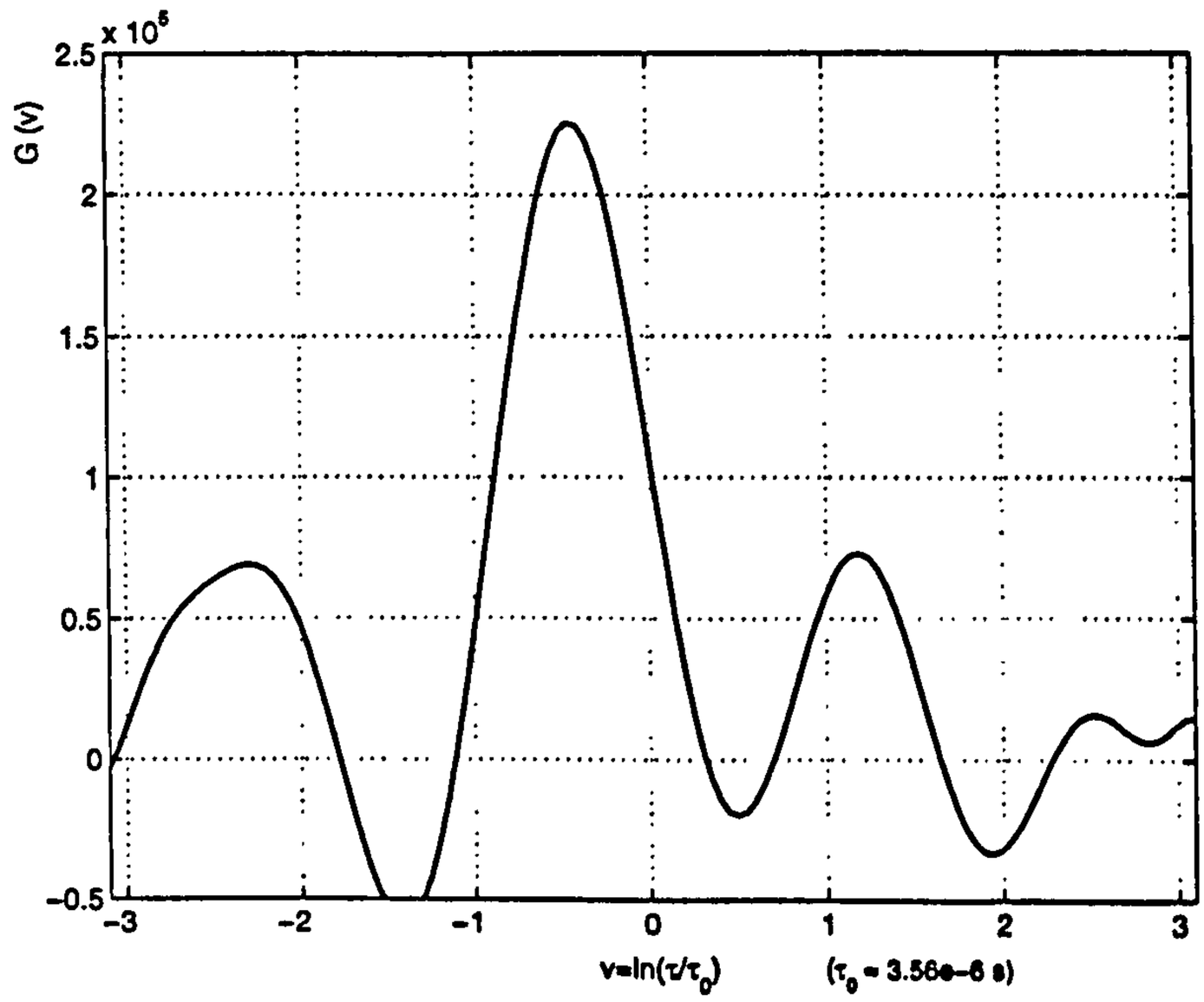

Figure 6.7: *Reconstruction of a time constant distribution using 189 sample points of* $(\mathrm{S}''_u)_i$ *using Tikhonov regularisation* ($\mu = 0.001$).

There are three positive peaks corresponding to three time constants:

$$\tau_1 = 0.39\ \mu s \qquad \tau_2 = 3.2\ \mu s \qquad \tau_3 = 19\ \mu s$$

The time constants calculated from the component values are:

$$\tau_1 = R1C1 = 0.42\ \mu s \qquad \tau_2 = R2C2 = 3.3\ \mu s \qquad \tau_3 = R3C3 = 13\ \mu s$$

The GRIM shows a good estimation of relaxation time constants although the resolution is low due to the narrow range of frequencies. In order to check the statement about the pulse area, Eqn. 6.9, the area under each peak of the time

distribution, and the ratio between them, have been calculated numerically. Using Equation 6.9 the correct weights (capacitor values) for the delta–functions are 0.018, 0.49 and 0.49. So the ratio between the first weight and the second weight is approximately 27. The second and third peaks should be weighted equally. The ratios between the areas of pulses, calculated by Simpson's integration rule, for the physical electrical model show similar results: 28.3 and 0.95 respectively. This confirms that the areas and not the heights should be considered for finding the relative capacitor values.

The results for this experiment confirm that the GRIM is an appropriate method for analysing permittivity spectroscopy data: with the GRIM the distributions and the amplitudes of the relaxation time constants can be identified. Obviously, the resolution of the method could be improved with more data.

6.4 Biological Material during Ischemia

Patho–physiological events in biological tissue result in changes in its electrical properties. EIS is a noninvasive technique that is capable of recording these changes. It is very important to interpret the data correctly and to extract those parameters which are really related to physiological processes. In previous sections it has been demonstrated that the GRIM can isolate more parameters within the data than other conventional methods. Therefore, there are good reasons to suppose that dielectric relaxation time spectroscopy may be able to provide information about cell properties and processes inside tissues.

In this section GRIM is applied to biological impedance data. The study presents the electrical properties of some different types of tissue under ischemia. Investigation of the characterisation of tissues and the study of ischemia in different organs is very important for the development of methods for protecting and preserving human tissues during clinical procedures, such as surgical operations and transplants. This section shows that the GRIM may become a useful technique for detecting different states of ischemic tissues.

6.4.1 Biological aspects of ischemia

Ischemia means that there is no blood flow to supply the tissue cells with oxygen and energy rich substrates and to remove metabolic end products. Ischemia of organs can occur during heart failure, thrombosis or surgical procedures, *e.g.* transplantation. The survival time of organs under ischemia depends on the energy

reserves and the energy consumption in the cells as well as on the consequences of the acidification of the tissue by metabolic products. Metabolic processes produce ions which result in increasing conductivity and cell edema (abnormal fluid accumulation) because of the raised osmotic pressure. Irreversible damage occurs over time and the organs die.

Adjacent cells in some tissues can communicate through low–resistance intercellular pathways called *gap junctions* by means of molecules or ions. Each cell controls the opening or closing of gap junctions. If the conditions for normal life are disturbed, affected cells disconnect from the surrounding cells by closing the junctions. Electrically the gap junction can be modelled as a resistance shunted by the capacitance of the cell wall.

The main changes in organs after the beginning of ischemia are, [76]:

1. acidification of tissue (decreasing pH value) because of the accumulation of metabolic products such as H^+ ion;

2. fluid shift from extracellular space into the cells to maintain the osmotic balance and, consequently, cell swelling and narrowing of the extracellular space;

3. closing of the gap junctions which happens when cells are entering an abnormal state, *e.g.* decrease in pH value and/or a lack of energy. The gap junctions closure is thought to be related to the transition from reversible to irreversible stage.

Much work has been reported on monitoring the state of organs by measuring the electrical properties and their dependence on ischemia time, [77], [78], [79]. In the case of myocardium and liver, characteristic changes were found in the electrical impedance spectrum that show clearly the transition from reversible to irreversible damage, [71], [80]. In the particular case of porcine liver, at low frequencies (a few Hz), there was found an additional dispersion (α–dispersion) that vanishes in time, [81]. The disappearance of the α–dispersion is proposed as a possible indicator for irreversible damage to the liver tissue and can be explained by the closure of gap junctions. However, there is no α–dispersion seen in the electrical spectra of canine liver. Also interpretation of changes of electrical properties of tissues is difficult and not completely understood. Interpretation is only possible by establishing a direct link between some particular electrical property of tissue and cell characteristics. This fact motivated the present study of electrical properties and the reconstruction of the relaxation time distributions of porcine and canine liver tissues.

6.4.2 Experimental Setup

All experiments with ischemic tissues have been carried out in cooperation with Dr. M. Schäfer, from the Department of Experimental Surgery at Heidelberg University, under existing ethnical approval.

The experiments were performed with canine and porcine livers from 6 dogs and 2 pigs. At the beginning of the surgical operations animals were anaesthetised with a gas mixture and then their chests were opened. The blood circulation was then stopped. The main blood vessels to and from the liver were cut and connected to an external circulation. Livers were perfused with Ringer solution (Ringer, Braun Melsungen AG, Melsungen, Germany) at 8^0 C for 8 min after 3 min of pure ischemia in order to prolong the survival time (by minimising energy consumption and buffering the pH–value). Thereafter, the livers were excised and cut into pieces of 2 cm x 2 cm x 2 cm. The organ samples were incubated in measuring chambers at two different temperatures: 5 ^{0}C and 25 ^{0}C and measured within 3–7 hours of the sacrifice of the animals. The dielectric measurements were made in the frequency range from 12 Hz to 10 MHz using the impedance technique (Solartron 1260 device + preamplifier + four electrode probe) of Gersing *et al*, [63]. The experimental technique and the temperature–controlled measuring chambers are described in Schäfer *et al*, [82]. The special probe used for the liver measurements consists of 4 electrodes with a fractal surface. The area of each electrode is 8 mm x 0.5 mm. The electrodes are arranged in parallel and the distance between the outer current driving electrodes is 13 mm. The inner, potential measurement electrodes are 7 mm apart. The electrode system was installed in the floor of the measuring chamber in order to guarantee a constant pressure between the electrodes and the tissue during the time–dependent measurements.

The system was calibrated by using three different saline solutions with known electrical properties. The absolute accuracy of the measured values mainly depends on the calibration standards. Between 100 Hz and 10 MHz errors in the real and imaginary parts of the impedance are $\leq 1\%$. Below 100 Hz, increasing errors occur because of electrode polarisation.

6.4.3 Electrical properties and DRT of porcine liver tissue

For the porcine liver, Gersing *et al*, [76] showed that monitoring of the impedance spectra at low frequencies (α–dispersion) allows the closing of gap junctions to be followed. Figure 6.8 represents the measured impedance spectra in different states: at 3 min after the end of the blood circulation, at 48 min and at 98 min:

The intra–ischemic temperature of the porcine liver was 25 ^{0}C.

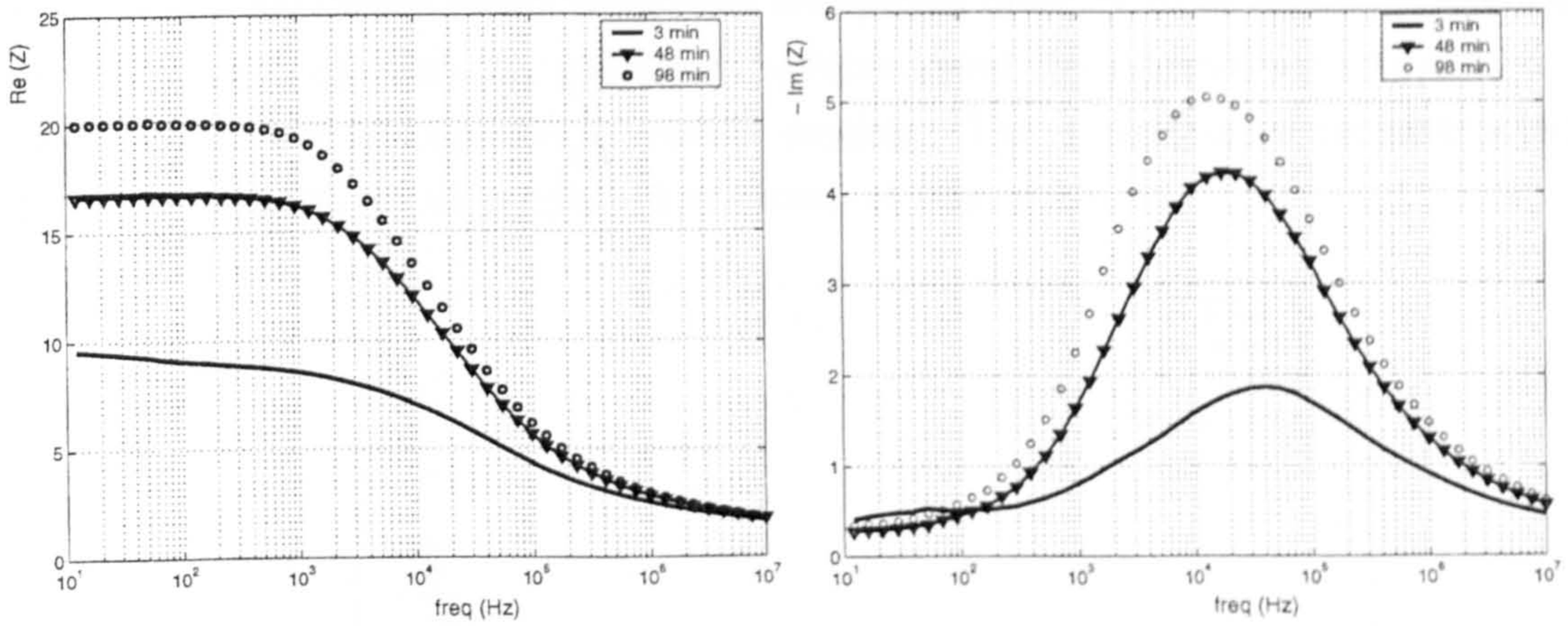

Figure 6.8: *Impedance spectra of the porcine liver at 25 ^0C at different time after the end of the blood circulation.*

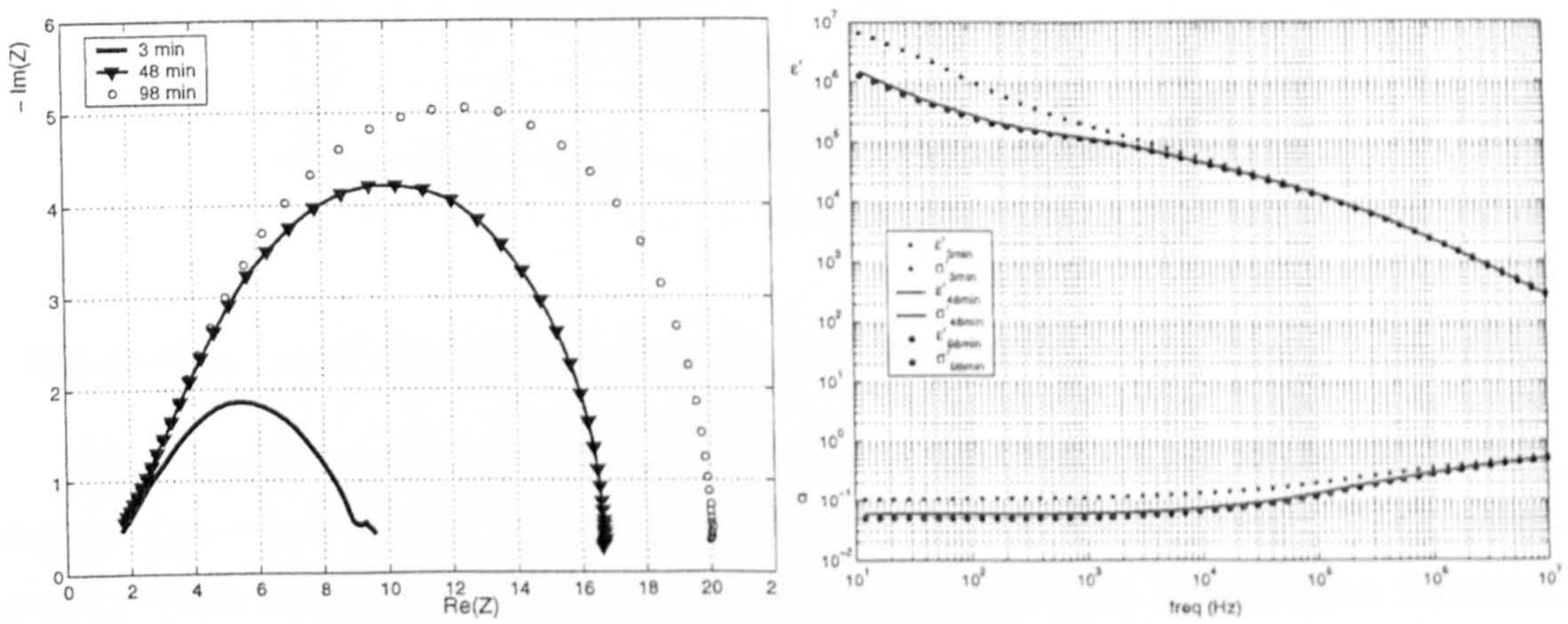

Figure 6.9: *Cole–Cole plots and permittivity spectra of porcine liver respectively.*

The electrical impedance spectrum corresponding to three min after the end of the blood circulation clearly shows two dispersions at 40 Hz (α–dispersion) and 40 kHz (β–dispersion), Fig. 6.8. After 48 min the impedance spectra shows only a β–dispersion shifted to 20 kHz. The α–dispersion has vanished. According to Gersing *et al*, [83], [84], the existence of the α–dispersion may be due to open gap junctions. The resistance at low frequencies increases during ischemia. The dielectric permittivity spectra and Cole–Cole plots at three different times of ischemia are illustrated in Fig. 6.9.

Quantitative description and physical interpretation of the measured data with traditional EIS methods (see chapters 2 and 3) are difficult. Using the GRIM, distributions of relaxation times have been computed directly from the experimental impedance data without any prior assumption about the internal structure of the tissue in the form of equivalent circuit models. The evolution of reconstructed DRT distributions during ischemia is shown in Fig. 6.10.

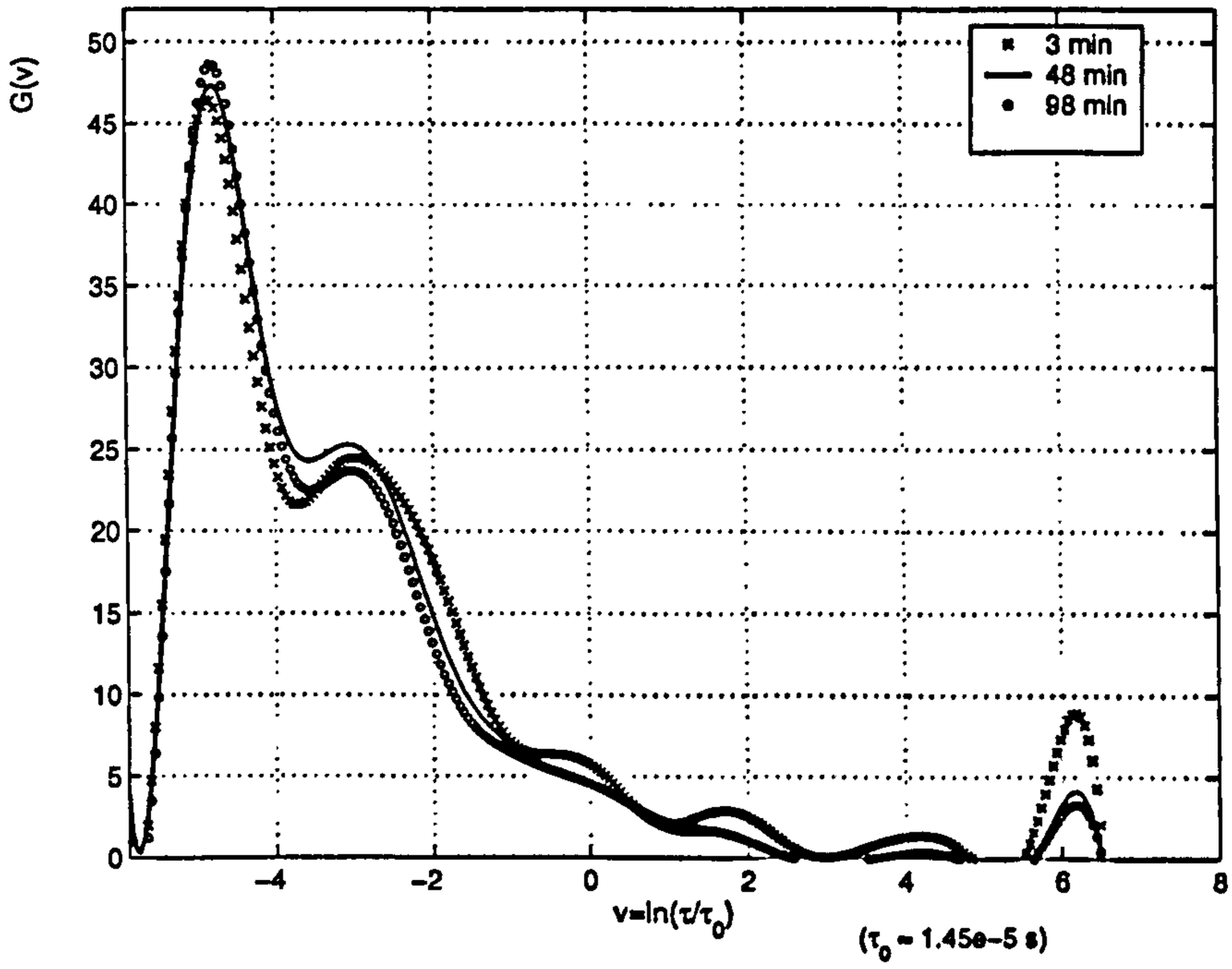

Figure 6.10: *DRT distribution of porcine liver at three times during ischemia.*

Whereas the relaxation processes overlap in the impedance curve (Fig. 6.9), several processes can be clearly distinguished in the distribution. Each relaxation process is represented by one or several peaks in the distribution function. The characteristic parameters of the peaks are the time constant, the amplitude and the area. The areas under each peak can be evaluated by a simple numerical integration, (*e.g.* Simpson's rule) when peaks are well separated or by fitting Gaussian functions when peaks overlap. It was noticed that the dispersion amplitudes change during ischemia. The amplitude of the peak at $v = 6.2$ or $\tau \simeq 7$ ms ($f \simeq 20$ Hz) decreases during ischemia. This peak corresponds to the α–dispersion that disappears when gap junctions are closed. Thus, it can be concluded that the DRT distribution may carry information about processes inside the tissue at the cell level. Also the decrease in the amplitude of the peak at $v \simeq -3$ ($f \simeq 220$ kHz or $\tau \simeq 0.72$ μs) can be observed. Similar behaviour has been found in canine livers and it will be discussed in section 6.4.4.

In the course of ischemia, organ tissue exhibits characteristic changes in the

impedance spectra mainly because of cell swelling, closing gap junctions and accumulation of metabolic products, [84]. It has been shown that the resistance of porcine liver tissue increases at low frequencies during ischemia. The same effect will be demonstrated for the canine liver. The characteristic evolution of resistance in time is a common feature in organs consisting of cells connected together by gap junctions, [85]. However, up to now, a separate α–dispersion has been found only in porcine liver. Canine liver and other organs with gap junctions, showing a steep increase in impedance at low frequencies, do not exhibit a visible α–dispersion. It is assumed that it is hidden in a wide β–dispersion. Further studies have been performed with canine liver and are presented in the next section.

6.4.4 Electrical properties and DRT of canine liver tissue

The full experimental protocol has been described in section 6.4.2. The experiments with canine livers have been carried out at two incubation temperatures: 5 ^{0}C and 25 ^{0}C. Figures 6.11 illustrates a single but typical example of impedance spectra of canine liver at 25 ^{0}C showing the characteristic increase in resistance at low frequencies and a small decrease at high frequencies during ischemia. Additionally, remarkable changes in the imaginary part of impedance can be observed. Figure 6.12 illustrates Cole–Cole plots and permittivity spectra of liver at three times during ischemia.

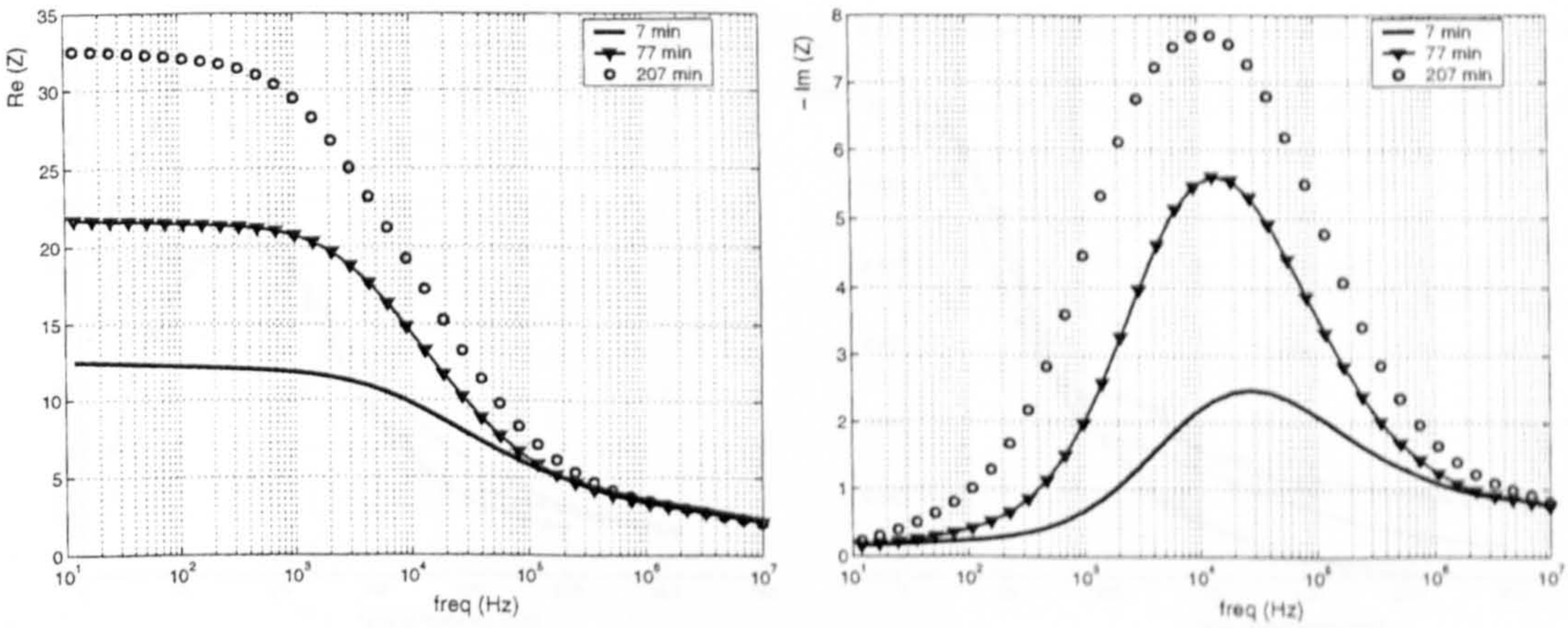

Figure 6.11: *Impedance spectra of ischemic canine liver at 25 ^{0}C.*

The time courses of the dielectric permittivity and conductivity for three different samples of canine liver at 25 ^{0}C at 13 kHz, a frequency between the α–dispersion and β–dispersion, are presented in Fig. 6.13. The steep increase in

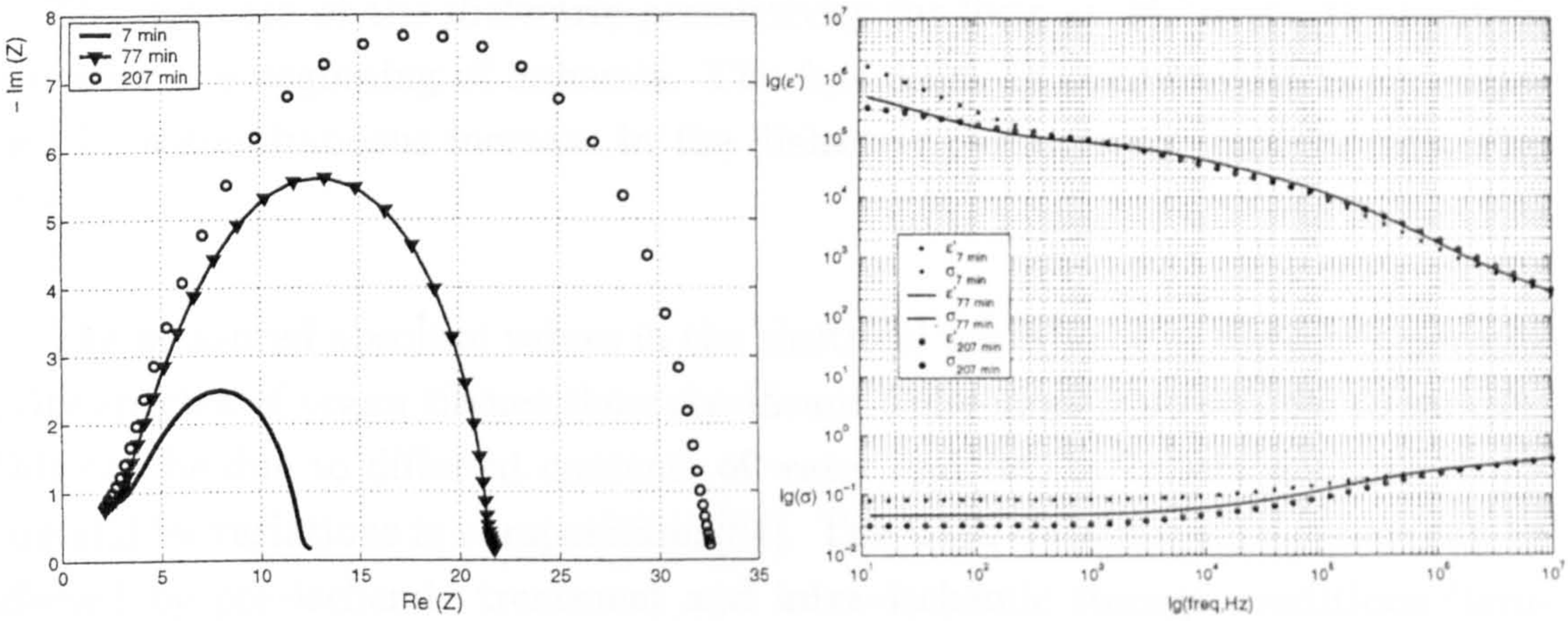

Figure 6.12: *Cole–Cole plots and dielectric permittivity spectra of ischemic canine liver at 25 ^0C respectively.*

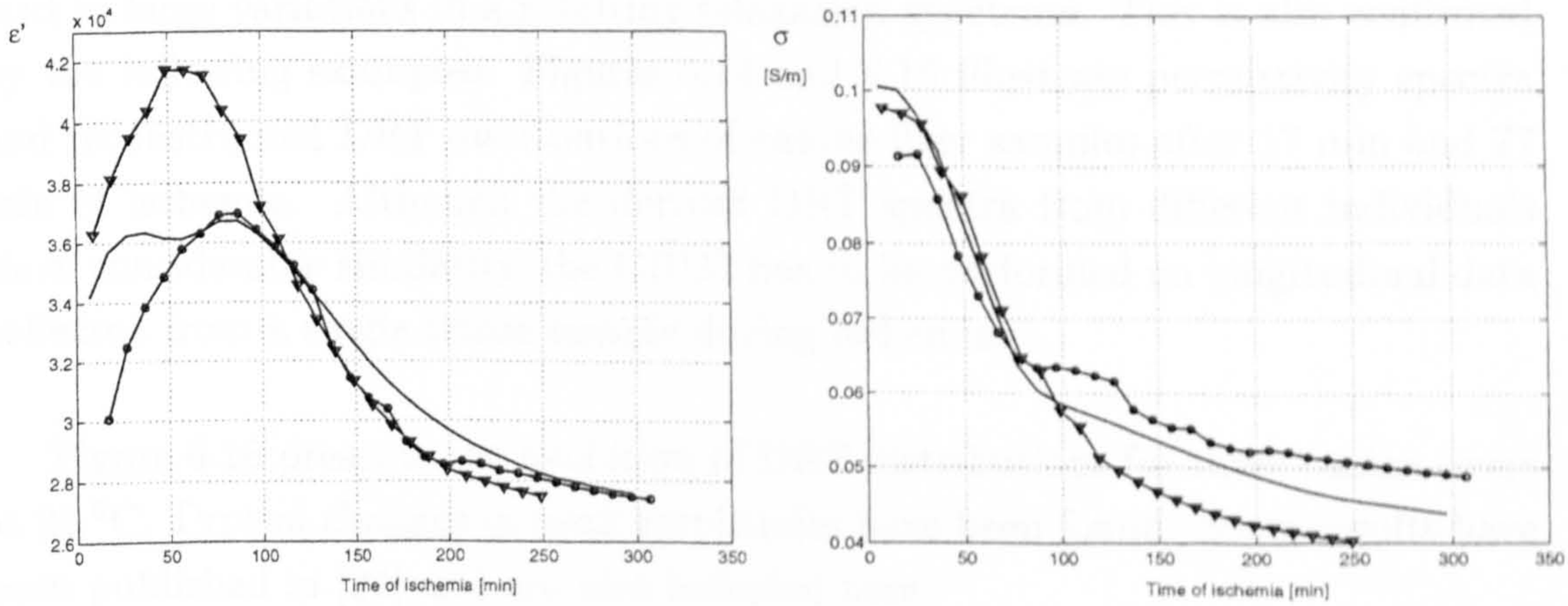

Figure 6.13: *Time courses of dielectric permittivity (ε') and conductivity (σ) for three canine livers at 25 ^0C at 13 kHz.*

resistance (decrease in conductivity) at low frequencies can be explained by the behaviour of the extracellular conducting pathways which narrow due to cell swelling.

The decrease of the dielectric permittivity for liver at 25 ^{0}C starts about 70 min after the beginning of ischemia. The fast decay in conductivity is accompanied by a simultaneous increase in the dielectric permittivity until 70 min, Fig. 6.13.

The measured absolute values in the electrical impedance or dielectric permittivity spectra of organ tissues show significant differences from sample to sample. This can be due to different contents of water and fat, by inhomogeneous structure and by variations in composition, [84]. The intra–ischemic time course can be affected by pre–ischemic treatment and intra–ischemic storage conditions (temperature, humidity, *etc.*). The observed differences can also be as a result of systematic errors in the measurement process. Care has been taken to eliminate all known sources of systematic errors. However, below 1 kHz, the measurement accuracy of the complex dielectric permittivity decreases because of electrode polarisation and the limited resolution of the phase angle measurements.

The GRIM has been applied in order to derive a quantitative data description and to understand the time evolution of relaxation processes during ischemia. The reconstruction of the DRT distribution is an inverse problem that has been discussed in chapter 4. It has been shown that small changes in a data vector can lead to large variations in a resulting relaxation spectrum. This is also confirmed by the following examples. Figures 6.14 and 6.15 illustrate permittivity spectra and reconstructed DRT distributions of canine liver samples after 17 min and 77 min of ischemia. Although the derived DRT spectra from different individuals show considerable similarity, the GRIM has to be performed on longitudinal data collected from a single tissue sample during ischemia.

Figure 6.16 presents the evolution of DRT distributions for three canine livers at 25 ^{0}C. Typical changes in peak amplitudes have been found. Some results have been published in [24] and are also included here.

Each DRT distribution shows at least three clear peaks and so at least nine parameters (time constants, amplitudes and areas) can be extracted. Remarkably, a similar behaviour of distribution amplitudes during ischemia has been found for all samples of canine liver at 25 ^{0}C. It has been noticed that the amplitudes rise until a specific ischemia time. In the presented examples the amplitude increases until about 70 min, Fig. 6.16. After that times the amplitudes for the peak at

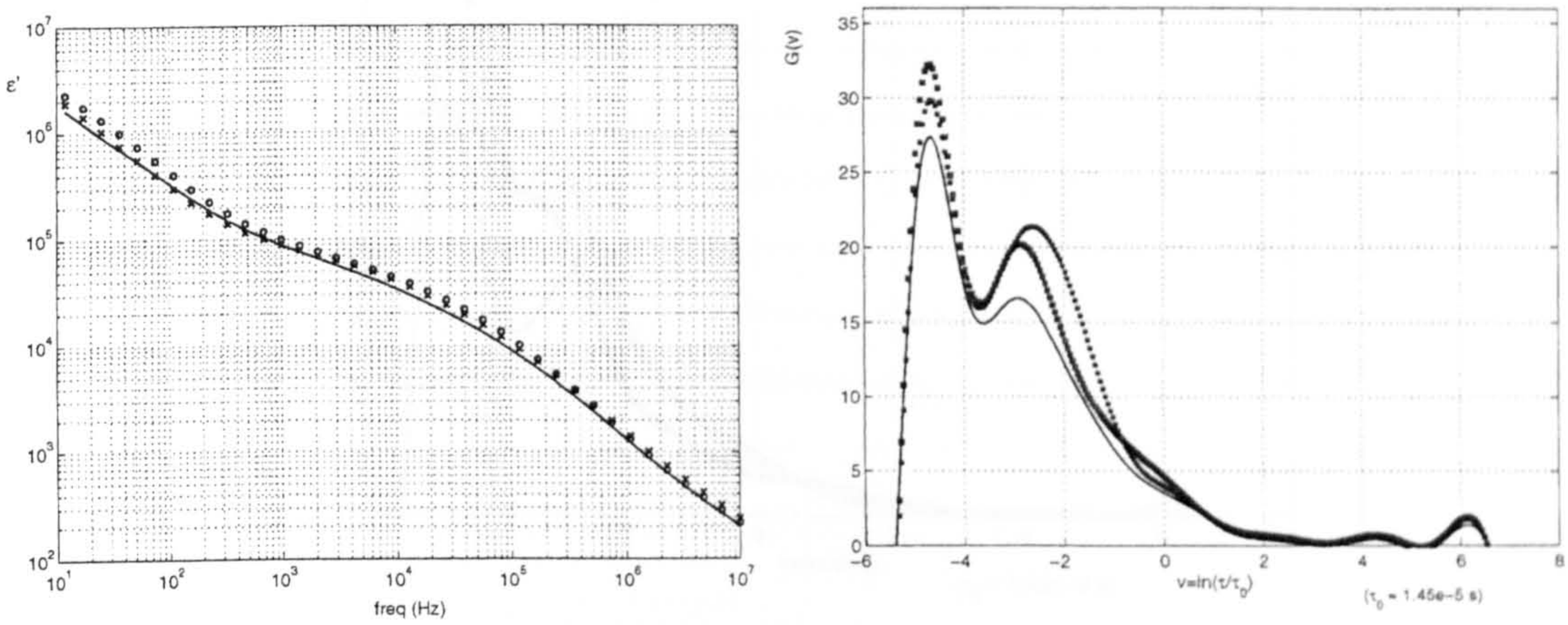

Figure 6.14: *Real part of permittivity and DRT distribution of three canine liver samples at 25 ^0C after 17 min of ischemia.*

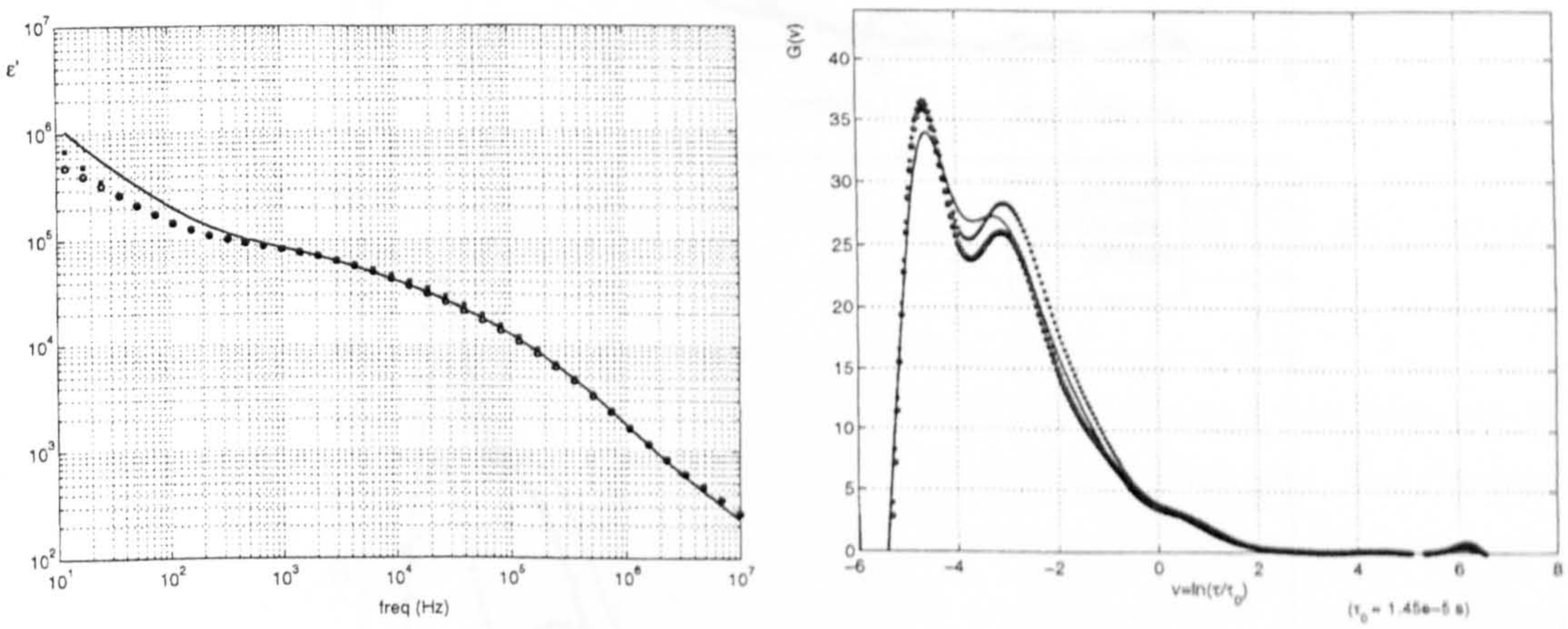

Figure 6.15: *Real part of permittivity and DRT distribution of three canine liver samples at 25 ^0C after 77 min of ischemia.*

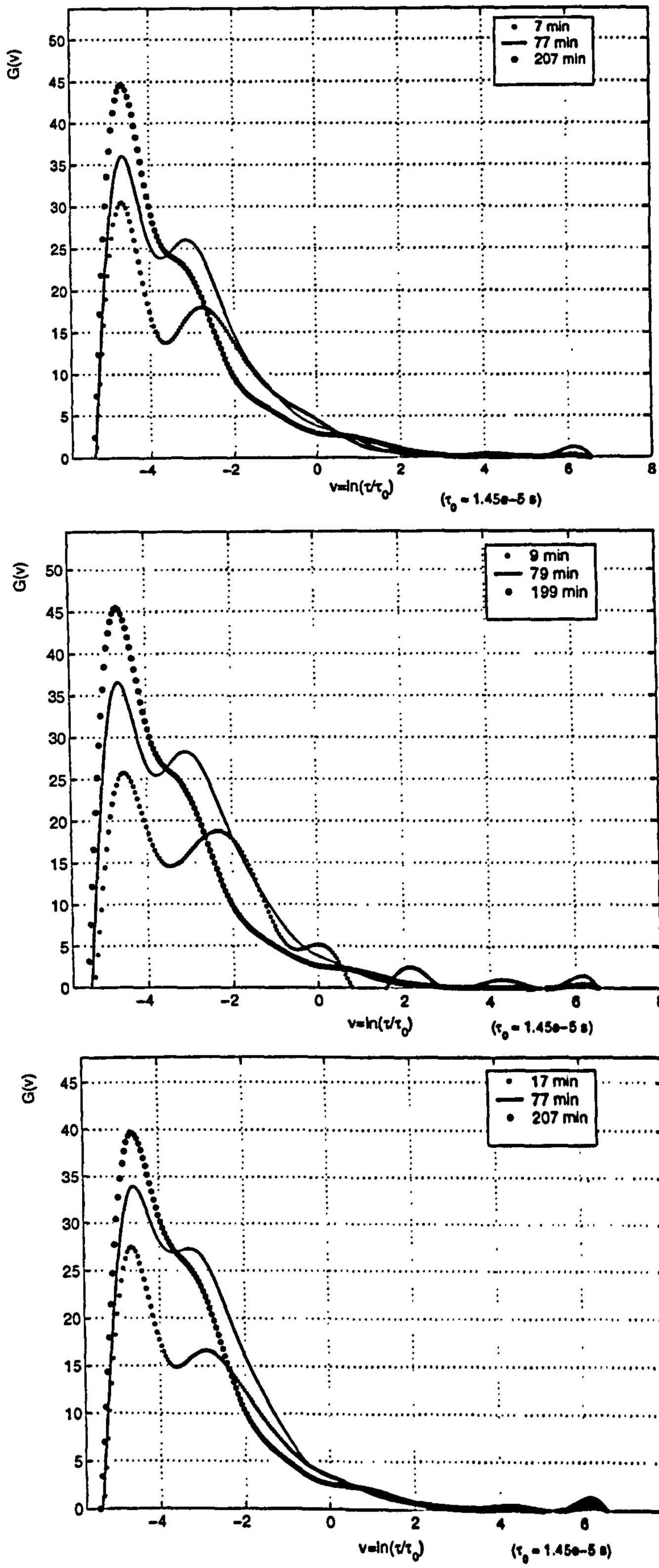

Figure 6.16: *Evolution of DRT for three canine livers at 25 ^0C.*

$v \simeq -3$ corresponding to 220 kHz ($\tau \simeq 0.72\ \mu s$) begin to decrease. The analysis of Figure 6.13 helps in understanding this behaviour. The distributions are reconstructed as delta–functions weighted according to the capacitance (Eqn. 6.9). According to the Figure 6.13 the permittivity ε' rises during the first 70 min. The changes in dispersion amplitudes follow ε' changes against time of ischemia, Fig. 6.17. They also follow the decrease in the conductivity σ that may be linked to the gap junction closure, [86]. The further decrease of both ε' and σ may be a result of this process continuing. It can be seen that the GRIM is capable not only of tracking changes in the permittivity and conductivity of the material but also in providing extra quantitative parameters.

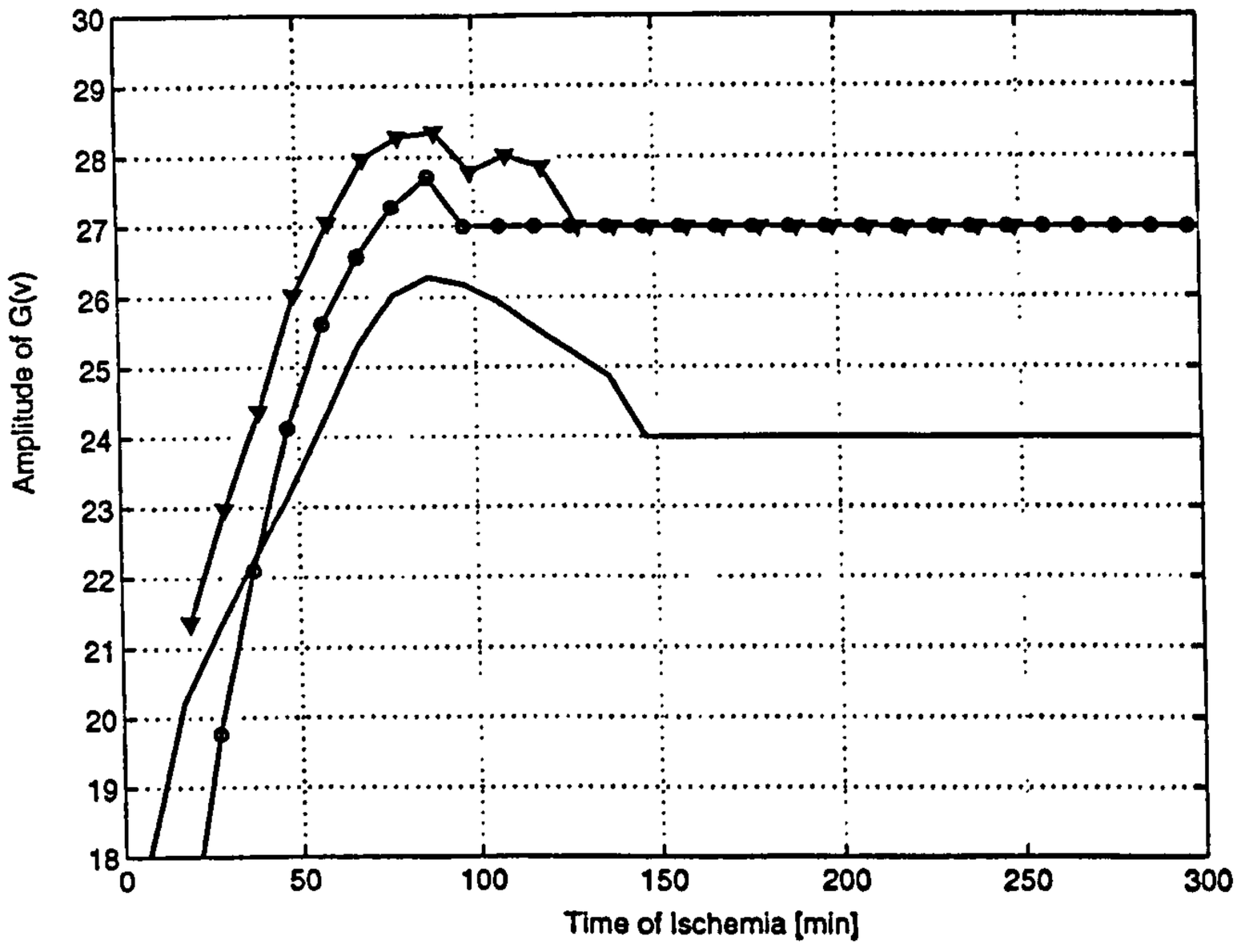

Figure 6.17: *The time evolution of the dispersion amplitude at 220 kHz for three canine livers at 25 ^0C.*

It has been found that the DRT distribution of porcine liver exhibits similar changes in the amplitude of the peak at $v \simeq -3$ (220 kHz). However, the decrease of the amplitude for porcine liver starts earlier than for canine liver incubated at the same temperature, after just 48 min. Such changes in the peak amplitude at 220 kHz (β–dispersion) coincides with the disappearance of the α–dispersion and, therefore, the gap junction closure. Although canine liver does not show a separate α–dispersion, the time course of the dispersion amplitude at 220 kHz could be an indicator for monitoring the gap junction closure.

Further analysis has been carried out for canine liver at 5 ^{0}C. Impedance spec-

tra are shown in Fig. 6.18. Again, as for canine liver at 25 ^{0}C, a great increase in resistance at low frequencies during ischemia time followed by a small decrease at high frequencies has been found.

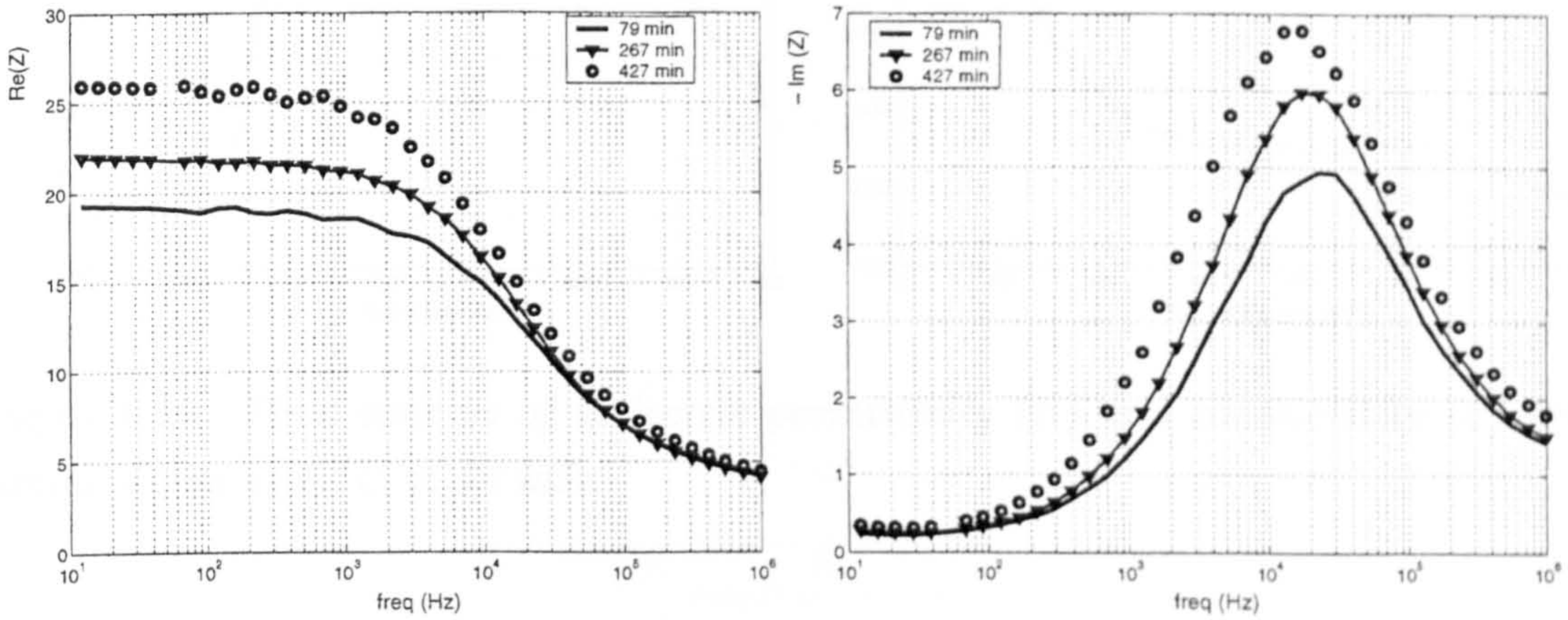

Figure 6.18: *Impedance spectra of ischemic canine liver at 5 ^0C.*

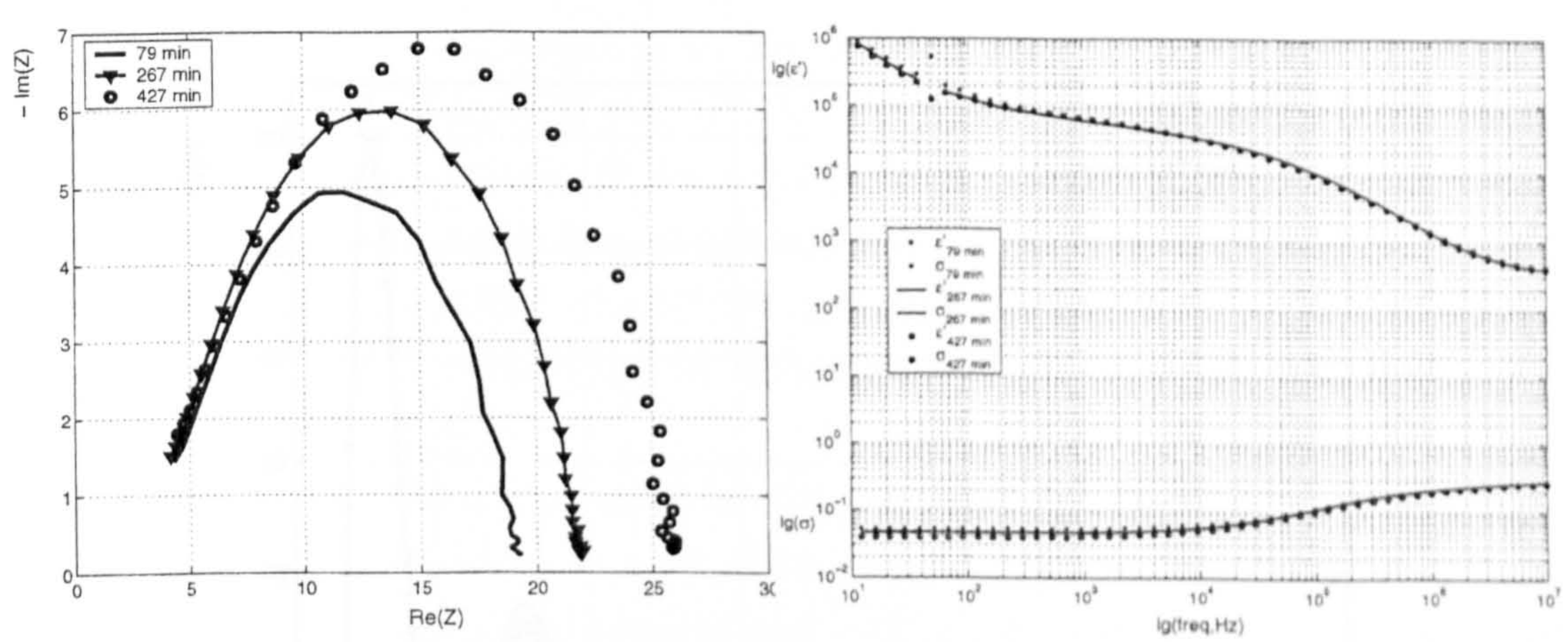

Figure 6.19: *Cole–Cole plots and real parts of permittivity for canine liver at 5 ^0C during ischemia respectively.*

Due to the slowing of metabolic processes at low temperatures, the decrease of the dielectric permittivity for liver at 5 ^{0}C starts only after 200 min of ischemia, 130 min later than the results obtained for 25 ^{0}C temperature conditions. This is illustrated in Fig. 6.20.

Canine liver at 5 ^{0}C has a similar behaviour in conductivity σ as liver at 25 ^{0}C. It decreases rapidly as the permittivity increases until a maximum at about 200 min. The evolution of DRT distributions shown in Fig. 6.21 exhibits the same

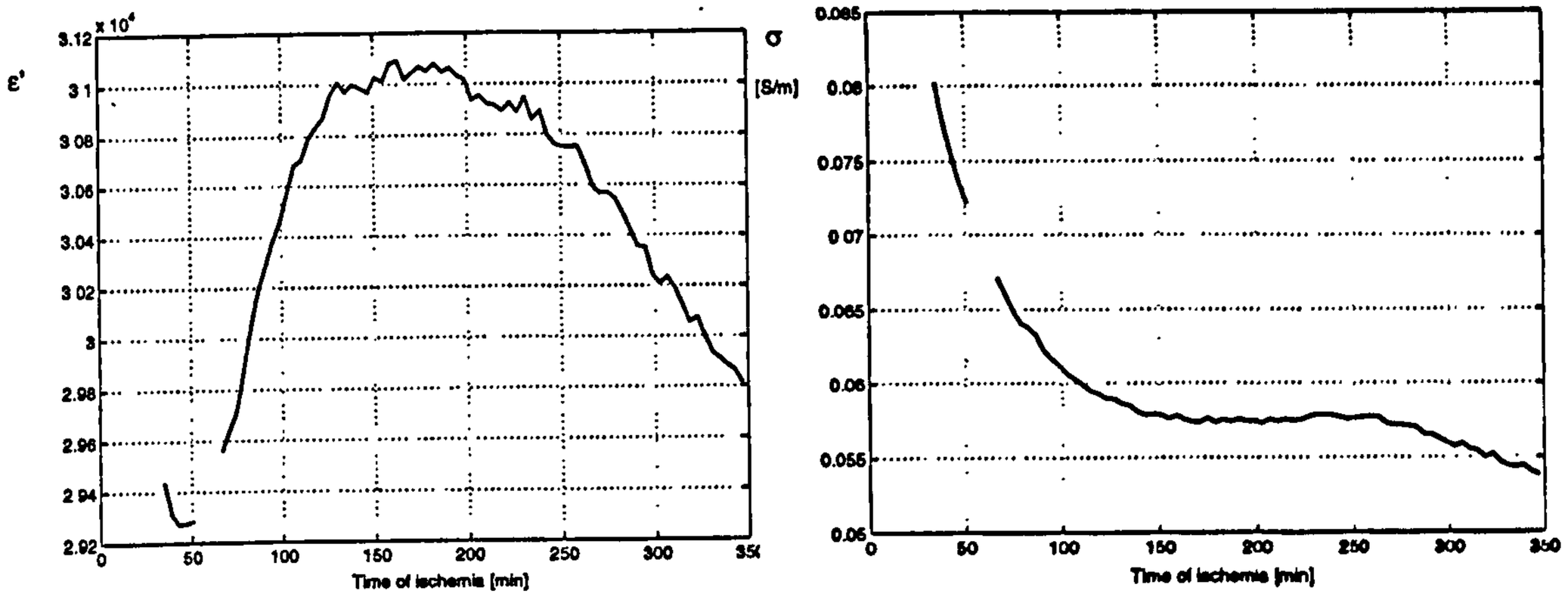

Figure 6.20: *Time courses of dielectric permittivity (ε') and conductivity (σ) for canine livers at 5 ^0C at 13 kHz.*

changes found for canine and porcine livers at 25 ^{0}C with only a difference in the specific time when the amplitude of the peak at $v \simeq -3$ ($\tau \simeq 0.72\ \mu s$) starts to decrease.

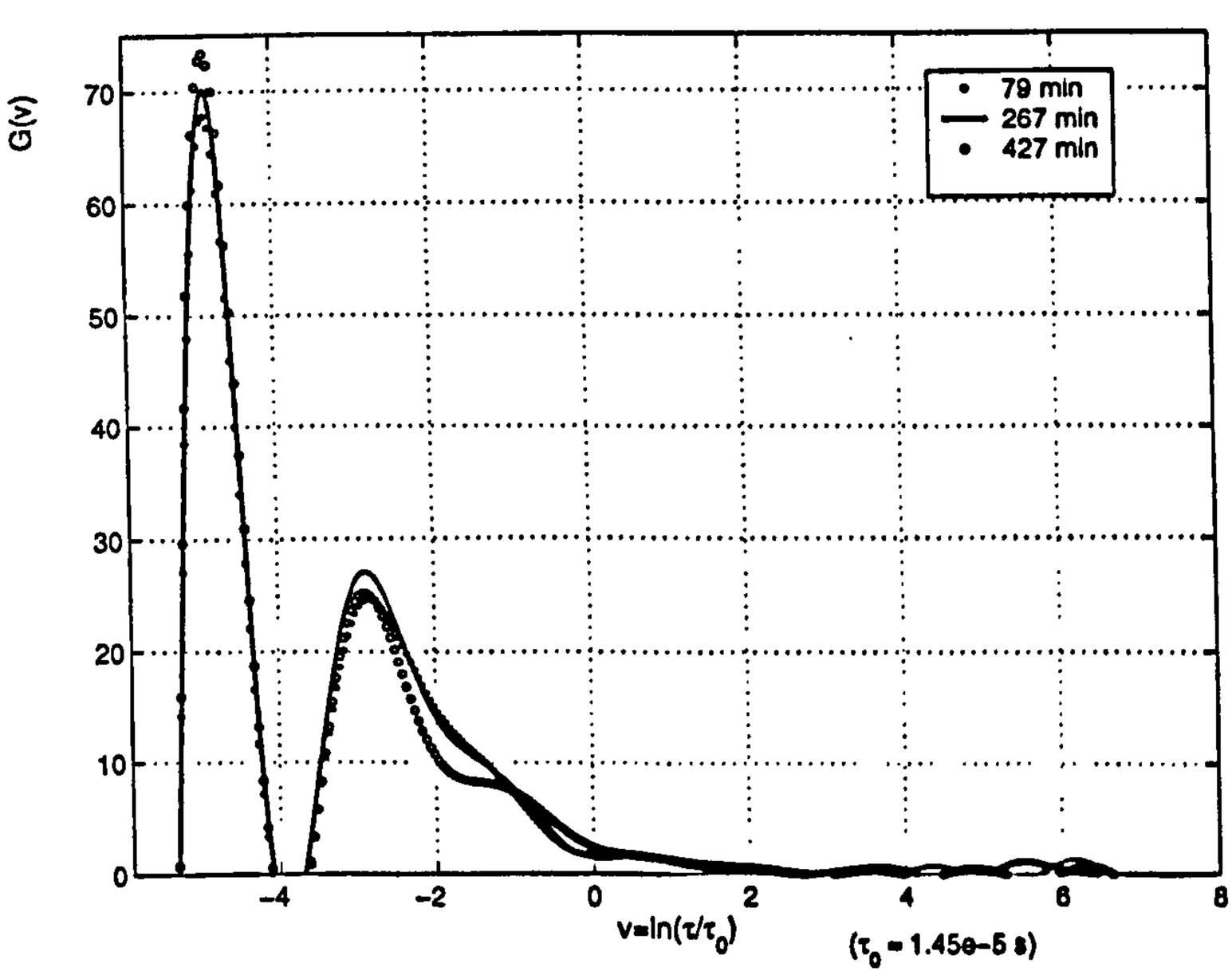

Figure 6.21: *Evolution of DRT for canine livers at* 5^0 *C.*

The DRT peak amplitude at $v \simeq -3$ decreases after about 200 min of ischemia when the permittivity decays. The time course of the dispersion amplitude is presented in Fig. 6.22. According to these results several relaxation processes take place during ischemia that can be described by time constants, their amplitudes

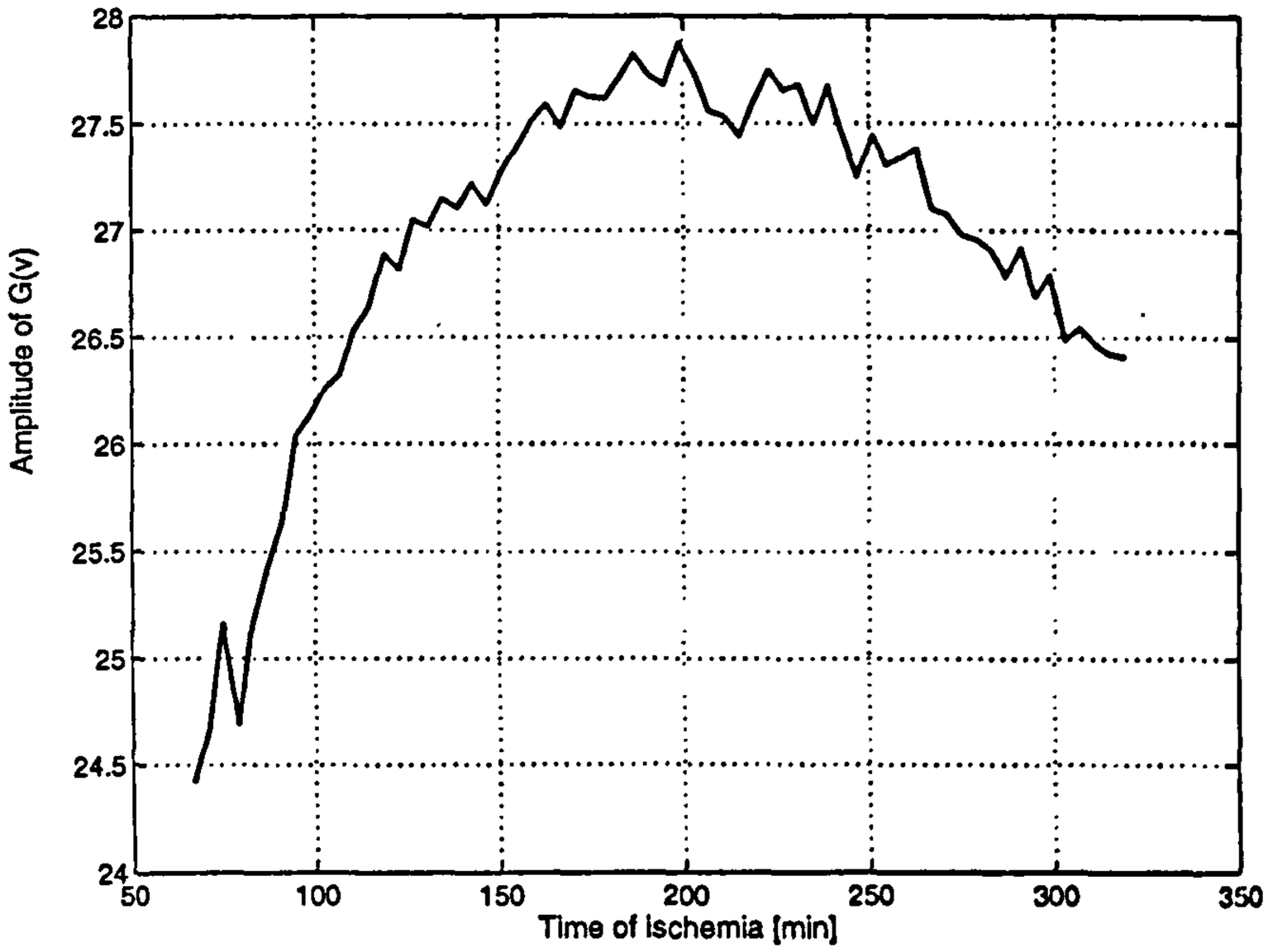

Figure 6.22: *The time evolution of the dispersion amplitude at 220 kHz ($v \simeq -3$) for canine livers at 5 ^0C.*

and peak areas. All these parameters are independent and their evolutions can be easily followed by means of the GRIM. They are directly linked to physical processes and tissue structure. If the α–dispersion is related to the gap junction closure then the decrease in the amplitude of the peak at $\tau \simeq 0.72\ \mu s$ is also related to this process. Thus, the GRIM may be a helpful tool for detecting important states of an organ affected by ischemia.

Applying conventional equivalent circuit methods, different curves or electrical models would be required to fit each data set collected during ischemia. Apart from a problem with non–uniqueness and difficulties with the interpretation of the derived parameters, such data analysis is also time consuming and clumsy . Usually single examples are reported. The breakthrough might be provided by using GRIM for the calculation of the evolution of relaxation spectra and their parameters leading to a common variables for data interpretation.

6.5 *In Vivo* studies

In the present study, the EIS technique has been used for measurements *in vivo*. The measurements were carried out on dog organs (liver, spleen, muscle and kidney) and pig liver. Data were obtained from the open chest of anaesthetised animals during surgical operation. The tissue impedance was measured with the

equipment described in 6.4.2 consisting of a Solartron 1260 device and a preamplifier. Wires of length 40 cm were introduced between the preamplifier and probe. The measurements covered the frequency range from 0.1 Hz to 10 MHz. Below 1 kHz, increasing measurement errors in the complex dielectric permittivity occur due to electrode polarisation and limited phase angle measurement accuracy. So, the data have been analysed in the frequency range from 1 kHz to 10 MHz which covers 4 decades. According to the sampling theorems (see 3.4.3), the DRT distribution can be found over 2.6 decades. In this frequency range only the β–dispersion takes place. However, it is anticipated that the shape of the reconstructed distribution consists of superimposed α– and β–dispersions.

An important point for EIS application is to determine the comparison criteria that can be used for tissue identification as well as for tissue characterisation. Figures 6.23 and 6.24 show dielectric and conductivity spectra of canine organs respectively. The dielectric permittivity ε' curves are smoothed by the continuous distributions of relaxation times. The GRIM makes it possible to identify these distributions for each type of tissue. To achieve this, the static conductance, the static permittivity and the permittivity at very high frequencies have been estimated from the data by extrapolation. Figure 6.25 illustrates the calculated DRT distributions corresponding to canine organs.

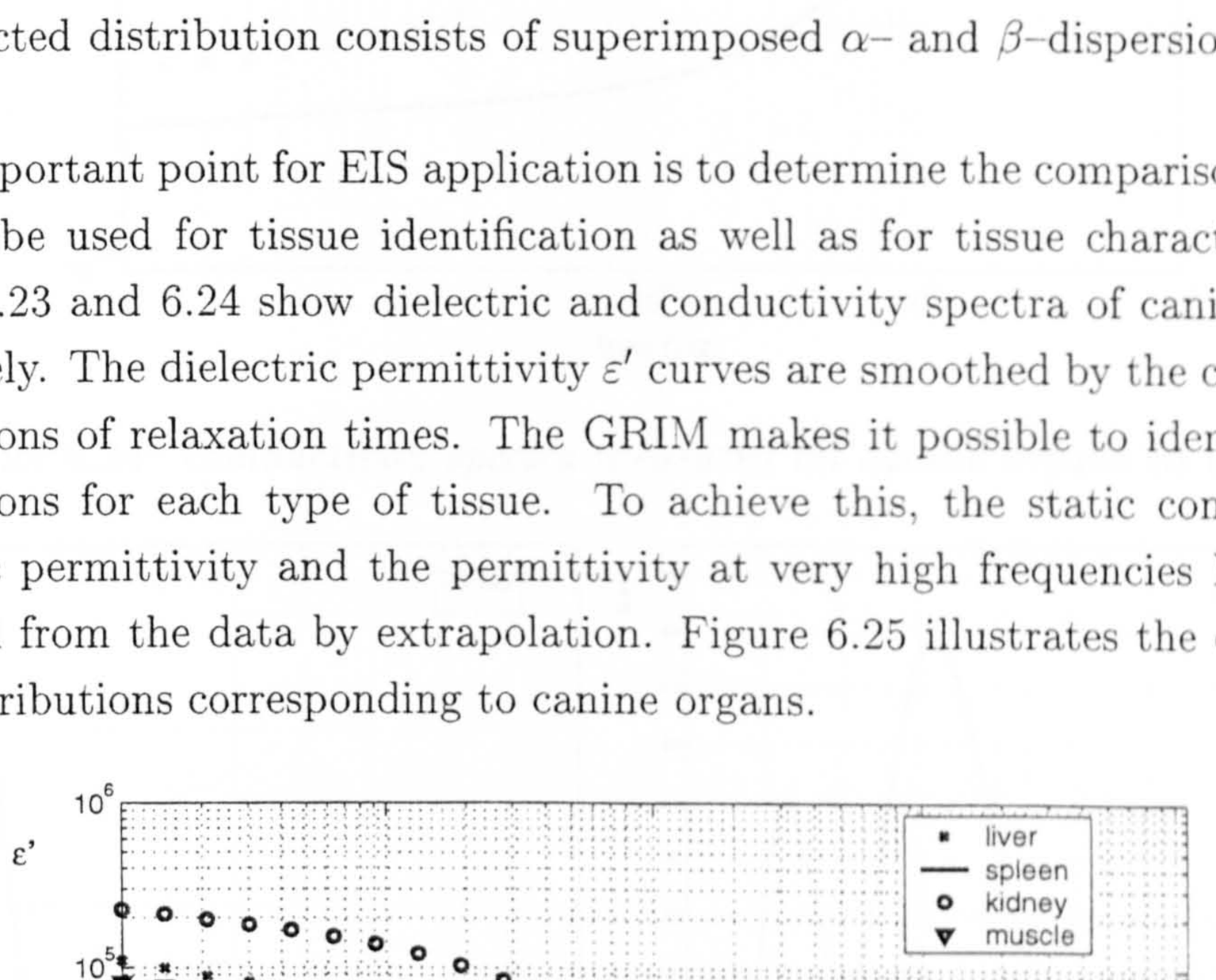

Figure 6.23: *Dielectric permittivity spectra measured on canine organs in vivo.*

Several peaks can be distinguished in each DRT distribution. Comparison between relaxation spectra indicates the differences in relaxation processes that

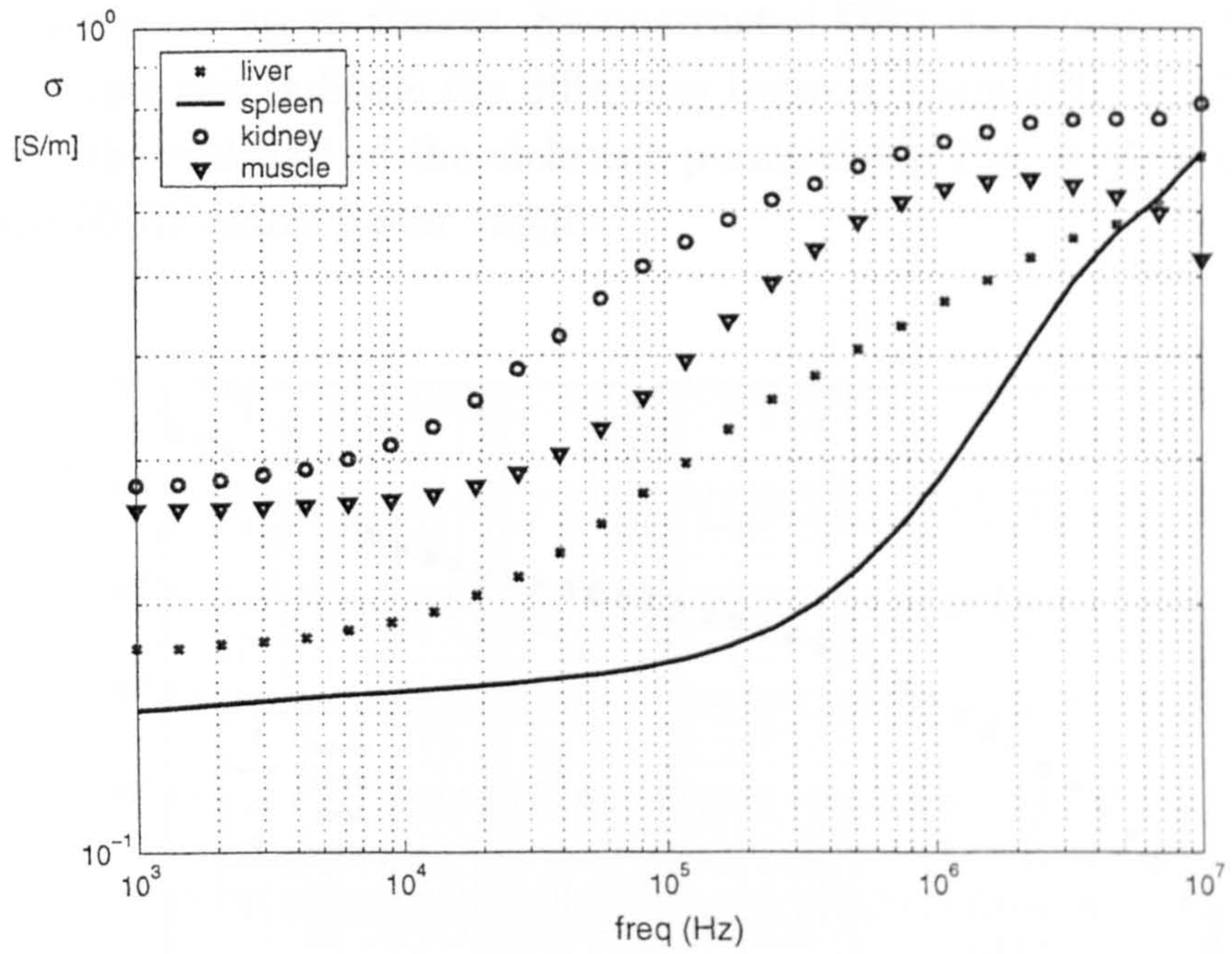

Figure 6.24: *Conductivity spectra measured on canine organs in vivo.*

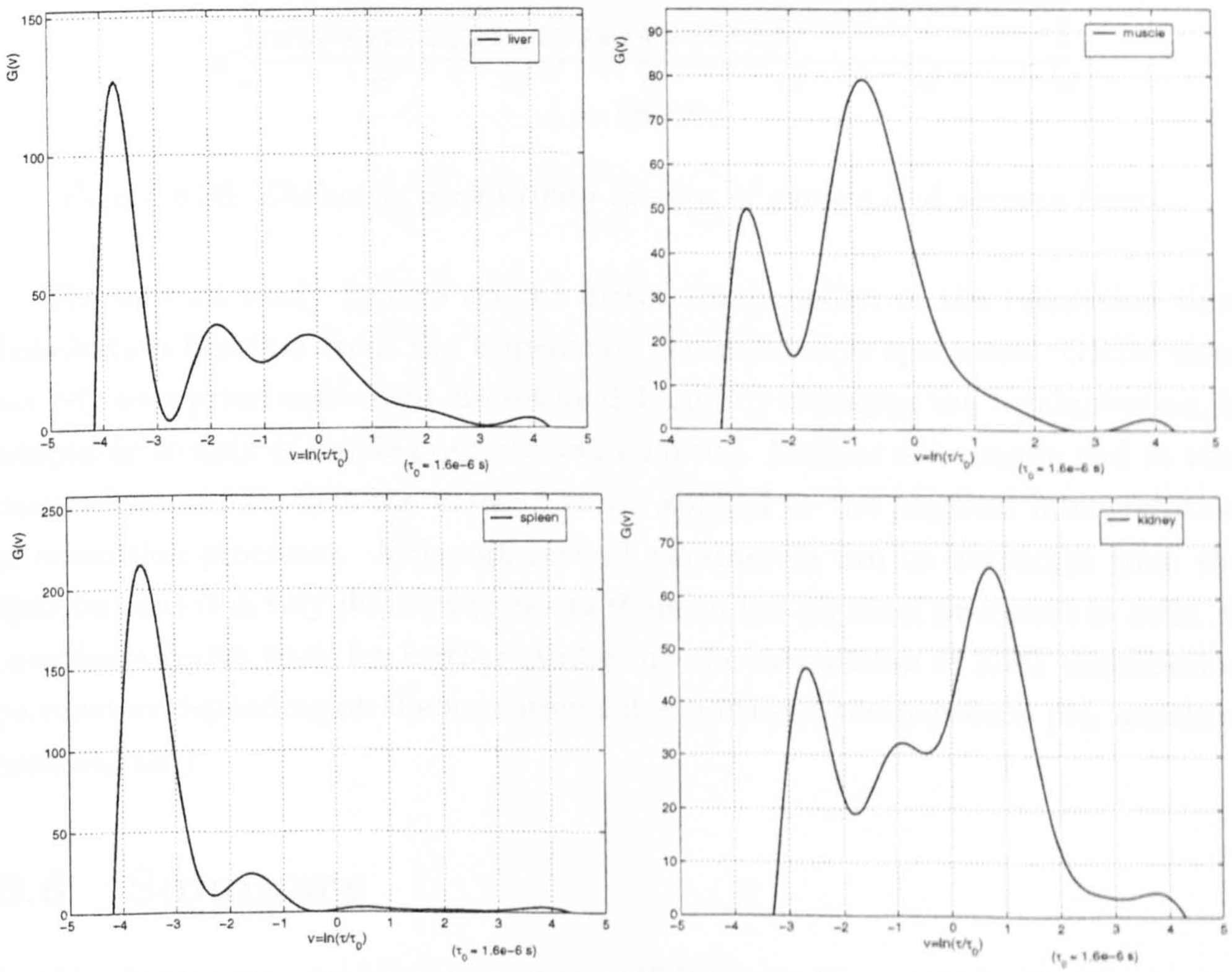

Figure 6.25: *DRT distributions for different types of canine tissue (measurements in vivo).*

take place in canine organ tissues. Reconstructed DRT distributions for porcine and canine livers also indicate the difference between them (Fig. 6.27). A small distortion in the real part of the dielectric permittivity, Fig. 6.26, is due to pick up from the 50 Hz mains power supply.

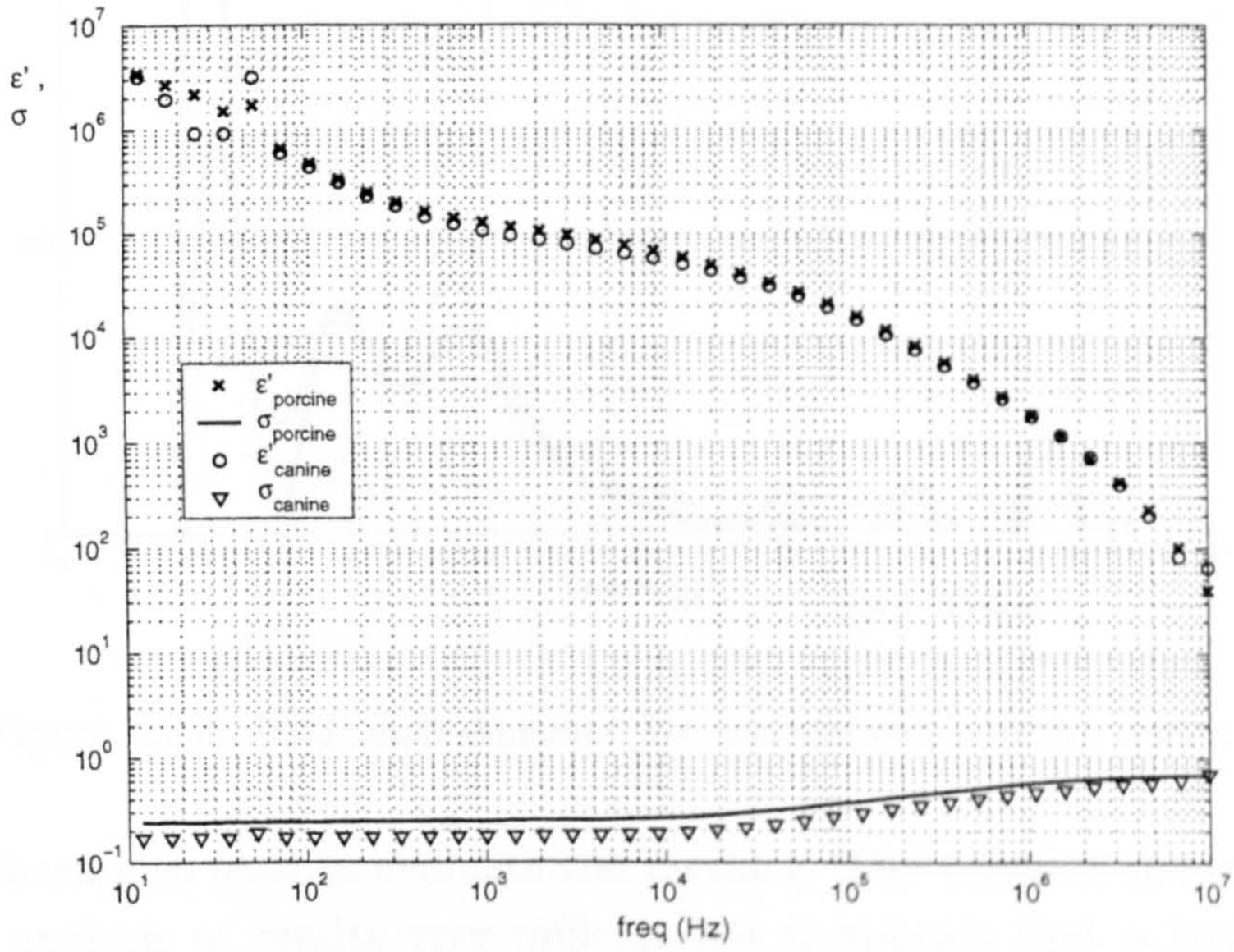

Figure 6.26: *Dielectric permittivity spectra of canine and porcine livers.*

The current study focuses on the direct computation of the relaxation time distribution function from the impedance (permittivity) spectrum. GRIM does not rely on a priori equivalent circuit model and, by changing the regularisation, is adaptable to data of varying quality and quantity. Studies of ischemic and *in vivo* tissues have shown that the method ca be applied to the physical interpretation of relaxation processes. Although several parameters can be extracted from the distributions it is very difficult to relate them to the physical processes in cells. It provides a frame work for further studies on the acquisition of DRT distribution parameters depending on the measurement conditions (temperature, pH, moisture content, *etc.*).

6.6 Summary

In this chapter some applications of the GRIM have been presented. Firstly, the method has been tested with simulated, noiseless data and the results have been displayed. A good agreement between the initial parameters and the derived time constants has been shown. Biological data, measured *in vivo* and on ischemic tis-

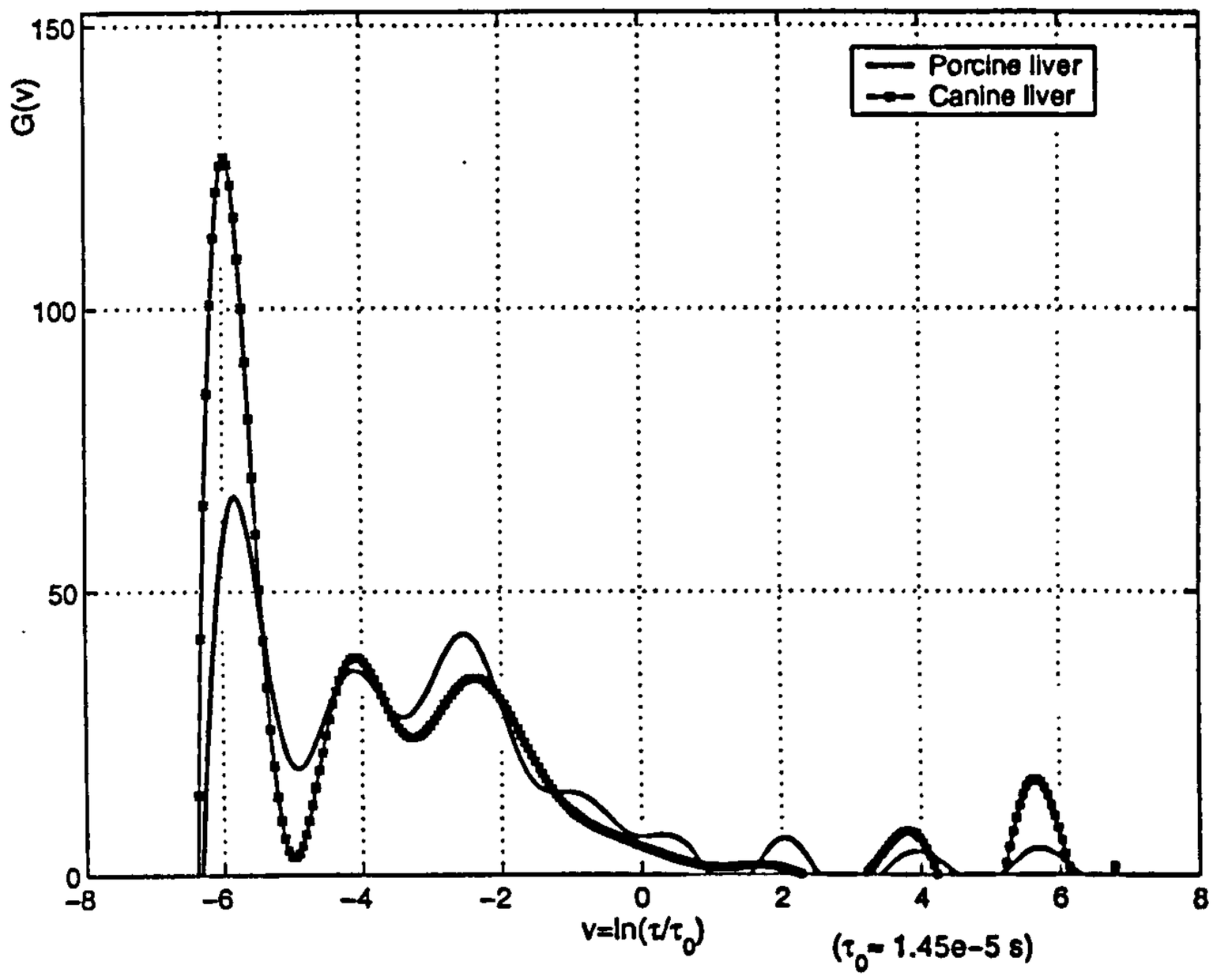

Figure 6.27: *DRT distributions for canine and porcine livers.*

sues, have been also used to evaluate the method. The complex tissue structure makes the analysis of results very difficult but it appears that a large number of independent parameters can be obtained using the GRIM. A comparison has been made between the DRT distribution of different types of canine tissues and between DRT distributions of canine and porcine livers. The chapter has also presented studies of ischemic tissues and analysis of obtained results. A distinction can be seen between DRT distribution of living liver (canine and porcine) and excised liver. The results are very exciting and show a method with so much resolving potential that it is obviously just the beginning of a whole set of experiments.

Chapter 7

Conclusions

7.1 Introduction

This chapter summarises the work carried out in the preparation of the thesis, discusses some of the thesis topics and outlines the future work necessary to continue the development of EIS.

7.2 Aim of Research

The original aim of the research was to develop EIS as a noninvasive technique for biological tissue characterisation to distinguish pathological conditions. The EIS method has been considerably improved through the development of GRIM although it has not been possible to carry out full clinical trials in the timescale available for the research. The work reported in this thesis can be divided into two main parts:

1. Development of a fast and more informative procedure for data analysis.

2. Development of instrumentation and design of experiments with their execution.

7.3 Summary of major Achievements

7.3.1 Data Analysis

In this work, different approaches for tissue characterisation have been studied and their disadvantages have been explored in the corresponding chapters. Many authors still try to model electrical measurements made on tissue using simple electrical circuits with paths for extra– and intra–cellular conduction. In many

cases the impedance of circuit elements have been calculated from Cole plots. This strategy has many problems including the non–uniqueness of circuit models and difficulties with the interpretation of non–physical lumped–constant elements as shown in chapter 2.

When aiming to derive physiological information about tissue cells, the microscopic electrical properties of tissue such as conductivity and permittivity need to be considered. The relationship between these parameters as well as relaxation phenomena occurring inside tissue when an electrical field is applied, have been described in chapter 2. Understanding the mechanisms leading to the permittivity spectra is of prime importance. It was understood that dispersions were caused by distributions of dielectric relaxation time constants. It has been shown that these distributions may be directly related to cell characteristics (size, shape, *etc.*), establishing a link between physiological and electrical properties of living tissue. During this research a number of different analytical methods for the calculation of dielectric relaxation time spectra directly from frequency response data have been investigated in chapter 3. It has been concluded that they suffer several disadvantages that make them inappropriate for practical applications.

In chapter 4 a novel mathematical method known as GRIM was described which calculates the dielectric relaxation time distribution. The computation of DRT distribution from permittivity spectra is notoriously difficult due to the ill–posedness of the inverse problem. In this chapter, a concise review on the theory of inverse and ill–posed problems was given. The underlying algorithm of the GRIM is based on standard mathematical techniques. A numerical solution of the integral equations 4.2 has been shown in detail. The quantitative procedure provides information about time constants, their distribution and their amplitudes. Also the reconstructed distribution carries additional information about the area enclosed under each peak which is proportional to capacitance. The relaxation spectrum can be derived from the real or imaginary parts of conductivity (permittivity) and for perfect data will be the same in both cases. Therefore, the problem of DRT reconstruction is technically over–determined. The GRIM is flexible and a range of regularisation schemes may be used. The Tikhonov regularisation technique has been introduced and successfully applied using SVD. It was found that, by comparison with the extremely ill–posed EIT problem, the calculation of DRT distributions is much better conditioned. The proposed method allows the data to be checked for consistency. Furthermore, the method provides estimates of the singular functions and values which theory shows to be strictly conservative. The GRIM has been examined for its robustness to random noise.

Also the method is adaptable, via regularisation, to the noise spectra of particular instruments and experimental protocols. The optimal Tikhonov parameter and number of basis functions were established for considered data sets.

As a conclusion of the proposed method, the following can be said. The developed algorithm for the computation of the DRT distribution has a number of advantages over the conventional methods used so far:

- It eliminates the discrete circuit model completely and, thus, avoid hazards of ambiguities and non–physical lumped–constant elements.
- Unlike methods based on fitting semi–circles or other standard response curves to the permittivity spectrum, the number of independent parameters imaged by this method is limited only by the quality and quantity of the electrical measurements.
- The choice of a regularisation technique can be matched to the characteristics of the noise and to the parameters of interest.
- The proposed method was shown to be stable to random noise unlike existing analytical solutions and some other published numerical calculations, [50], [87], [88] that have been found sensitive to noise and even for noiseless data have limited resolution.
- It has been found that the GRIM works very well with simulated data and also with biological data as demonstrated in chapter 6.
- The application to real data measured on ischemic tissue showed that the GRIM is a useful tool for distinguishing pathological conditions.

Finally, the GRIM has been programmed in MatLab. The list of MatLab programs and source code are included in Appendix A. The procedure for computing DRT distribution, described in section 4.10, is found to be fast as many of the parameters and functions can be pre–calculated.

Although this method was tested with simulated data and real measurements made on biological tissues, it does not mean that it can only be used in this context. The GRIM is fully applicable in many other situations, for instance, for characterisation of electrochemical systems. From a methodological point of view the proposed method is not restricted to be used in EIS inverse problem but can be applied in many other relaxation spectra inverse problems, *e.g.* inverse problems in rheology.

7.3.2 Instrumentation Development

Along with the development of a new method for data analysis, two systems for EIS measurements have been considered: a bespoke EIS system and a system based around a commercial device.

This PhD project started with an experimental two channel multi-frequency EIS system operated at four frequencies. It provided four measuring points allowing the conventional method (Cole model) to be applied. However, it became clear that for tissue characterisation at cell level, impedance spectroscopy has to be performed over a very wide frequency range. Section 5.4 explored the possibilities for building a bespoke EIS system. Its data acquisition hardware was designed incorporating two current sources: one adopted from the existing EIS system and the other an operational transconductance amplifier. The components of the current source from the existing system were also replaced with components which showed better characteristics (section 5.4.4). In order to maximise the system accuracy, a calibration resistor was implemented on the board eliminating the need for the separate calibration. The hardware design of the EIS system was extended to include measurements of current and voltage on the current driving electrode. Easy–to–use data acquisition software was written in Delphi. Its operational sequence is described in section 5.4.5 and its graphical panels are shown in Appendix B.

The second approach was to use a commercially available HP Impedance Analyser (section 5.5). Further development of the GRIM demands an instrument able to measure complex impedance in a frequency range of several decades. And so, the HP4192A impedance analyser was adapted for spectroscopic data acquisition. The data acquisition software was created in LabView and its front panel is shown in Fig. 5.9. The measurements *in vitro* and *in vivo* were carried out using this device and DRT distributions were reconstructed (chapter 6). Ischemic data were also acquired using a Solartron 1260 device.

The Impedance Analyser based system was used to test the method because of its accuracy and broad frequency range. However, the system is too slow, expensive and bulky for routine use where a bespoke system can be designed around these problems and with the added ease of electrical isolation for clinical studies. The pros and cons were discussed in chapter 5 and table 7.1 summarises the main differences of two EIS systems implemented during this project.

Table 7.1: Comparison of EIS systems implemented during PhD project.

Bespoke system	Impedance Analyser
from 2.5 kHz to 2.5 MHz	from 5 Hz to 13 MHz
accurate	very high accuracy
fast	relatively low speed
isolated	non–isolated
compact, portable, external power supply	large, heavy
easy–to–use software	easy–to–use software
limited number of sampling points	sampling with a step of 5 Hz
relatively cheap	expensive
probe can be connected directly	requires measurement interface

7.3.3 Reconstructed Distributions

In chapter 6 the GRIM was successfully implemented and the relaxation time distributions were reconstructed from simulated and biological data. Simulations were performed with different resistor–capacitor electrical circuits. It has to be stressed that these electrical circuits were used only for simulations of frequency responses and not for interpretation of tissue structure. Obtained results demonstrated a good agreement with chosen parameters. The method measures as many meaningful parameters as the data can yield. It identifies the number and the configuration of lumped–constant elements for a ladder network. From the results it can be concluded that the GRIM can be used for characterisation of a complex system without any prior assumptions about its internal structure.

The EIS technique combining a developed method and instrumentation was applied to biological material. Measurements were carried out mainly on ischemic tissue. The impedance data were used to directly calculate relaxation spectra (section 6.4). It was postulated that variations of DRT parameters (time constants, their amplitudes and areas under each peak) were linked to physical changes during ischemia. It was found that due to systematic measurement errors the GRIM has to be done on longitudinal data. However, the DRT curves for different species measured at the same ischemia time group together, Fig. 6.14 and 6.15. It means that cross sectional analysis is possible but requires further resolution improvement.

Furthermore, the distribution of relaxation time constants was reconstructed from impedance data collected *in vivo*. Differences in shape and parameters (time

constants, their amplitudes, areas) were found. Comparison was made between relaxation spectra for different living organs as well as for the same type of organ for different species. It can be concluded that the GRIM is capable of separating not only different classes of tissue but also may characterise tissue itself. However, further experiments are required as discussed in the next section.

7.4 Discussion and Future Work

Future work can improve this project, some of which is described below.

7.4.1 Resolution of the Method

The resolving power of the GRIM was defined in section 4.8. Further improvement is required. When the data contain only discrete time constants, the calculated DRT spectra have broad peaks due to noise and frequency limitations in the data. If neighbouring time constants are too close to each other, the corresponding peaks overlap. One of the ways to separate peaks is to fit Gaussian distributions. After this, the characteristic parameters - time constant, amplitude and area - can be found. However, the fitting procedure is not very accurate. Also the contribution of the side–lobes of one peak to the size of another peak will result in significant errors. The present solution to this problem is to use more basis functions than it is needed, to calculate data vector at all sampling points and to apply Tikhonov regularisation. Further improvement of resolving power will provide the possibility for cross sectional analysis between different organs of the same type. It is very important for ischemia studies as it will define the characteristic criteria for each organ state.

7.4.2 Commercial Instrument

The adoption of HP4192A impedance analyser was to enable biological tissue to be characterised by means of the reconstructed DRT distributions. The impedance amplitude and phase were measured over a wide frequency range with a high accuracy defined by the characteristics of the analyser. The experiments were mainly carried out *in vitro*. In order to use the impedance analyser *in vivo* some further work on the isolation is required. The instrument needs to be fully isolated from the mains supply. A possible solution is to use isolation transformers and a laptop computer operated from a battery.

The measurement interface needs to be introduced between the measurement probe and the impedance analyser in order to reduce the measurement errors

causes by probe leads. Some possible solutions were discussed in section 5.5.1.

Some work is also necessary to produce a "hospital friendly" system that is robust, transportable, unintimidating to the patient and simple to operate and interpret for the hospital staff.

7.4.3 Design of EIS systems

The use of a bespoke system for clinical purposes has two important advantages over commercial device. Firstly, the speed of data acquisition is high and further improvements can enable measurements at a real–time frame rate. The second important feature of the system is isolation.

However, as an experimental system it has two main disadvantages: a limited and invariable frequency range and a limited number of sampling points. To solve this problem, a DDS Synthesiser, introduced in section 5.4.6, was suggested.

Further work has to be done on current sources with high output impedance and a wide bandwidth. The present design includes current measurement and so impedance can be measured accurately even though the output impedance of the current source is lower than required by specification of the EIS system (section 5.4.1).

7.4.4 Interpretation of Results and Clinical Studies

Studies of ischemic tissue were carried out and evolutions of DRT distributions were displayed in chapter 6. However, the full data interpretation can be done only after experiments with different tissue conditions (temperature, pH, perfusing solution, *etc.*). Then recording the differences in DRT distributions during the variations of a single condition parameter will help to understand the physiology of the observed relaxation processes.

More experiments are required *in vivo* in order to determine the characteristic parameters for different types of living tissue.

For the system to be useful in a medical environment, it is necessary to make all the mentioned improvements and to carry out experiments to determine whether medical conditions can be accurately assessed. It would be very useful if simple mathematical models of cellular tissue could be built to identify the effect of block

characteristics (cell size, shape, extra- to intra–cellular volume ratio, *etc.*) on the electrical response between the $\alpha-$ and β–dispersions.

7.5 Summary

The aim of this research work was to develop an EIS technique for tissue characterisation to discern pathology. Progress has been made towards understanding permittivity spectra and linking dielectric relaxation time constants to specific physiological processes and tissue structures. An EIS system suitable for *in vivo* experiments was developed. Of the above future work, the completion of the system, the resolution improvement and further experiments on biological tissues including normal and pathological are the next logical steps.

As a whole, the research work presented in this thesis has made some contribution to the development of EIS. It can be concluded that the EIS technique is a promising tool for clinical applications and may be a complement to existing medical methods.

Bibliography

[1] J. M. Fildes, P. Chen, X. Zhan, Application of Electrochemical Impedance Spectroscopy, Color Visible Imaging, and Infrared Imaging For Non-Destructive Evaluation of Anti-Corrosion Coatings, Sensors Expo Conference, Boston, MA May 16-18, 1995.

[2] R. J. Lytle, R. M. Bevensee and D. L. Lager, Three–dimensional subsurface delineation via a novel method for determining the subsurface electrical profile, UCRL-21685 Lawrence Livermore Lab., Livermore, CA, 1974.

[3] H. Griffiths, Tissue spectroscopy with electrical impedance tomography: computer simulation, IEEE Trans. Biomed. Eng., 42, pp 948-954, 1995.

[4] H. Griffiths and J. Jossinet, Bioelectrical spectroscopy from multi-frequency EIT, Physiol. Meas., 15, A59-A63, 1994.

[5] K. S. Cole, Permeability and impermeability of cell membranes for ions, Cold Spring Harbor Symposium, Quant. Biol., 8, pp 110-122, 1940.

[6] B. Blad, P. Wendle, M. Jönsson and K. Lindström, An Electrical Impedance Index to Distinguish Between Normal and Cancerous Tissues, X International Conference on Electrical Bio-Impedance, Barcelona 1998, pp 51-54.

[7] E. Gersing, Monitoring Temperature Induced Changes in Tissue During Hyperthermia by Impedance Methods, X International Conference on Electrical Bio-Impedance, Barcelona 1998, pp 37-40.

[8] J. Jossinet and M. Schmitt, Alternative Parameters for the Characterisation of Breast Tissue, X International Conference on Electrical Bio-Impedance, Barcelona 1998, pp 45-48.

[9] R. Hober, Eine methode, die elektrische Leitfahigkeit im Innern von Zellen zu messen, Arch. Ges. Physiol., Vol. 133, pp 237-259, 1910.

[10] M. Philippson, Les lois de la resistance electrique des tissus vivants, Bull. Acad. R. Belgique Clinic. Sci., Vol. 7, pp 387-403, 1921.

[11] Lapicque, Rescherches quatitatives sur I'exitation electrique des nerf traitee comme une polarisation, J. Physiol. Pathol. Gen., Vol. 9, pp 620-635, 1907.

[12] H. Fricke and S. Morse, The elctric resistance and capacity of blood for frequencies between 800 and 4 1/2 million cycles, J. Gen. Physiol., Vol.9, pp 153-167, 1925.

[13] K. S. Cole, Electric phase angle of cell membranes, J. Gen. physiol., Vol. 15, pp 641-649, 1932.

[14] K. R. Foster and H. P. Schwan, Dielectrical properties of tissues and biological materials, A critical review, Crit. Rev. Biomed. Eng., 17, pp25-104, 1989.

[15] E. T. McAdams and J. Jossinet, Tissue impedance: An historical overview, Physiol.Meas.,16(suppl. 3A), A1-A13, 1995.

[16] C. Gabriel, S. Gabriel and E. Corthout, The dielectrical properties of biological tissues: I. Literature survey, Phys.Med.Biol., Vol. 41, 1996.

[17] S. Gabriel, R. W. Lau and C. Gabriel, The dielectrical properties of biological tissues: II. Measurements in the frequency range 10 Hz to 20 GHz, Phys.Med.Biol., Vol. 41,1996.

[18] S. Gabriel, R. W. Lau and C. Gabriel, The dielectrical properties of biological tissues: III. Parametric models for the dielectric spectrum of tissues, Phys.Med.Biol., Vol. 41, 1996.

[19] D. Murphy, The Oxford Polytechnic Adaptive Current Tomograph, Department of computing and mathematical sciences, research report N 14, Oxford Polytechnic, 1988.

[20] Q. S. Zhu, Presicion electrical impedance tomography instrumentation, PhD thesis, Oxford Brookes University, 1992.

[21] K. S. Paulson, M. K. Pidcock and C. N. McLeod, An impedance measurement probe for live tissue, Innov. Tech. Biol. Med., 16(6), pp 752-757, 1995.

[22] K. S. Paulson, S. Jouravleva, C. N. McLeod, Dielectric Relaxation Time Spectroscopy, IEEE Trans. Biomed. Eng., 11, 2000.

[23] S. Jouravleva, C. N. McLeod, K. S. Paulson, A distribution of dielectric relaxation times as a new tool for characterising the biological features of tissue, Proceedings of the EMBE conference, Vol.37, suppl.2, 1999.

[24] S. Jouravleva, M. Schäfer, C. N. McLeod, K. S. Paulson, Dielectric relaxation time distributions in ischemic canine liver tissue, Proc. of XI ICEBI, Oslo, 2001.

[25] A. K. Jonscher, Dielectric relaxation in solids, J.Phys.D.: Appl. Phys., 32, pp R57-70, 1999.

[26] B. H. Cornish, B. J. Thomas, L. C. Ward, Improved prediction of extra–cellular and total body water using impedance loci generated by multiple frequency bio–electrical impedance analysis, Phys. Med. Biol., 38, pp 337-46, 1993.

[27] H. P. Schwan, Electrical properties of tissues and cell suspensions, Adv. Biol. Med. Phys., 5, 147-209, 1957.

[28] J. R. Bourne, Crit. Rev. Biomed. Eng., vol 24, N 4-6, 1996.

[29] J. C. Maxwell, A treatise on electricity and magnetism, 2nd ed., Oxford: Clarendon Press, 1881.

[30] P. Debye, Polar Molecules, New York: The chemical catalog, 1929.

[31] H. Fricke, The theory of electrolytic polarization, Phil. Mag., pp 310-318, 1932.

[32] J. R. Macdonald, Impedance Spectroscopy, John Wiley and Sons, 1987.

[33] K. S. Cole and R. H. Cole, Dispersion and absorption in dielectrics. I. Alternating current chracteristics. J. Chem. Phys., 9, pp 341-351, 1941.

[34] L. A. Dissado and R. W. Hill, Constant–phase–angle and power–law regimcs in the frequency response of a general determinate fractal circuit, Phys. Rev. B, 37(7), pp 3434-3439, 1988.

[35] D. N. Smith, Tissue impedivity and electro–mathematical modelling of bioimpedances, Innov. Tech. Biol. Med., 16(6), pp 694-702, 1995.

[36] W. D. Hurt, Multiterm Debye dispersion relations for permittivity of muscle, IEEE Trans. Biomed. Eng., 32, 60-4, 1985.

[37] Brown B. H., Barber D. C., Lethard A. D., Lu L., Wang W., Smallwood R. H. and Wilson A. J., High frequency EIT data collection and parametric imaging, Proc. CAIT Meeting on Hardware for Multifrequency EIT (Toulouse, 1994), Innov. Tech. Biol. Med., 15, pp 1-8.

[38] B. Rigaud, L. Hamzaoui, M. R. Frikhat, N. Chauveau and J. P. Morucci, In vitro tissue characterization and modelling using electrical impedance measurements in the 100 Hz–10 MHz frequency range, Physiol. Meas., 16, A15-A28, 1995.

[39] N. Chauveau, L. Hamzaoui, P. Rochaix, B. Rigaud, J. J. Voigt and J. P. Morucci, Ex Vivo Discrimination between normal and pathological tissues in human breast surgical biopsies using bioimpedance spectroscopy, Electrical Bioimpedance Methods:applications to medicine and biotechnology, NY academy of sciences, ANYAA9 873, pp 42-50, 1999.

[40] C. Aligne, N. Chauveau, B. Rigaud and J. P. Morucci, Normal and tumoral tissue modelling from in vivo spectrometric measurements of electrical bioimpedance, Innov. Tech. Biol. Med., 16(6), pp 688-693, 1995.

[41] H. Kanai, K. Sakamoto and M. Haeno, Electrical measurement of fluid distribution in human legs: Estimation of extra- and intracellular fluid volume, J. Microw. Power, 18, pp 234-243, 1983.

[42] J. G. Kirkwood and R. M. Fuoss, Anomalous Dispersion and Dielectric Loss in Polar Polymers, J. Chem. Phys., 9, pp 329-340, 1941.

[43] D. W. Davidson and R. H. Cole, Dielectric Relaxation in Glycerol, Propylen Glycol, and *n*-Propanol, J. Chem. Phys., 19, pp 1484-1490, 1951.

[44] K. R. Foster, J. L. Schepps, R. D. Stoy and H. P. Schwan, Dielectric properties of brain tissue between 0.01 and 10 GHz, Phys. Med. Biol., 24, 1979.

[45] C. W. Groetch, Inverse Problems in the Mathematical Sciences, Vieweg, Wiesbaden, 1993.

[46] J. R, Macdonald and M. K. Brachman, Linear System Integral Transform Relations, Reviews of Modern Physics, 28, No. 4, pp 393-422, 1956.

[47] A. Talbot, The Accurate Numerical Inversion of Laplace Transforms, J. Inst. Math. Appl., 23, 1979.

[48] M. Rizzardi, A Modification of Talbot's Method for the Simultaneous Approximation of Several Values of the Inverse Laplace Transform, ACM Trans. Math. Software, 21, No. 4, pp. 347-371, 1995.

[49] A. R. Davies and R. S. Anderssen, Sampling Localization in Determining the Relaxation Spectrum, J. Non-Newtontian Fluid Mechanics, Vol. 73, pp 163-179, 1997.

[50] R. S. Anderssen and A. R. Davies, Simple Moving Average Formulae for the Direct Recovery of the Relaxation Spectrum, Mathematics Research Report No. MMR 016-98, 1998.

[51] A. R. Davies and R. S. Anderssen, Sampling Localisation, Duality Algorithms and the Kramers-Kronig Relations, Mathematics Research Report No. MMR 017-98.

[52] D. Porter and D. S. G. Stirling, Integral Equations, Cambridge Texts in Applied Mathematics, Cambridge, U.K.: University Press, 1990.

[53] C. W. Groetch, The theory of Tikhonov requalarisation for Fredholm equations of the first kind, Pitman, London, 1984.

[54] W. R. Breckon, Image Reconstruction in Electrical Impedance Tomography, PhD thesis, Oxford Polytechnic, 1991.

[55] J. Honerkamp and J. Weese, Tikhonov regularisation method for ill–posed problems, Continuum Mech. Thermodyn., 2, pp 17-30, 1990.

[56] M. Vauhkonen, Electrical Impedance Tomography and Prior Information, PhD thesis, University of Kuopio, 1997.

[57] J. R. Pere and C. Lapaz, Practical Limits of the Kramers-Kronig Relationships applied to experimental bioimpedance data, Electrical Bioimpedance Methods: applications to medicine and biotechnology, New York Academy of Sciences, New York, 1999.

[58] M. Osypka and E. Gersing, Tissue impedance spectra and the appropriate frequencies for EIT, Physiol. Meas., Vol 16, pp A49-A55, 1995.

[59] C. W. L. Denyer, F. J. Lidgey, Q. S. Zhu and C. N. McLeod, A high output impedance current source, Physiol. Meas., Vol 15, pp A79-A82, 1994.

[60] C. W. L. Denyer, Electronics for real–time and three–dimensional electrical impedance tomographs, PhD thesis, Oxford Brookes University, 1996.

[61] R. E. Schmukler and J. W. Dixon, Microprocessor controlled bioimpedance measurements, Proc. 14th Annual Int. Conf. IEEE–EMBS ed J. P. Morucci, R. Plondey, J. L. Coatrieux and S. Laxminarayan (Piscataway, NJ: IEEE), pp 2381-2, 1992.

[62] B. Rigaud, L. Hamzaoui, N. Chauveau, M. Granie, J-P. S. Di Rinaldi and J. P. Morrucci, Tissue characterisation by impedance: a multifrequency approach, Physiol. Meas., 15, A13-A20, 1994.

[63] E. Gersing, Measurement of electrical impedance in organs - measuring equipment for research and clinical applications, Biomedizinische Technik, 36(4), 6-11, 1991.

[64] J. Conway, Electrical impedance tomography for thermal monitoring of hypethermia treatment: an assessment using *in vitro* and *in vivo* measurements, Clin. Phys., Physiol. Meas., 8, Suppl. A, pp 141-6, 1987.

[65] H. P. Schwan, Electrode polarization impedance and measurement in biological materials, Ann. Biomed. Eng., 20 (3), pp 269-288, 1992.

[66] P. Steendijk, G. Mur, E. T. Van der Velde and J. Baan, The four electrode resistivity technique in anisotropic media: theoretical analysis and the application on myocardial tissue *in vivo*, IEEE Tran. Bio. Med. Eng., Vol. 40, 11, 1993.

[67] H. P. Schwan, Determination of biological Tissues, Physical Techniques in Biological Research, New York Academic, 1963.

[68] M. Valentinuzzi, J. P. Morucci, C. J. Felice and E. Martinez, Bioelectrical impedance techniques in medicine - Part II - Monitoring of physiological events by impedance, Crit. Rev. Biomed. Eng., vol 24, N 4-6, 1996.

[69] K. R. Visser, R. Lamberts and W. G. Zijlstra, Resistivity of stationary and flowing human blood, Proc. VIth Int. Conf. Electrical Bioimpedance, pp 69-72, 1983.

[70] M. A. Stuchly and S. S. Stuchly, Dielectrical properties of biological substances–tabulated., J. Microwave Power, Vol 15, pp 19-26, 1980.

[71] E. Gersing, E. Burger, M. M. Gebhard, G. Kehrer, A. Mari, A. Meissner and H. J. Bretschneider, Impedance spectroscopy of tissue structure alternations during organ ischemia, Proc. 8th ICEBI, Kuopio, Finland, Kuopio: Kuopio university printing office, pp 176-178, 1992.

[72] M. Schäfer, H. J. Kirlum, C. Schlegel and M. M. Gebhard, Dielectric properties of skeletal muscle during ischemia in the frequency range from 50 Hz to 200 MHz, Electrical Bioimpedance Methods: Applications to medicine and Biotechnology, New York Academy of Sciences, pp 59-64, 1999.

[73] H. P. Schwan, Analysis of dielectric data: experience gained with biological materials, IEEE Trans. Electr. Insul., EI-20.6, pp 913-922, 1985.

[74] P. Heroux and M. Bourdages, Monitoring living tissues by electrical impedance spectroscopy, Ann. Biomed. Eng., 22, pp 328-337, 1994.

[75] M. P. Bolton, L. C. Ward, A. Khan, I. Campbell, P. Nightingale, O. Dewit and M. Elia, Sources of error in bioimpedance spectroscopy, Physiol. Meas., Vol. 19, pp 235-245, 1998.

[76] E. Gersing, G. Kehrer and M. Schäfer, Characterization of organ tissue during the transition from life to death: impedance of the liver, Proc. of EMBEC, Vol 37, Suppl. 2, pp 98-99, 1999.

[77] O. Casas, R. Bragos, P. J. Riu, J. Rosell, M Tresanchez, M. Warren, A. Rodriguez–Sinovas, A. Carreno, and J. Cinca, *In vivo* and *in situ* ischemic tissue characterization using electrical impedance spectroscopy, Electrical Bioimpedance methods: applications to medicine and biotechnology, NY Academy of Sciences, Vol. 873, pp 51-58, 1999.

[78] D. Voloder, M. Petrunic, I. Tonkovic, The detection of leg's ischemic didorders using bioimpedance measurement, Proc. of EMBEC, Vol 37, Suppl. 2, pp 96-97, 1999.

[79] H. G. Linhart, E. Gersing, M. Schäfer and M. Gebhard, The electrical impedance of the ischemic heart at low frequencies, IX ICEBI, pp 207-210, Heidelberg, 1995.

[80] M. M. Gebhard, E. Gersing, C. J. Brockhoff, PH. A. Schnabel, H. J. Bretschneider, Impedance specroscopy: a method for surveillance of the ischemia tolerance of the heart, Thorac. Cardiovacs. Surg., vol. 35, pp 26-32, 1987.

[81] E. Gersing, B. Hofmann, G. Kehrer and R. Pottel, Modelling based on tissue structure - the example of porcine liver, Innov. Tech. Biol. Med., vol. 16, N 6, pp 671-678, 1995.

[82] M. Schäfer, C. Schlegel, H–J. Kirlum, E. Gersing, M.M. Gebhard:Monitoring of damage to skeletal muscle tissues caused by ischemia, Bioelectrochemistry and Bioenergetics, 45, pp 151-155, 1998.

[83] G. Kehrer, A. Aminalai, E. Gersing, P. Lamesch, A. Meissner, W. D. Schareck, J. Richter and H. J. Bretschneider, Glycogen effect on energy state and passive electric properties of liver during protection, Z. Gastroenterol., 28, pp 147-156, 1990.

[84] E. Gersing, Impedance spectroscopy on living tissue for determination of the state of organs, Bioelectrochemistry and Bioenergetics, 45, pp 145-149, 1998.

[85] M. Gheorghiu, E. Gersing, A unitary, quantitative procedure to analyse impedance spectra of ischemic tissue, Proc. of EMBEC, Vol 37, Suppl. 2, pp 94-95, 1999.

[86] M. Schäfer, E. Gersing and M. M. Gebhard, Characterisation of organ tissue during the transition between life and death: cardiac amd skeletal muscle, Proc. of EMBEC, Vol 37, Suppl. 2, pp 100-101, 1999.

[87] H. Schichlein, A. Muller, M. Voigts, A. Krugel and E. Ivers–Tiffee, System indentification of SOFC oxygen reaction parameters by distribution of relaxation times, Solid oxide Fuel Cells VII, Electrochem. Soc. Proc. Ser., Pennington NJ, 2001.

[88] H. Schichlein, A. Muller, A. Krugel and E. Ivers–Tiffee, Calculation of the distribution of polarisation mechanisms in SOFC single cell operation by Fourier analysis of impedance spectra, Proc. 4th European SOFC forum, A. McEvoy, Editor, p.325, Luzern, 2000.

List of Figures

List of Tables

Appendix A

MatLab programming

A.1 List of software

1. *DRT_eps.m* and *DRT_z_data.m* - these two main programs reconstruct DRT distributions from permittivity or impedance data respectively and display it as well as find time constants and their amplitudes. The programs include several functions listed below:

   - *Kevin.m* - the main function that returns vectors $\mathbf{G}'$, $\mathbf{G}''_{even}$, $\mathbf{G}''_{odd}$ and $\mathbf{G}$. It calls the following subprograms:
     - *gauleg.m* - returns Gauss–Legendre abscissas and weights;
     - *k1pipj.m* - calculates matrix $\mathbf{K}'$;
     - *k2pipj.m* - calculates matrices $\mathbf{K}''_{even}$ and $\mathbf{K}''_{odd}$;
     - *k.m* - calculates the total matrix $\mathbf{K}$;
     - *data_vector.m* - returns data vectors $\mathbf{S}'$ and $\mathbf{S}''$;
     - *inverse.m* - solves equation 4.50 applying SVD and Tikhonov regularisation and returns vectors $\mathbf{G}'$, $\mathbf{G}''_{even}$ and $\mathbf{G}''_{odd}$;
     - *inversetot.m* - returns vector $\mathbf{G}$;
   - *Kevin_trapez.m* - the same function as *Kevin.m* but applying trapezoidal rule for calculating data vectors. This program calls all functions listed above.
   - *S_funct.m* - a program–function for inversion $Z \rightarrow \sigma \rightarrow \varepsilon \rightarrow Q \rightarrow S$.
   - *distribution.m* - projection of vectors $\mathbf{G}'$, $\mathbf{G}''_{even}$ and $\mathbf{G}''_{odd}$ into the space spanned by the basis functions.
   - *time_peaks.m* - finds maximums of DRT distribution: their amplitudes and time constants.

2. *fit.m* - fits Gaussian curves and calculates areas under each peak. It calls a function *fit_gauss* which does a least squares curve fitting.

3. *area.m* - calculates area of well–separated DRT peaks.

4. *time_evolution.m* - displays the evolution of permittivity and conductivity during ischemia time at any frequency.

5. *noise.m* - a noise simulation code.It calls *raw_data.m* that generates a frequency responses doe single, two and three RC circuits.

6. *readLabView_txt.m* - a program for reading data from a file saved by LabView control program;

A.2 MatLab Source Code

The main program for DRT reconstruction:

```
%% Program for reconstruction of DRT %%

clear;

i=0;
for k=20:20 % for liver_5

%%  Input data: load file  %%

filename=strcat('C:\Work\Schaefer\Liver_5\Permit\liv_eps.',num2str(k),'7');
data=load(filename);
freq=data(:,1);
Eps_Re=data(:,2);
loss=data(:,3);
Sig_Re=data(:,4);

%%   setting of the same frequency range %%

ind1=find(freq==12.022649769999992);
freq=freq(ind1:length(freq));
Eps_Re=Eps_Re(ind1:length(Eps_Re));
loss=loss(ind1:length(loss));
Sig_Re=Sig_Re(ind1:length(Sig_Re));
```

```
Sig_0=Sig_Re(1);

%%  Setup of extreme values %%

omega=freq.*2*pi;
Eps0=8.85*1e-12; Eps_inf=50;
Eps_st=3e+008;
%Eps_inf=0;
Eps_Im=loss+Sig_0./(Eps0.*omega);

%%   Transfer permittivity to S-functions  %%

Q_Re=(Eps_Re-Eps_inf)./(Eps_st-Eps_inf);
Q_Im=Eps_Im./(Eps_st-Eps_inf);
S_Re=-Q_Im.*omega;
S_Im=Q_Re.*omega;

%%  Display re & im parts of permit against log(freq)  %%

figure(1);
loglog(freq,Eps_Re,'kx','LineWidth',1.5,'MarkerSize',3);
xlabel('lg(freq,Hz)','FontSize',12);
hold on;
loglog(freq,-Eps_Im,'k');
grid on;
hold on;
loglog(freq,Sig_Re,'kx','LineWidth',1.5,'MarkerSize',3);
hold on;

%%  Display re(permit) against im(permit) %%

figure(2);
plot(Eps_Re,-Eps_Im);
hold on;
grid on;

%%  Setup of parameters for DRT  %%

N=length(freq); Fmin=freq(1); Fmax=freq(length(freq));
```

```
a=log(Fmax/sqrt(Fmin.*Fmax)); v=[-a:0.05:a];
omega0=2*pi*sqrt(Fmin.*Fmax); t=exp(v)/omega0; tau0=1/omega0;

%% Generating vector of ischemia times  %%

%if k==0
%   time=7;
%else
%   time=strcat(num2str(k),'7'); %for liver5
%   time=str2num(time);          %for liver5
%    time=k;                     %for liver2
%end % if

%TIME(:,i)=time;

%%%  Calculation of DRT  %%

Mu=0.001;                % Tikhonov parameter
M=20;                    % 2*M - number of the basis functions

for j=1:1
   [G2e,G2o,G1,G]=kevin(omega,S_Re,S_Im,Mu,M);
   [dis1,dis2,dis]=distribution(a,v,G2o,G2e,G1,G,M);
   [taus1,amp1]=time_peaks(t,dis1);
   [taus2,amp2]=time_peaks(t,dis2);
   [taus,amp]=time_peaks(v,dis);

   DIS1(:,j)=dis1;                % from real part
   DIS2(:,j)=dis2;                % from imaginary part
   DIS(:,j)=dis;                  % total from real+imag
%   TAUS2(i,:)=taus2(1:3);
%   AMP2(i,:)=amp2(1:3);
%   TIME(:,i)=time;
   Mu=Mu*10;
end %for j

%%  Display of DRT   %%

figure(4);
```

```
%subplot(1,3,1);
%plot(v,DIS1,'r');
%ylim([0 20000]);
%ylim([0 11e+3]);
%title('DRT for canine liver during ischemia');
%hold on;
%grid on;

%subplot(1,3,2);
%plot(v,DIS2,'k');
%axis([-5 5 0 1.5e+5])
%grid on;
%hold on;

%subplot(1,3,3);
plot(v,DIS,'b','LineWidth',3,'MarkerSize',3);
xlabel('v=ln(\tau/\tau_0)','FontSize',14);
ylabel('G(v)','FontSize',14); text(3,0,['(\tau_0 \approx
',num2str(tau0),' s)'],'FontSize',12); ylim([0
(max(amp)+max(amp)/5)]);
%xlim([-5 5]);
grid on; hold on;

end % for k

%% Display of evolution of DRT amplitudes during ischemia  %%

%figure(4);
%plot(TIME,AMP2(:,3),'k');
%grid on;
%hold on;

%% Display of evolution of DRT time constants during ischemia  %%

%figure(5);
%ylim([0 1e-7]);
%plot(TIME,TAUS2(:,3),'k');
%grid on;
%hold on;
```

The program for the inversion of impedance data into permittivity data:

```
function [S_Re,S_Im]=Sfunc(omega,z,ph);

%calculates S-functions
%note: frequency is in Hz

Sigma=1./z;
PhSigma=-ph;
%omega=freq.*2*pi;


Sig_Re=Sigma.*cos(PhSigma*pi/180);
Sig_Im=Sigma.*sin(PhSigma*pi/180); Sigma0=Sig_Re(1);

EpsV=8.85e-12;
k=(1./(omega*EpsV));
b=diag(k);
Eps_Re=b*Sig_Im;                % ~ Sig_Im/(omega*EpsV)
Eps_Im=-b*(Sig_Re-Sigma0); % ~(Sig_Re-Sigma0)/(omega*EpsV)

%Epsinf=4;
Eps0=Eps_Re(1);
Epsinf=Eps_Re(length(Eps_Re));

Q_Re=(Eps_Re-Epsinf)./(Eps0-Epsinf);
Q_Im=Eps_Im./(Eps0-Epsinf);

S_Re=-diag(omega)*Q_Im;      % ~-Q_Im*omega
S_Im=diag(omega)*Q_Re;
```

The MatLab implementation of the GRIM:

```
function [G2e,G2o,G1,G]=kevin(omega,S_Re,S_Im,Mu,M)

%the program solves the inverse problem K*Gv=S &
%returns Gv as input to distribution.m

%use: splines are used to get S-vectors for Gauss points
```

```
Fmin=omega(1);                    % freq*2*Pi
Fmax=omega(length(omega));    % freq*2*Pi
N=length(omega); a=log(Fmax/sqrt(Fmin*Fmax));
omega0=sqrt(Fmin*Fmax);

% CALCULATE GAUSS-LEGENDRE INTEGRATION WEIGHTS

[Xomg,Womg]=gauleg(-a,a,2*M); %Gauss abscissas and weights
Xtau=Xomg;
Wtau=Womg;
xlomg=Xomg./a;                    % scale to [-1,1]

% CALCULATE LEGENDRE POLYNOMIALS AT GAUSS-POINTS

for j=1:2*M
   p0omg=legendre(j,xlomg);
   pomg(j,:)=p0omg(1,:);
end
Pomg=cat(1,ones(1,2*M),pomg);  % Legendre polynomial for basis function

% NORMALISE MONIC LEGENDRE POLYNOMIALS TO ORTHONORMALISE

i=[1:2*M+1]';
NORM=sqrt((i-1+1/2)/a);
NORMd=diag(NORM);
Bomg=NORMd*Pomg;                  % basis functions
Btau=Bomg;

% CALCULATE DISCRETISD MATRIX K1

[K1]=k1pipj(Bomg,Btau,Xomg,Xtau,Womg,Wtau,M);% return K1

% CALCULATE DISCRETISD MARICES K2even, K2odd

[K2even,K2odd]=k2pipj(Bomg,Xomg,Womg,M); %return K2even, K2odd

%CALCULATE COMPLETE MATRIX Ktot=(K1,K2)
```

```
[Ktot]=k(K1,K2even,K2odd,M);

% CALCULATE DATA MATRIX S1

omega_sp=omega0*exp(Xomg);
S_Re_sp=spline(omega,S_Re,omega_sp);    % finding reals at Gauss points
[S1]=data_vector(Bomg,Womg,S_Re_sp);    %using 16 Gauss points
S1=S1(1:2*M)';

% CALCULATE DATA MATRIX S2even and S2odd

S_Im_sp=spline(omega,S_Im,omega_sp);    % finding Imags at Gauss points
[S2]=data_vector(Bomg,Womg,S_Im_sp);    %only 20 Gauss points
S2=S2(1:2*M)';
p1=1:2:length(S2);                      %odd rows
p2=2:2:length(S2);                      %even rows
S2even=S2(p1); S2odd=S2(p2);

% CALCULATE COMPLETE DATA VECTOR Stot

Stot=cat(2,S2,S1);

% SOLVE K2even*Gv2e=S2even

[G2e,ue,se,ve,s1e]=inverse(K2even,Mu,S2even);

%SOLVE K2odd*Gv2o=S2odd

[G2o,uo,so,vo,s1o]=inverse(K2odd,Mu,S2odd);

%SOLVE K1*Gv1=S1

[G1,u,s,v,s1]=inverse(K1,Mu,S1);

%SOLVE Ktot*G=Stot

[G,ut,st,vt,s1t]=inversetot(Ktot,Mu,Stot,M);

%CALCULATE VECTOR Gve, Gvo and Gv1
```

```
Btau=Btau(1:2*M,:); p1=1:2:length(Btau); p2=2:2:length(Btau);
dise=Btau(p1,:)'*G2e; diso=Btau(p2,:)'*G2o;
dis=dise+diso;   % reconstruction of DRT only at Gauss points

% PICTURES
%amplification factor A=f(singular values)

%figure(1);
%subplot(1,3,1);
%plot(diag(se),1./s1e,'k');
%y=axis;
%xlabel('singular values');
%ylabel('Aeven');
%grid on;
%hold on;

%subplot(1,3,2);
%plot(diag(so),1./s1o,'k');
%axis(y);
%title('Amplification factor');
%xlabel('singular values');
%ylabel('Aodd');
%grid on;
%hold on;

%subplot(1,3,3);
%plot(diag(s),1./s1,'k');
%xlabel('singular values');
%ylabel('A');
%grid on;
%hold on;

% singular values

%figure(2);
%subplot(1,3,1);
%le=(diag(se));
```

```
%plot(1:length(se),log(le),'k');
%hold on;
%xlabel('n');
%ylabel('log(Sval)');
%grid on;

%subplot(1,3,2);
%lo=(diag(so));
%plot(1:length(so),log(lo),'k');
%title('Log Singular Value of K"e, K"o,K''');
%hold on;
%xlabel('n');
%ylabel('log(Sval)');
%grid on;

%subplot(1,3,3);
%l=(diag(s));
%plot(1:length(s),log(l),'k');
%hold on;
%xlabel('Singular Number');
%ylabel('log(Singular Value)');
%grid on;

% plot of S-data

%figure(6);
%subplot(1,2,1);
%plot(1:length(S2),S2);
%title('S"-data');
%hold on;
%grid on;

%x=u'*S2';

%subplot(1,2,2);
%plot(1:length(x),x);
%title('U*S');
%hold on;
%grid on;
```

Appendix B

Data Acquisition Control program (Delphi)

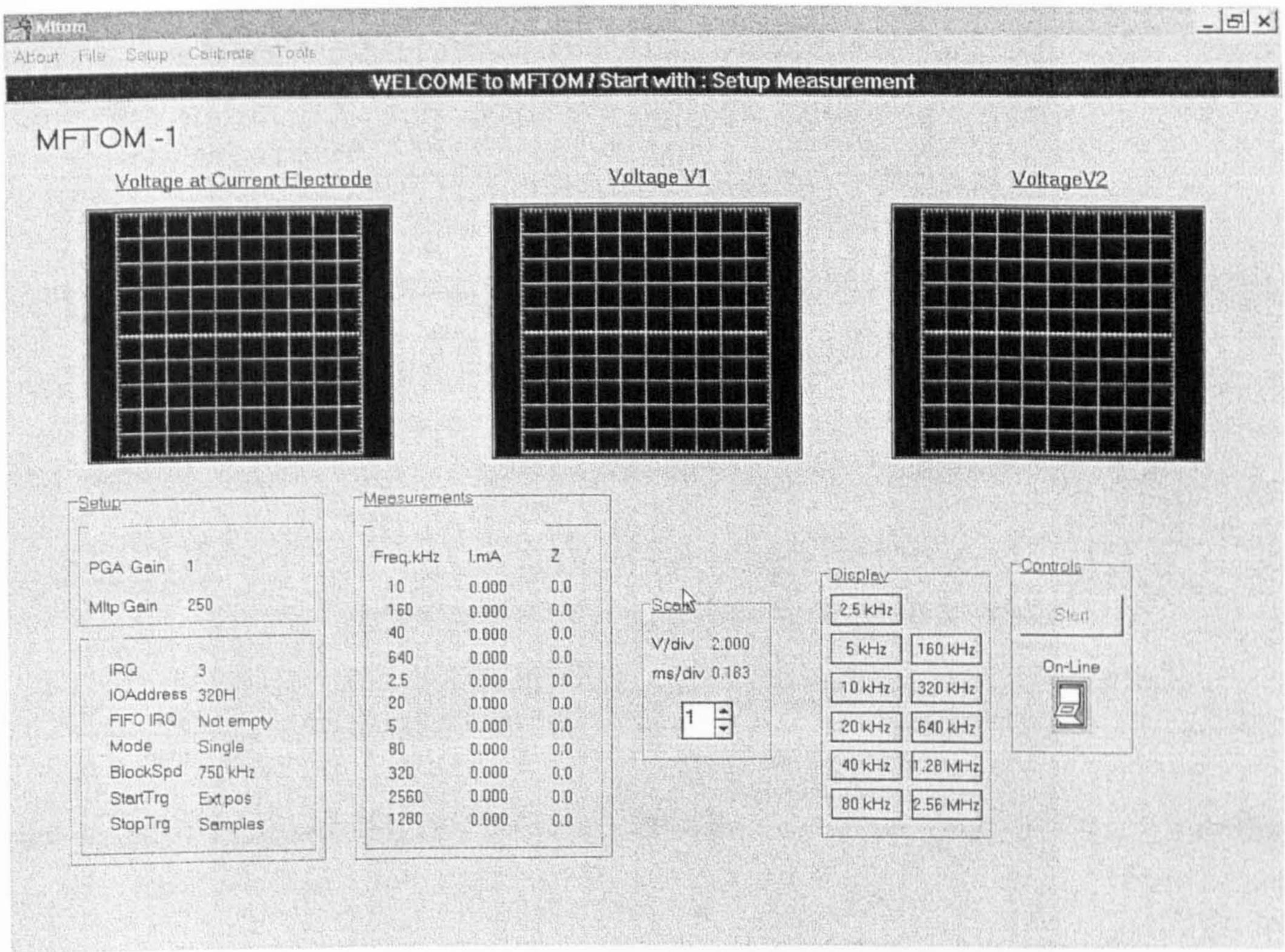

Figure B.1: *The main front panel of Delphi program.*

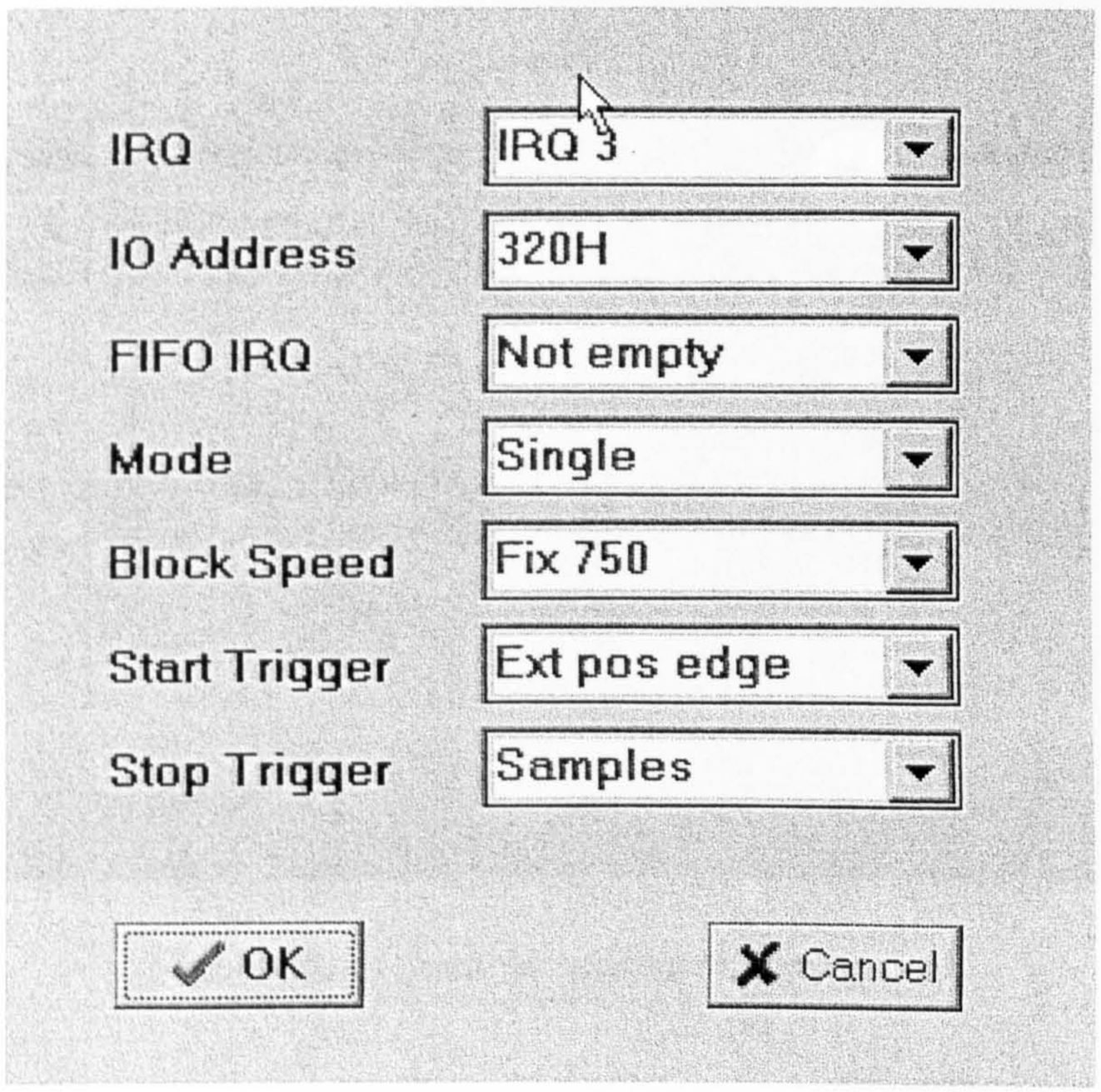

Figure B.2: *ADC panel.*

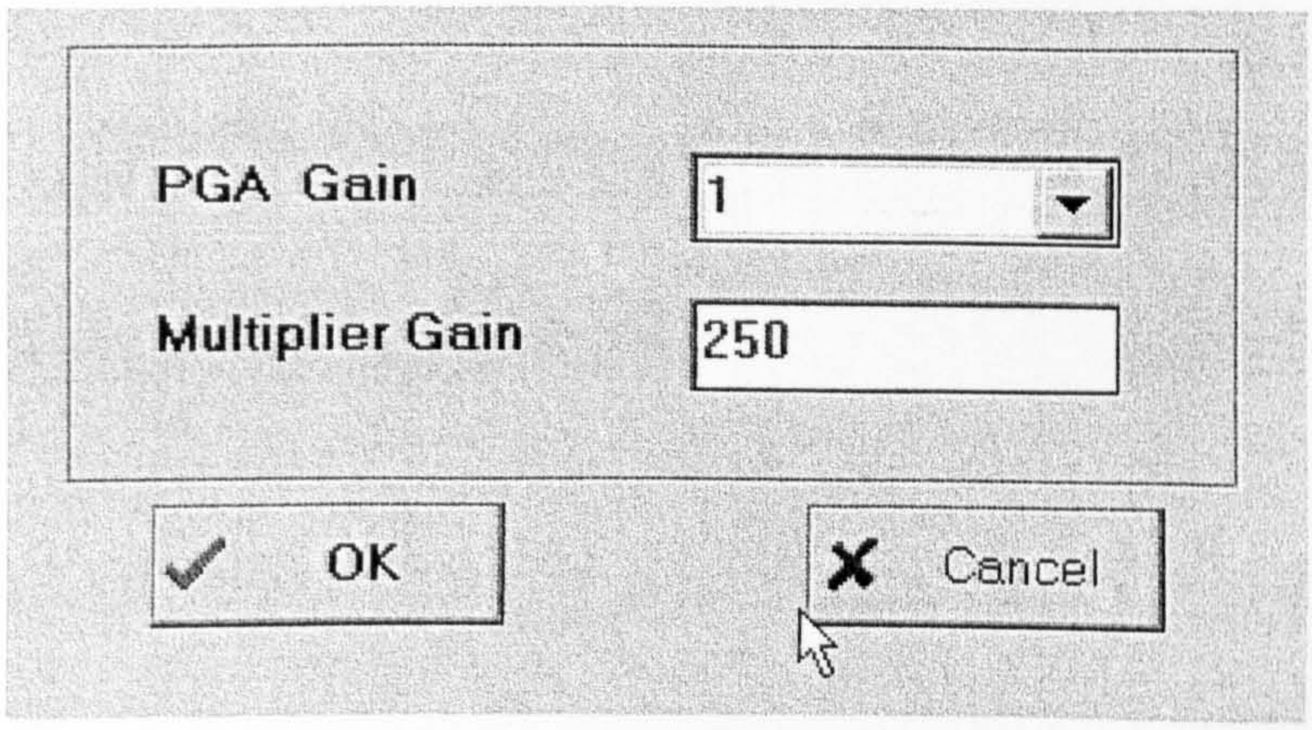

Figure B.3: *Gain panel.*

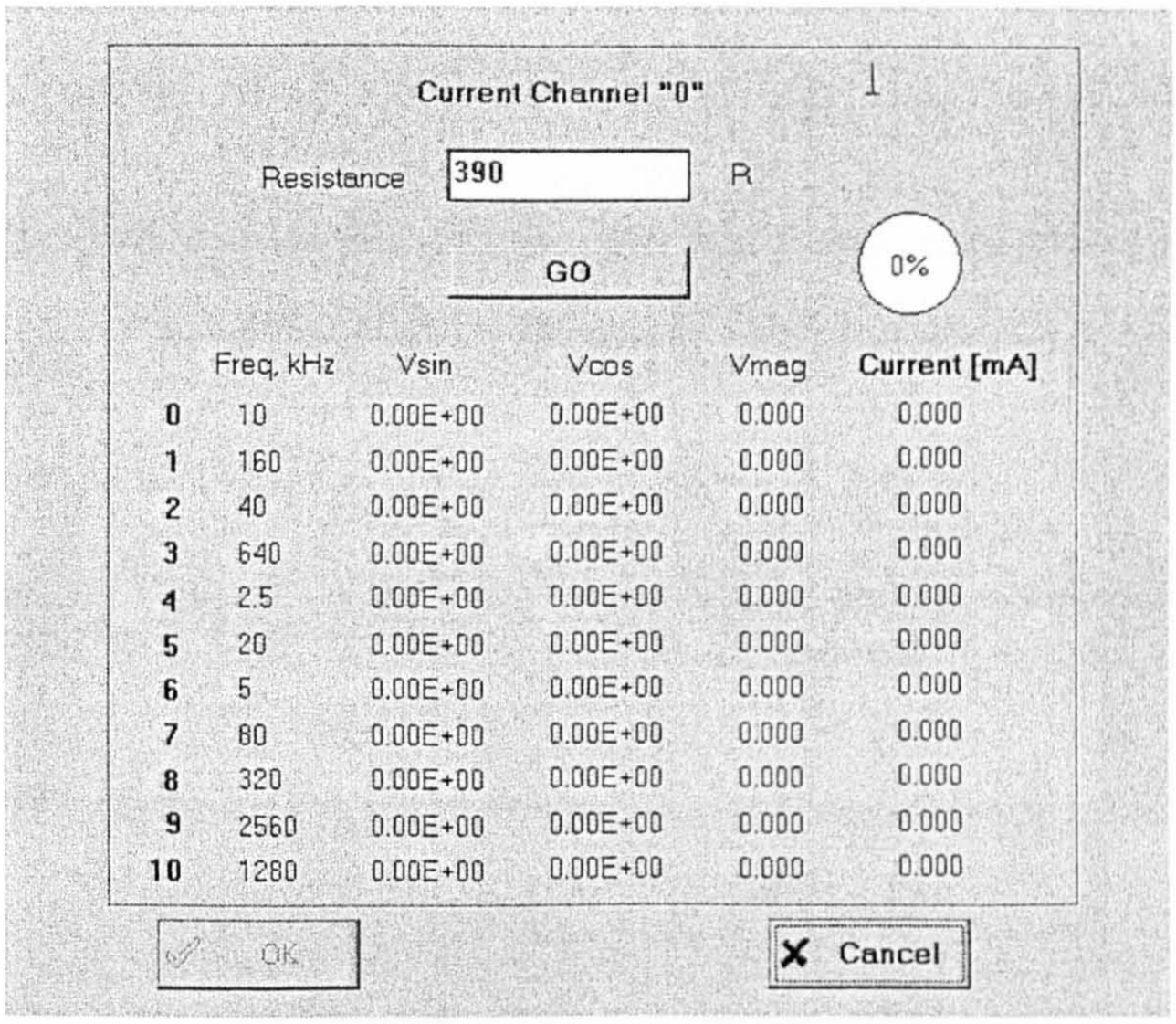

Figure B.4: *Current measurements panel.*

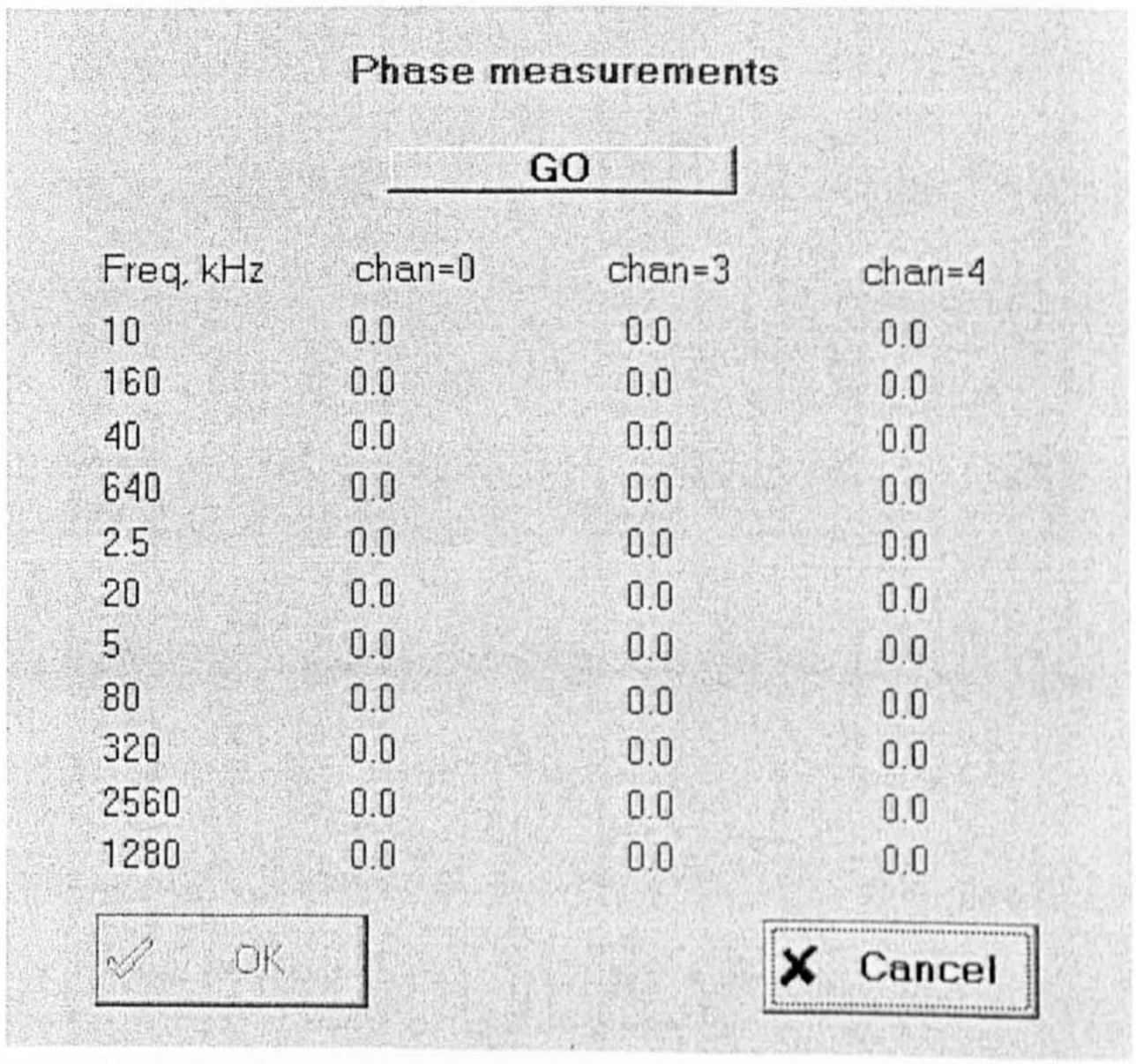

Figure B.5: *Phase measurements panel.*

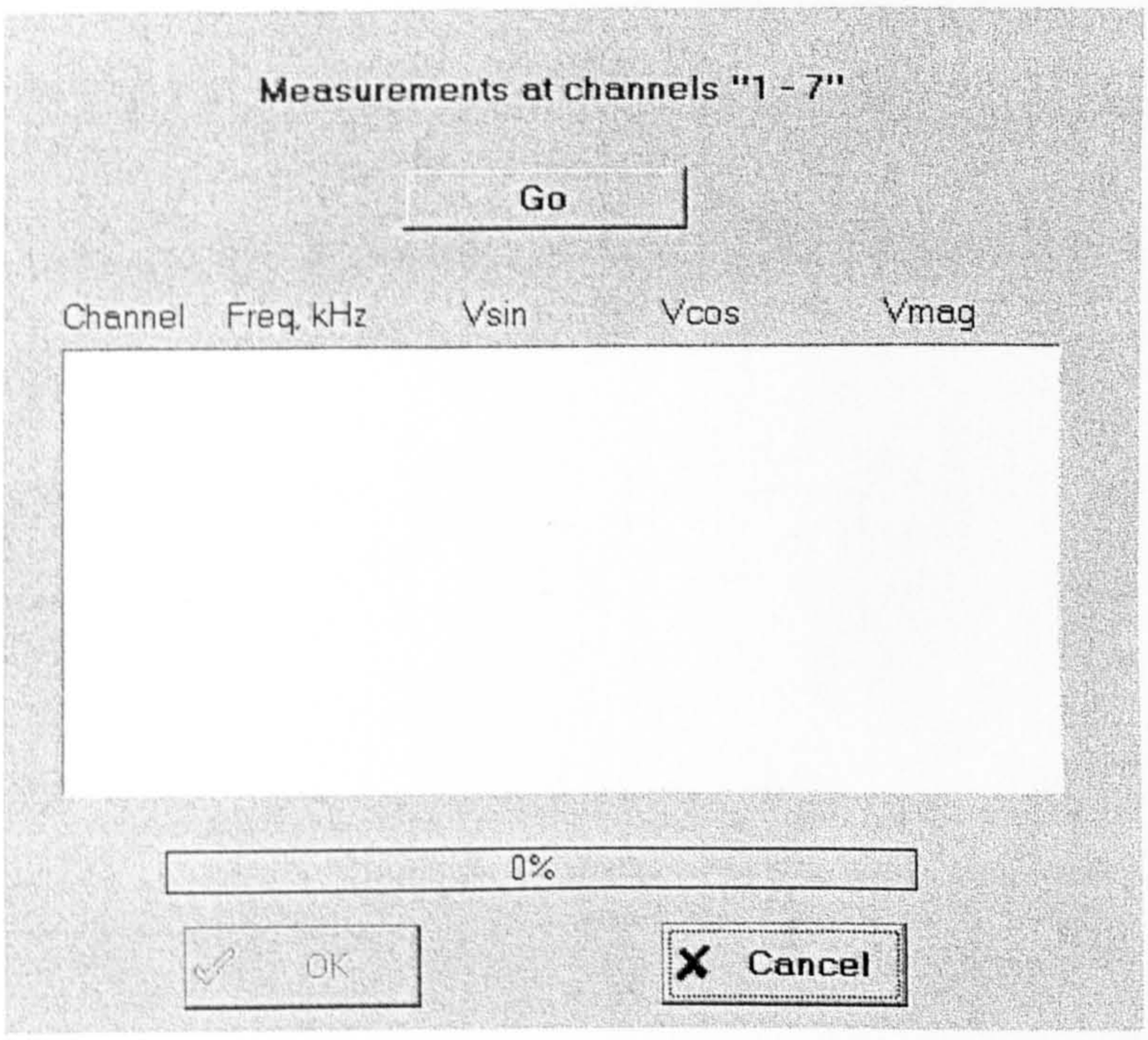

Figure B.6: *Voltage measurements panel.*

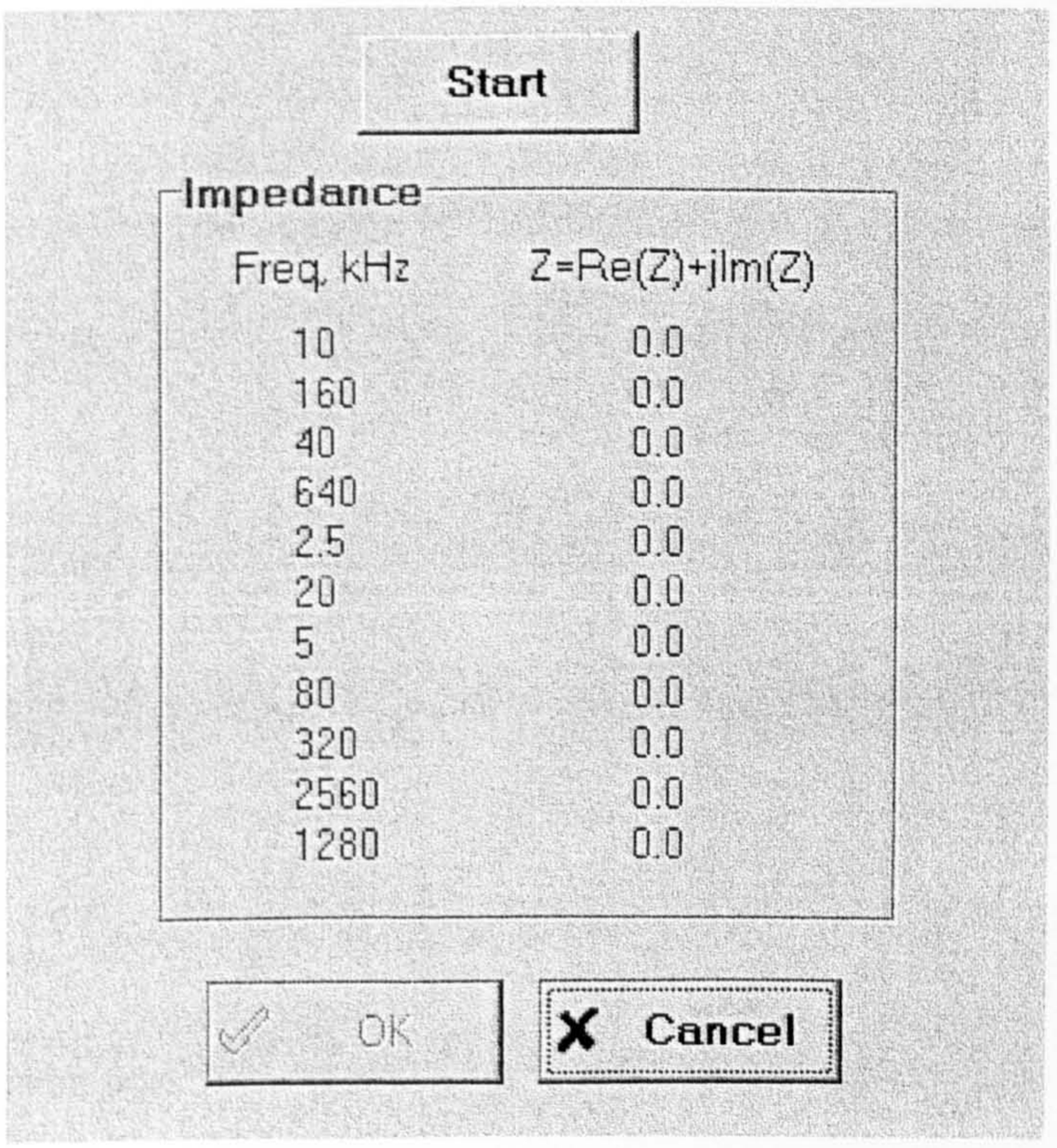

Figure B.7: *Impedance panel.*